STATISTICAL ANALYSES FOR COASTAL HAZARD DATASETS PHAM T. D. 2016

NANYANG TECHNOLOGICAL UNIVERSITY

STATISTICAL ANALYSES FOR COASTAL HAZARD DATASETS: CASE STUDIES OF WASHOVER SEDIMENTATION FROM STORMS AND TSUNAMIS, AND SEA-LEVEL RECORDS FROM TIDE GAUGES.

PHAM TIEN DAT

ASIAN SCHOOL OF THE ENVIRONMENT

2016

STATISTICAL ANALYSES FOR COASTAL HAZARD DATASETS: CASE STUDIES OF WASHOVER SEDIMENTATION FROM STORMS AND TSUNAMIS, AND SEA-LEVEL RECORDS FROM TIDE GAUGES.

PHAM TIEN DAT

PHAM TIEN DAT

Asian School of the Environment

A thesis submitted to the Nanyang Technological University
in fulfilment of the requirement for the degree of Doctor of Philosophy

2016

Acknowledgements

I would not have completed my five-year Ph.D. without the help of others. I have been most fortunate in having Dr. Adam Switzer as my advisor, for he has directed me toward a research topic that best suited my interests and my future career, encouraged me when I felt low and always believed in what I did.

I am also grateful to my two mentors, Dr. Chris Gouramanis and Dr. Aron Meltzner, whose challenging questions have developed my critical thinking. Chris guided me through statistical techniques and taught me during many field trips. Aron provided me with feedback on my initial ideas of tide and sea-level studies and greatly contributed to my research. Special thanks go to Drs. Emma Hill and Charles Rubin for their help during the early days of my Ph.D. I also owe a big thanks to Pavel Adamek, who patiently taught me writing and presentation skills and helped me improve the clarity of my research publications.

Other people I am indebted to for helping me in various ways include my international collaborators, Kruawun Jankaew, Brian Jones, Paul Carr, Gabriel Huerta, Ben Horton, Nguyen Minh Huan and Nguyen Xuan Hien. My friends and groupmates also deserve a special word of appreciation: Lea Soria, Constance Chua, Wenshu Yap, Jedrzej Majewski (Yen), Stephen Chua, Sorbi Ildefonso, Dr. Li Linlin, Dr. Fengling Yu, Dr. Park Hee Yoon, Dr. Jeremy Pile, Riovie Ramos, Qiu Qiang, Yudha Djamil, Sagar Masuti, Christina Tee, Taufiq Mohta, Jani Tanzil, Liqing Jiao.

Finally, my heartfelt thanks must go to my wife, Nguyen Thi Minh Hue, and my daughter, Pham Anh Vien (Vivian), for their unconditional support and patience during my absence from home.

Table of Contents

Summary

Coastal hazard assessments commonly require the integration of different data sets that, in turn, require different statistical techniques to reveal underlying processes. In this thesis, I present three studies in which I apply and develop different statistical methods for a broad sedimentological data set and sea-level time series. In the first study, I use a number of statistical analyses to examine the use of grain size parameters, mineral composition and trace element geochemistry in determining the provenance of tsunami (the 2004 Indian Ocean Tsunami (IOT) and three paleo-tsunami) deposits and the 2007 storm surge deposit on Phra Thong Island, Thailand. I also evaluate whether the 2004 IOT tsunami and 2007 storm deposits could be discriminated using grain size and geochemistry. The key findings are that geochemistry data are statistically inadequate to distinguish the provenance of modern storm and tsunami deposits, but the mean grain size is probably a good discriminator. In addition, the sediment sources of each of the overwash deposits are diverse. In the second study, I investigate interannual sea-level variations using sea-level records at ten tide gauges (TGs) around the South China Sea (SCS). The results reveal that the ENSO significantly contributes to interannual sea-level signals but that its influences vary across the study area, whereas the winter monsoon clearly impacts sea level in the northern SCS. In the third study, I examine spatio-temporal variation of extreme sea level (ESL) around the SCS. The results reveal contrasting mechanisms for generating surges in the northern and southern SCS; and that the changes in ESL are broadly consistent with the changes in mean sea level. I also calculate the temporal variability of the return levels and show they are significantly correlated with climatic variability in the region.

List of Figures

List of Tables

Chapter 1:

Introduction

When you can measure what you are speaking about, and express it in numbers, you know something about it.

- Lord Kelvin -

Coastal zones are home to approximately 625 million people and most mega-cities on earth, and the coastal population is predicted to further rise to between 879 million and 949 million people by 2030 [*Neumann et al.*, 2015]. Despite having favorable conditions and rich natural resources, coastal zones are highly susceptible to coastal processes and hazards impacting at different time frames: from hours to days (e.g., typhoons, tsunamis, coastal flooding events) to years, decades or centuries (e.g., sea-level rise) [e.g., *Hanson et al.*, 2011; *Switzer et al.*, 2014; *Syvitski et al.*, 2009]. Recent studies suggest that more than 200 million people are at risk of coastal flooding by extreme events [e.g., *Nicholls*, 2010]. Since the dawn of the 21st century, the world has witnessed a series of destructive (mostly) tsunamigenic and cyclonic events that have occurred across different ocean basins including the 2004 Indian Ocean tsunami, Hurricane Katrina (2005), Cyclone Nargis (2008), the Tohoku-oki tsunami (2011), Hurricane Sandy (2012), Typhoon Haiyan (2013) and Hurricane Patricia (2015).

Severe damage and devastating loss caused by these disasters have been reported elsewhere, but such coastal hazards highlight concerns as to how we can better assess coastal risks and prepare coastal communities. To do that, collecting, processing and analyzing coastal hazard data sets are crucial [*Switzer et al.*, 2014].

Storms and tsunami events are among the deadliest coastal disasters globally and they can result in massive damage immediately as they slam into low-lying coastal areas. Increasingly frequent coastal flooding events have occurred recently and globally, which invariably leads to “where and when is next” questions regarding the recurrence intervals of both storms and tsunamis. To determine the recurrence of such events at given sites, modern and historical events need to be studied in order to characterise the worst plausible extreme event and when (roughly) similar cases might happen [*Switzer et al.*, 2014]. In this sense, historical written records can help to uncover past events [*Williamson et al.*, 2015]. For example, *Li et al.* [2015] utilized historical records to reconstruct and unveil the cause of an 18th-century tsunami event in southwest Taiwan, which was considered the second deadliest tsunami after the 2004 Indian Ocean Tsunami [*Bryant*, 2008]. Likewise, *Soria et al.* [2015] found records of a typhoon event in 1897 which was very similar to the devastating Typhoon Haiyan in 2013 in the central Philippines. The use of historical documents, however, calls for careful checks and validation due to the possibility of inconsistencies, misinterpretations or incorrect data [e.g., *Lau et al.*, 2010; *Paris et al.*, 2014]. More importantly, in some affected areas, written records are absent or only cover a short period (i.e., 100-200 years or so), and thus they provide limited insight into events at centennial scales.

Geological records, on the other hand, are able to capture events (both storm and tsunami) dating back centuries and longer [*Cisternas et al.*, 2005; *Jankaew et al.*, 2008]. Geological records may shed light on how and when extreme events occurred so that we can determine their recurrence intervals. In the last two decades, a growing number of studies have uncovered geological records and inferred past extreme events from them [see *Switzer et al.*, 2014 for a review and examples]. One notable example came from *Jankaew et al.* [2008] who brought to light at least four different sandsheets that were very likely deposited by different paleo-tsunamis on Phra Thong Island, Thailand. A paleo-tsunami is described as a "tsunami occurring prior to the historical record for which there are no written observations" [*Intergovernmental Oceanographic Commission*, 2016]. In *Jankaew et al.*'s study, the inference of paleo-tsunami deposits was mainly based on the geographical absence of tropical cyclones. Thus, a challenge remains: how can we accurately identify the cause of geological records for unknown events, be they tsunami(s) or storm(s)? Do we have a universally applicable approach to distinguishing storm and tsunami deposits? These questions have been extensively debated and researched in numerous studies [e.g., *Kortekaas and Dawson*, 2007; *Morton et al.*, 2007; *Switzer and Jones*, 2008]. Despite such efforts, widely accepted criteria are not yet available. The various criteria proposed to date have relied on sedimentological and stratigraphic signatures that in many cases can be found in both tsunami and storm deposits. This suggests the need for developing and testing new approaches and data sets in order to accurately characterise storm and tsunami events; and in the case of more than one event derived from the same cause as described in *Jankaew et al.* [2008], can we identify the provenance of the sediments in each event deposit?

While studying coastal extreme events is of undeniable importance, they must be considered within the context of sea-level changes both local and regional. The regional sea-level history should never be ignored since the changes in sea level are now considered as an additional coastal threat [*Lowe et al.*, 2010]. Understanding sea-level changes on various time scales is fundamental for assessing coastal risks [*Pugh and Woodworth*, 2014]. Sea-level variations, however, are far more complicated than simply defining the long-term trend, an issue that is of primary interest today. Sea level commonly varies on different time scales (or frequencies): hours (extreme sea levels), months (seasonal cycles), years (interannual variability) and multiple years (decadal to multi-decadal signals); and from place to place (i.e., regional sea-level changes) [*Pugh and Woodworth*, 2014]. Sea levels respond differently to a variety of different atmospheric/oceanic forcings, and consequently produce large spatial variability [*Milne et al.*, 2009]. *Milne et al.* [2009] also note a significant deviation of regional sea level from the global mean and suggest that regional studies will be important for decades to come. Recently, regional sea level has been examined in a number of studies, which mostly focused on the major physical processes (i.e., forcings) governing sea-level variations on specific time scales and how an examination of how they contribute to sea-level variability spatially and temporally. The answers for such questions significantly contribute to coastal preparation and adaptation in coastal regions that are highly vulnerable to coastal hazards. One such area is the South China Sea – a rapid growing socio-economic region, which has been particularly affected by extreme coastal flooding events in the present and is expected to remain so in the decades to come [e.g., *Muis* *et al.*, 2016; *Neumann et al.*, 2015; *Nicholls*, 2010]. Thus studying sea-level variations in the South China Sea is of significant importance.

1.1. Research questions

Given the above context, in this thesis I address three main aims/questions:

1. To develop and examine a new statistic-based approach to study

a) the provenance of coastal overwash deposits, and

b) compare different extreme events at the same site.

I will accomplish this by using a combination of grain size parameters, mineralogy and geochemistry data sets. The data sets were collected from different sedimentological environments on Phra Thong Island – a well-known study site described by *Jankaew et al.* [2008].

2. What major forcings govern sea-level variability on an interannual time scale and how does sea level around the South China Sea respond to them?

3. How do extreme sea levels around the South China Sea vary temporally and spatially and are the return levels stationary through time?

Sea-level data sets for questions (2) and (3) are derived from tide gauges located around the South China Sea.

To address the aforementioned aims and questions, I accordingly apply a wide range of statistical techniques for each data set used in this work. Before focusing on individual case studies, an overview of the characteristics of each data set and the chosen statistical treatments will be briefly highlighted below.

1.2. Characteristics and statistical treatments for the data sets

1.2.1. Sedimentological, mineral and geochemical data sets

To test our new statistics-based approach for coastal overwash deposits, we collected sediment samples on Phra Thong Island (Thailand) from different sedimentological environments including modern onshore, nearshore and offshore (site descriptions are provided in more detail in chapter 2). Samples were grouped by their environment (i.e., offshore, onshore, non-tsunami, tsunami and storm). For each sample, I analyzed the grain size parameters (the mean, sorting, skewness and kurtosis), mineralogy (from X-ray diffraction) and trace element geochemistry (from X-ray fluorescence). I then investigated underlying relationships between each environment and overwash deposit from each subset by applying a series of multivariate statistical techniques.

The analytical results for each subset formed typical multivariate data sets used in chapter 2. Each group of variables can be expressed as a multi-dimensional $N \times M$ data matrix, where N is the number of observations (i.e, collected samples) and M is the number of variables of each i^{th} observation ($i=1,2, \ldots, N$). That is, each observation (i.e., dependent/response variable) is represented by several variables (i.e., independent/predictor variables) [*Tabachnick and Fidell*, 2013]. For example, each observation in the grain size group is characterized by four parameters: the mean, sorting, skewness and kurtosis. A combination of these parameters (i.e., independent variables) will accordingly predict a value (or score) on a given observation. As a result, the predicted values (of each observation) derived from independent variables in turn affect the variance-covariance within groups and hence, between groups. Therefore, exploring relationships between groups and within groups is a complicated task involving multiple analysis techniques [*Davis*, 2002].

Undoubtedly, the relationships of independent variables in observations greatly contribute to the underlying structure of multivariate data set. Independent variables might exhibit either high correlations or high variability with others variables. Additionally, this relationship varies between groups resulting in complicated interpretations. For instance, in trace element subsets, the absolute value (ppm) of zirconium (Zr) might be several hundred times greater than that of bismuth (Bi) (see chapter 2). Similarly, the proportion (%) of quartz minerals dominates the mineral subset. It is apparent, then, that there are considerable divergences within groups and between groups of the data sets. Thus the selected statistical methods should take such high variability into account so that the use of high-value variables does not bias the results.

The choice of suitable statistical methods should be based on attributes of the data sets [*Tabachnick and Fidell*, 2013]. So far, the use of statistical analyses in the study of coastal overwash deposits, surprisingly, has received less attention. Only simple analyses, mostly correlation and cluster analyses, or single multivariate analysis (e.g., PCA) have been applied in recent studies [e.g., *Brill et al.*, 2014; *Chagué-Goff et al.*, 2012a; *Chagué-Goff et al.*, 2012b; *Jagodziński et al.*, 2012; *Kain et al.*, 2014; *Kuwatani et al.*, 2014; *Sawai et al.*, 2009]. However, given the complicated characteristics of multivariate data sets, a single technique is inadequate to dig into hidden interactions of variables and groups in the data sets. Thus, we selected and applied a series of statistical analyses, namely: Partitioning Around Medoids (PAM), Principal Component Analysis (PCA) and Discriminant Function Analysis (DFA).

All these techniques have been widely used outside of the coastal hazard community as they can deal with multivariate data sets and provide useful information about the underlying structure of data sets. I briefly introduce those statistical techniques below:

- PAM is a type of cluster analysis that can be used to identify potential groups without prior knowledge of groups in a population [*Kaufman and Rousseeuw*, 2005]. PAM was used in this thesis as a tool to explore the underlying structure of the sediment data sets.
- PCA simplifies multivariate data sets by transforming the original data to a new lower-dimensional (principal component) data set to investigate the relationships between variables and the relationships among observations in a data set [*Everitt and Hothorn*, 2011].
- DFA is a powerful classification technique that seeks the greatest separation between well-defined or known groups of populations by using linear discriminant functions [*Davis*, 2002]. We use this technique to compare the modern environmental parameters with those of the overwash deposits to gain insight into the provenance of the sediments and compare the different overwash deposits.

More details of the above-mentioned methods are provided in chapter 2.

1.2.2. Sea-level data sets

Sea-level measurements have been traditionally observed by a simple instrument, the so-called ‘tide gauge’. However, the sea-level observations at tide gauges (mostly coastal tide gauges) are total sea level: a tide gauge measures not only tides but other effects from atmospheric and/or oceanic forcings. Hence, the term ‘sea-level gauge’ might fully reflect the meaning of sea-level measurements [*Pugh and Woodworth*, 2014]. It is important to note that the sea-level measurements at the tide gauges are 'relative sea level', i.e., relative to the height of nearby land such as a benchmark or datum, compared to 'absolute sea level', i.e., with respect to the Earth's center of mass, as measured from satellite altimetry [e.g., *Holgate et al.*, 2013; *Milne et al.*, 2009]. In this thesis, I focus only on relative sea level (RSL) derived from tide gauges, as RSL is more related to the coastal impact assessments [*Church et al.*, 2013].

The sea-level records at each tide gauge are time series data (vectors of sequential data points) measured regularly at specific time intervals but most commonly at an hourly basis. Based on that, longer time-interval averaged records such as monthly or yearly records are generated depending on research purposes. As a result, a sea-level record can be expressed by a vector $Y(t)$ as a function of time: $Y(t) = (x_{t1}, x_{t2}, \ldots x_{tn})$, where n is the number of observations and x_i is the observed value at time index t_i ($i = 1,2, \ldots, n$). Nevertheless, one should bear in mind that the sea-level records at different sites may cover different durations. Here, time series analysis attempts to unveil the variety of temporal variations of $Y(t)$ throughout the records and, if applicable, predict future values of a given time series [*Trauth*, 2015]. Temporal behavior of climate-related data sets like sea-level records, however, are either non-linear or non-stationary [e.g., *Hamlington et al.*, 2011; *Huang and Wu*, 2008]. That is, there are non-linear physical processes producing irregular temporal patterns in sea-level data. For instance, the El Niño-Southern Oscillation (ENSO), a major climate mode of the equatorial Pacific accounting for large sea-level variability in the equatorial Pacific, takes place once every ~ 3-7 years and differs in magnitudes between episodes [e.g., *Pugh and Woodworth*, 2014]. Consequently, the amplitudes of sea-level signals responding to ENSO also vary over time [*Hamlington et al.*, 2011]. This feature indicates that traditional methods that rely on assumptions of stationary sea-level might not be able to capture time-varying signals. Other common attributes of sea-level records include noise and gaps in data (particularly in less well-controlled quality data sets) which, in turn, require careful data processing.

In this thesis, I address research questions (2) and (3) by investigating sea-level variations around the South China Sea – the largest semi-closed marginal sea in the western Pacific [*Wyrtki*, 1961]. The South China Sea experiences a complex air-sea interaction system including monsoonal winds (winter and summer monsoons) and effects of tropical cyclones and other ocean-atmosphere coupled systems such as the El Niño-Southern Oscillation (ENSO) and Indian Ocean Dipole (IOD). This suggests complicated sea-level variations both temporally and spatially.

To study interannual sea-level variability and extreme sea level (chapter 4), I obtained two sea-level data sets with different temporal resolutions and spatial distributions. I briefly describe these below, along with their associated analysis methods.

Monthly mean sea-level data sets and statistical methods for interannual sea-level variability analysis (chapter 3). I acquired monthly relative mean sea level (RMSL) at 10 tide gauges (TGs) around the South China Sea (details in chapter 3). The data came from the worldwide sea-level data supplier, Permanent Service for Mean Sea Level (PSMSL), and from the Vietnam Marine Hydro-meteorological Center. The methods used in this chapter is listed below:

- *Empirical Mode Decomposition/Hilbert-Huang Transform (EMD/HHT):* to study interannual sea-level variability, the most important task is to determine how we can accurately extract the interannual signals out of the sea-level records. Previous studies have used various techniques, such as low-pass filtering or empirical orthogonal functions (EOF) [e.g., *Soumya et al.*, 2015; *White et al.*, 2014]. Nevertheless, the use of each of these approaches has been somewhat problematic because they assumed that the data is stationary [e.g., *Huang and Wu*, 2008; *Wu et al.*, 2007]. As mentioned above, sea-level records are non-linear and non-stationary. Thus, in this study I used Empirical Mode Decomposition/Hilbert-Huang Transform (EMD/HHT) to isolate the interannual sea-level signals. EMD/HHT is an adaptive (i.e., data-based) analysis method, which can be used to decompose nonlinear and non-stationary time series into different time-dependent frequencies (i.e., modes) [*Huang et al.*, 1998; *Wu and Huang*, 2009]. I applied EMD/HHT method to time series data and then extracted ~2-7 year signals.

- *Cross-correlation and Wavelet Coherence analysis:* to explore what forcings govern the interannual sea-level variability around the South China Sea, I examine how sea levels correlate with climate indices (ENSO and ENSO Modoki), monsoons and ocean volume transport, by applying cross-correlation and wavelet coherence analyses [*Grinsted et al.*, 2004; *Torrence and Compo*, 1998]. These analyses allow one to observe quantitatively the correlation of sea level and climate indices and to examine how those correlations vary with time.
- *Multiple Linear Regression model:* to investigate how much each index contributes relatively to interannual sea-level variations by using a multiple linear regression model of sea level [*Groemping*, 2006].

Hourly sea-level data and statistical methods for extreme sea level’s study (chapter 4). I obtained hourly sea-level data at 30 tide gauges from two sources: The University of Hawaii Sea Level Center (UHSLC, 26 tide gauges) and the Vietnam

Marine Hydro-meteorological (4 tide gauges). The methods used in this chapter is listed below:

- *Long-term trends and standard errors*: I use the Ordinary Least Square regression to calculate the long-term trends of extreme sea level for each sea-level record. The significance of trends was tested at 95% confident intervals. The autocorrelation in residuals was checked with the Durbin-Watson test [*Durbin and Watson*, 1950, 1951, 1971] and then corrected using the Newey-West Estimator [*Newey and West*, 1987].
- *The Dynamic Linear Model for Generalized Extreme Values (DLM-GEV)*: In this study, I also examine whether the extreme events change with time, something rarely studied in previous investigations. However, that goal cannot be solved with a simple linear model. To achieve this, I adapt a Dynamic Linear Model (DLM) which is based on a Bayesian approach. I then use the DLM to fit the extreme distribution of each sea-level record (the model then is a so-called DLM-GEV). Details of the model will be described in chapter 4.

1.3. Thesis structure

The next chapters in this thesis are structured as follows: in chapter 2, I study the provenance of coastal overwash deposits on Phra Thong Island, Thailand; in chapter 3, I present a new perspective on interannual sea-level variability around the South China Sea; in chapter 4, I assess the temporal and spatial variations of extreme sea level around the South China Sea by using a Dynamic Linear Model; and, finally in chapter 5, I summarize and discuss future work stemming from this thesis. Chapters 2, 3, and 4 are presented in a research paper format as required by the respective journals.

Chapter 2

Elemental and mineralogical analysis of marine and coastal sediments from Phra Thong Island, Thailand: Insights into the provenance of coastal hazard deposits.

(submitted to *Marine Geology*)

Dat T. Pham[1,2], Chris Gouramanis[3], Adam D. Switzer[1,2], Charles M. Rubin[1,2], Brian G. Jones[4], Kruawun Jankaew[5], Paul F. Carr[4]

[1]*Asian School of the Environment, Nanyang Technological University, Singapore 639798*

[2]*Earth Observatory of Singapore, Singapore 639798*

[3]*Department of Geology, Faculty of Arts and Social Sciences, National University of Singapore, Singapore 117570.*

[4]*School of Earth and Environmental Sciences, University of Wollongong, NSW 2522, Australia*

[5]*Department of Geology, Faculty of Science, Chulalongkorn University, Bangkok 10330, Thailand*

Abstract:

Sediment records left by coastal hazards (e.g. tsunami and/or storms) may shed light on the sedimentary and hydrodynamic processes happening during such events. Thus, studies of the provenance of coastal overwash deposits left by such events are essential. Also, to accurately assess the recurrence of such disastrous events, tsunami and storm deposits need to be accurately discriminated. However, the use of traditional criteria (mostly sedimentological and stratigraphic characteristics) are still problematic or only applied for known events. In this study, we adopt a statistic-based approach (including cluster analysis, principal component analysis and discriminant function analysis) using grain size parameters, mineralogy (from X-ray diffraction) and trace element geochemistry (from X-ray fluorescence). We collected modern sediment samples from onshore, offshore, the 2004 Indian Ocean Tsunami and three palaeotsunami, and a 2007 storm deposit from Phra Thong Island, Thailand.

Our results show that the mineral content and trace element geochemistry are statistically inadequate to distinguish the provenance of the modern storm and tsunami deposits at this site, but the mean grain size can potentially discriminate these overwash deposits. We found that the 2007 storm surge deposits were most likely sourced from the onshore sediment environment. In addition, our analyses show that all four tsunami units statistically differ from each other indicating that the sediment sources of each of the tsunami deposits are diverse. In most of our statistical analyses, the nearshore samples and 2004 tsunami deposits are very similar suggesting that the nearshore marine sediments significantly contributed to the 2004 tsunami deposits. The first palaeotsunami deposits were possibly derived from both onshore and nearshore materials while the second and third palaeotsunami showed no clear evidence of the sediment sources. Such complexity raises questions about the origin of the sediments in the tsunami and storm deposits and strongly suggests that local context and palaeogeography are important aspects that cannot be ignored in tsunami provenance studies.

Key words: tsunami deposit, storm deposit, provenance, trace elements, mineral compositions, grain size parameters, cluster analysis, principal component analysis, bootstrap analysis, discriminant function analysis.

2.1. Introduction

Coastal areas offer favourable conditions to support dense human populations and critical infrastructure [*Syvitski et al.*, 2009]. These areas, however, are also vulnerable to coastal hazards, of which tsunamis and storms are the most disastrous [e.g. *Switzer et al.*, 2014]. A series of such disasters have occurred in the last decade, including the 2004 Indian Ocean Tsunami (IOT), Hurricane Katrina (2005), Cyclone Nargis (2008), the Tohoku-oki earthquake-induced tsunami (2011), Hurricane Sandy (2012), Typhoon Haiyan (2013) and Hurricane Patricia (2015). These disasters highlight the need for accurate coastal vulnerability assessments including the examination of the recurrence interval of such events that, in turn, is crucial for future risk assessment [e.g., *Switzer et al.*, 2014]. Due to the insufficient and short-time historical records (i.e. frequently less than 100 years) in many affected areas, the geological record preserved along coasts captures a much longer timeframe and provide evidence for historical occurrences and allow the determination of the recurrence intervals of tsunamis [e.g. *Jankaew et al.*, 2008; *Minoura et al.*, 2001; *Monecke et al.*, 2008] and storms [e.g. *Liu and Fearn*, 2000; *Nott*, 2011].

Both tsunami and storm deposits are the result of overwash processes caused by high-energy events, and in many cases they exhibit very similar sedimentary signatures [e.g. *Kortekaas and Dawson*, 2007; *Switzer and Jones*, 2008]. Thus, in order to accurately assess how frequently catastrophic events affect coastal regions, it is necessary to know whether the identified coastal washover deposit was caused by a tsunami or a storm event [e.g. *Switzer et al.*, 2014].

Tsunami and storm deposits have been compared in numerous studies with an expectation of developing a suite of diagnostic criteria to distinguish deposits formed by different coastal overwash processes [e.g. *Goff et al.*, 2004; *Kortekaas and Dawson*, 2007; *Morton et al.*, 2007; *Nanayama et al.*, 2000; *Phantuwongraj and Choowong*, 2012; *Switzer and Jones*, 2008; *Tuttle et al.*, 2004]. Nonetheless, criteria that have been used are still problematic and site specific or only valid for known events [*Gouramanis et al.*, 2014b]. Many of these studies have relied on sedimentological and stratigraphic signatures that can be found in both tsunamigenic and cyclonic deposits. For example, *Shanmugam* [2012] reviewed 15 sedimentological criteria that had been found in both tsunami and storm deposits and drew the conclusion that “there are no reliable sedimentological criteria for distinguishing paleo-tsunami deposits in various environments” (p.23). *Gouramanis et al.* [2014b] used a multi-proxy approach (granulometric, loss on ignition, heavy minerals and microfossils) to statistically compare the 2004 IOT deposit and 2011 Cyclone Thane deposit superimposed at the same location along the southern coast of India. The *Gouramanis et al.* [2014b]'s study indicated that tsunami and storm deposits from the same site could not be distinguished using the standard sedimentological parameters typically used to identify coastal hazard deposits.

Thus, the difficulty of using conventional diagnostic criteria in differentiating coastal washover deposits requires the development of novel proxies.

In this study, we seek to test two hypotheses:

1. that the mineral composition, metal geochemistry and grain size parameters of modern onshore, nearshore and offshore environments can be used to determine the provenance of the 2004 IOT and paleo-tsunami deposits, and the 2007 storm surge deposit preserved on Phra Thong Island, Thailand (Fig. 2.1); and,
2. that the 2004 IOT, paleo-tsunami and the 2007 storm surge deposits can be distinguished using mineral composition, metal geochemistry and grain size parameters.

To investigate these hypotheses, we apply several novel and seldomly-used (to coastal hazard deposits) statistical techniques to gain insight into the provenance of the washover deposits and compare the deposits from different events and causal mechanisms (i.e. storm, recent and paleo-tsunami).

To date, little attention has focused on the mineralogy and geochemistry of overwash deposits [*Chagué-Goff*, 2010 and references therein]. It is believed that the geochemical signature and mineral composition of tsunami sediments are source-dependent [*Chagué-Goff et al.*, 2011; *Goff et al.*, 2012], and are expected to reflect the origin of coastal overwash deposits [*Chagué-Goff et al.*, 2015; *Font et al.*, 2013]. Addressing these issues will contribute a greater understanding of the sedimentation and hydrodynamic processes (i.e. erosion and deposition) occurring during coastal overwash sediment deposition [e.g. *Goff and Dominey-Howes*, 2013; *Sugawara et al.*, 2014; *Switzer et al.*, 2012].

2.2. Site description

Phra Thong Island is approximately 125 km north of Phuket on the west coast of southern Thailand in the Andaman Sea (Fig. 2.1). Phra Thong Island is characterized by a series of north-south trending, sandy Holocene beach ridges and marshy swales on the western side, and dense tidal mangroves on Pleistocene sand dunes on the eastern side [*Brill et al.*, 2015; *Brill et al.*, 2012a; *Jankaew et al.*, 2008; *Scheffers et al.*, 2012].

From the early 1900s to the 1970s and sporadically since, tin and other heavy metals were mined both from the onshore and offshore environments of Phra Thong Island [*Jankaew et al.*, 2011]. This activity would have influenced the mineral phases transported onshore in the last 120 years.

During the 2004 IOT event, the maximum observed tsunami wave height was 20 m - the highest recorded wave height along the Thai coast [*Tsuji et al.*, 2006]. More importantly, on Phra Thong Island, the sedimentary signatures of the 2004 IOT and at least three different past tsunami events (preserved as 5 to 20 cm thick sand sheets in coastal swales) were identified by *Jankaew et al.* [2008].

Since *Jankaew et al.* [2008]'s study, the 2004 IOT tsunami and paleo-tsunami deposits on Phra Thong Island have been extensively studied to determine the chronology and potential tsunami recurrence interval [*Brill et al.*, 2012a; *Fujino et al.*, 2009; *Prendergast et al.*, 2012], micropaleontology [*Sawai et al.*, 2009], sedimentology and stratigraphy [*Brill et al.*, 2015; *Brill et al.*, 2012a; *Brill et al.*, 2012b; *Fujino et al.*, 2009; *Fujino et al.*, 2008], flow conditions [*Brill et al.*, 2014; *Choowong et al.*, 2008; *Sawai et al.*, 2009] and a ground penetrating radar survey to image the thin tsunami beds [*Gouramanis et al.*, 2014a; *Gouramanis et al.*, 2015].

Phra Thong Island is rarely impacted by storms [*Brill et al.*, 2014; *Jankaew et al.*, 2008] but in early May 2007 an unusual tropical depression that formed in the upper part of Gulf of Thailand moved across southern Thailand [*Thai Meteorological Department*, 2007]. As the tropical depression moved into the Andaman Sea, the depression interacted with the southwest monsoon resulting in heavy rain (200 to 400 mm) and intense onshore waves along the north-western coast of Thailand [*Thai Meteorological Department*, 2007]. The resultant storm surge deposited sands upon the youngest berm of Phra Thong Island.

Although the shallow marine environment is considered to be the source of the sediments comprising the 2004 IOT deposit on Phra Thong Island based on evidence from diatom assemblages [*Sawai et al.*, 2009] and grain size distribution [*Fujino et al.*, 2010; *Fujino et al.*, 2008], the provenance of the older deposits has not been identified. Thus, we aim to identify the provenance and compare the granulometry, mineralogy and geochemistry of the 2004 IOT tsunami, paleo-tsunami and 2007 storm deposits.

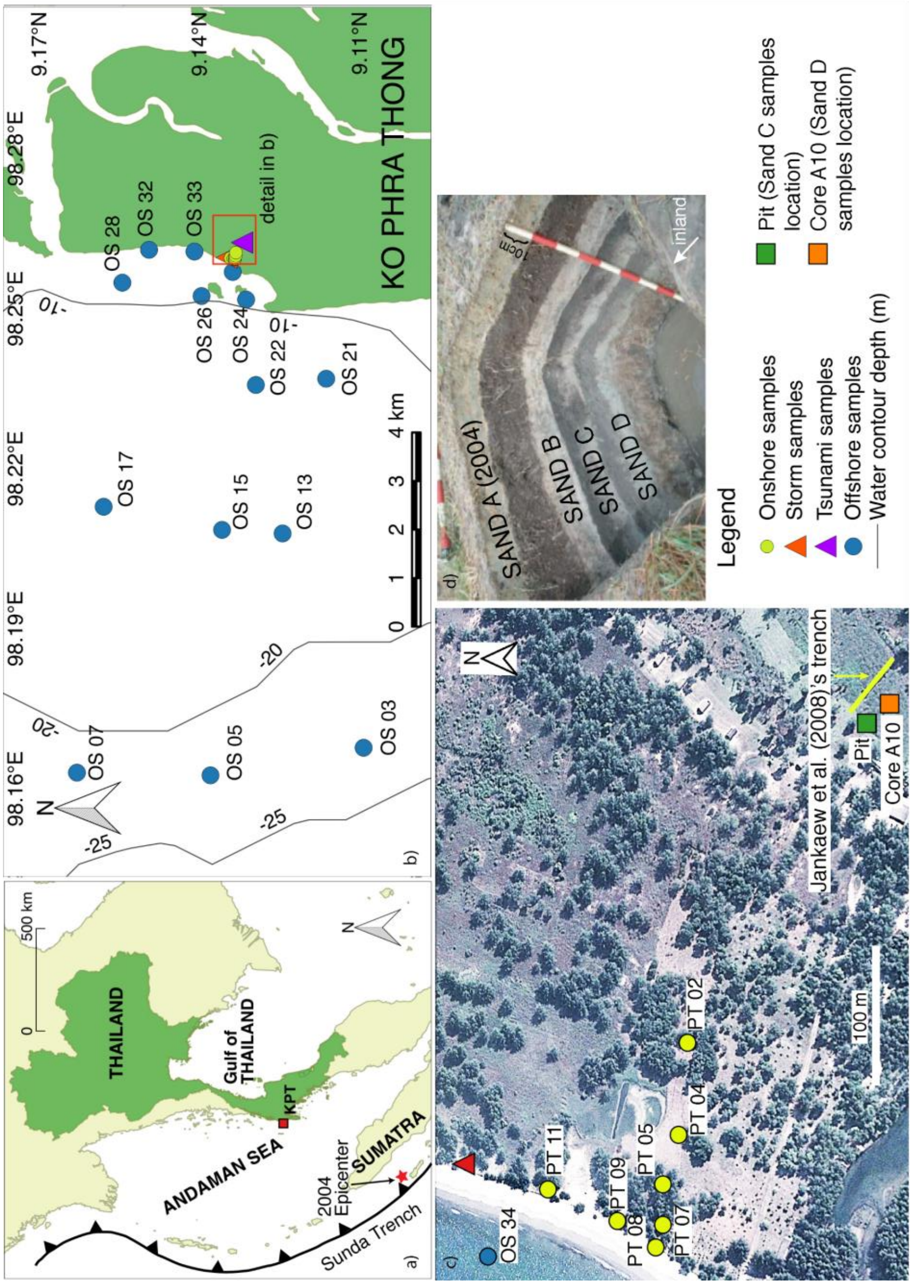

Figure 2. 1: a) The regional map shows the location of Phra Thong Island (Ko Phra Thong - KPT), Thailand (red square); b) the detailed map shows the locations of the offshore sample, onshore samples and the local bathymetry; c) A close-up view of the pre-2004 onshore samples (yellow dots), storm samples (red triangle), Sand C (green square, samples were collected from 40-43 cm depth from a pit), Sand D (orange square, samples were collected from 75-77 cm depth from an auger core (A10)) and the Jankaew *et al.* (2008)'s trench where Sand A and Sand B were taken; d) The stacked tsunami sand sheets from Jankaew *et al.* (2008).

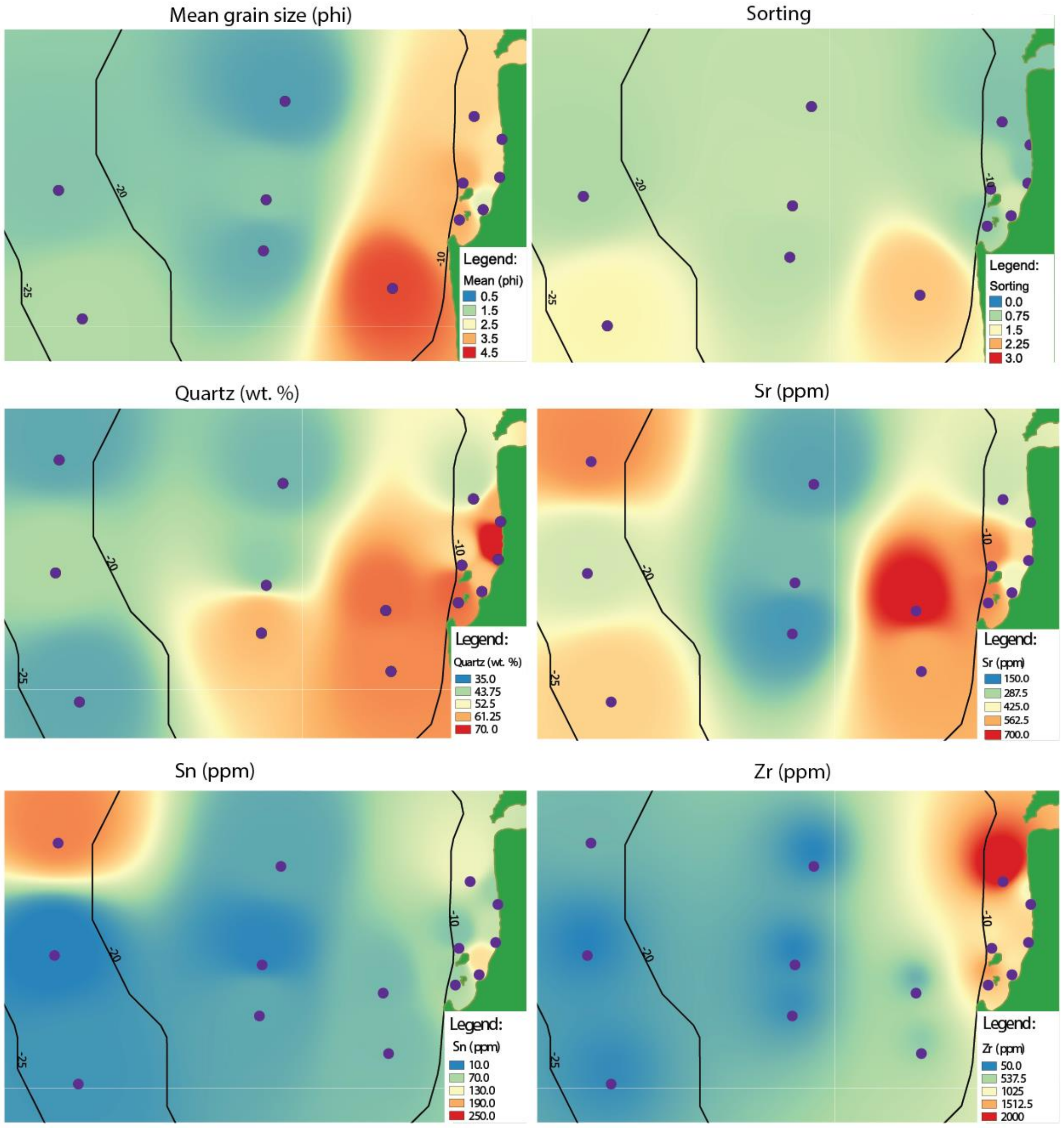

Figure 2. 2: Surface interpolation maps of the offshore sediment sample grain size parameters (the mean and sorting), quartz mineral (finer fraction) and selected trace elements. Refer to Figure 2.1 for sample's name code. The black lines indicate the depth contours.

2.3. Methods

2.3.1. Sample collection

Sediment samples were collected in March 2012 from the offshore and nearshore marine environment, the modern beach and beach ridges inland, pits that contained the 2004 IOT and three paleo-tsunami deposits (e.g. Jankaew et al., 2008), and pits through the 2007 storm deposit. All sampling was undertaken in the northwestern section of Phra Thong Island, Thailand as this is where the best preserved examples of the paleo-tsunami deposits are located (e.g. Jankaew et al., 2008), and the only recognized 2007 storm deposit.

The 31 offshore and nearshore sediments were collected using a Van Veen grab sampler in water depths ranging from 3 to 25 m and up to 10 km away from the modern shoreline (Fig. 2.1). The onshore samples comprised nine beach ridge and swale sediments that were collected along a transect perpendicular to the shoreline. The pre-2004 IOT sediments were identified from pits as those sediments deposited prior to the capping of the beach ridges and swales by the 2004 IOT. Samples were collected between 5 to 12 cm depth. Four modern beach deposits were also collected.

The 2004 IOT deposits (hereafter Sand A) and the most recent prehistoric tsunami (Sand B) were sampled (March 2012) from a trench aligned perpendicular to the modern shoreline, and situated in a wet, peaty swale *ca*. 0.5 km inland [*Jankaew et al.*, 2008]. In this trench, three distinct and well-preserved tsunami deposit layers correspond to the 2004 IOT event and two other prehistoric tsunamis [*Jankaew et al.*, 2008]. Approximately 100 to 150 g of sediment was sampled from the top sand layer (Sand A) and the most recent prehistoric sand layer (Sand B) from the exposed trench.

Due to the high groundwater table in the trench, sediment samples from the second paleo-tsunami layer (Sand C) were collected from a pit 8.5 m south of the trench in May 2013 when the water table was lower (Fig. 2.1). The third paleo-tsunami deposit (Sand D) was sampled from an auger core recovered 12 m south of the trench (Core A10; Fig. 1; *Gouramanis et al.*, 2015).

A subset of the sediment samples from each group was selected for analysis. These samples reflect the diversity of sedimentary environments and sedimentary units for geochemical and mineralogical comparison. The selected samples came from the Offshore (*n*=14), Onshore (*n*=8), Sand A (*n*=4), Sand B (*n*=4), Sand C (*n*=3), Sand D (*n*=2) and Storm (*n*=3) groups (Fig. 2.1). We maintain these group names throughout the remainder of this study.

2.3.2. Sediment analyses

Grain size analysis was performed at the Asian School of the Environment, Nanyang Technological University, Singapore, and X-ray diffraction (XRD) and X-Ray fluorescence (XRF) analyses were carried out at the X-ray laboratory, University of Wollongong, Australia.

2.3.2.1 Grain size analysis

Prior to grain size analysis, all of the sediment samples were treated in hydrochloric acid (HCl) to eliminate carbonate, and hydrogen peroxide (H_2O_2) to remove organic matter. The analysis of grain size parameters (i.e. mean, sorting, skewness and kurtosis) followed 60 s of ultrasonic dispersion, and grain size measured in triplicate using a Malvern Mastersizer 2000 (size range 0.02 µm to 2 mm). Granulometric parameters were obtained and described based on the logarithmic graphical method of *Folk and Ward* [1957] using the GRADISTAT package [*Blott and Pye*, 2001]. The grain size was not measured for two offshore samples (PT-OS 07 and PT-OS 22) due to insufficient sample material and these two samples were excluded from further examination.

2.3.2.2 X-ray Diffraction (XRD)

Samples were dried in an oven at 60^{o}C, and using 1 and 2 mm sieves, the organic fragments (e.g. roots) were removed. Small rootlets that remained in the samples do not affect XRD analyses since organic material does not produce XRD diffraction patterns. Dried samples were then crushed using a tungsten mill in order to obtain a very fine powder. In the laboratory, 1 to 2 g of the powdered sample were smeared uniformly on a glass slide, pressed in to an aluminum sample holder and then packed into a sample container. The XRD analysis was conducted using a Philips PW 1771/00 diffractometer with Cu Kα radiation, X-tube at 1 kW and a Spellman DF3 generator (the angle of two theta ranged from 4 to 70˚, with a step size of 0.02˚). The raw XRD profiles derived from the diffractometer were analyzed using the TRACES 4.0 software. The corrected profiles were then processed in SIROQUANT software, which calculated the weight % (wt. %) of each mineral phase present [*Williams et al.*, 2012].

Analysis of bulk mineral contents for the Deep-Offshore, Nearshore, Onshore, Sand A and Sand B samples was analysed using quantitative XRD. Unfortunately, the very high concentration of quartz (>80 wt. %) in the bulk analyses would dampen the influence of the lower concentration minerals in the statistical analyses. Sand C, Sand D and 2007 Storm samples were not analysed but the dominance of quartz in these samples suggests a similar composition across the data set. So to investigate the role of the non-quartz component, the finer sediment fraction (63 to 125 μm) was analysed using XRD. The finer fraction XRD mineral composition was used in the statistical analyses.

2.3.2.3 X-ray Fluorescence (XRF)

Approximately 5.5 g of the powdered sample was mixed with 10 drops of polyvinyl alcohol binder and converted to a pellet at 2500 p.s.i in a hydraulic press. The pellets were left to oven dry at 80° C for 2 to 3 days and weighed. Each sample was analyzed using the SPECTRO XEPOS energy dispersive X-ray fluorescence spectrometer and the data compared to a suite of calibration standards [*Wien et al.*, 2005].

2.3.3. Statistical methods

To determine the provenance of the sediments deposited by the 2004 IOT, paleo-tsunami and 2007 storm and to compare the overwash deposits, three multivariate statistical techniques (Partitioning Around Medoids (PAM), Principal Component Analysis (PCA) and Discriminant Function Analysis (DFA)) were employed. Each technique was applied separately to grain size characteristics, mineral contents and trace element data. All statistical analyses were executed in *R* [*R Core Team*, 2014] by using the ***cluster*** [*Maechler et al.*, 2014], ***vegan*** [*Oksanen et al.*, 2016] and ***boot*** [*Canty and Ripley*, 2016] packages.

2.3.3.1. Partitioning Around Medoids - PAM

PAM is a type of cluster analysis that can be used to identify potential groups without prior knowledge of groups in a population [*Kaufman and Rousseeuw*, 2005]. The main purpose of PAM is to choose representative object(s) for group(s) from the data set and then form cluster(s) by locating other objects to the closest representative object that has been defined. The representative object (the medoid) is selected so that the average dissimilarity to other objects in the same cluster is smallest. The PAM algorithm comprises two phases: BUILD and SWAP phases. In the BUILD phase, the medoids and clusters are determined first and then the results are refined in the SWAP phase by comparing the average dissimilarity from the previous chosen medoid with that of the other objects in the same cluster. If the new average dissimilarity is lower than previous one, a new medoid is obtained and then a new cluster is formed. These two phases are repeated until PAM finds the best medoid of a cluster, and also the best clusters that have a minimal average dissimilarity. PAM also provides the second-best cluster or neighbor cluster for each object in the data set. To present the clustering results, PAM produces a silhouette plot that can be used to evaluate how well objects are classified within a cluster and estimate the quality of the clustering [*Kaufman and Rousseeuw*, 2005; *Rousseeuw*, 1987]. In each cluster, a silhouette width is generated for each object with a range of values from *-1* to *1*. An object is considered well classified when its silhouette width is close to 1 and misclassified if the silhouette width moves toward *-1*. A special case appears when the silhouette value is close to *0*. In such cases, the object forms a group that only includes itself, and is considered an intermediate case [*Kaufman and Rousseeuw*, 2005]. Based on the silhouette width of each individual object, the average silhouette width of each cluster (or group) is calculated and the result is the overall average silhouette width of all clusters (see Fig. 2.3 as an example).

In PAM, the number of clusters (k) is defined prior to the analysis, which means that the overall average silhouette width will vary with k. This leads to the questions: which is the optimal number of clusters of the data set and how many clusters should be defined after analysis? As recommended in *Kaufman and Rousseeuw* [2005] PAM should be evaluated with various *k*'s and compared to the overall average silhouette widths (*k* should be less than the number of objects in entire data set). An appropriate *k* is obtained if the average silhouette width is maximized resulting in a more accurate clustering. To obtain the optimal *k*, in this study PAM were run with *k* varying from 2 (smallest number of groups that can be found) to 8 (maximum number of groups) to compare the average silhouette widths and the largest average silhouette width value [*Kaufman and Rousseeuw,* 2005]. The Euclidean distance was used to compute the matrix of dissimilarities of the entire data set prior to the PAM analysis. PAM provides more accurate clustering results than commonly used hierarchical techniques as it attempts to find the *best* clusters by iterating BUILD and SWAP phases. Furthermore, the use of medoids is less susceptible to outliers compared to the mean [*Kaufman and Rousseeuw,* 2005].

2.3.3.2. Principal Component Analysis – PCA

PCA simplifies multivariate data sets by transforming the original data to a new lower-dimensional (principal components) data set to reduce variance [*Everitt and Hothorn,* 2011]. The number of components is equal to the number of original variables. Mathematically, principal components are eigenvectors extracting from either a variance-covariance matrix or a correlation matrix [*Davis,* 2002]. The choice of matrix from which eigenvectors are extracted depends on the nature of dataset. If original variables are measured in different units or scales and the magnitude of the variance of each variable is large, constructing a correlation matrix is recommended [*Everitt and Hothorn,* 2011]. When principal components are extracted, the observations for each component will be presented as *scores,* such that any two components can be plotted in two-dimensional space. Consequently, PCA can investigate the relationships between variables and the relationships among observations in a data set. For variables, the angle of arrows demonstrates how well variables are correlated to each other (e.g. the wider the angle is, the less correlation there is).

PCA was employed to study the interaction of all variables and the distribution of samples using granulometric data, mineralogy and geochemistry. All data sets were standardized prior to analysis and the correlation matrix was used to extract components due to different units and large variances in the data sets [*Everitt and Hothorn*, 2011]. To retain the significant components from PCA analysis, the broken stick method and Kaiser-Guttman criteria were applied [e.g., *Legendre and Legendre*, 2012]. The eigenvalue of each component was plotted on a *scree plot* in descending order.

The broken stick method defines components to be retained when the proportion of the explained variance is greater than the variance produced by a broken stick distribution [*Jackson*, 1993]. Meanwhile, the Kaiser-Guttman criteria are based on the bootstrap simulation [*Jackson*, 1993]. As the sample size (n = 36) and the number of variables (p) varies depending on the PCA performed ($p_{Grain\ size}$ = 4, $p_{Mineralogy}$ = 10 and $p_{Geochemistry}$ = 22), we test the significance, and hence stability, of each significant principal component (PC) [e.g., *Jackson*, 1993]. To test for stability in each significant PC, the individual eigenvalues ($\hat{\lambda}$) were bootstrapped using ordinary non-parametric bootstrap technique [e.g., *Efron and Tibshirani*, 1993] with 10,000 iterations and individual histograms investigated. Depending on the histogram resembles a normal-family distribution or skewed distribution, then the 95%

confidence intervals on the resampled eigenvalues ($\hat{\lambda}^*$) are calculated using the percentile or the bias-corrected methods [*Canty*, 2002; *Efron and Tibshirani*, 1993].

2.3.3.3. Discriminant Function Analysis - DFA

DFA is a powerful classification technique that can be used for maximizing the separation between well-defined or known groups of population by using linear discriminant functions [*Davis*, 2002]. Discriminant functions are linear combinations of a set of independent variables (predictors) and create scores that are used to allocate group memberships. DFA concentrates on discriminating groups and the regression coefficients of the discriminant functions maximize the ratio of between-group mean differences and within-groups variance differences [*Tabachnick and Fidell*, 2013].

DFA was performed on the grain size, mineralogy and geochemistry of the sediment samples to identify which samples formed groups. Variables were transformed to standardized scores to make them comparable across each sample. The DFA groupings were then graphically compared based on the *a priori* sedimentary environment groupings. The focus was on how different the individual groups are rather than looking at the data structure or variables.

2.4. Results

2.4.1. Analytical results

2.4.1.1. Grain size analysis

The offshore area is characterized by a shallow-gradient shelf dominated by quartz, and minor carbonates (aragonite and calcite), feldspars (microcline, orthoclase, labradorite), heavy minerals (cassiterite, zircon, garnet), muscovite, monazite and kaolinite (Fig. 2.2 and Supp. Info Figs.S2.1-S2.2). The grain size varies from medium- to fine-sand in the nearshore and medium- to coarse-sand in water deeper than 15 m (Fig. 2.2). This grain size distribution is similar to the offshore sediment grain size described from offshore Pakarang Cape approximately 40 km south of Phra Thong Island [*Feldens et al.*, 2012]. The Offshore group presents a wide range of grain size characteristics and can be divided into two sub-groups: the Deep-Offshore group (>10m water depth; samples include: PT-OS 03, PT-OS 05, PT-OS 13, PT-OS 15 and PT-OS 17) and the Nearshore group (<10m water depth; samples include: PT-OS 24, PT-OS 26, PT-OS 28, PT-OS 32, PT-OS 33, PT-OS 34) (Fig. 2.1, Table 2.1).

The Deep-Offshore group is characterized by coarse to medium, poorly to moderately sorted, very fine to finely skewed and mesokurtic to very leptokurtic sand (Fig. 2.2, Table 2.1). The Nearshore group, in contrast, is composed of very fine to fine, moderately to moderately well sorted, very finely skewed to symmetrical and mesokurtic to very leptokurtic sand (Fig. 2.2, Table 2.1). Sample PT-OS 21, which lies between the Deep-Offshore and the Nearshore group (Fig. 2.1), is characterized by very coarse very poorly sorted, finely skewed and leptokurtic silt (Fig. 2.2, Table 2.1).

The Onshore group consists of predominantly medium, moderately well sorted, symmetrical and mesokurtic sand, except PT-04, which is classified as a fine sand (Table 2.1). The Sand A and Sand B groups are very similar and composed of very fine, moderately to moderately well sorted, coarsely skewed to symmetrical and mesokurtic to leptokurtic sand (Table 2.1). The Sand C group is a fine, poorly sorted, finely skewed to symmetrical and very leptokurtic sand (Table 2.1). The Sand D and the Storm groups are both medium, moderately sorted to moderately well sorted, mesokurtic sands, but they differ slightly in skewness, with Sand D samples finely skewed and the Storm samples typically symmetrical (Table 2.1).

2.4.1.2. Mineralogy

Both bulk sediment mineralogy suggests a relative homogeneity of the sediments with quartz dominating (>80 wt. %) and minor aragonite, calcite, and garnet are present. The fine sediment fraction mineralogy is still dominated by quartz (*ca*. 52 wt. % on average), though a range of other minerals are present including orthoclase, microcline, aragonite, zircon, cassiterite, monazite, kaolinite, muscovite and labradorite (Table 2.2). Calcite and garnet were not present in the finer fraction suggesting that these minerals are only present as coarse grains.

The XRD results of the bulk sediment analyses show that quartz dominates the marine sediments with minor contributions of calcite, aragonite, zircon and garnet (Supp. Info. Fig. S2.1). Notably, aragonite has high concentrations in the nearshore environment south of the onshore sampling locations (~15 wt. %) and deeper offshore (~12 wt. %) but persists in most samples at very low concentrations (Supp. Info. Fig. S2.1).

For the fine mineralogical fractions, quartz dominates (>45 wt. %) the nearshore environment to depths of 15 to 20m, but other minerals have locally high concentrations demonstrating the mineralogical heterogeneity of the marine environment in the north of Phra Thong Island (Fig. 2.2 and Supp. Info. Figs. S2.2-S2.3). In the fine fraction, aragonite and muscovite are present throughout the marine environment but have locally high concentrations (aragonite: 12-15 wt. %, muscovite:10 wt. %) in deeper environments (Supp. Info. Figs. S2.2). The northern nearshore environment and deep offshore environments contain high zircon (8 and 6 wt. %), orthoclase (16 wt. % in both environments) and microcline (9 and 12 wt. %), suggesting a consistent mineral assemblage (Supp. Info. Figs. S2.3). Microcline also occurs in high concentrations in the nearshore zone south of the onshore sampling sites and between 10 and 20 m water depth to the north (Supp. Info. Figs. S2.3). Cassiterite, which has been extensively mined for tin (Jankaew et al., 2011) is found adjacent to the sampled overwash deposits in the nearshore environment (~1.5 wt. %) and in water depths ranging from 10 to 20 m (Supp. Info. Figs. S2.2).

Table 2.1: Grain size parameters (mean, sorting, skewness and kurtosis) of sediment samples performed by the Malvern Mastersizer 2000.

Groups	Sample codes	Mean	Sorting	Skewness	Kurtosis	Description
Deep-Offshore	PT-OS 03	1.577	1.601	0.465	1.59	Medium sand, poorly sorted, very fine skewed, very leptokurtic
Deep-Offshore	PT-OS 05	1.218	0.782	0.105	0.962	Medium sand, moderately sorted, fine skewed, mesokurtic
Deep-Offshore	PT-OS 13	0.999	0.89	0.242	1.246	Coarse sand, moderately sorted, fine skewed, leptokurtic
Deep-Offshore	PT-OS 15	1.275	0.994	0.228	1.398	Medium sand, moderately sorted, fine skewed, leptokurtic
Deep-Offshore	PT-OS 17	0.842	0.951	0.318	1.293	Coarse sand, moderately sorted, very fine skewed, leptokurtic
Deep-Offshore	PT-OS 21	4.153	2.01	0.176	1.223	Very coarse silt, very poorly sorted, fine skewed,leptokurtic
Mean		1.67	1.2	0.25	1.28	
Nearshore	PT-OS 24	3.458	0.613	0.134	1.161	Very fine sand, moderately well sorted, fine skewed, leptokurtic
Nearshore	PT-OS 26	3.448	0.874	0.311	1.997	Very fine sand, moderately sorted, very fine skewed, very leptokurtic
Nearshore	PT-OS 28	3.021	0.527	0.014	0.935	Very fine sand, moderately well sorted, symmetrical, mesokurtic
Nearshore	PT-OS 32	2.798	0.527	0.002	0.935	Fine sand, moderately well sorted, symmetrical, mesokurtic
Nearshore	PT-OS 33	2.843	0.541	0.006	0.931	Fine sand, moderately well sorted, symmetrical, mesokurtic
Nearshore	PT-OS 34	2.202	1.164	0.044	0.784	Fine sand, poorly sorted, symmetrical, platykurtic
Mean		2.96	0.7	0.085	1.12	
Onshore	PT-02	1.971	0.557	0.01	0.938	Medium sand, moderately well sorted, symmetrical, mesokurtic
Onshore	PT-04	2.17	0.62	0.003	0.924	Fine sand, moderately well sorted, symmetrical, mesokurtic
Onshore	PT-05	1.856	0.57	0.004	0.937	Medium sand, moderately well sorted, symmetrical, mesokurtic
Onshore	PT-07	1.996	0.671	-0.012	0.94	Medium sand, moderately well sorted, symmetrical, mesokurtic
Onshore	PT-07(s)	1.24	0.639	0.027	0.921	Medium sand, moderately well sorted, symmetrical, mesokurtic
Onshore	PT-08	1.75	0.667	0.035	0.933	Medium sand, moderately well sorted, symmetrical, mesokurtic
Onshore	PT-09	1.692	0.62	0.021	0.932	Medium sand, moderately well sorted, symmetrical, mesokurtic
Onshore	PT-11	1.848	0.674	0.015	0.936	Medium sand, moderately well sorted, symmetrical, mesokurtic
Mean		1.81	0.63	0.01	0.93	

Table 2.1 (Cont.)

Groups	**Sample codes**	**Mean**	**Sorting**	**Skewness**	**Kurtosis**	**Description**
Sand A	PT-CT04 19	3.157	0.707	-0.068	1.061	Very fine sand, moderately sorted, symmetrical, mesokurtic
Sand A	PT-CT04 18	3.205	0.639	-0.064	0.989	Very fine sand, moderately well sorted, symmetrical, mesokurtic
Sand A	PT-CT04 11	3.052	0.812	-0.196	1.16	Very fine sand, moderately sorted, coarse skewed, leptokurtic
Sand A	PT-CT04 09	3.09	0.624	0.04	1.046	Very fine sand, moderately well sorted, symmetrical, mesokurtic
Mean		3.126	0.7	0.072	1.064	
SandB	PT-CTpaleo-06	3.061	0.858	-0.239	1.247	Very fine sand, moderately sorted, coarse skewed, leptokurtic
SandB	PT-CTpaleo-07	3.152	0.567	0.063	1.049	Very fine sand, moderately well sorted, symmetrical, mesokurtic
SandB	PT-CTpaleo-11	3.165	0.585	-0.017	0.937	Very fine sand, moderately well sorted, symmetrical, mesokurtic
SandB	PT-CTpaleo-10	3.028	0.657	-0.077	0.991	Very fine sand, moderately well sorted, symmetrical, mesokurtic
Mean		3.1	0.67	0.067	1.056	
SandC	SandC 1	2.696	1.188	0.008	1.63	Fine sand, poorly sorted, symmetrical, very leptokurtic
SandC	SandC 2	2.818	1.074	0.165	1.675	Fine sand, poorly sorted, fine skewed, very leptokurtic
SandC	SandC 3	2.839	1.039	0.18	1.706	Fine sand, poorly sorted, fine skewed, very leptokurtic
Mean		2.78	1.1	0.12	1.67	
SandD	SandD 1	1.315	0.961	0.24	1.092	Medium sand, moderately sorted, fine skewed, mesokurtic
SandD	SandD 2	1.557	1.164	0.287	1.115	Medium sand, poorly sorted, fine skewed, leptokurtic
Mean		1.44	1.06	0.26	1.1	
Storm	Storm 1	1.554	0.552	0.01	0.934	Medium sand, moderately well sorted, symmetrical, mesokurtic
Storm	Storm 2	1.588	0.605	0.016	0.926	Medium sand, moderately well sorted, symmetrical, mesokurtic
Storm	Storm 3	1.583	0.559	0.002	0.934	Medium sand, moderately well sorted, symmetrical, mesokurtic
Mean		1.57	0.57	0.01	0.93	

Table 2.2: Mineral contents of finer fraction (in wt. %).

Groups	**Sample**	**Quartz**	**Labradorit**	**Orthoclas**	**Microclin**	**Aragonit**	**Zircon**	**Cassiterit**	**Monazit**	**Kaolinit**	**Muscovit**
Deep-Offshore	PT-OS 03	38.8	2.2	9.6	4.8	12.6	1.4	0.5	3.5	2.6	7.8
Deep-Offshore	PT-OS 05	44	2	16.1	10.1	13.7	5.3	0.7	3	0.9	3.8
Deep-Offshore	PT-OS 07	38.7	1.8	12	1.3	9.7	1.2	0.2	2.9	1.3	9.3
Deep-Offshore	PT-OS 13	59.9	0.5	10.5	5.7	6.4	3.1	0.7	2.2	1.7	6.2
Deep-Offshore	PT-OS 15	42.1	3.2	7.4	7.8	8.7	2.2	0.8	3.5	3.5	9.4
Deep-Offshore	PT-OS 17	40.1	2.9	10.5	10.5	10.1	4.5	1.7	4.2	1.8	6.7
Deep-Offshore	PT-OS 21	63.3	0.6	7.8	9.1	5.3	2.1	0.6	1.9	1.5	3.9
Deep-Offshore	PT-OS 22	64.7	1.6	9.1	8.2	5.3	2.4	0.6	1.5	1.9	2
Nearshore	PT-OS 24	65.5	0.8	9.3	6.7	9.2	3.4	1.1	1.4	0.8	1.6
Nearshore	PT-OS 26	56.3	0.5	12.5	8.4	11.4	4.2	1.1	2.3	0.6	2.7
Nearshore	PT-OS 28	46.5	1.1	14.5	9.5	11.1	6.6	0.9	2.6	1.7	4.8
Nearshore	PT-OS 32	61.1	0.7	12.4	7.6	7.4	4.1	1	1.9	1.1	2.8
Nearshore	PT-OS 33	78.4	0.3	7.5	5.2	3.3	2.4	0.4	1.5	0.6	3.1*
Nearshore	PT-OS 34	58.7	1	11.1	8	9.6	3.4	1.6	1.7	0.9	3.9
Onshore	PT-02	53.4	1.7	14.3	8.7	8.2	5.6	1.2	2	1	3.9
Onshore	PT-04	56.3	0.9	13.6	8.4	7.8	4.6	1.6	2.2	1	3.5
Onshore	PT-05	45.7	1.6	14.9	10.6	10	7.3	0.8	2.4	1.2	4.4
Onshore	PT-07	57.1	1	12.5	8.5	7.3	5.3	1.1	2.4	1	2.6
Onshore	PT-07 (s)	37.6	1	14.9	13.1	12.3	8.3	1	1.8	1.7	6.6
Onshore	PT-08	49.6	1.7	14	9.4	8.9	7.7	1.1	2.2	0.9	4.4
Onshore	PT-09	37.3	1.2*	12.7	9.4	9.2	13.5	3.8	1.3	2.6	6.6
Onshore	PT-11	47.8	0.5	10.7	8.2	6.7	12.3	3.1	1.4	1.4	5.7
SandA	PT CT 04	52.1	1.4	13.8	9	12	4.6	1	2.4	0.9	2.9
SandA	PT-CT 04	57	0.3	11.8	8.7	10.1	3.7	1.4	1.8	1.2	3.9
SandA	PT-CT 04	51.2	1.5	14	9	12.4	4.8	0.9	2.5	0.9	2.8
SandA	PT-CT 04	53.8	1.1	12.9	9.8	11	4.7	1.1	2.2	0.5	2.8
SandB	PT-CT 06	44.6	2.6	13.6	10.8	11	6.3	0.6	2.9	1.3	4.9
SandB	PT-CT 07	48.5	1.4	14.5	9.9	8.9	6.2	1	2.6	1.3	4.8
SandB	PT-CT 10	53.2	1.4	13.3	8.5	9.2	6.7	1	2.4	1.2	3.1
SandB	PT-CT 11	53.9	1.5	11.7	9.6	8.1	6.4	1.2	2.1	1.2	4.1

*: We replaced the missing values of muscovite mineral in sample PT-OS 33 by taking the mean of muscovite mineral of the group that the sample belong to. We repeated the same calculation for labradorite mineral in sample PT-09.

2.4.1.3. Trace element geochemistry

The results of 34 trace elements analysed show significant heterogeneity across the marine environment and in the onshore and overwash deposits (Fig. 2.2, Supp. Info. Figs S2.4-S2.6, Table 2.3). Several of the analysed elements are excluded from further discussion including:

- sulfur (S), chlorine (Cl) and bromine (Br) because they are typically marine elements with very high concentrations in the offshore samples and low in the other samples, and therefore they were likely to saturate the results;
- zinc (Zn), germanium (Ge), molybdenum (Mo), cadmium (Cd), antimony (Sb) and mercury (Hg) because they showed no variation between the groups and contribute little to dissimilarity tests; and,
- cobalt (Co), tantalum (T) and tungsten (W) because the high values of these elements were caused by contamination during the grinding process.

From this, 22 trace elements (V, Cr, Ni, Cu, As, Se, Rb, Sr, Zr, Nb, Sn, Ba, La, Ce, Hf, Pb, Th, U, Y, Cs, Ga, Bi) were included in the statistical analyses (Table 2.3).

Of these 22 trace elements, distinct elemental zones exist in the marine environment west of Phra Thong Island (Fig. 2.2 and Supp. Info. S2.4-S2.6). Notably, the nearshore zone contains a high degree of trace element heterogeneity which mirrors the mineralogical heterogeneity.

Immediately offshore from the onshore sampling sites the trace elements have high concentrations of Sr, Nb, Sn, La, Rb, Th, U, Y and Zr (Fig. 2.2 and Supp. Info. Fig. S2.4). Further offshore in intermediate depth waters (10 to 20 m) As, Cr, Pb, V, Ba and Sr have high elemental concentrations (Fig. 2.2 and Supp. Info. Fig. S2.5). In the northern nearshore zone Ce, La, Th, U, Y and Zr have higher elemental concentrations than to the south, but also have high concentrations of Bi, Hf, Nb and Se (Fig. 2.2 and Supp. Info. Figs. S2.4, S2.6). The nearshore environment south of the onshore sampling sites has high concentrations of Ba, Cr, Cu, Cs, Ga, Ni, Rb, Pb and V (Supp. Info. Figs. S2.4, S2.5 and S2.6). The trace elemental concentrations in the water deeper than 20 m have high Sr concentrations and in the northern section, high Sn (Fig. 2.2).

Table 2.3: Trace element concentrations of bulk samples (in ppm).

Groups	**Sample codes**	**V**	**Cr**	**Ni**	**Cu**	**As**	**Se**	**Rb**	**Sr**	**Zr**	**Nb**	**Sn**
Deep-Offshore	PT-OS 03	18.7	22.2	12	7.5	0.5	3.3	20.4	501.7	91.7	5.8	23
Deep-Offshore	PT-OS 05	7	13.2	5.5	5.8	0.5	2.9	19.8	356.2	50.1	3	7.2
Deep-Offshore	PT-OS 07	15.5	17.8	5.9	7.8	0.5	3.1	32.1	592.6	328.3	11.2	206
Deep-Offshore	PT-OS 13	9.7	8.4	5.6	6.1	3.2	3.4	10.3	184.8	119.5	8.4	35.6
Deep-Offshore	PT-OS 15	12.8	12.9	5.4	7.2	9	2.9	11.8	235.7	60	3.4	12.6
Deep-Offshore	PT-OS 17	10.3	12.3	7	6.8	3	3.9	11.1	204.2	57.4	4.5	35.2
Deep-Offshore	PT-OS 21	46.9	36.6	16.7	12.5	8.6	2.6	160.8	563.8	438.7	24.3	47.9
Deep-Offshore	PT-OS 22	44	39.8	12.5	10.1	17.2	1.4	100.7	729.6	306.6	17.5	45.9
Nearshore	PT-OS 24	5	15.1	9.9	8.5	1	3.1	117.8	601.8	1581	29.4	63.6
Nearshore	PT-OS 26	11	16	8.8	7.8	3.7	2.3	113.5	595.8	1144	24.4	52.6
Nearshore	PT-OS 28	5.4	16.9	11.8	8.6	0.5	3.5	63.7	345.9	2687	45.4	120.3
Nearshore	PT-OS 32	5.2	10.1	6.3	7.9	1.2	2.7	62.8	376.3	936.6	18.9	63.2
Nearshore	PT-OS 33	4.8	11.1	5.7	7.2	1.4	2.3	70.2	483.5	1269	21.6	91.3
Nearshore	PT-OS 34	6.7	12.4	5.3	7.2	2	2.1	64.6	406.6	1163	65.8	152.7
Onshore	PT-02	11.1	7.5	9.7	7.8	0.5	4.8	11.1	3.2	497.2	18	61.8
Onshore	PT-04	8	5.8	9.9	7.9	0.5	5.8	18.3	4.5	376	14.3	45.4
Onshore	PT-05	6.6	8.5	11.4	8.3	0.5	5.7	11	66.7	1062	48.2	100.2
Onshore	PT-07	5.4	7.8	6.3	10.3	0.5	4.4	20.9	108.9	703.5	34.4	64.6
Onshore	PT-07 (s)	0.5	13	6.8	12.3	0.5	4.4	10	127.8	1190	85	164.9
Onshore	PT-08	7.3	13.4	11.7	8.3	0.5	7	10.2	116.1	1536	116.6	273.3
Onshore	PT-09	0.5	25.6	9.7	7.2	0.5	1.9	8.6	92.6	4724	400.3	1276
Onshore	PT-11	0.5	23.1	11.1	7.5	0.5	3.5	11.7	127.3	5069	329.8	952
SandA	PT CT 04 09	16	16	11	9	0.5	6.6	81	488	831	22	64
SandA	PT-CT 04 11	13.5	12.7	6	8.6	1.8	1.2	81.2	495.6	906.7	23.8	78.8
SandA	PT-CT 04 18	13.9	14	5.9	14.4	0.5	2.3	83.2	468.4	937.3	24	79.6
SandA	PT-CT 04 19	11.7	16.1	5.7	8.8	0.5	1.4	82	535.8	820.2	21.8	65.5
SandB	PT-CT 06	7	15	13	4	0.5	10	93	19	2134	35	144
SandB	PT-CT 07	2.1	14.6	15.4	11.4	0.5	6.8	93.8	15.9	2192	35.6	152.8
SandB	PT-CT 10	2.9	11.5	14.1	12.6	0.5	6.2	90.5	15.3	1818	35.1	137.2
SandB	PT-CT 11	0.5	11.7	12.6	12.2	0.5	5.5	90.2	15.1	1895	35.3	150.3
SandC	SandC 1	3	9	6	6	0.3	3	37	7	196	7	28
SandC	SandC 2	1	6	5	5	0.3	3	29	5	121	4	9
SandC	SandC 3	4	10	6	6	0.3	3	70	20	609	13	39
SandD	SandD 1	0.5	17	7	5	0.3	3	10	30	2844	191	701
SandD	SandD 2	0.5	15	7	4	0.3	3	11	29	2679	155	443
Storm	Storm 1	0.5	10.1	7.2	5.7	0.3	3.1	62.8	15	779.5	16	52
Storm	Storm 2	0.5	14.5	5.6	7.2	0.3	3	11.5	26.9	1240	95.3	241.4
Storm	Storm 3	1.8	11	6.7	5.9	0.3	2.9	70.5	16.6	677.1	14.9	42.4

Table 2.3 (Cont.)

Groups	**Sample codes**	**Ba**	**La**	**Ce**	**Hf**	**Pb**	**Th**	**U**	**Y**	**Cs**	**Ga**	**Bi**
Deep-Offshore	PT-OS 03	31.5	5.9	8.1	0.4	6.2	9.6	0.5	9.2	7.3	5	2.1
Deep-Offshore	PT-OS 05	24.8	6.7	0.7	0.5	3.3	5.4	0.5	5.6	2	2.4	2.1
Deep-Offshore	PT-OS 07	48.8	8.6	35.3	4.5	6.3	14	1.6	13.9	2	4.6	2.1
Deep-Offshore	PT-OS 13	22.3	7.1	10.9	3.6	3.4	9.2	0.5	8.6	2	3	2.2
Deep-Offshore	PT-OS 15	17.8	4.5	4.5	0.3	4.4	9.8	0.5	7.5	2	2.9	2.3
Deep-Offshore	PT-OS 17	1.5	10.8	13.1	1.7	3	7.7	0.5	6.8	2	3	2.9
Deep-Offshore	PT-OS 21	111.6	41.9	108.3	8.8	35.2	49.2	0.5	35.2	18.8	15.7	2.9
Deep-Offshore	PT-OS 22	84.9	12.5	66.3	7.6	28.8	33.6	4.8	27.2	2	10.3	1.9
Nearshore	PT-OS 24	81.2	101.7	266	32.1	18.9	105.5	16.7	87.9	2	7.1	2.8
Nearshore	PT-OS 26	75.6	82.5	183	24.4	21.1	80.4	10.4	69.8	2	7.2	2.6
Nearshore	PT-OS 28	49.6	159	346	55.8	14.7	152.7	24.7	139.3	2	5.1	3.3
Nearshore	PT-OS 32	54.8	75.7	131.3	17.9	10.6	54.5	6.8	45.5	2	5.1	2.3
Nearshore	PT-OS 33	58.8	67.3	181.4	23.7	12.1	81.3	9.9	61.6	2	4.5	2
Nearshore	PT-OS 34	57.3	38.9	71.4	21.2	12.4	44.3	7.6	49.3	2	5.2	1.8
Onshore	PT-02	1.5	15.2	33.4	13.1	0.8	14.8	1.6	15.9	2	3	3.3
Onshore	PT-04	23.4	15.1	0.5	10.8	1.4	10.5	0.6	13.4	11.3	3.5	3.2
Onshore	PT-05	1.5	33.5	63.6	22.7	2.6	26.5	5.9	35	2	5	3.5
Onshore	PT-07	26.8	17.5	0.5	14	3.9	12.8	3.9	19.3	2	4.1	2.6
Onshore	PT-07 (s)	1.5	32.2	63.3	25.3	5.3	25.6	7.8	38.7	2	4.4	2.8
Onshore	PT-08	21.6	38.5	95.6	35.2	5.6	34.1	9.5	55	2	6.7	4.2
Onshore	PT-09	15.4	105.6	253	94.2	22.7	97.1	31.7	170.4	2	5.1	0.5
Onshore	PT-11	1.5	85.6	230	102.9	18.6	110	35.3	165.8	2	5.9	2.2
SandA	PT CT 04 09	63	48	104	20	1	46.1	9.2	41	3.5	8	0.5
SandA	PT-CT 04 11	64	50	108.6	20.3	13.5	47.9	10.9	44.7	2	2.9	0.5
SandA	PT-CT 04 18	62.4	46.1	103.9	17.9	13.6	51.8	11.8	46.3	11.8	6	2.2
SandA	PT-CT 04 19	60.1	48.3	101.3	17.8	13.8	44.9	9.9	42.1	2	3.3	0.5
SandB	PT-CT 06	70	162	379	53	1	159.7	20.2	117	3.5	8	0.5
SandB	PT-CT 07	76.1	174.6	362	49.1	15.8	165.8	21.7	118.4	10.3	7.8	4.9
SandB	PT-CT 10	66.2	122.1	278	41	14.1	129.6	17.5	96.6	2	8.2	4.3
SandB	PT-CT 11	64.7	141.9	281.7	41.2	14.5	135.4	19.1	100.7	8.7	7	3.8
SandC	SandC 1	52	15	35	4	5	8.4	1.1	10	3.5	4	2
SandC	SandC 2	42	1	15	3	4	6.3	1	7	3.5	3	2
SandC	SandC 3	67	39	72	13	12	31.1	4.1	30	3.5	5	2
SandD	SandD 1	23	69	129	56	10	60.2	20.4	90	3.5	4	2
SandD	SandD 2	23	71	121	53	9	49.4	16.5	86	3.5	3	0.5
Storm	Storm 1	66.5	62.9	83.8	15.9	10.9	40.6	6.6	34.4	3.5	4.8	2
Storm	Storm 2	0.7	22.7	49.7	23.6	5.4	26.6	7.6	41.3	3.5	5	2.4
Storm	Storm 3	74.3	48.9	77.7	13.4	12.4	34.6	5.7	32.3	3.5	4.3	1.7

2.4.2. Statistical results

In this section, the terms denoted by a subscript *GS, MIN* and *CHEM* are statistical analyses (i.e. PAM, PCA and DFA) for the grain size parameters, mineral contents and trace elements, respectively.

2.4.2.1 Grain size parameters

Four granulometric parameters (mean, sorting, skewness and kurtosis) were examined using PAM_{GS}. The PAM_{GS} (Fig. 2.3) indicates that eight clusters can be identified (overall average silhouette is 0.53). Cluster 1 includes one Sand A and one Sand B sample (Fig. 2.3). Cluster 3 comprises all of Sand C and one Nearshore sample. Cluster 4 incorporates most of the Sand A, Sand B (three samples for each group) and four Nearshore samples (Fig. 2.3). Cluster 6 is composed of three samples Deep-Offshore and all of Sand D samples. Cluster 7 is the largest cluster and is made up of all of Onshore and Storm samples. Clusters 2, 5 and 8 contain only a single sample for each group and their silhouette widths are zero (Fig. 2.3). The zero silhouette width of these clusters implies a “neutral case” and samples in these clusters can be also equally assigned to either neighboring cluster [e.g. the second-best choice; *Kaufman and Rousseeuw*, 2005].

The PCA_{GS} result is consistent with the PAM_{GS} analysis (Fig. 2.4a). The broken stick model (Fig. 2.4b) and Kaiser-Guttman criteria (Supp. Info Table S2.1) suggest that only the first two principal components are necessary to explain most of the variance in the grain size data set. The first two principal components ($PC1_{GS}$ and $PC2_{GS}$) are sufficient to explain the grain size dataset and account for 82% of the explained variance (Fig. 2.4b and Supp. Info Table S2.1). The ordinary non-parametric bootstrap analysis of $\hat{\lambda}^*$ does not differ significantly from the $\hat{\lambda}$ determined from the PCA for either $PC1_{GS}$ and $PC2_{GS}$ indicating the stability of each principal component using the available data. Histograms and quantile-quantile plots for $PC1_{GS}$ (Supp. Info Fig S2.7) and $PC2_{GS}$ (Supp. Info Fig S2.7) demonstrate the relative normality of the distributions of $\hat{\lambda}^*$ and that $\hat{\lambda}$ ($PC1_{GS} = 2.08$ and $PC2_{GS} =1.206$) resides within the percentile 95% confidence interval of $\hat{\lambda}^*$ ($PC1_{GS} = (1.803, 2.616)$; and $PC2_{GS} = (0.94, 1.395)$).

$PC1_{GS}$ explains 52% of the variance and is defined by sorting, skewness and kurtosis. Along $PC1_{GS}$, there is very little difference between the Sand A, Sand B, Onshore, Storm (Fig. 2.4a). Each of these deposits overlaps with the region defined by the Nearshore sediments and reflects well-sorted and symmetric sediments. $PC1_{GS}$, also results in significant overlap between the grain size parameters of the Nearshore, Deep offshore, Sand C and Sand D (Fig. 2.4a).

$PC2_{GS}$ explains 30% of variance and is defined by the mean sediment grain size. $PC2_{GS}$ shows extensive overlap between each of the overwash deposits and environments with the mean grain size of the Deep offshore environment (Fig. 2.4a). However, $PC2_{GS}$ does separate Sands A, B and C that are situated within the Nearshore sediments, from the Storm deposits that are very similar to the Onshore deposits (Fig. 2.4a).

Both $PC1_{GS}$ and $PC2_{GS}$ show a large scatter in the distribution of Deep-Offshore and Nearshore sediments as seen in the Folk-Ward Classification (Table 2.1). In both principal components, Sand A and Sand B samples, and the Onshore and Storm samples overlap. There is a gradation in mean grain size from the Sand A and Sand

B samples to the Onshore and Storm samples with the Nearshore sediments interspersed between these deposits. The Deep-Offshore sediments show a wide distribution in $PC1_{GS}$ and $PC2_{GS}$ that reflects a high diversity of grain size characteristics.

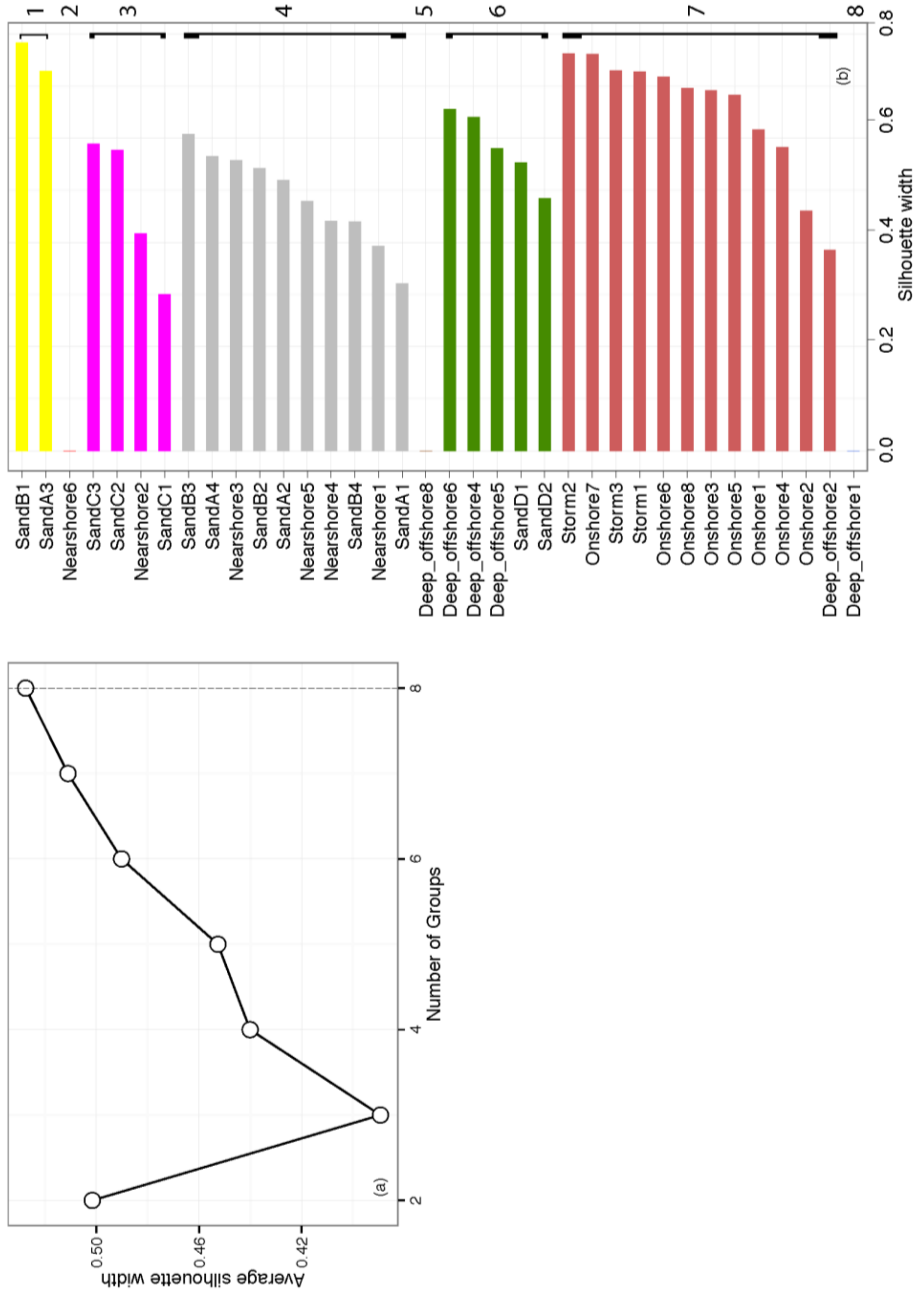

Figure 2. 3: The PAM analysis for grain size parameters. (a) The number of groups and equivalent silhouette width. (b) The clustering structure of sample set, different colors differentiate clusters.

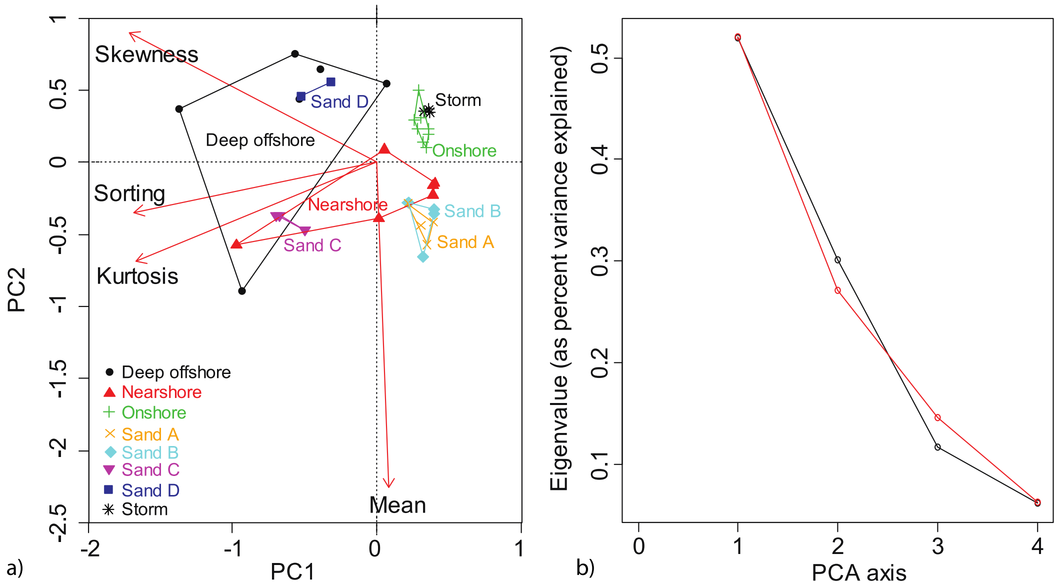

Figure 2. 4: The PCA analysis for grain size parameters. (a) The first two principal components (PCA1 versus PCA2); (b) The screeplot shows the ordination analysis (black line) versus the broken stick rule (red line).

In the DFA$_{GS}$, discriminant function 1 (DF1$_{GS}$) is highly significant (percentage separation is 75%) and separates Sand D and the Deep-Offshore groups from Sand A, Sand B and most Nearshore samples (Fig. 2.5). Discriminant function 2 (DF2$_{GS}$; accounts for 17% separation) discriminates Sand C from the remaining sediment samples (Fig. 2.5). The similarity of Sand A and Sand B is demonstrated in the DFA$_{GS}$, and these two groups are situated close to the three Nearshore samples (Fig. 2.5) as observed in the PCA$_{GS}$ (Fig. 2.4a). The Storm and Onshore groups agree with the PCA$_{GS}$ results (Fig. 2.4a) and are defined by DF2$_{GS}$, which separates these samples from Sand C.

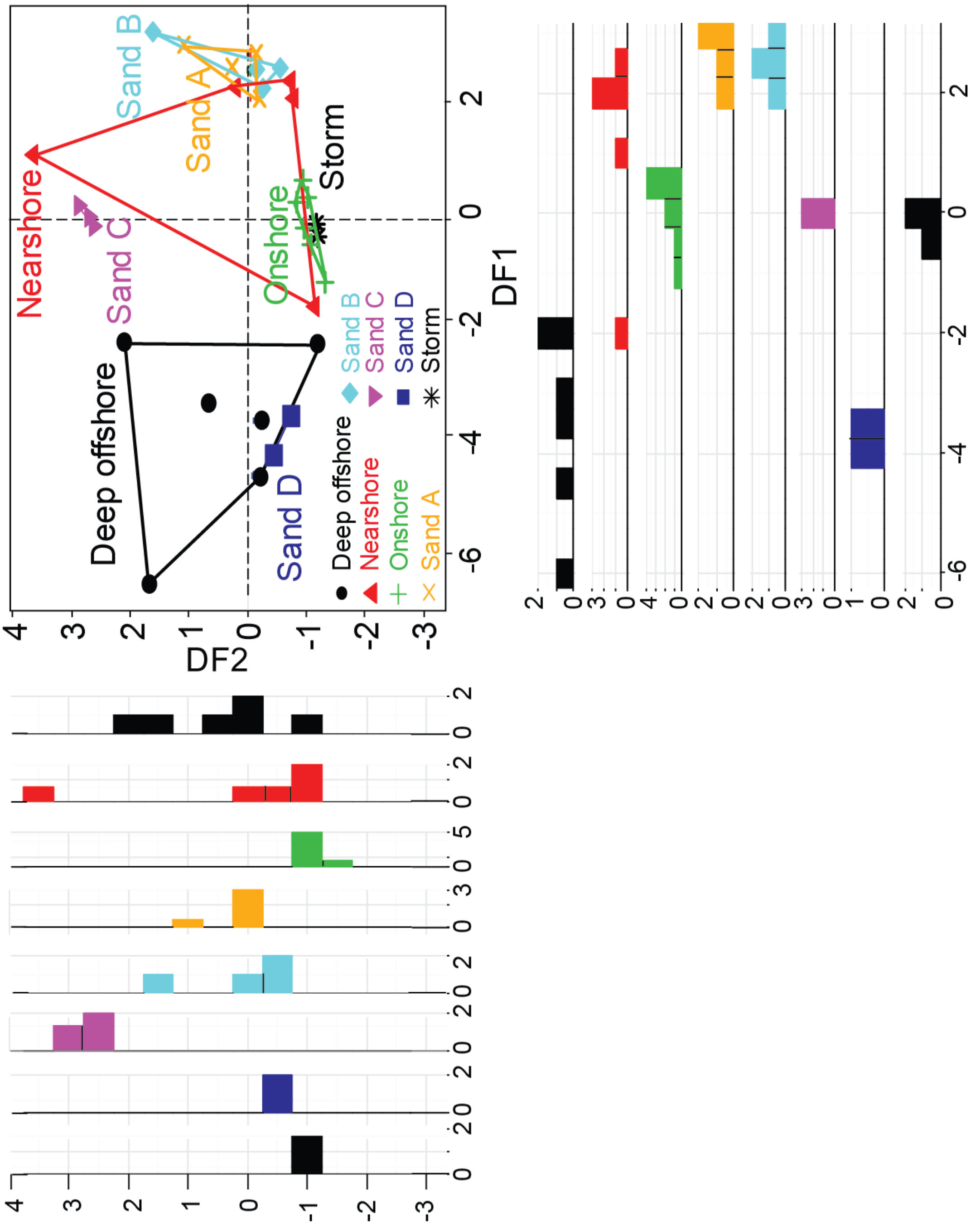

Figure 2. 5: The DFA analysis for grain size parameters. The graph shows the first two discriminant function analysis (DF1 versus DF2). The stacked histograms show the scores and power of separation of each group relative to the other groups.

2.4.2.2. Mineral content

The PAM_{MIN} determined only two clusters with an average silhouette width of 0.4. The first large cluster includes all of the Onshore, Sand A, Sand B, Nearshore samples, and half of the Deep-Offshore group while the second cluster comprises the rest of the Deep-Offshore group (Fig. 2.6).

The PCA_{MIN} result (Fig. 2.7a) is consistent with the PAM_{MIN} (Fig. 2.6) analysis showing a broad mineralogical transition from the Nearshore and Onshore deposits to the two most recent tsunami deposits (Sand A and Sand B). The broken stick model (Fig. 2.7d) and Kaiser-Guttman criteria (Supp. Info Table 2.2) suggest that the first three principal components are necessary to explain most of the variance in the mineralogy data set. The first three principal components ($PC1_{MIN}$, $PC2_{MIN}$ and $PC3_{MIN}$) are sufficient to explain the mineralogy dataset and account for 81% of the explained variance (Fig. 2.7d and Supp. Info Table 2.1).

The ordinary non-parametric bootstrap analysis of $\hat{\lambda}^*$ does not differ significantly from the $\hat{\lambda}$ determined from the PCA_{MIN} for either $PC1_{MIN}$, $PC2_{MIN}$ or $PC3_{MIN}$ indicating the stability of each principal component using the available data. Histograms and quantile-quantile plots for $PC1_{MIN}$ (Supp. Info Fig S2.8), and $PC2_{MIN}$ (Supp. Info Fig S2.8) are relatively normally distributions of $\hat{\lambda}^*$ and that $\hat{\lambda}$ ($PC1_{MIN}$ =3.58 and $PC2_{MIN}$ =2.69) resides within the percentile 95% confidence interval of $\hat{\lambda}^*$ ($PC1_{MIN}$ = (3.259, 4.98) and $PC2_{MIN}$ = (2.01, 3.31)). The histogram and quantile-quantile plot of $PC3_{MIN}$ (Supp. Info Fig S2.9) is skewed and a normal distribution cannot be assumed. However, $\hat{\lambda}$ ($PC3_{MIN}$ =1.83) resides within the bias-corrected percentile 95% confidence interval of $\hat{\lambda}^*$ ($PC3_{MIN}$ = (1.27, 2.61).

$PC1_{MIN}$ (~36% of the variance) is positively correlated with quartz content and is negatively correlated with labradorite, monazite, kaolinite and muscovite (Fig. 2.7a). Conversely, quartz does not significantly contribute to variations in $PC2_{MIN}$ (~27% of the variance) but zircon, orthoclase, microcline and cassiterite positively contribute to $PC2_{MIN}$. Labradorite, monazite, kaolinite and muscovite are also weakly negatively correlated with $PC2_{MIN}$ (Fig. 2.7a). $PC3_{MIN}$ (18% of the variance) is positively correlated with orthoclase, monazite and aragonite, and negatively correlated with muscovite, kaolinite, zircon and cassiterite when compared with $PC1_{MIN}$ (Fig. 2.7b). However, comparison between $PC2_{MIN}$ and $PC3_{MIN}$ (Fig. 2.7c) shows that orthoclase and aragonite are orthogonal to monazite, and muscovite and kaolin are orthogonal to zircon and cassiterite. Of note, aragonite appears to influence a single Deep offshore sample and a single Sand B sample, likely due to the presence of coral rubble, which is not present in any other samples.

The first three principal components together show that Sand A and Sand B are mineralogically indistinguishable (Fig. 2.7a-c) and that most of the Nearshore and Onshore sediments cluster around the origin of the three principal component plots highlighting the relative mineralogical homogeneity (Fig. 2.7a-c). Even after the removal of coarse-grained quartz, the Nearshore samples are influenced by increasing concentrations of fine-grained quartz, whereas the Onshore sediments have relative higher concentrations of zircon, orthoclase, microcline and cassiterite (Fig. 2.7a-c). The Deep offshore samples have elevated labradorite, muscovite, monazite and kaolinite concentrations relative to other minerals (Fig. 2.7a-c).

The DFA_{MIN} shows that the Deep-Offshore group is distinct and dispersed from other groups, especially along the $DF2_{MIN}$ (Fig. 2.8). $DF1_{MIN}$ (52% of the separation) discriminates the Deep-Offshore, Nearshore and Sand A from Sand B and Onshore group very well (Fig. 2.8). In contrast, $DF2_{MIN}$ (39% of the separation) only separates Sand A group from Sand B samples, but that these two deposits overlap with the Nearshore and Onshore sediments (Fig. 2.8). Combined, both $DF1_{MIN}$ and $DF2_{MIN}$ show that Sand A sediments are mineralogically similar to the Nearshore sediments, and that Sand B and the Onshore sediments have a similar mineralogy (Fig. 2.8).

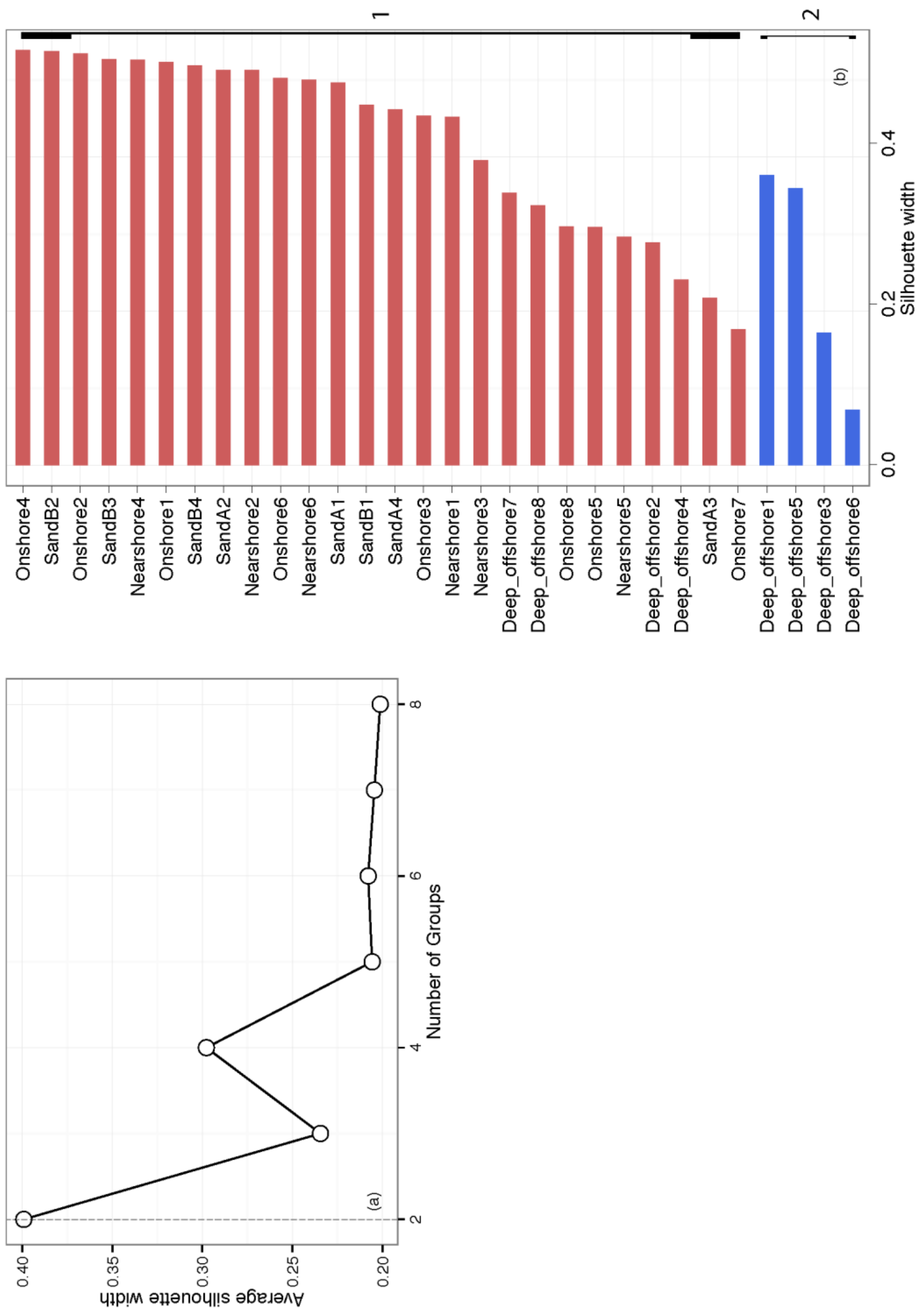

Figure 2. 6: The PAM analysis for mineral contents. (a) The number of groups and equivalent silhouette width. (b) The clustering structure of sample set, two colors differentiate clusters.

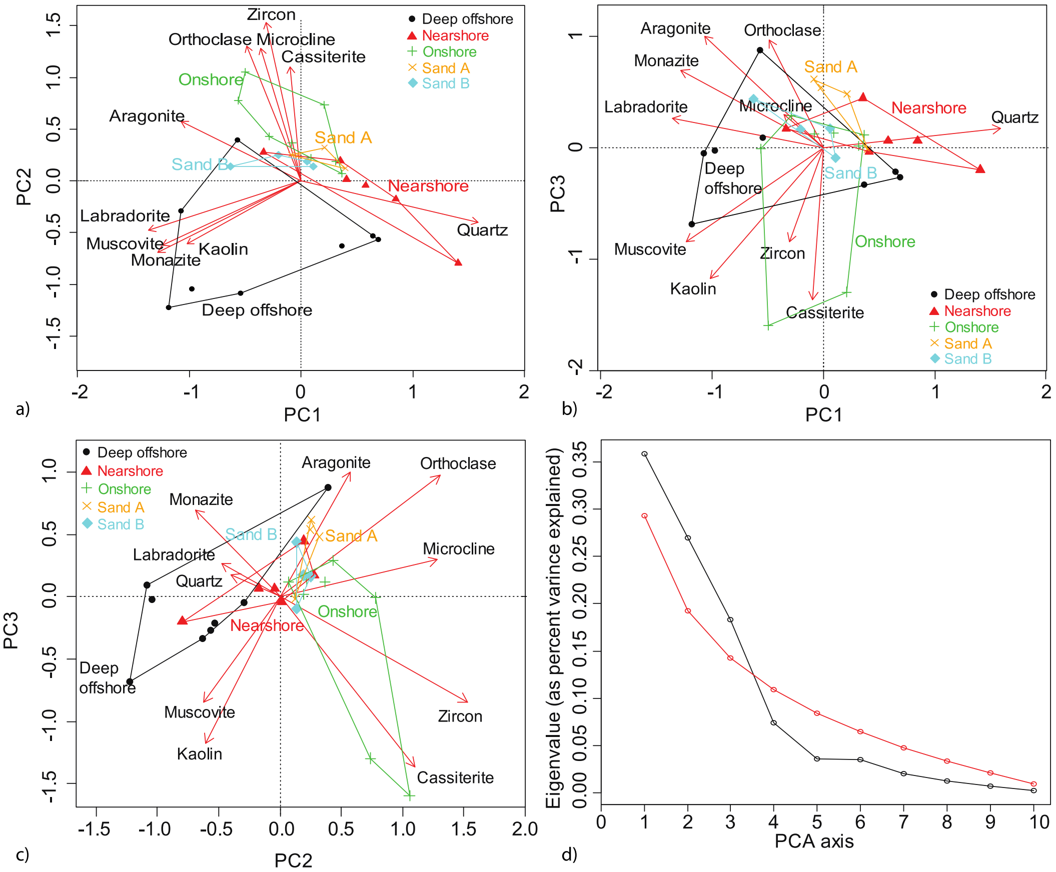

Figure 2. 7: The PCA analysis for mineral contents. (a) The first two principal components PCA1 versus PCA2; (b) PCA1 versus PCA3; (c) PCA2 versus PCA3; (d) The screeplot shows the ordination analysis (black line) versus the broken stick rule (red line).

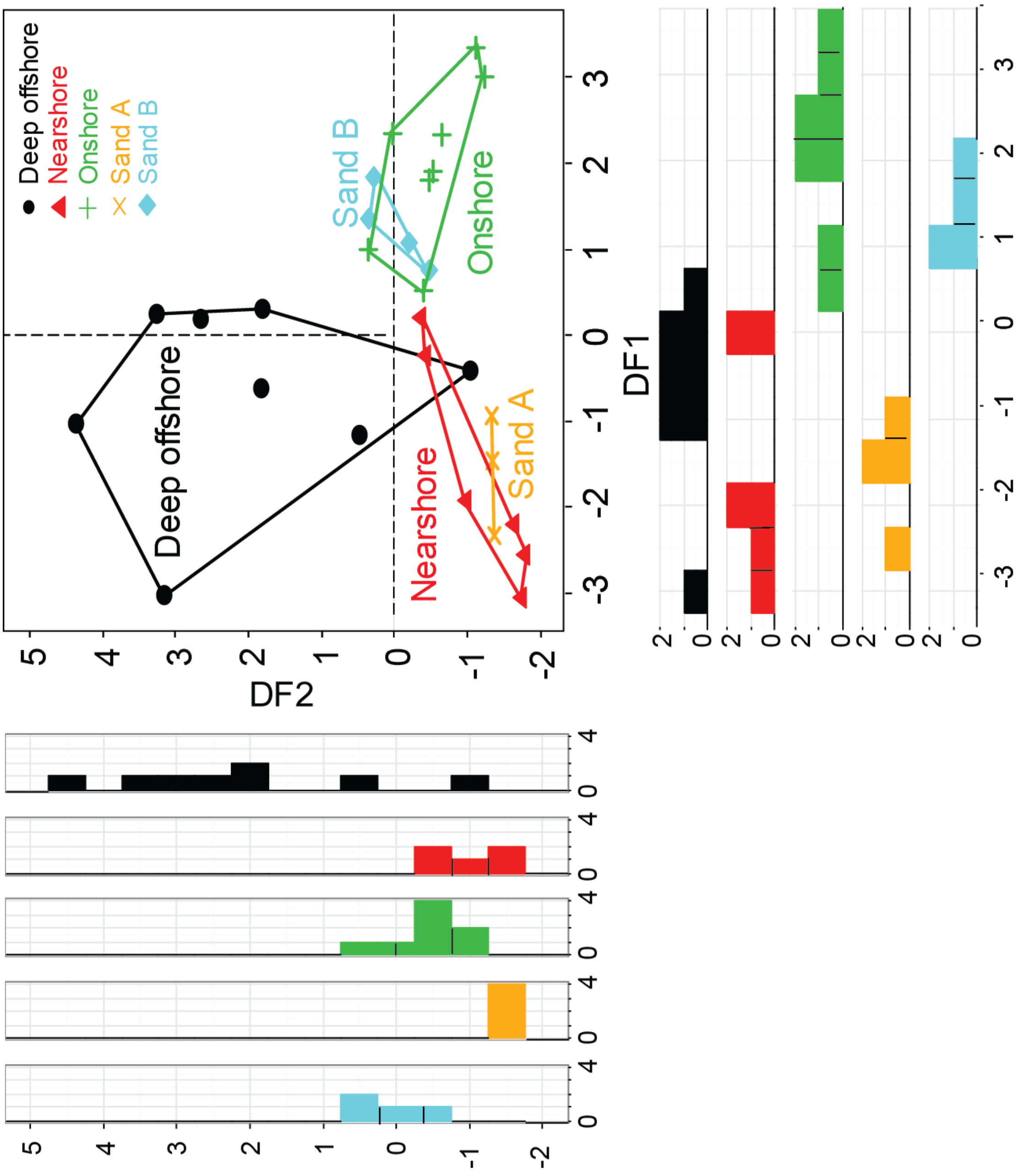

Figure 2. 8: The DFA analysis for mineral contents. The graph shows the first two discriminant function analysis (DF1 versus DF2). The stacked histograms show the scores and power of separation of each group relative to the other groups.

2.4.2.3. Trace elements

Twenty-two trace elements were used to investigate the relationship between the groups using PAM, PCA and DFA analyses. In the first iteration of PAM$_{CHEM}$ analysis, only two clusters were identified with an overall average silhouette width of 0.40 (not shown) but the first cluster includes one sample from Sand D and two Onshore samples (PT 09 and PT 11) that contains high Zr concentrations. The second iteration, which excluded those Zr-rich samples, identified two clusters (average silhouette width of 0.36). The first cluster consists of all the Sand B samples, one Nearshore sample, one Deep-Offshore and one Sand D sample (Fig. 2.9). The two latter samples, however, are misclassified suggesting that these two samples would have been assigned to the second cluster (i.e. the second best choice). In the case of two clusters, *Kaufman and Rousseeuw* [2005] suggested that misclassified samples can be shifted to the second cluster, with their silhouette width values inverted. The large second cluster comprises all of the remaining samples (Fig. 2.9) indicating a similarity of chemical composition between the Onshore, Sand A, Sand C, Sand D, Nearshore and Storm groups. The PAM$_{CHEM}$ suggests that the two Zr-rich samples should be removed from the PCA$_{CHEM}$ and the DFA$_{CHEM}$ to avoid the influence of high-Zr concentrations.

The first two principal components of the PCA$_{CHEM}$ are shown in Figure 2.10a, although the broken stick model (Fig. 2.10d) suggests that four principal components are necessary to explain the variance in the geochemistry data. The Kaiser-Guttman criteria (Supp. Info Table 2.3) suggest that the first five principal components (PC1$_{CHEM}$ = 37%, PC2$_{CHEM}$ = 27%, PC3$_{CHEM}$ = 10%, PC4$_{CHEM}$ = 9% and PC5$_{CHEM}$ = 5%) are necessary to explain the variance in the geochemistry data set (88%).

PC3$_{CHEM}$ and PC4$_{CHEM}$ are very close to the cut-off for significance and PC5$_{CHEM}$ is well below the broken stick cut-off. Thus, for the simplicity of interpretation, PC3$_{CHEM}$, PC4$_{CHEM}$ and PC5$_{CHEM}$ are not discussed further.

As with the grain size and mineralogical data, the ordinary non-parametric bootstrap analysis of $\hat{\lambda}^*$ does not differ significantly from the $\hat{\lambda}$ determined from the PCA$_{CHEM}$ for either PC1$_{CHEM}$ or PC2$_{CHEM}$ indicating the stability of each principal component using the available data. Histograms and quantile-quantile plots for PC1$_{CHEM}$ (Supp. Info Fig S2.10) and PC2$_{CHEM}$ (Supp. Info Fig S2.10) are skewed and a normal distribution cannot be assumed. However, $\hat{\lambda}$ (PC1$_{CHEM}$ =8.23 and PC2$_{CHEM}$ =5.95) resides within the bias-corrected percentile 95% confidence interval of $\hat{\lambda}^*$ (PC1$_{CHEM}$ = (7.23, 9.46) and PC2$_{CHEM}$ = (3.79, 7.62)).

The PC1$_{CHEM}$ shows positive correlations with Sand B, Sand D and most of the Nearshore samples (Fig. 2.10a), whereas most of the Deep-Offshore, Onshore and all of the Sand C and Storm sediments are negatively correlated to PC1$_{CHEM}$ (Fig. 2.10a). PC1$_{CHEM}$ is positively correlated with a cluster of variables including La, Ce, Th, Zr, Y, U and Hf. This cluster strongly drives variations along the PC1$_{CHEM}$ and thus separates Sand B from the other groups (Fig. 2.10a). The Deep offshore, Onshore, Sand C and the Storm deposits are depleted in all of the analysed elements (Fig. 2.10a). PC2$_{CHEM}$ is characterized by strong positive correlations with As, V and Sr that separate two of the Deep offshore samples from the other samples (Fig. 2.10a), and negative correlations with Nb, Sn. Nb and Sn are only found in high concentrations in Sand D (Fig. 2.10a).

It can be clearly seen that all groups cluster around the origin of this axis (i.e. from -1 to 1 standard deviation), except for Sand D (distinct negative correlation) and two samples of the Deep-Offshore (PT-OS 21 and 22, distinct positive correlation) (Fig. 2.10a). Along $PC2_{CHEM}$, V, As and Sr are the dominant contributors to this axis (Fig. 2.10a).

$PC1_{CHEM}$ and $PC2_{CHEM}$ show that most of the sediment samples cluster around the origin of the axes (i.e. within [-1,1] standard deviation), and only two Deep offshore samples, one Nearshore sample, Sand B and Sand D contribute most of the variation in the PCA_{CHEM}.

The PCA_{CHEM} shows that many of the elements are highly correlated suggesting that many elements can be excluded from the DFA, but still explain most of the variance of the data set. Here, elements that have high correlation coefficients (i.e. $r \geq 0.9$) with other elements were eliminated to avoid significant loss of information. Thus, from the cluster of highly correlated variables La, Ce, Y, Hf, Zr, U and Th (Supp. Info. Table S2.4), La, Ce and Y were excluded as they are rare earth elements and are less reliably determined when analyzed by XRF. Hf was also eliminated due to a smaller loading value (0.86) in $PCA1_{CHEM}$ compared to U (0.9) and Th (0.94). Zr was retained since this element has been attributed to high-energy environments [*Chagué-Goff et al.*, 2011] and is present in high concentrations in zircon.

Rb is also highly correlated with Ba (r = 0.94, Supp. Info. Table S2.4) but Ba was selected because it occurs in carbonate minerals. Similarly, the correlation coefficient between Sn and Nb is very high, r = 0.98, but Sn was used in DFA_{CHEM} because it is associated with cassiterite and is important to the island's historical mining activities.

The results of the DFA$_{CHEM}$ analysis show that the first two discriminant functions yield a complex arrangement of each environment and sediment group’s relationship to the other groups (Fig. 2.11). DFA1$_{CHEM}$ accounts for 32% of the separation and is a gradation between three pairs of indistinguishable and overlapping groups: Sand C-Storm, Nearshore-Sand B and Sand A-Onshore (Fig. 2.11). The DFA1$_{CHEM}$ separates the three pairs of groups and also discriminates the Deep-Offshore group. Sand D has one sample overlapping with the Nearshore-Sand B and another sample located close to the Sand C-Storm groups along DFA1$_{CHEM}$ (Fig. 2.11).

DFA2$_{CHEM}$ (24% of the separation) cannot separate the Deep-Offshore from the Nearshore group and there is a little overlap in their scores with the Sand C group’s score (Fig. 2.11). These three groups are well discriminated from the Storm, Sand A and Onshore group in which the Storm and Sand A are almost identical. The DFA2$_{CHEM}$ also discriminates Sand B and Sand D from other groups (Fig. 2.11).

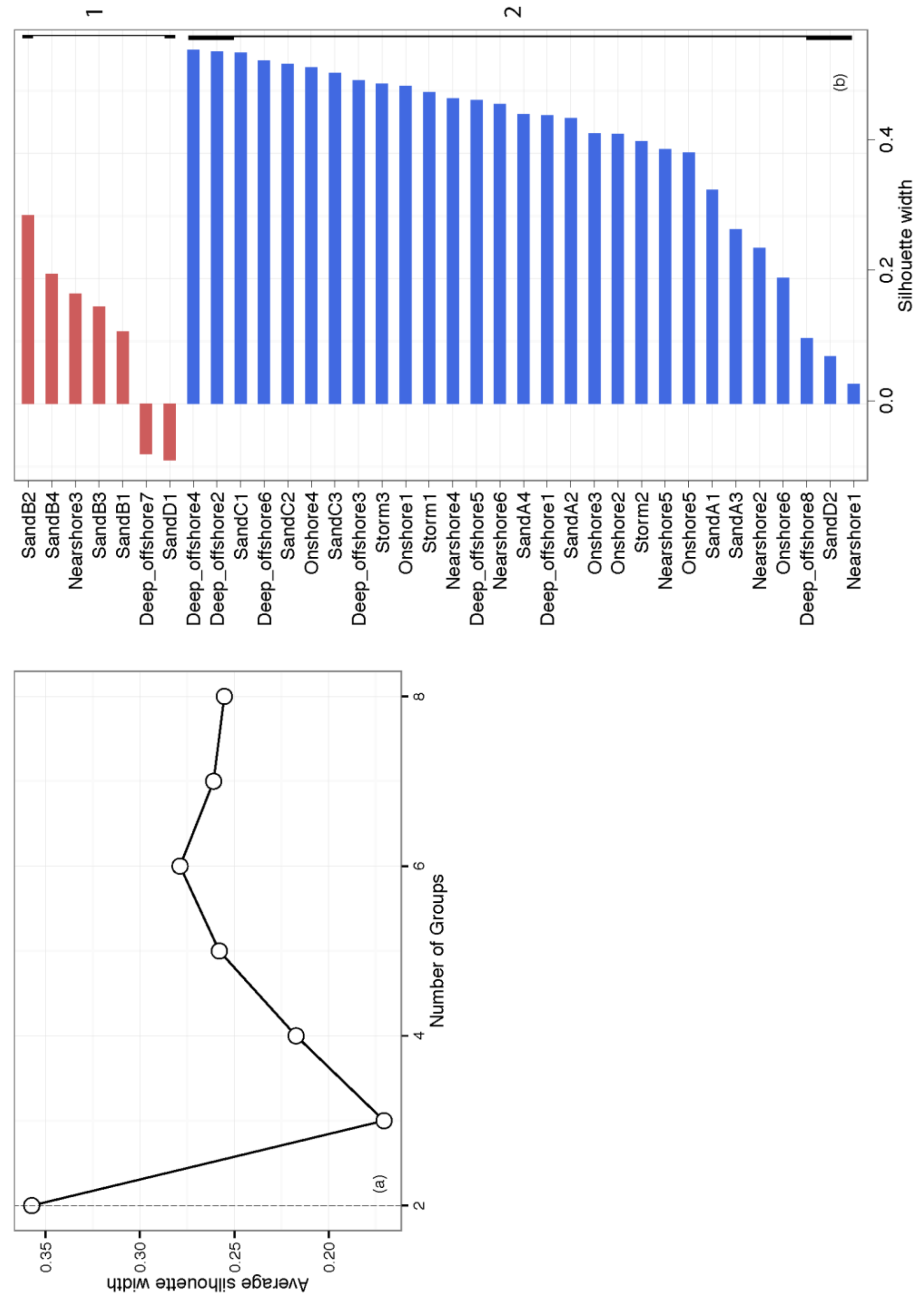

Figure 2. 9: The PAM analysis for trace elements. (a) The number of groups and equivalent silhouette width. (b) The clustering structure of sample set, two colors differentiate clusters.

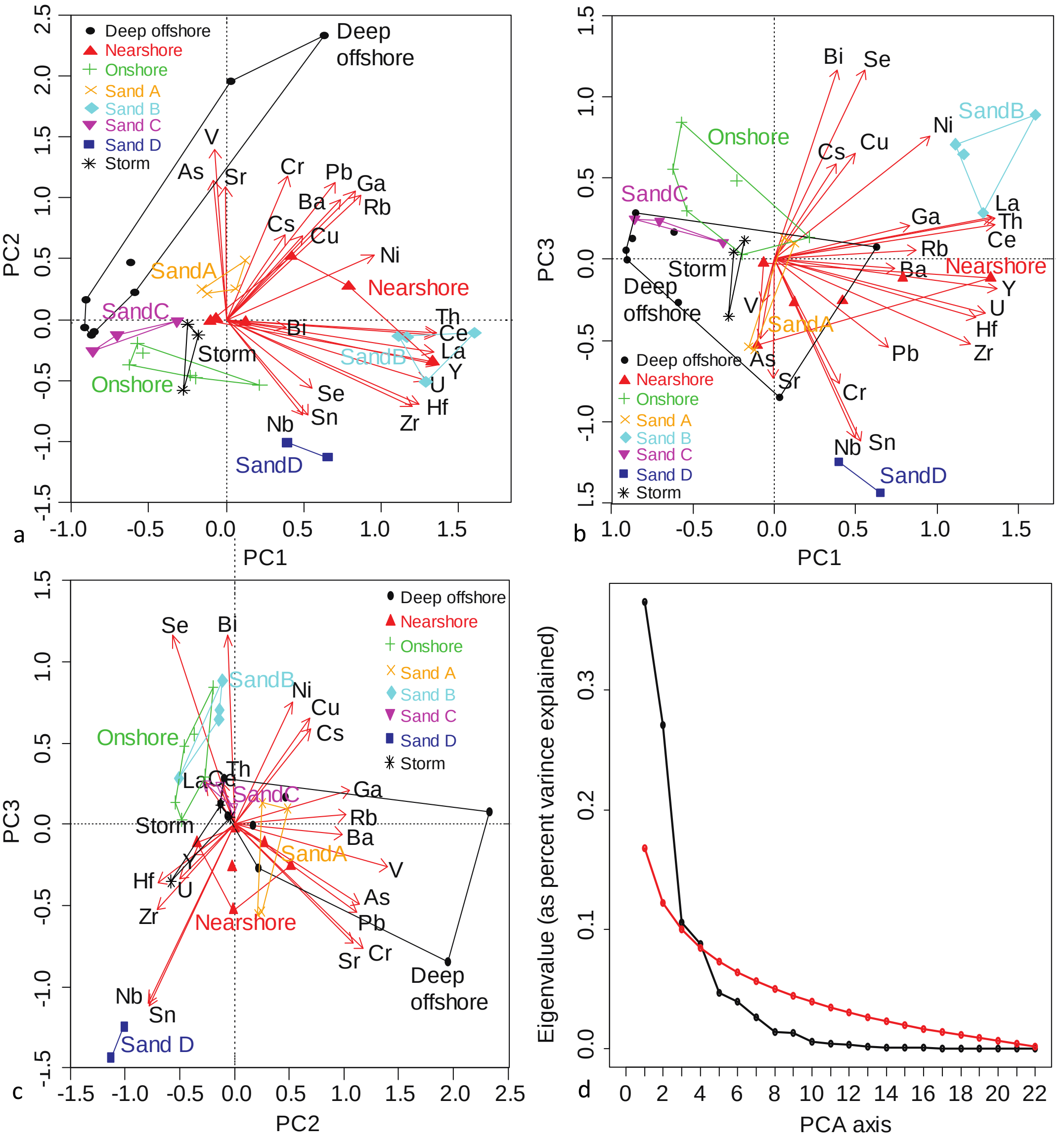

Figure 2. 10: The PCA analysis for trace elements. (a) The first two principal components PCA1 versus PCA2; (b) PCA1 versus PCA3; (c) PCA2 versus PCA3; (d) The screeplot shows the ordination analysis (black line) versus the broken stick rule (red line).

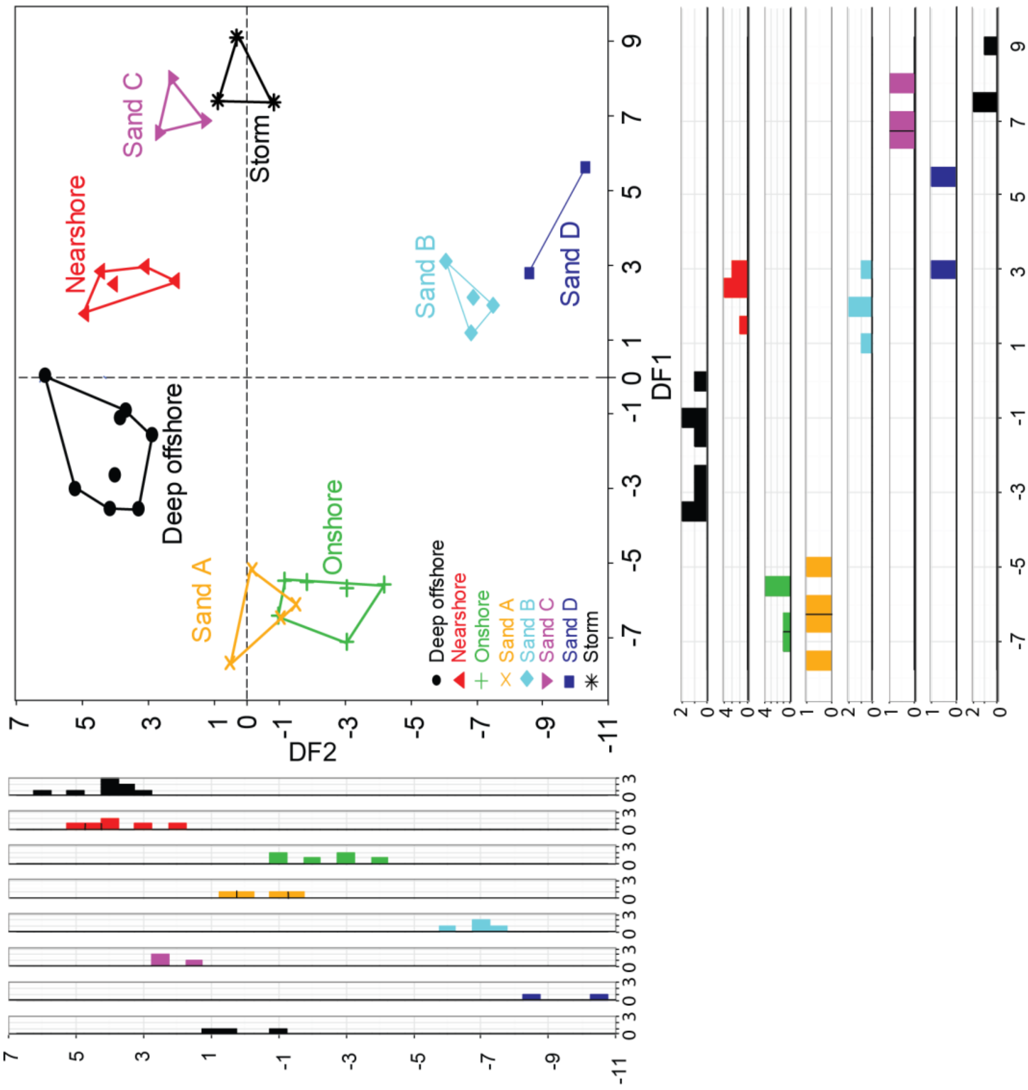

Figure 2. 11: The DFA analysis for trace elements. The graph shows the first two discriminant function analysis (DF1 versus DF2). The stacked histograms show the scores and power of separation of each group relative to the other groups.

2.5. Discussion

2.5.1. Proxies and impact factors in the study site

2.5.1.1. Geochemical signatures

The use of sediment geochemistry as a tool for studying coastal overwash deposits is still in its early stages even though an increasing number of studies have utilized geochemical signatures [see *Chagué-Goff*, 2010 for a review]. For example, *Chagué-Goff et al.* [2012a] traced the maximum inundation of the 2011 Tohoku-oki event using marine-derived salts in mud deposits (i.e. S and Cl) and suggested these as potential identifiers for paleo-tsunamis. *Font et al.* [2013] combined geochemical signatures with other proxies to identify the sediment source of the 1755 Lisbon tsunami deposits. Geochemical signatures (e.g. water-soluble salts and metalloids) also have been used for environment impact assessments in the short time after tsunami events in both tropical settings [e.g. *Szczuciński et al.*, 2005] and temperate environment [e.g.*Chagué-Goff et al.*, 2012b].

The major challenge comes from the impact of post-depositional changes (e.g. dilution or weathering processes) that may alter the concentration of elements after events occurred [*Chagué-Goff*, 2010; *Font et al.*, 2013; *Shanmugam*, 2012; *Szczuciński et al.*, 2007]. For instance, a cyclone-related event normally causes heavy rainfall that can quickly dilute concentration of marine salts in storm deposits and therefore might bias the interpretation. Similarly, *Szczuciński et al.* [2007] also reported a major decrease of water-soluble salts in the 2004 tsunami deposits due to rainy season in several locations in Thailand, south of Phra Thong Island. These studies reveal that saltwater signatures (i.e. salt) are very sensitive to environmental changes (e.g. dilution or leaching processes). And as Phra Thong Island is also affected by heavy precipitation (the rainy season is from April to November with approximately 1900 mm of rainfall, based on 1971-2000 data period, *Thai Meteorological Department* [2012]) that causes significant vertical movement of the fresh watertable resulting in remobilization of the marine-derived salts in both tsunami and storm deposits. *Szczuciński et al.* [2007] concluded that other elements, such as heavy metals and metalloids, were not affected by rainfall and therefore could be used to study the provenance of sediments deposited during tsunami inundation [e.g. Chile; *Chagué-Goff et al.*, 2015]. Thus, taking that into account, the present study focused on using a wide range of metalloid and heavy metals.

In the modern marine environment trace elements vary spatially and can provide insights into the sediment source of coastal overwash deposits. Understanding the depth at which elements and minerals are concentrated in the modern environment may shed light on the depth at which the elements and minerals were mobilized prior to deposition as overwash deposits. This is akin to the analysis of microfauna and microflora to determine depths of scour during coastal overwash [e.g. *Tanaka et al.*, 2012].

Using the spatial distributions of elements in offshore samples (Fig. 2.2 and Supp. Info. Figs. S2.4-S2.6), major differences were found in the concentration of minerals and elements between the Nearshore and Deep-Offshore environments (Fig. 2.2 and Supp. Info. Figs. S2.4-S2.6). In general, the elemental concentrations in the Nearshore are much higher than in the Deep-Offshore area (e.g. Zr and U, Fig. 2.2 and Supp. Info. Figs. S2.4) because of heavy mineral concentration in the high-energy environment. In some cases, the elemental concentrations in some of Deep-Offshore samples are also high (e.g. Sr and Sn, Fig. 2.2)

2.5.1.2. Grain size parameters

Granulometric characteristics can provide useful information about sediment origin, sedimentation and hydrodynamic processes and have been extensively used in comparing tsunami and storm deposits [e.g. *Goff et al.*, 2004; *Gouramanis et al.*, 2014b; *Kortekaas and Dawson*, 2007; *Morton et al.*, 2007; *Nanayama et al.*, 2000; *Tuttle et al.*, 2004] or in interpreting tsunami or storm events [e.g., *Switzer and Jones*, 2008].

The spatial distribution of mean grain size from offshore Phra Thong Island shows that the shallow marine samples are generally finer than those from deeper water (Fig. 2.2). In addition, the mean grain size and selected trace elements are highly positively correlated (Supp. Info Table S2.5). The correlation reflects that most trace elements are found in heavy minerals that are finer and possibly concentrated nearshore over time.

In regard to temporal variability, *Szczuciński et al.* [2007] reported the effect of rainfall on the mean grain size of the 2004 IOT deposits after one year and found a coarsening in half of the sandy tsunami samples. This change was ascribed to heavy rain that had removed the finer fraction from sandy tsunami deposits during the rainy season and, therefore, the effect of rainfall over time should be taken into account in paleo-tsunami studies in tropical climate [e.g. Thailand; *Szczuciński et al.*, 2007]. In contrast to tropical regions, fine-grained deposits are more likely to be eroded quickly by eolian forces in arid regions [e.g. Peru; *Spiske et al.*, 2013].

2.5.1.3. Mineral contents

Mineral compositions have recently been used as a useful tool (mostly with the focus on heavy mineral assemblages) in washover deposit studies [e.g. *Cuven et al.*, 2013; *Font et al.*, 2013; *Gouramanis et al.*, 2014b; *Jagodziński et al.*, 2012; *Jagodziński et al.*, 2009; *Switzer et al.*, 2005; *Switzer et al.*, 2012; *Szczuciński et al.*, 2006; *Szczuciński et al.*, 2005]. The mineral content of the bulk samples from Phra Thong Island is dominated by quartz (>80 wt%). This result is consistent with mineral compositions reported by *Jankaew et al.* [2011] who noted a very high concentration of quartz (*ca*. 85 to 90 weight%) and a very small concentration of heavy minerals (*ca*. 1.7 to 2% and mostly of small cassiterite grains) in both the 2004 deposits and paleo-tsunamis deposits on Phra Thong Island.

Our analytical analysis of the finer sand fraction (0.063 to 0.125 mm) considerably reduced the concentration of quartz and more minor minerals were detected implying that the finer sediment mineralogical fraction provides more meaningful information on the mineralogical variability of the overwash deposits. Unfortunately, due to the coarse grain size of Sand C, Sand D and the Storm samples, insufficient material prevented mineral analysis of the fine fraction. This difficulty prevented contrasting the older tsunami deposits and the storm deposit, but with the dominance of quartz across our sample set, we suggest that the use of mineral composition in this case is unlikely to be useful. Likewise, *Jagodziński et al.* [2012] could not use heavy mineral assemblages as a proxy to distinguish Tohoku-oki tsunami deposits from onshore sediments but noted that the result might differ when using a smaller size fraction (e.g. mud fraction). Similarly, *Gouramanis et al.* [2014b] also highlighted the difficulty of using heavy minerals in conjunction with key grain size parameters to discriminate tsunami and storm deposits due to the significant variations between and within pits on the southern Indian coastline.

2.5.2. Implications for studying coastal overwash deposits.

2.5.2.1. The discrimination of modern tsunami and storm deposits

Due to a lack of mineral content data for the storm deposit and oldest paleo-tsunami deposits, we only use the statistical results from the elemental concentrations and granulometric parameters to investigate whether the Storm and Sand A can be discriminated.

In the PAM_{CHEM} (Fig. 2.9), our results show that both the Sand A deposits and those of the 2007 Storm cannot be discriminated using geochemistry. This result implies that the Storm and Sand A deposits are likely composed of the same minerals, the geochemical data are inadequate for distinguishing the two deposits and that the mechanism in which the sediments were deposited cannot be defined (Fig. 2.9).

The PCA_{CHEM} shows that the Sand A deposit is similar to the Storm deposit but that these deposits cluster around the origin of the two first principal components (within 1 standard deviation; Fig. 2.10) suggesting that none of the trace metals contribute significantly to discriminating the two deposits. However, the DF_{CHEM} discriminates Sand A from the Storm deposit due to the subtle loadings of each trace element (most likely Sr, As and V) on $DF1_{CHEM}$ (Fig. 2.11). The granulometric data (PAM_{GS}, PCA_{GS}, DFA_{GS}) suggest that the 2007 Storm and Sand A deposits can be discriminated. In the PAM_{GS}, these two groups occur in different clusters (Fig. 2.3) indicating a significant difference in grain size parameters between the two recent overwash deposits. The PCA_{GS} reveals that the mean grain size is the only key feature to distinguish the 2007 Storm deposits (medium sand) from those of the Sand A (very fine sand; Fig.2. 4 and Table 2.1). This result is mirrored in the DFA$_{GS}$ analysis (Fig. 2.5). The results of other granulometric parameters (sorting, skewness and kurtosis) show very little difference between the deposits of the Storm and Sand A.

2.5.2.2. The provenance of the tsunami deposits

Sand A

The results for trace element (PCA$_{CHEM}$), mineralogy (PCA$_{MIN}$, DFA$_{MIN}$) and grain size (PAM$_{GS}$, PCA$_{GS}$ and DFA$_{GS}$) analyses suggest that most of the Sand A deposit is predominantly derived from the shallow nearshore environment, although some contribution from onshore beach sediment cannot be discounted (e.g. DFA$_{CHEM}$). This conclusion agrees with Sawai et al. (2009)'s examination of the diatoms preserved in Sand A on Phra Thong Island from the same sites examined here, and *Jagodziński et al.* [2009] who suggested that the heavy mineral suite of the seafloor sediments, beach sediment and local soils combined to form the tsunami deposits on Kho Khao Island (~20km south of Phra Thong Island).

Paleo-tsunami

While the provenance of Sand A deposits has been identified, the provenance of prehistoric tsunami deposits is less clear. Our statistical results show that all three paleo-tsunami deposits differ from each other and the Sand A deposit, and thus suggest variable sources of the paleo-tsunami sediments or potential diagenetic alteration.

The grain size, mineralogical and trace element analysis of Sand B presents a complex interpretation. The grain size analysis (PAM$_{GS}$, PCA$_{GS}$, and DFA$_{GS}$)

indicates a strong similarity to Sand A and are closely related to the Nearshore sediments. Mineralogically, Sand B and Sand A are very similar in (PAM_{MIN} and PCA_{MIN}) with overlap with the Nearshore sediment mineralogy. However, DFA_{MIN} suggests that Sand B is closely related to the Onshore sediments. Geochemically, Sand B contains high concentrations of Th, Ce, La, Y and U similar to the Nearshore (PCA_{CHEM}) and these elements define $DF1_{\mathrm{CHEM}}$. Thus Sand B is very likely a mixture of Onshore and Nearshore sediments.

Prendergast et al. [2012]'s beach ridge plain evolution model suggested that the formation of a new beach ridge complex occurs 500 years on average, so Sand B, which was deposited between *ca*. 350 to 430 years ago [from optically stimulated luminescence (OSL), *Prendergast et al.*, 2012] and *ca.* 550-700 years ago [from 14C Accelerator Mass Spectrometry, *Jankaew et al.*, 2008] may have been affected by the presence of a new beach ridge. However, the significant difference in the trace metal composition between Sand B and Sand A deposits may indicate that either post-depositional processes could have modified the deposit and/or the offshore sediment geochemistry has been strongly modified since Sand B was deposited.

The interpretations of the provenance of the Sand C and Sand D deposits are also complex. The grain size (PAM_{GS}, PCA_{GS} and DFA_{GS}) and geochemical (PAM_{CHEM}, PCA_{CHEM} and DFA_{CHEM}) analyses demonstrate that these two tsunami deposits differ substantially from each other and Sands A and B. PCA_{GS} and DFA_{GS} analyses show Sand D is similar to the Deep-Offshore sediments, while Sand C differs significantly from all of the other groups (Figs 2.4 and 2.5). The PCA_{CHEM} shows that Sand D is geochemically dissimilar to the other tsunami and storm deposits (Fig. 2.10), but Sand D shares similarities with Sand B in the DFA_{CHEM} (Fig. 2.11). For Sand C, multivariate techniques reveal that both Sand C and the Storm group appear to be similar in their geochemical composition (Figs 2.10 and 2.11).

This suggests that Sand C and Sand D were possibly derived from sediment sources different from Sand A and Sand B. Nevertheless, the complexity of results and the lack of historical and geological evidence prevent us from determining exactly where the deposits originated. For example, the similarity of Sand C and the Storm deposits in their geochemistry might lead to a suggestion that Sand C was deposited by a paleo-storm and not by a paleo-tsunami [c.f. *Jankaew et al.*, 2008]. However, Sand C is the thickest and most far-ranging paleo-overwash deposit preserved on Phra Thong Island, and Phra Thong Island is not impacted by storms capable of distributing sediments on this scale due to its geographical setting [*Jankaew et al.*, 2008]. Thus, the use of geochemical information in deriving a cause for such deposits is difficult to reconcile. In such cases, the term “large marine overwash event” proposed by *Switzer et al.* [2014] should be used when the causes and provenance remain unknown.

2.5.2.3. The provenance of the storm deposit

The provenance of the Storm deposits is most likely from the onshore sediments preserved on the modern beach and beach berm based on the grain size (PAM_{GS}, PCA_{GS}, and DFA_{GS}) and trace element (PCA_{CHEM}) analysis. The DFA_{CHEM} analysis indicates separation of the Storm and Onshore deposits, but that the Storm deposits are very similar to those deposited by Sand C.

2.5.2.4. Temporal geochemical variations – Insights into post-depositional changes

It is important to study the temporal variations of elemental concentrations in order to understand the impacts of post-depositional changes and to validate the usefulness of sediment chemistry in paleo-tsunami deposits. However, only a few publications have investigated how tsunami deposits have become geochemically altered across different time scales and climate regions [e.g. *Chagué-Goff et al.*, 2012a; *Chagué-Goff et al.*, 2012b; *Szczuciński et al.*, 2006; *Szczuciński et al.*, 2007]. Geological evidence on Phra Thong Island offers a unique opportunity to compare the modern tsunami deposits with three other paleo-tsunamis that, in turn, could provide more detail on geochemical signatures with more elements compared to previous works.

The concentration of 22 trace elements that have significant variations were plotted to compare between all of the tsunami deposits (Fig. 2.12). The results show that there is no consistent variability in the different tsunami deposits. In general, the trace elements can be divided into three sub-groups that have the same trend based on the elements relative concentration in each tsunami deposit. The first sub-group includes Sr, V and Cu that have high or very high concentrations in Sand A but low or very low in the older tsunamis (Fig. 2.12); the second sub-group consists of elements that have the highest concentration in Sand B (Ni, La, Ce, Pb, Th, U, Y, Ba and Rb; Fig. 12); and, the third sub-group consist of elements that have the highest value in Sand D (Zr, Nb, Sn and Hf; Fig. 2.12). In two-thirds of cases, Sand C deposits contain the lowest concentrations compared to the other three tsunami deposits (Fig. 2.12).

All observations in Sand A and paleo-tsunami deposits reveal that there is no simple trend in the temporal variation of the trace element chemistry on Phra Thong Island. This complexity might not be fully explained due to the lack of knowledge about how heavy-metal elements spatially vary in the marine system over time. In addition, local settings and depositional environment also play an important role in chemical alterations [*Chagué-Goff et al.*, 2011]. For example, based on the variations of Sr in our data set, we observe that Sr concentration is much higher in the modern deposits and very low in the three other prehistoric tsunami deposits (Fig. 2.12). The low Sr concentration in deeper and older sand layers possibly corresponds to the lack of inorganic and biogenic carbonate microfossils in the deposits, which are rapidly dissolved due to elevated ambient temperatures and high volumes of precipitation causing significant groundwater fluctuation through acidic peat-rich environments [*Jankaew et al.*, 2008; *Sawai et al.*, 2009]. In contrast to our results, *Chagué-Goff et al.* [2012a] reported a very little difference of Sr concentration between the 2011 Tohoku-oki tsunami deposits and the 869 A.D. Jogan tsunami deposits in Japan highlighting the site-specific feature of geochemical signatures.

The evidence presented here from Phra Thong Island raises questions about the reliability of using geochemical signatures for studying paleo-tsunami deposits (e.g. sediment provenance). Therefore, there is a concern with the recent study of *Kuwatani et al.* [2014] in which a set of chemical elements was proposed that could be used to identify tsunami deposits from surrounding sediments. The method used in this study suggested that elements such as Na, Ca and Mg could be useful in discriminating tsunami deposits from other sediments, but this study lacks validation using paleo-tsunami deposits. Ca and Sr have very similar chemical behaviour and our data show that Sr is strongly depleted in prehistoric deposits in Thailand (Fig. 2.12). Similarly, other metals that are easily transported as salts and carbonates (i.e. Na and Mg) also can be very quickly remobilized in short time periods. *Kuwatani et* *al.* [2014] also proposed other heavy metal elements (e.g. Cr, Cu, Pb) are useful to identify tsunami deposits, but our data show that these elements vary considerably between overwash deposits recorded at the same site. Hence, there is no guarantee for this set of elements can be widely applied.

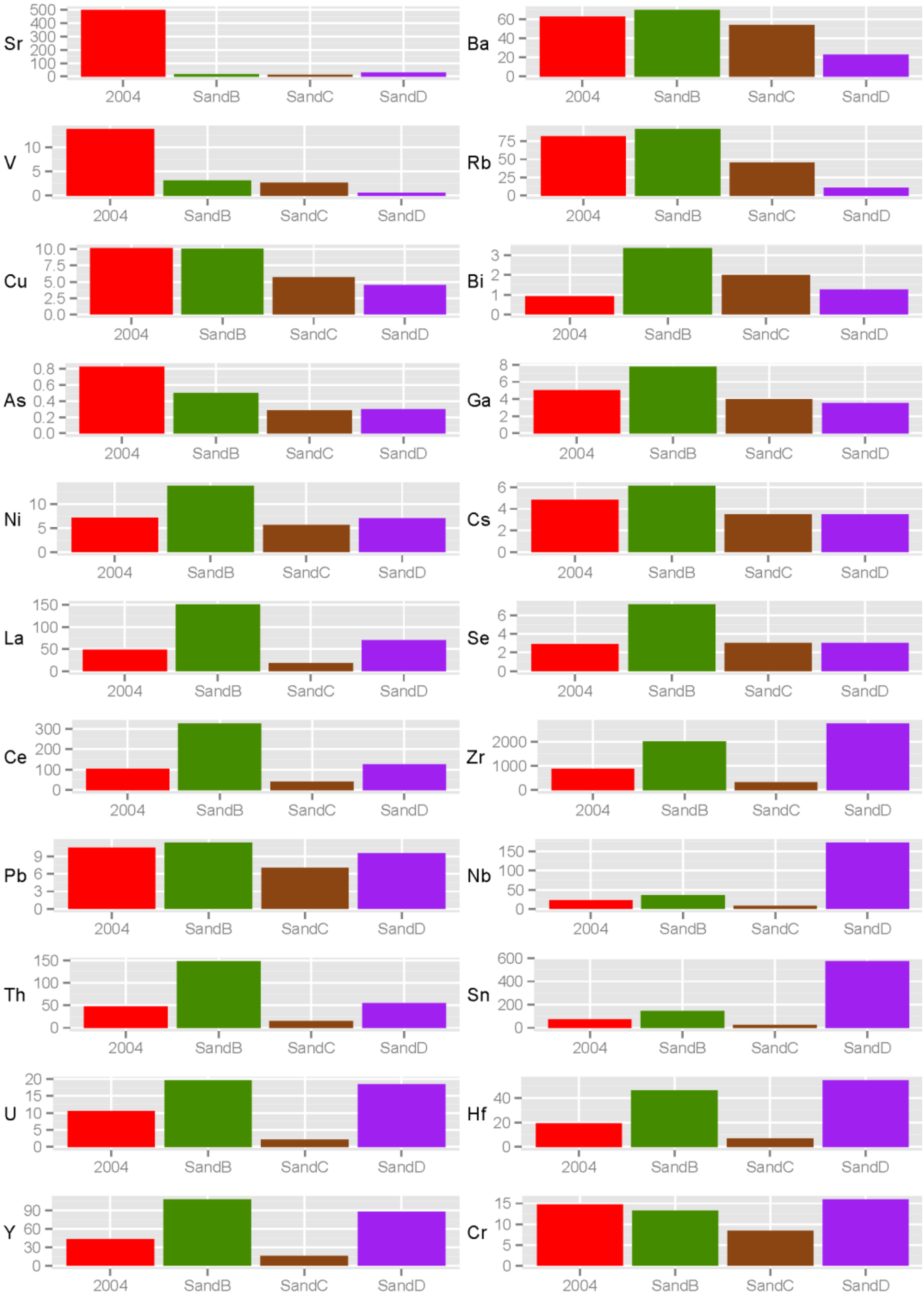

Figure 2. 12: The temporal variations of 22 trace elements between the 2004 IOT and three infered paleo-tsunami deposits.

2.5.2.4. Comparison of the statistical analyses

The use of three different statistical techniques allows us to compare between the techniques.

PAM analysis is based on simple Euclidean distance into assign samples, but both PCA and DFA have to solve more complicated matrices within and between groups. Our PAM results showed significant differences in the environments and overwash deposits with eight groups identified when the grain size parameters were examined. However, for the mineralogy and geochemistry, there was insufficient separation between the deposits and environments and in each case only two groups with samples from multiple environments and deposits recognized. The mineralogical and geochemical analyses using PAM therefore were of little use in discriminating the deposits and identifying the provenance of the sediments in each deposit.

The PCA analysis proved to be a significant improvement on gaining insight into the complexity and inter-relationship between each of the grain size, mineralogical and geochemical parameters investigated. Applying bootstrap analysis to the eigenvalues to test for stability in the derivation of principal components has not been previously applied in coastal hazard studies and is a necessary step in evaluating the significance of each principal component. Achieving stability in the principal components indicates that the principal components derived from the data are not significantly different from random resampling of the data. This validation of the principal components demonstrates that the sample size used in each PCA is sufficient to provide meaningful and accurate results on the relationship between parameters and sampling sites.

The results of the DFA analysis differed from the PCA analysis and were expected to do so. The PCA analysis seeks to define axes which maximizes the variance of each variable to compare variables and individual samples in multivariate space, whereas the DFA seeks to identify a model of all of the variables to extract the maximum separation in multidimensional space. Thus the two methods can be used simultaneously and different information gleaned. Where the two methods agree further credence is added to identifying the provenance of overwash deposits or comparing between deposits. Where the two methods disagree, both methods can provide valuable insight into the nature of the sedimentary deposits.

2.6. Conclusions

In this study, we examined the use of grain size parameters, mineral composition and trace element geochemistry in determining the provenance of tsunami (the 2004 IOT and three paleo-tsunami) deposits and the 2007 storm surge deposit on Phra Thong Island, Thailand. We also evaluated whether 2004 tsunami and 2007 storm deposits could be discriminated using grain size and geochemistry. Our statistical analyses, including cluster analysis, PCA and DFA, suggest that the two modern washover deposits are geochemically indistinguishable whereas the mean grain size of the sediment appears to be the only good discriminator of the storm and the 2004 tsunami deposits. Therefore, the trace element composition cannot be used as diagnostic criteria to distinguish known tsunami and storm deposits from Phra Thong Island. If known storm and tsunami deposits cannot be distinguished using these criteria, can these criteria be used to distinguish unknown or hypothesised overwash processes?

Regarding the provenance of coastal overwash deposits, our statistical results reaffirm that the 2004 IOT deposits were mainly generated from the shallow nearshore environment, which is consistent with previous studies. Meanwhile, the provenance of palaeotsunami tsunami deposits are rather complicated and might not be fully explained by the data sets used in this study. Sand B is very likely a mixture of onshore and nearshore sediments but the sources of Sand C and Sand D are unclear. The difficulty in accurately identifying the provenance of the palaeotsunami deposits is probably compounded by past long-term offshore mining activities (for Sand B) and/or diagenetic alteration (for Sand C and Sand D). Thus, our findings cast doubt on the utility of performing sediment chemistry to discriminate overwash deposits, and to characterize the sediment source and source environment of overwash sediments. However, the statistics-based approach in this study is capable of providing meaningful insights into studies of coastal overwash deposits and shows promise for other locations where overwash deposits are preserved.

Acknowledgements

This research is supported by National Research Foundation Singapore (National Research Fellow Award No. NRF-RF2010-04) and the Singapore Ministry of Education under the Research Centres of Excellence initiative. KJ thanks the part of A1B1-2 grant (RES-A1B1-34) from the Faculty of Science, Chulalongkorn University for financial support to collect storm deposit samples. We thank Joshua Katik for the finer fraction assistance, Ronnakrit Rattanasriampaipong for fieldwork assistance and Chuoi Tongjin for his hospitality. This work comprises Earth Observatory of Singapore contribution no. 88.

Supporting Information

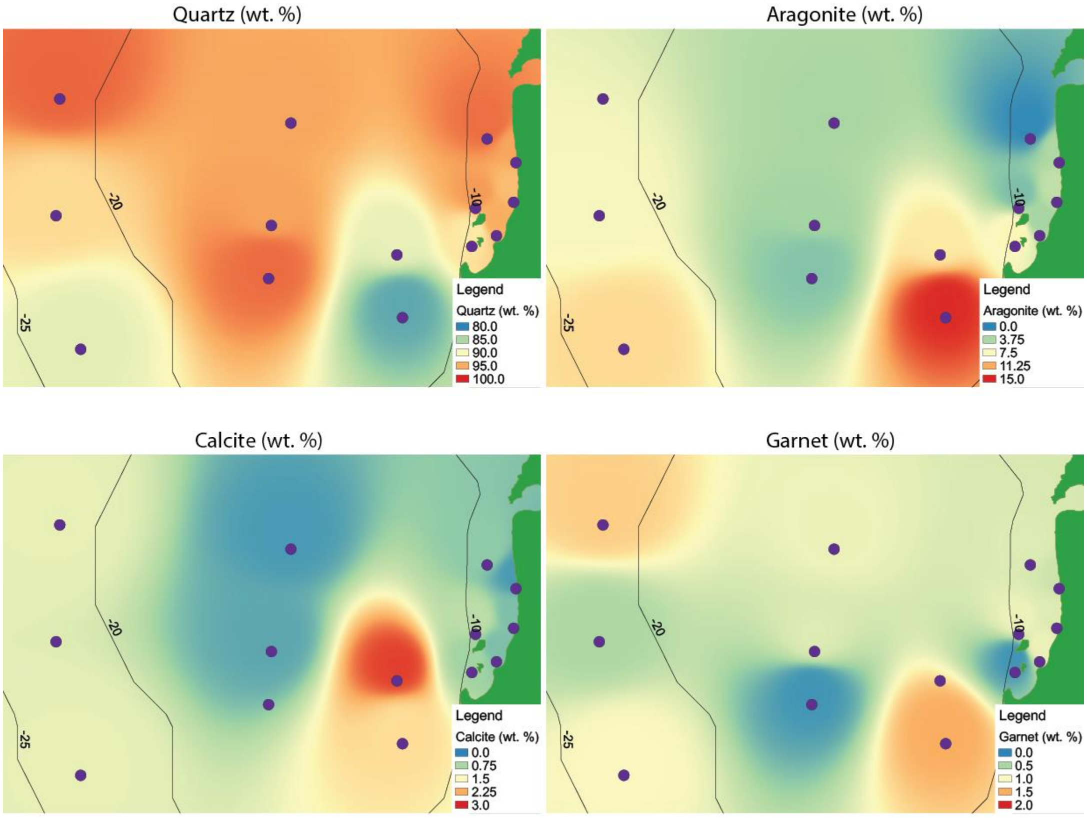

Figure S2. 1: Surface interpolation maps of the mineralogy of the offshore sediment samples using the full grain size suite: Quartz, Aragonite, Calcite and Garnet. Refer to Figure 2.1 for sample's name code. The black lines indicate the depth contours.

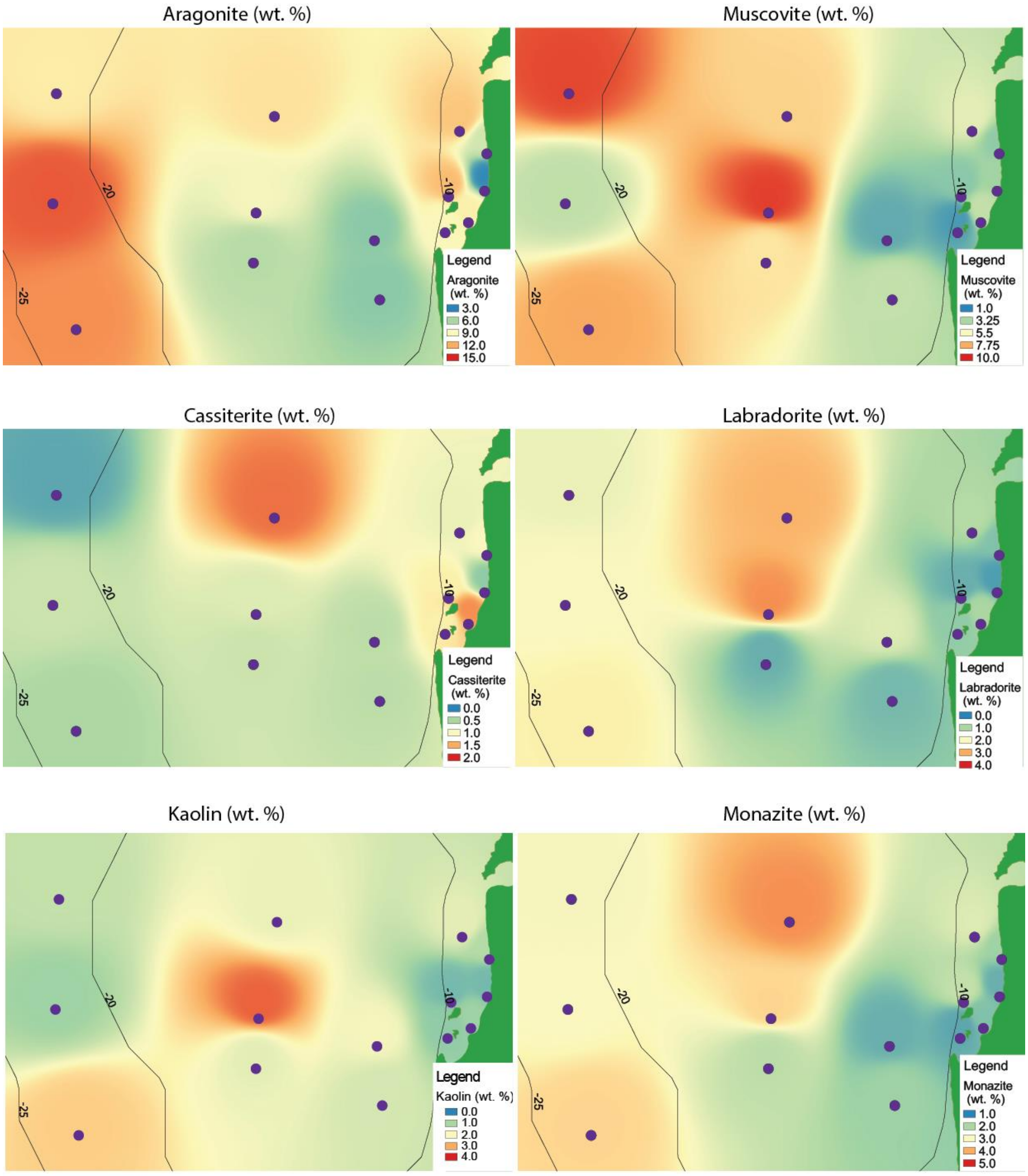

Figure S2. 2: Surface interpolation maps of the < 0.125mm mineralogy of the offshore sediment samples: Aragonite, Muscovite, Cassiterite, Labradorite, Kaolin and Monazite. Refer to Figure 2.1 for sample's name code. The black lines indicate the depth contours.

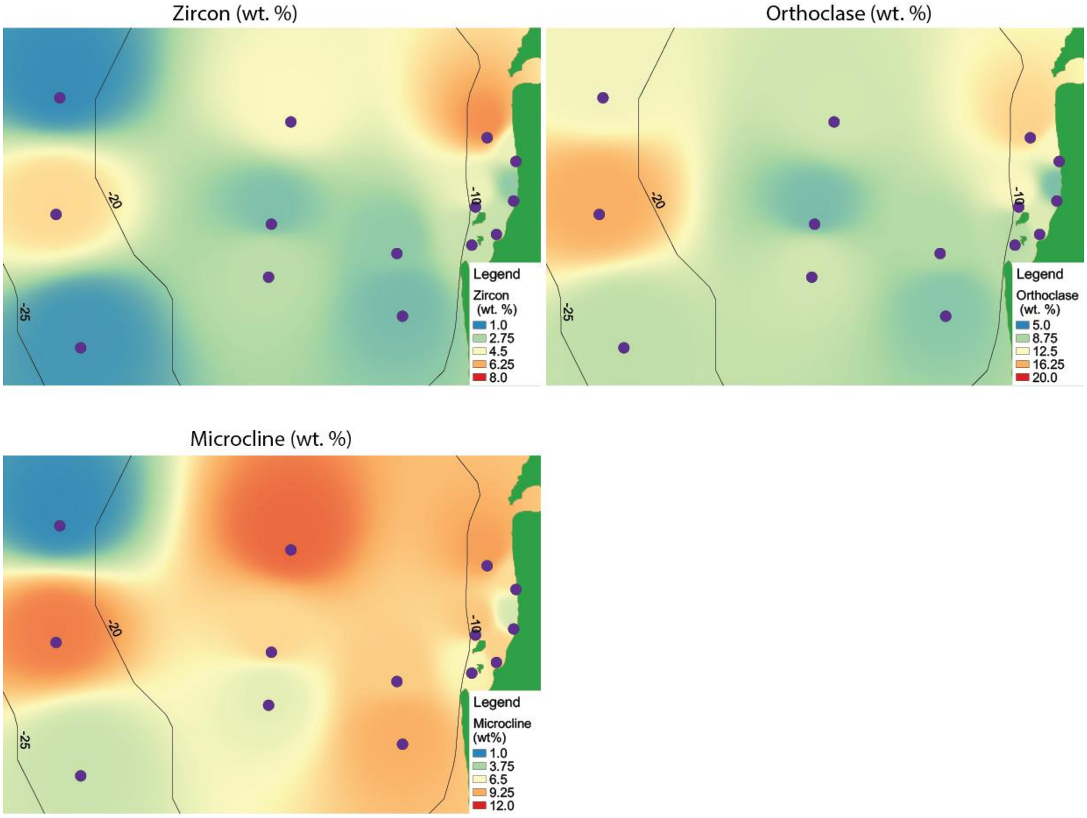

Figure S2. 3: Surface interpolation maps of the < 0.125 mm mineralogy of the offshore sediment samples: Zircon, Orthoclase and Microcline. Refer to Figure 2.1 for sample's name code. The black lines indicate the depth contours.

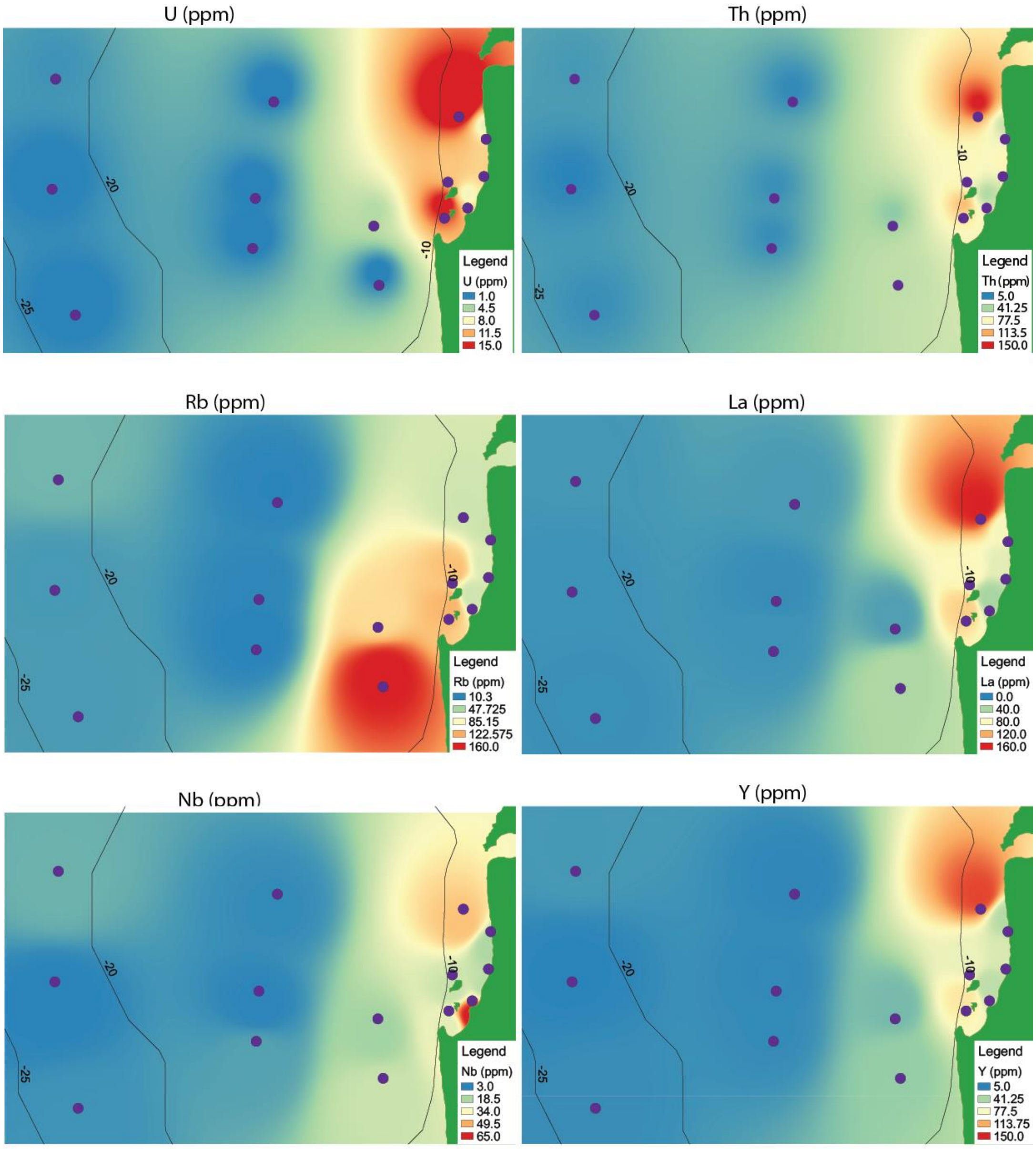

Figure S2. 4: Surface interpolation maps of the trace element geochemistry of the offshore sediment samples: U, Th, Rb, La, Nb, Y. Refer to Figure 2.1 for sample's name code. The black lines indicate the depth contours.

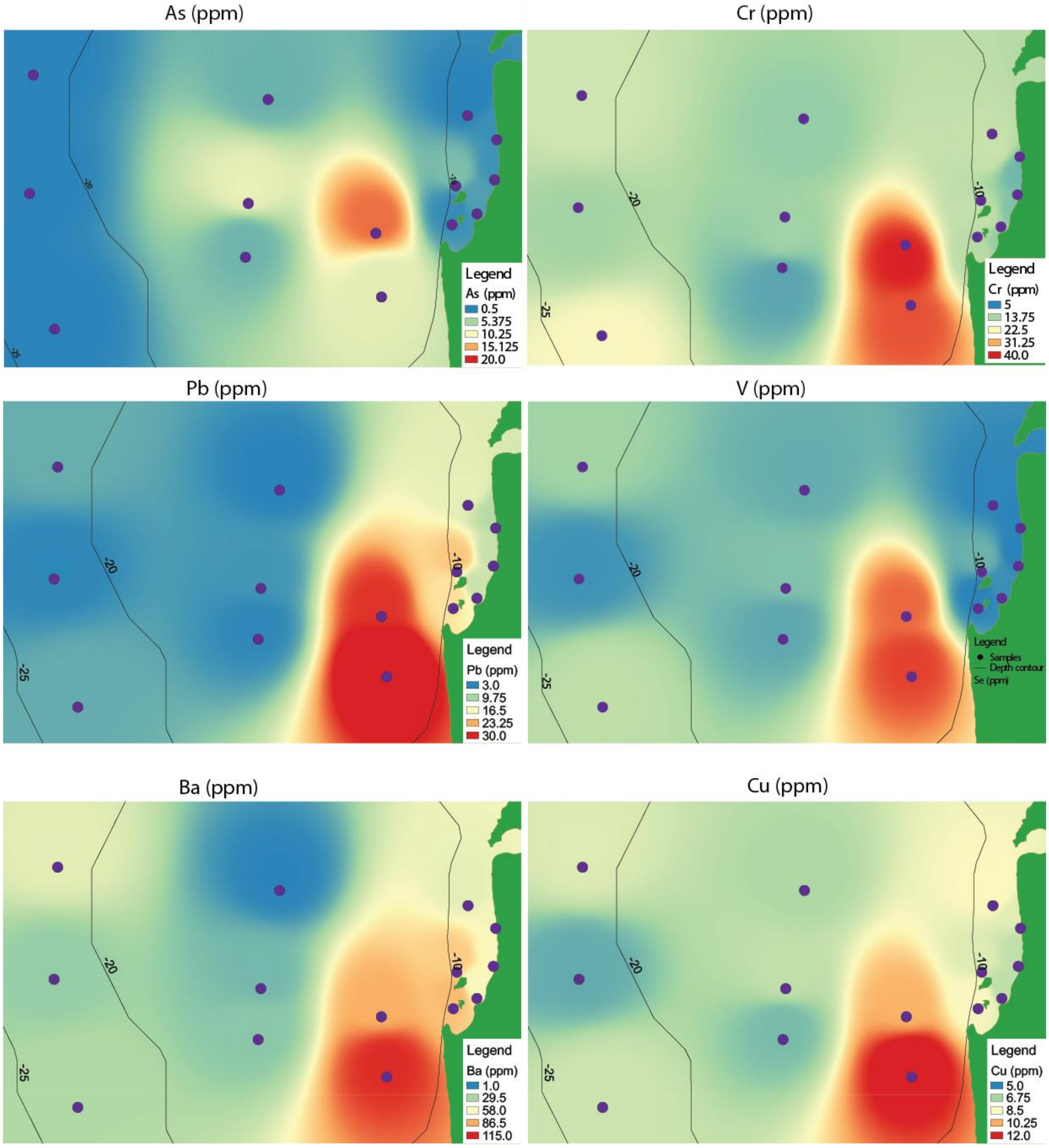

Figure S2. 5: Surface interpolation maps of the trace element geochemistry of the offshore sediment samples: As, Cr, Pb, V, Ba and Cu. Refer to Figure 2.1 for sample's name code. The black lines indicate the depth contours.

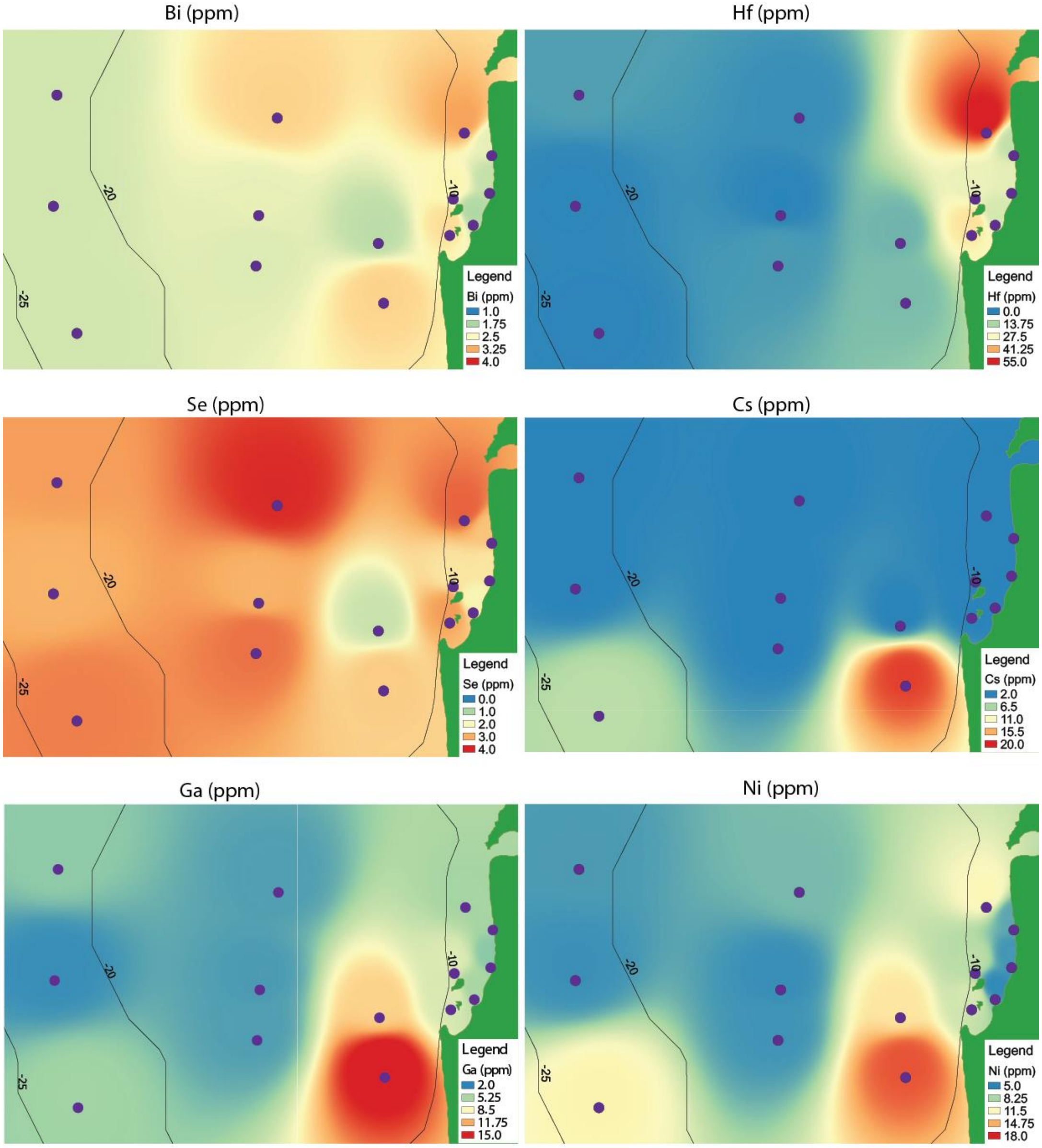

Figure S2. 6: Surface interpolation maps of the trace element geochemistry of the offshore sediment samples: Bi, Hf, Se, Cs, Ga and Ni. Refer to Figure 2.1 for sample's name code. The black lines indicate the depth contours.

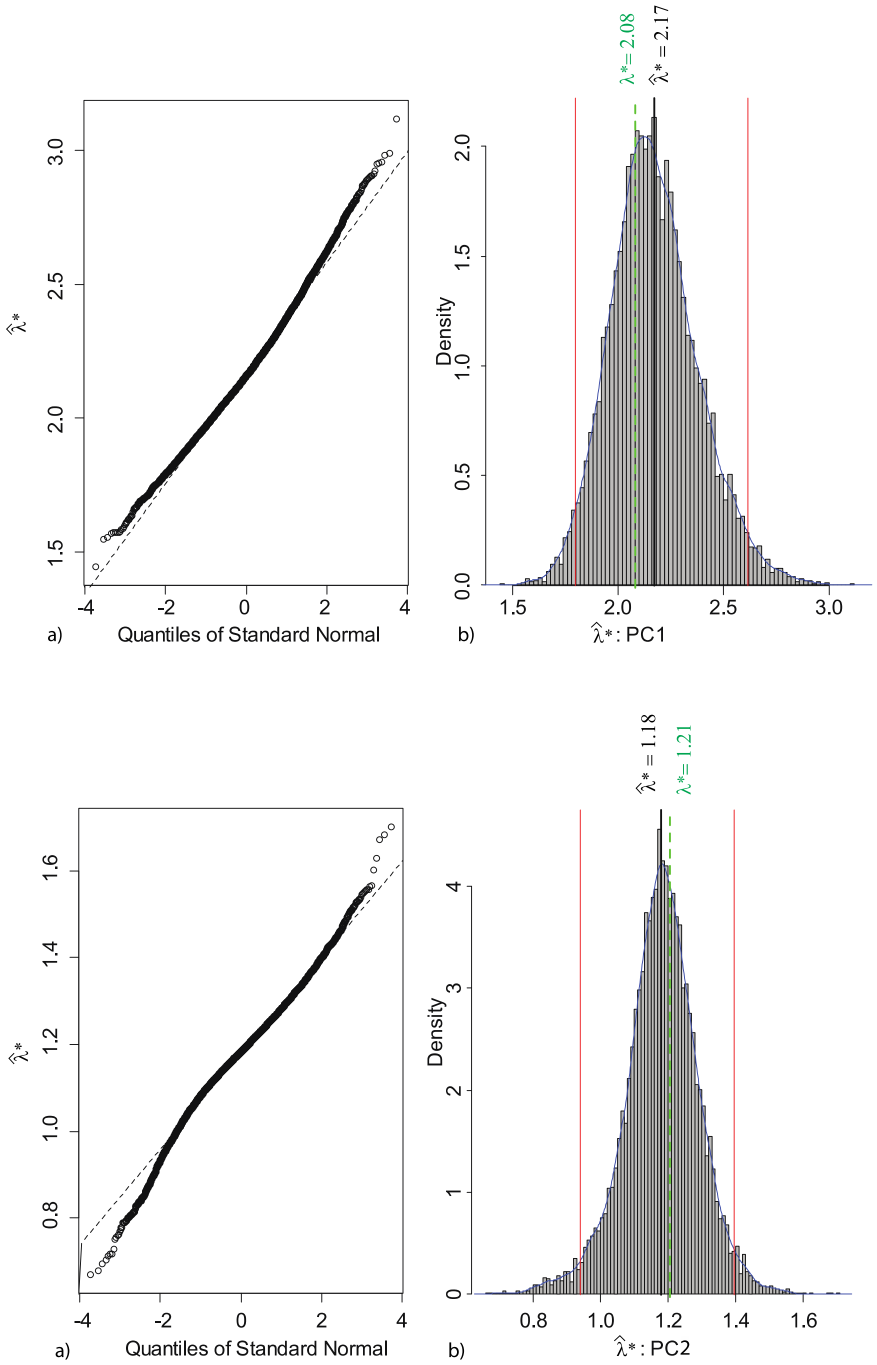

Figure S2. 7: Bootstrap analysis of PC1 (two top panels) and PC2 (two bottom panels) of the grain size data showing a) a quantile plot and b) a histogram of the bootstrapped eigenvalues ($\hat{\lambda}^*$) and showing the bootstrapped confidence interval (red lines), mean of the bootstrapped eigenvalue ($\hat{\lambda}^*$ black solid line) and determined eigenvalue (λ^*green dashed line).

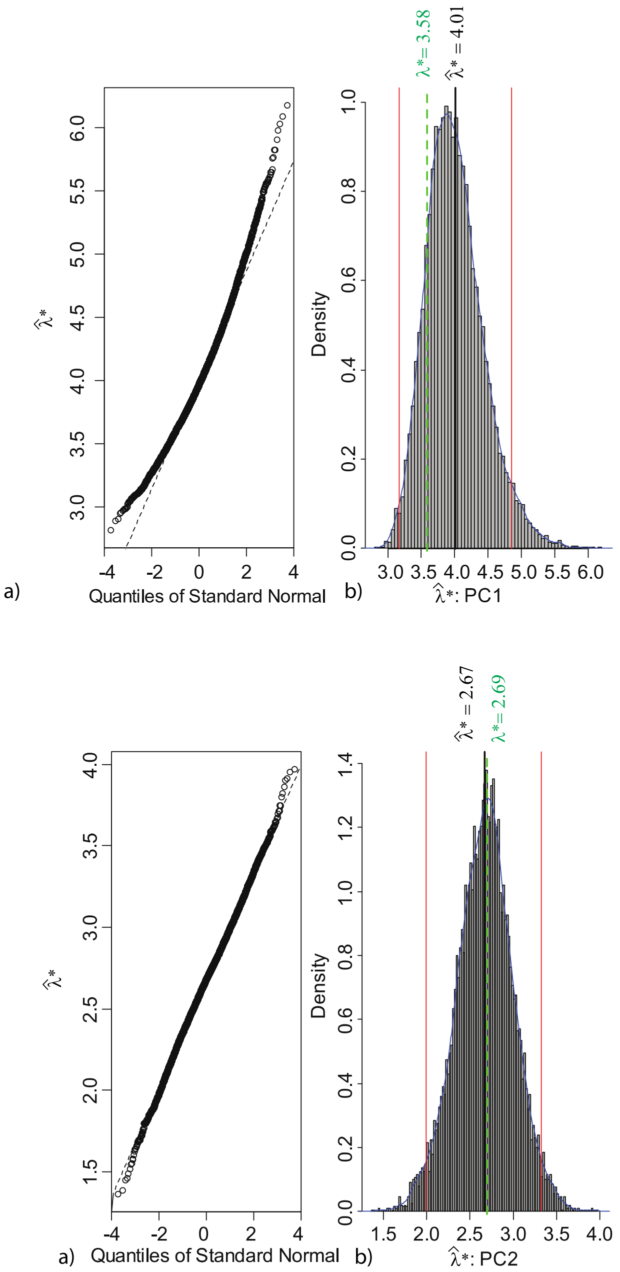

Figure S2. 8: Bootstrap analysis of PC1 (two top panels) and PC2 (two bottom panels) of the mineralogy data showing a) a quantile plot and b) a histogram of the bootstrapped eigenvalues ($\hat{\lambda}^*$) and showing the bootstrapped confidence interval (red lines), mean of the bootstrapped eigenvalue ($\hat{\lambda}^*$black solid line) and determined eigenvalue (λ^*green dashed line).

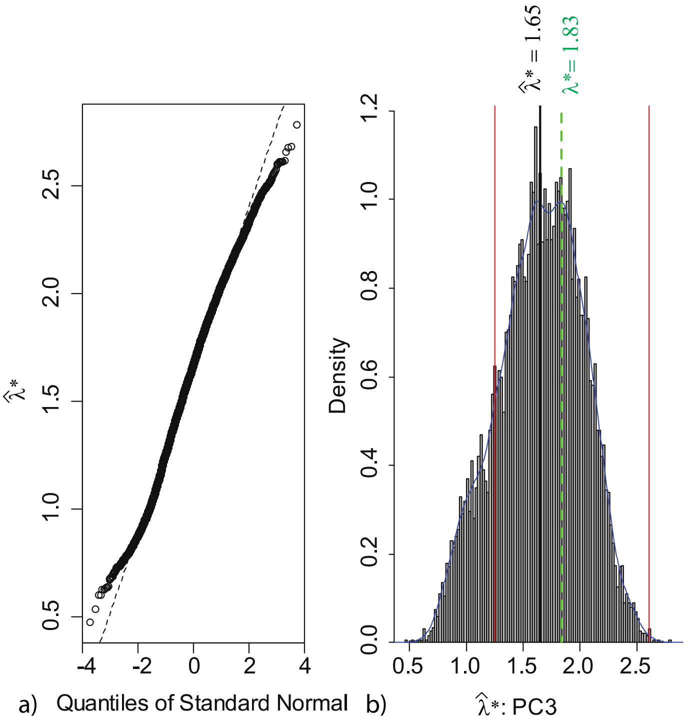

Figure S2. 9: Bootstrap analysis of PC3 of the mineralogy data showing a) a quantile plot and b) a histogram of the bootstrapped eigenvalues ($\hat{\lambda}^*$) and showing the bootstrapped confidence interval (red lines), mean of the bootstrapped eigenvalue ($\hat{\lambda}^*$black solid line) and determined eigenvalue (λ^*green dashed line).

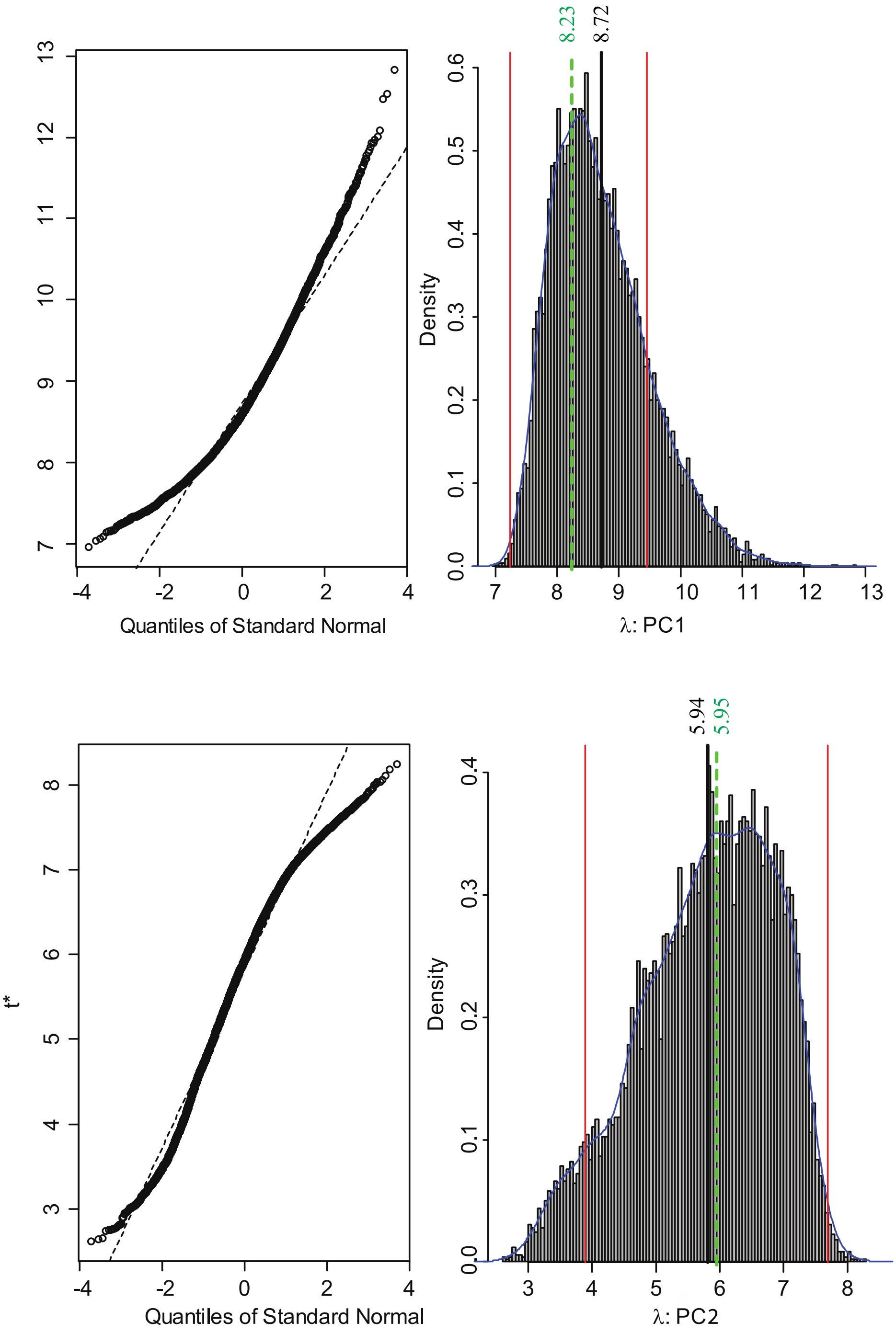

Figure S2. 10: Bootstrap analysis of PC1 (two top panels) and PC2 (two bottom panels) of the geochemistry data showing a) a quantile plot and b) a histogram of the bootstrapped eigenvalues ($\hat{\lambda}^*$) and showing the bootstrapped confidence interval (red lines), mean of the bootstrapped eigenvalue ($\hat{\lambda}^*$black solid line) and determined eigenvalue (λ^*green dashed line).

Table S2. 1: Table showing for each principal component of the grain size data the eigenvalues (λ), the percent variance explained by each eigenvalue and whether the Kaiser-Guttman criteria defines the principal component as significant or not [*Legendre and Legendre*, 2012]

PC	**Eigenvalue (λ)**	**% explained**	**Kaiser-Guttman criteria**
1	2.08	52	Significant
2	1.21	30	Significant
3	0.47	12	Not significant
4	0.25	6	Not significant

Table S2. 2: Table showing for each principal component of the mineralogy data the eigenvalues (λ), the percent variance explained by each eigenvalue and whether the Kaiser-Guttman criteria defines the principal component as significant or not [Legendre and Legendre, 2012]

PC	**Eigenvalue (λ)**	**% explained**	**Kaiser-Guttman criteria**
1	3.59	36	Significant
2	2.69	27	Significant
3	1.83	18	Significant
4	0.74	7	Not significant
5	0.36	4	Not significant
6	0.35	4	Not significant
7	0.2	2	Not significant
8	0.13	1	Not significant
9	0.08	0.8	Not significant
10	0.02	0.2	Not significant

Table S2. 3: Table showing for each principal component of the geochemistry data the eigenvalues (λ), the percent variance explained by each eigenvalue and whether the Kaiser-Guttman criteria defines the principal component as significant or not [*Legendre and Legendre*, 2012]

PC	**Eigenvalue (λ)**	**% explained**	**Kaiser-Guttman criteria**
1	8.23	37	Significant
2	5.95	27	Significant
3	2.32	10.5	Significant
4	1.94	8.8	Significant
5	1.03	4.7	Significant
6	0.88	4	Not significant
7	0.59	2.7	Not significant
8	0.32	1.5	Not significant
9	0.3	1.4	Not significant
10	0.14	0.62	Not significant
11	0.1	0.45	Not significant
12	0.08	0.38	Not significant
13	0.04	0.2	Not significant
14	0.03	0.12	Not significant
15	0.02	0.1	Not significant
16	0.019	0.09	Not significant
17	0.01	0.04	Not significant
18	0.006	0.03	Not significant
19	0.004	0.02	Not significant
20	0.003	0.01	Not significant
21	0.0014	0	Not significant
22	0.0006	0	Not significant

Table S2. 4: Correlation coefficients of 22 trace elements used in statistical analyses.

	V	Cr	Ni	Cu	As	Se	Rb	Sr	Zr	Nb	Sn	Ba	La	Ce	Hf	Pb	Th	U	Y	Cs	Ga
V																					
Cr	0.71***																				
Ni	0.36*	0.49**																			
Cu	0.34*	0.25	0.42**																		
As	0.78***	0.65***	0.21	0.19																	
Se	-0.21	-0.27	0.54***	0.07	-0.30																
Rb	0.45**	0.37*	0.43**	0.42**	0.31	-0.04															
Sr	0.66***	0.53***	0.01	0.28	0.47**	-0.47**	0.49**														
Zr	-0.40*	0.25	0.31	-0.02	-0.27	0.12	-0.08	-0.25													
Nb	-0.30	0.32	0.11	-0.12	-0.17	-0.07	-0.35*	-0.25	0.88***												
Sn	-0.30	0.32	0.10	-0.15	-0.18	-0.08	-0.34*	-0.24	0.87***	0.98***											
Ba	0.42**	0.32*	0.31	0.27	0.29	-0.09	0.94***	0.45**	-0.16	-0.40*	-0.36*										
La	-0.30	0.09	0.54***	0.18	-0.24	0.38*	0.45**	-0.15	0.67***	0.27	0.30	0.37*									
Ce	-0.22	0.19	0.57***	0.20	-0.16	0.36*	0.48**	-0.05	0.69***	0.31	0.33*	0.38*	0.98***								
Hf	-0.39*	0.23	0.36*	0.00	-0.27	0.20	-0.05	-0.27	1.00***	0.85***	0.84***	-0.14	0.71***	0.73***							
Pb	0.46**	0.74***	0.41*	0.39*	0.49**	-0.44**	0.66***	0.44**	0.33*	0.26	0.26	0.60***	0.35*	0.41*	0.31						
Th	-0.21	0.18	0.58***	0.24	-0.14	0.36*	0.49**	-0.06	0.68***	0.28	0.31	0.38*	0.98***	0.99***	0.72***	0.41*					
U	-0.38*	0.23	0.37*	0.09	-0.25	0.16	0.11	-0.16	0.96***	0.73***	0.74***	0.02	0.81***	0.83***	0.96***	0.37*	0.83***				
Y	-0.32*	0.27	0.46**	0.09	-0.21	0.20	0.18	-0.15	0.94***	0.70***	0.71***	0.08	0.86***	0.88***	0.96***	0.43**	0.88***	0.98***			
Cs	0.41*	0.28	0.46**	0.46**	0.11	0.11	0.41*	0.03	-0.11	-0.15	-0.13	0.38*	0.10	0.07	-0.10	0.34*	0.10	-0.09	-0.03		
Ga	0.61***	0.68***	0.76***	0.51**	0.45**	0.21	0.73***	0.32*	0.12	0.00	-0.02	0.63***	0.35*	0.42**	0.15	0.67***	0.42**	0.18	0.27	0.54***	
Bi	-0.06	-0.17	0.44**	0.48**	-0.02	0.37*	0.02	-0.24	-0.07	-0.20	-0.22	-0.07	0.17	0.14	-0.04	0.02	0.19	-0.04	0.02	0.25	0.22

***: significant for $p < 0.001$; **: significant for $p < 0.01$; *: significant for $p < 0.05$

Table S2. 5: Correlation coefficients of the mean grain size and selected trace elements.

	Ni	Rb	Sr	Zr	Sn	Ba	Hf	Pb	Th	U	Ga
Ni											
Rb	0.63*										
Sr	0.55	0.81**									
Zr	0.21	0.46	0.36								
Sn	0.00	0.33	0.19	0.77**							
Ba	0.61*	0.98***	0.83***	0.46	0.37						
Hf	0.23	0.46	0.34	1.00***	0.74**	0.45					
Pb	0.74**	0.97***	0.74**	0.40	0.29	0.95***	0.40				
Th	0.34	0.58*	0.46	0.97***	0.64*	0.56	0.98***	0.52			
U	0.18	0.39	0.33	0.98***	0.66*	0.37	0.98***	0.31	0.96***		
Ga	0.82**	0.88***	0.66*	0.15	0.12	0.87***	0.16	0.95***	0.29	0.06	
Mean grain size	0.61*	0.96***	0.80**	0.63*	0.42	0.96***	0.62*	0.93***	0.74**	0.56	0.80**

***: significant for $p < 0.001$; **: significant for $p < 0.01$; *: significant for $p < 0.05$

Chapter 3:

A new perspective on interannual sea-level variability around the South China Sea based on historical tide-gauge data

(submitted to *Global and Planetary Change*, in revision)

Dat T. Pham[1,2], Adam D. Switzer[1,2], Emma M. Hill[1,2], Aron J. Meltzner[2] and Hien X. Nguyen[3]

[1]*Asian School of the Environment, Nanyang Technological University, Singapore 639798*

[2]*Earth Observatory of Singapore, Nanyang Technological University, Singapore 639798*

[3]*Institute of Meteorology, Hydrology and Climate Change, Ha Noi, Vietnam*

Abstract:

What major forcings govern relative sea-level variability on an interannual time scale? How does relative sea level around the South China Sea (SCS) respond to them? Investigations of interannual variability around the SCS to date have focused on sea-level anomalies and sea surface height from ocean models. Here, sea-level records span different periods between 1940 - 2014 at ten tide gauges (TGs) have been used to explore the interaction between relative sea level and three major forcings in the region: the El Niño-Southern Oscillation (ENSO), monsoons, and oceanic currents (via Luzon Strait Transport). To extract the interannual mode, we applied Ensemble Empirical Mode Decomposition (EEMD), a new and robust method to decompose time series data into time-dependent frequencies, from which modes with ~2-7 year periods were analysed.

Our results show that while the role of oceanic volume transport measured at the TGs is minor, interannual relative sea-level variations are significantly impacted by ENSO. However, in contrast to other studies, our analyses reveal that ENSO signals are dominant only in the southern and central SCS (correlations of ~ -0.5- -0.8). In the northern SCS, relative sea level is more clearly influenced by winter wind stress, with the exception of the Gulf of Tonkin and the Gulf of Thailand, where local basin geography settings (e.g., location of tide gauges relative to the monsoon pathway) clearly play a role. We also note that, relative sea level in the SCS correlates more highly with the winter monsoon than the summer monsoon, indicating the relative strength of the winter monsoon across the SCS. Notably, this correlation is more evident from the mid-2000s to the present, which may reflect the recent amplification of the East Asian Winter Monsoon [*Wang and Chen,* 2013a].

Our study confirms that EEMD is capable of capturing the interannual mode from sea-level records and that, more importantly, the power of climate and ocean forcings on TGs are non-uniform and site specific. This challenges regional generalizations for future sea-level change planning.

Key words: interannual relative sea level; tide gauge; South China Sea; Empirical Mode Decomposition (EMD); ENSO; ENSO Modoki; monsoons; Luzon Strait Transport.

3.1. Introduction

Tide gauges (TGs) have long been used to examine sea-level trends, and to assess the impacts of relative sea-level rise and other coastal risks in low-lying coastal areas [e.g., *Church et al.*, 2013; *Church and White*, 2006; *Pugh and Woodworth*, 2014; *Pugh*, 1987; *Switzer et al.*, 2014]. However, relative sea-level variation from TGs is a combination of complex phenomena that operate on a range of spatial and temporal scales and both the amplitudes and rates of regional sea-level change can skew estimates of global averages and long-term trends [e.g., *Milne et al.*, 2009]. An understanding of regional relative sea-level changes on different timescales is therefore crucial.

Over the two last decades numerous studies have noted sea-level variations on timescales from seasonal [e.g., *Hill et al.*, 2007; *Tsimplis and Woodworth*, 1994] and interannual [e.g., *Vinogradov and Ponte*, 2011], to decadal or multi-decadal [e.g., *Jevrejeva et al.*, 2006]. However, while these works (and many more) focused on global sea-level variations at various frequencies, regional sea-level change studies truly rely on available data in areas of interest (temporal and spatial resolutions). For example, high-frequency sea-level signals (e.g., seasonal cycles) have been extensively studied due to sufficiency of data records extending back tens of years, but, in contrast, the analysis of lower frequency signals (e.g., decadal to multi-decadal) necessitate much longer data lengths (≥ several decades). The latter condition, however, is only obtainable in a few regions such as North America or Europe. Interannual signal, on the other hand, does not require such long data and with recent significant progress in obtaining and updating sea-level data around the world [*Holgate et al.*, 2013; PSMSL 2016], we now have adequate data to study interannual sea-level variability at multi-decadal time frames.

Sea-level variability on an interannual timescale is a product of large-scale climatic and oceanic changes [e.g., *Parker*, 1992; *Pugh and Woodworth*, 2014], and it commonly reflects the teleconnections between regional changes in an ocean-atmosphere coupled system [*Pugh and Woodworth*, 2014]. These teleconnections are more substantial in areas where interannual signals are more pronounced [*Pugh and Woodworth*, 2014]. One such area is the South China Sea (SCS), the largest semi-closed marginal sea in Southeast Asian waters [*Wyrtki*, 1961].

The primary physiography of the SCS consists of a deep basin (up to 5400 m deep) and two broad shallow continental shelves on the northern and southwestern margins (Fig. 1). Due to the regional geographical settings, circulation of the upper-layer of the SCS is strongly governed by basin-scale monsoonal winds and water exchange from the Pacific [see review in *Liu et al.*, 2008; *Wyrtki*, 1961]. The upper circulation of the SCS has recently been closely linked to El Niño-Southern Oscillation (ENSO) variability [*Liu et al.*, 2008; *Wang et al.*, 2006a; *Wang et al.*, 2006c], monsoonal winds [*Wang*, 2006], and ocean currents [e.g., *Wang et al.*, 2006b]. Yet, exactly how large-scale ocean-atmosphere dynamics affect sea level over basin-wide scale is still less understood. In order to overcome that, *Wu and Chang* [2005] proposed that ocean dynamics are better characterized by sea surface height (SSH) than by sea surface temperature (SST).

To date, the interannual variability of sea level in the SCS has been investigated by not many studies [*Chang et al.*, 2008; *Cheng et al.*, 2015; *Fang et al.*, 2006; *Han and Huang*, 2008a; *Peng et al.*, 2013; *Rong et al.*, 2007; *Soumya et al.*, 2015; *Wu and Chang*, 2005]. The majority of these studies are interpreted to a strong linkage between sea level over the SCS and ENSO signals, a correlation exemplified by the relationship between sea level and the strong 1997/98 El Niño event. The studies mentioned above used SSH observations from ocean models with altimetric data assimilation [e.g., *Chang et al.*, 2008; *Wu and Chang*, 2005], or observations from reconstructed sea-level data [e.g., *Cheng et al.*, 2015; *Peng et al.*, 2013]. In contrast, earlier studies relied upon coastal TGs that were sparse (e.g., *Rong et al.* [2007] deployed only four tide gauges) or had short time series [e.g., *Luu et al.*, 2015; *Soumya et al.*, 2015]. Although maps showing correlations of relative sea level from TGs and ENSO have been provided for the SCS in several studies [e.g., *Soumya et al.*, 2015], it is not clear how coastal TGs from different parts of the SCS respond to ENSO. Expanding on this theme, *Chang et al.* [2008] found a notable relationship between the interannual mode of SSH anomalies and El Niño Modoki, a newly identified type of El Niño during the summers of 1994 and 2002 (the Japanese word “Modoki” means “a similar but different thing”). El Niño (or ENSO) Modoki is represented by a tripole sea surface temperature anomalies (SSTA) pattern over the tropical Pacific from boreal summer to winter [*Ashok et al.*, 2007; *Ashok and Yamagata*, 2009]. In particular, the SSTA in a typical event of ENSO Modoki shows a warming in the central Pacific but is significantly cooler in the eastern and western Pacific [*Ashok et al.*, 2007; *Capotondi et al.*, 2014 for a review]. A detailed study by *Ashok et al.* [2007] shows that ENSO Modoki accounts for about 12% of the Pacific SST variability and that this ocean-atmosphere coupled phenomenon is distinct from conventional ENSO. To date, there has been no study of how ENSO Modoki affects relative sea level from tide gauges around the SCS.

Unlike ENSO, the role of monsoons and oceanic dynamics in relative sea-level variability at an interannual scale has received much less attention. The South China Sea Throughflow (SCSTF), which enters the SCS from the Luzon Strait and flows out through the Karimata, Mindoro and Taiwan Straits [*Wyrtki*, 1961], has recently been recognized as an important influence on climatic and oceanic circulation in the SCS [*Qu et al.*, 2009]. For example, in one recent study, *Soumya et al.* [2015] calculate volume transport through a region that is close to the Karimata Strait, and discuss how it drives relative sea level in the southern SCS. However, while suggestive of the SCSTF's influence, the study is limited to the region of outflow of the SCSTF, and might not reflect the SCSTF's impact on the whole SCS.

Similarly, the effect of monsoonal winds on relative sea level has only been investigated in a few studies, and most of them focused on the seasonal signals [e.g., *Amiruddin et al.*, 2015; *Saramul and Ezer*, 2014]. A focus on seasonal signals is not surprising because the winter and summer monsoon signals are very pronounced over the whole basin. As pointed out in aforementioned studies, seasonal winds are ascendant at the shelf areas of the SCS and the Gulf of Thailand. Also, as introduced earlier, monsoonal winds show interannual variability, but how this variability affects relative sea level at coastal TGs is unclear.

The importance of understanding SSH variability and the limitations in previous studies leads to three main questions:

1) What are the spatial and temporal variations of relative sea level (as measured by TGs) over the SCS under the influence of ENSO and ENSO Modoki?

2) How do monsoons and ocean dynamics contribute to relative sea-level variations (in both spatial and temporal scales) in the region?

3) How much of sea-level variance is explained by each forcing?

Studying interannual relative sea-level variability from TGs necessitates extracting interannual sea-level signals, which are not easy to quantify [*Parker*, 1992]. To isolate the signals, various techniques have been applied, such as low-pass filtering for sea-level anomalies [e.g., *Soumya et al.*, 2015; *White et al.*, 2014], a linear regression model [e.g., *Calafat and Chambers*, 2013], or empirical orthogonal functions (EOF) [e.g., *Chang et al.*, 2008; *Peng et al.*, 2013].

Nevertheless, the use of each of these approaches has potential problems. For instance, the drawback of low-pass filtering is that it relies on user-based selected cut-off frequencies that might be arbitrary and affect the results [*Sweeney-Reed and Nasuto*, 2007]. More importantly, both filtering and EOF assume that the data is stationary (i.e., time independent), which is rare with geophysical data such as sea-level records [*Hamlington et al.*, 2011; *Huang et al.*, 1998].

A possible solution is to apply a new and robust method: Empirical Mode Decomposition (EMD). EMD is an adaptive (i.e., data-based) analysis method, which can be used to decompose nonlinear and non-stationary time series into different time-dependent frequencies (i.e., modes) [*Huang et al.*, 1998; *Wu and Huang*, 2009]. Here, we used EMD as a low-pass filter to isolate the interannual signals from sea-level records. Although EMD has been applied to diverse fields [*Rao and Hsu*, 2008], surprisingly, it has infrequently been used to explore sea-level variations. Among the rare examples, *Ezer and Corlett* [2012] and *Ezer* [2013] utilized EMD in sea-level studies along the east coast of the United States, while *Breaker and Ruzmaikin* [2010, 2013] deployed EMD along the U.S. west coast. Recently, *Saramul and Ezer* [2014] used EMD to extract the variations of sea level along the coast of Thailand. All those studies confirm the applicability of EMD in sea-level research and the success of the studies elsewhere suggest that we can use the EMD method to answer the aforementioned questions for the SCS.

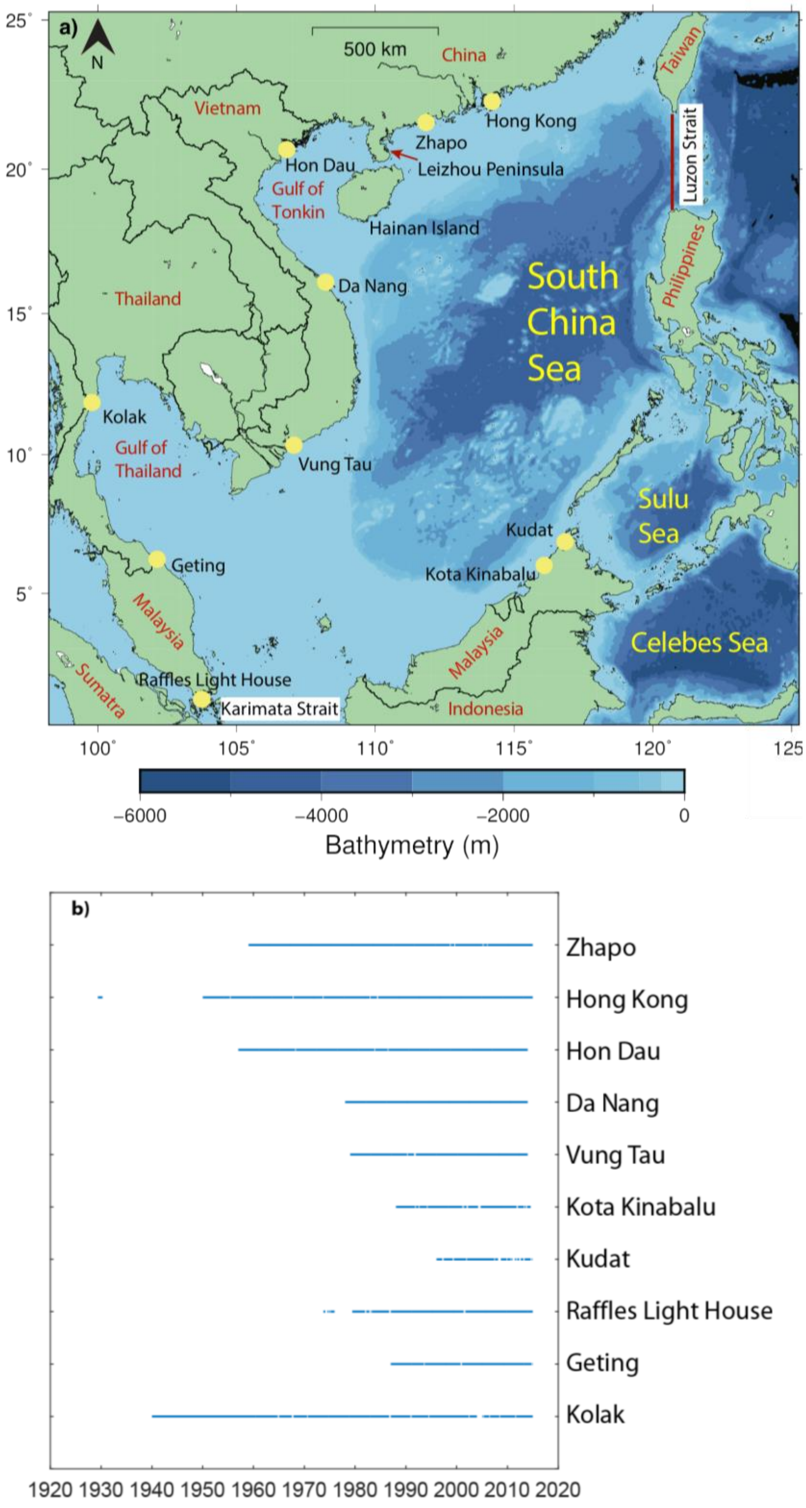

Figure 3. 1: (a) Location of tide gauges (yellow circles) in the South China Sea. The red solid line represents the Luzon Strait where Luzon Strait Transport was calculated. Bathymetry was obtained from the GEBCO website; (b) Available data lengths and data gaps (before processing) at each tide gauge from the PSMSL website.

3.2. Data acquisition and preparation

3.2.1. Sea-level data

In this study, we selected monthly mean sea-level records from 10 TGs around the SCS for analyses: Hong Kong, Zhapo, and Hon Dau, in the northern SCS; Da Nang and Vung Tau, in the central SCS; and Kolak, Geting, Raffles Light House, Kudat, and Kota Kinabalu, in the southern SCS) (Fig. 1). Monthly mean sea-level records (in the Revised Local Reference format, RLR, which is datum controled) were mainly derived from the Permanent Service for Mean Sea Level (PSMSL) (extracted from database 29 Feb 2016, from http://www.psmsl.org/data/obtaining/.) [*Holgate et al.*, 2013; PSMSL 2016]. Sea level time series for Hong Kong were obtained by merging data at North Point (from 1929 - 1985) and Quarry Bay (from 1986 - 2013). These two TGs are ~ 500m apart, but refer to the same datum with a small offset (~1.02 cm), and thus can be used as one data set, hereafter named as Hong Kong [*Ding et al.*, 2001; *Feng and Tsimplis*, 2014]. However, there is a long gap in monthly mean sea-level data at Hong Kong from 1930-1950 thus, we only used monthly data from 1950 - 2014 for our study. Similarly, sea-level data at Raffles Light House tide gauge starts from 1973 but has a gap from 1976-1979; hence, we decided to use data from 1980 - 2014.

We were also aware of vertical land motion caused by the M_W 9.2 Sumatra-Andaman earthquake that resulted changes in sea-level records at tide gauges along Thailand's coast [*Saramul and Ezer*, 2014; *Trisirisatayawong et al.*, 2011]. *Amiruddin et al.* [2015] found a ~ 10-cm discrepancy of monthly mean sea level at Kolak tide gauge and discarded all data after the 2004 earthquake. We did same treatment in this study.

At the time of writing, sea-level observations from 7 out of the 10 TGs have been updated to the end of 2014. Sea-level data from three TGs along the coast of Vietnam - Hon Dau, Da Nang and Vung Tau - had only been updated to the year of 2013. To get the data for 2014, we obtained sea-level data from the Vietnam Marine Hydrometeorological Centre. However, as those datasets are 'metric' data (not datum controled), we treated each dataset carefully by using historical benchmarks available from the PSMSL in order to convert the sea-level data into the RLR, datum-controled format [*Holgate et al.*, 2013]. We then plotted the processed sea-level records against the existing PSMSL records, and visually checked to eliminate any suspected outliers and datum shifts. The combined data from the two sources thus forms a continous record. The data length and gaps for each TG are shown in Figure 1b. We filled the data gaps, prior to analysis, using a cubic spline interpolation. Unfortunately, we could not use TGs in the eastern SCS (i.e. along the Philippine coastline) due to large contamination of the data by the effects of vertical tectonic land movement [*Rodolfo and Siringan*, 2006].

3.2.2. Climate indices

To compare sea level with climate modes, we used two different monthly indices of ENSO: the Multivariate ENSO Index (MEI) (available from: http://www.esrl.noaa.gov/psd/enso/mei/table.html) and the El Niño Modoki Index (EMI) (available from:

http://www.jamstec.go.jp/frcgc/research/d1/iod/DATA/emi.monthly.txt).

The MEI is built as the first unrotated principal component of six major variables over the tropical Pacific: sea-level pressure, zonal and meridional components of the surface wind, sea surface temperature, surface air temperature, and total cloudiness fraction of the sky [*Wolter and Timlin*, 1993, 1998]. Note that the sign of the MEI is opposite to other popular ENSO indices such as the Southern Oscillation Index (SOI), i.e., El Niño will be exhibited by positive values, whereas negative values demonstrate La Niña events.

The EMI is defined as the difference of the area-averaged SSTA over three regions of the tropical Pacific [*Ashok et al.*, 2007], as follows:

$$\mathrm{EMI} = [\mathrm{SSTA}]_A - 0.5*[\mathrm{SSTA}]_B - 0.5*[\mathrm{SSTA}]_C \qquad (3.1)$$

where A is the region of (165^{o}E - 140^{o}W, 10^{o}S-10^{o}N), B is (110^{o}W-70^{o}W, 15^{o}S-5^{o}N) and C is (125^{o}E-145^{o}E, 10^{o}S-20^{o}N). The sign of EMI is similar to that of MEI.

The impact of El Niño Modoki on interannual sea-level variability in the SCS has been investigated by *Chang et al.* [2008] but the study was limited to a short timescale (1993 - 2002) and did not use the coastal TGs. Here, we extend their study to the full time frame of the tide gauge at each site.

3.2.3. Wind stress and volume transport

We calculated wind stress and volume transport based on the Simple Ocean Data Assimilation (SODA) reanalysis of ocean climate variability (SODA v2.2.4, http://apdrc.soest.hawaii.edu/) [*Carton and Giese*, 2008] and zonal and meridional wind stress on a uniform resolution 0.5^o x 0.5^o grid domain with 40 vertical levels from ~ 5 to 5000 m depth. SODA outputs span the period 1870 – 2010, but for our study we extracted wind stress components and zonal velocity only for 1940 - 2010, for comparison with the sea-level records.

We used zonal and meridional wind stresses from SODA to calculate wind stress over the SCS (0.25°N - 25.25°N, 98.25°E - 125.25°E). We then averaged wind stress for the whole region for each month of the calendar year. To study the impact of monsoons on sea level, we calculated the winter (Nov-Dec-Jan-Feb) and summer (Jun-Jul-Aug) mean of monthly wind stress and sea level in the same year. The winter period we selected for this study differs slightly from conventional climatological seasons (i.e., the boreal winter is Dec-Jan-Feb) because we want to include the strength of the winter monsoon starting from November [*Liang et al.*, 2000].

The Luzon Strait Transport (LST) has been considered as an index of the SCSTF [e.g. *Wang et al.*, 2006b]. Calculations from previous studies revealed that the direction of the LST is mainly westward (i.e., from the Pacific into the SCS) [see *Qu et al.*, 2009 for a review]. However, *Qu et al.* [2004] used the Modular Ocean Model version 2 to study SCS circulation and found that the flow coming into the SCS is mostly confined to the upper layer (≤ 400 m depth) and that below this layer the net transport is negligible. Similarly, *Zhang et al.* [2015] utilized observational data and confirmed the "sandwiched" structure of the LST, i.e., the flow is westward in the upper (<500 m) and deeper (>2000 m) layers but reversed in the intermediate layer. Considering the factors mentioned above, we only estimated the LST from ~400m up to the surface in order to study the impact of the LST on sea level. To do that, we integrated the zonal velocity (from SODA) with depth, across the strait at 120.25°E, 17.25°N - 23.25°N (Fig. 3.1, thick red line).

3.3. Methodology

To accurately pick up the interannual signals of relative sea level, we adopted the Empirical Mode Decomposition (EMD), a component of Hilbert - Huang Transform data analysis tool [*Huang et al.*, 1998], which facilitates decomposing a time series data $X(t)$ into intrinsic mode functions IMF_i and a residual r, which is considered as the trend.

$$X(t) = \sum_{i=1}^{n} IMF_i + r \qquad (3.2)$$

An IMF extracted from given time series should satisfy two criteria: firstly, the number of extrema (maxima and minima) and the number of zero-crossing must be identical or differ at most by one throughout the data length; and secondly, the local mean value of the upper and lower envelopes, which are determined by the maxima and minima respectively, is zero. The process decomposes $X(t)$ as in (3.2) is so-called *sifting* process. We outlined the sifting process [*Huang et al.*, 1998; *Huang and Wu*, 2008] as follows:

1. Define the maxima and minima of $X(t)$
2. Connect all the local maxima/minima by interpolating a cubic spline line to produce the upper (e_{max})/lower (e_{min}) bound of the envelopes.
3. Calculate the mean of envelope $m = (e_{max} + e_{min})/2$
4. Subtract the local mean m from the envelope to form a "potential" IMF: $h = X(t) - m$.
5. Check whether h is an IMF satisfying the requirements described above.

5.1. If yes, save h as an IMF and compute the residual r by subtracting this new-detected IMF from the original data $r = X(t) - h$. Repeat step 2 with the residual r

5.2. If not, repeat step 2 for h

6. Iterate step 1 until we find the last residual r that does not meet the definitions of an IMF. In this case, the last r is considered as the long-term trend.

EMD does not ask for a priori knowledge or stationary assumptions like other traditional methods [*Huang and Wu*, 2008]. IMFs are locally and adaptively extracted based on data themselves, not on user-based selection. Amplitude and frequency of each IMF are time-dependent and, thus, EMD is useful for non-linear and non-stationary time series data (e.g., sea-level data). The number of IMFs (or modes, from high to low frequencies) depends on the number of observations and is generally defined as $\log_2(n)$, with n being the number of data points. From those modes, one might chose or combine specific frequencies to form meaningful signals of interest [e.g., *Breaker and Ruzmaikin*, 2010; *Ezer*, 2013]. One valuable implication of EMD is that it is capable of isolating low-frequency signals from high-frequency signals without losing meaningful structures [*Barnhart*, 2011; *Wu and Huang*, 2009]. As a result, studies of low frequencies in sea-level records are becoming increasingly popular [e.g., *Breaker and Ruzmaikin*, 2010; *Ezer*, 2013; *Ezer*, 2015].

One of the downsides to EMD is the occurrence of mode mixing that can appear when the decomposed data contain IMF(s) which have signals varying in different scales or signals in the same scale with other IMF(s) [*Wu and Huang*, 2009]. The mode mixing might cause inaccurate separation between IMFs and, as a consequence, the true and meaningful signal would be missed. To deal with that, *Wu and Huang* [2009] improved the original EMD by a noise-assisted technique, called ensemble EMD (EEMD). A finite amplitude white noise is added to each ensemble and the true IMF(s) are defined as the mean of an ensemble. In the present study, we will use EEMD analysis for our data sets with an ensemble size of 500, and a noise amplitude for the data sets of 0.5 standard deviations. An illustration of applying EEMD to sea-level time series is shown in Figure 3.2.

We applied EEMD to all time series, and for each time series we selected modes with ~2-7-year frequency and combined them to form a new time series. We then applied cross-correlation analyses to investigate how climate indices, seasonal monsoons and ocean transport are related to the interannual variations in sea level. The significance of correlation coefficients was evaluated with the *t-test* at 95% confidence level. We further examined how those relationships varied with time by carrying out a wavelet coherence analysis [*Grinsted et al.*, 2004; *Torrence and Compo*, 1998].

Finally, we investigated how much each index contributes relatively to interannual sea-level variations by using a multiple linear regression model of sea level (the response variable) and MEI, EMI, wind stress and LST indices (the predictor variable). After running the linear model, the relative importance of individual predictor variable was identified at each tide gauge. We executed the linear model and relative importance calculation using the ***MASS*** [*Venables and Ripley*, 2002] and ***relaimpo*** [*Groemping*, 2006] packages for *R* [*R Core Team*, 2014].

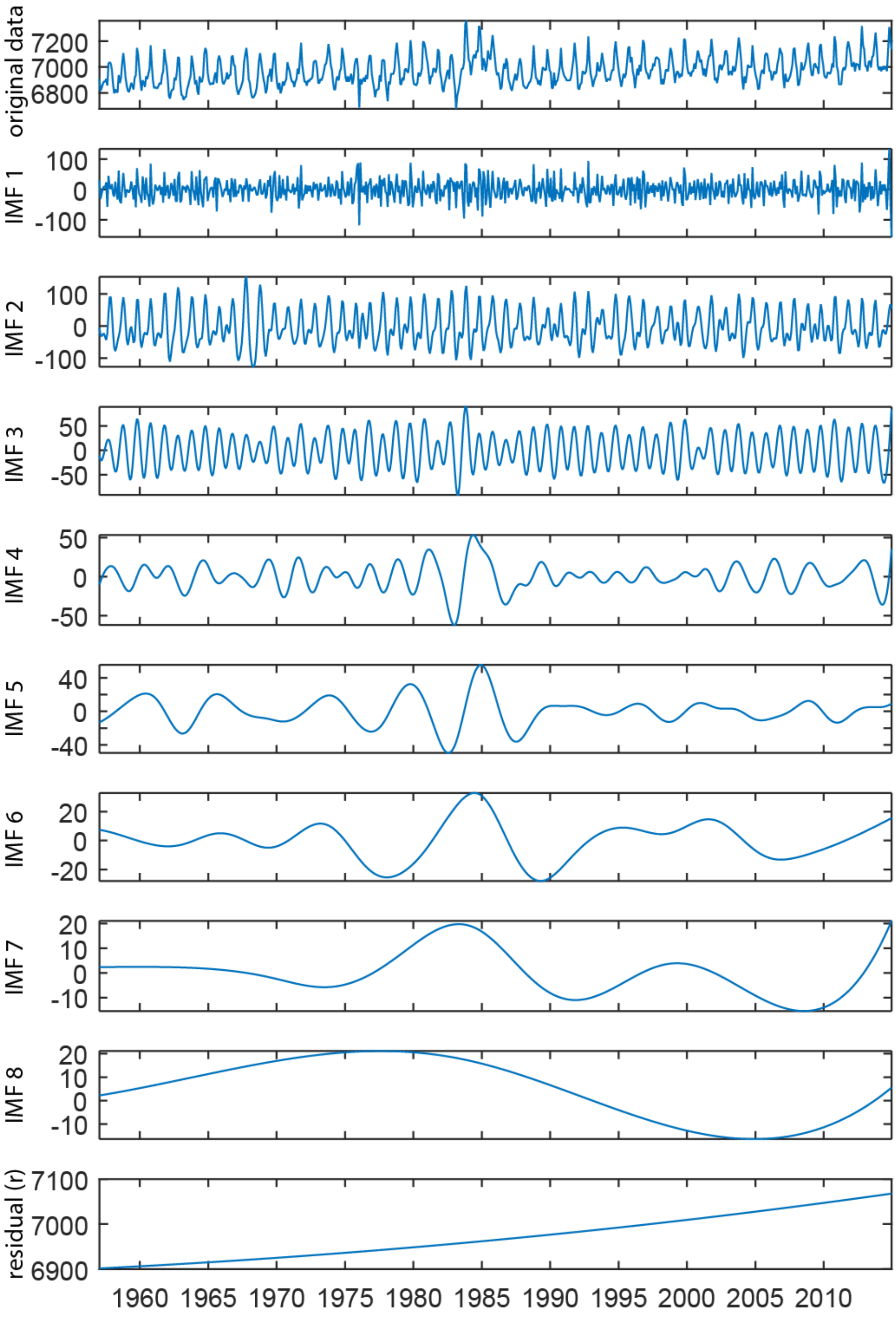

Figure 3. 2: Example of using EEMD to decompose monthly sea-level record (in mm) at the Hon Dau tide gauge. The original data (top panel) is decomposed into 9 intrinsic mode function components: IMF1 – IMF 8 and the last IMF is considered as the residual *r* (i.e., the trend).

3.4. Results and Discussions

For the ease of comprehension, in this section, TGs are classified according to their geographical locations: northern TGs (Zhapo, Hong Kong and Hon Dau), central TGs (Da Nang and Vung Tau), southwest TGs (Raffles Light House, Geting and Kolak) and southeast TGs (Kudat and Kota Kinabalu).

3.4.1. Linkage to ENSO and El Niño Modoki

Our analyses show that, overall, interannual sea-level variations around the SCS are significantly correlated with ENSO and that this correlation varies spatially (Fig. 3.3). In particular, the central and southern TGs are highly correlated, at zero time lag, with the MEI (r ~ -0.5 to -0.8), with the exception of the Kolak tide gauge in the Gulf of Thailand (r = -0.2). The highest correlations are seen at southeast TGs and Raffles Light House with r = ~ -0.8 (Fig. 3.3). Similar correlations are not reflected in the northern TGs, where the correlation is only ~ -0.3 to -0.4 (Fig. 3.3). This trend suggests that ENSO's influence is strongest in the central and southern SCS but weakens to the north. Similarly, ENSO power appears to decrease considerably westward. The Wavelet Coherence analysis supports this interpretation (Fig. 3.4) and demonstrates that ENSO and the northern TGs discontinuously co-vary only in specific periods, consistent with strong ENSO events. In contrast, the central and southern TGs vary coherently with ENSO signals throughout the records, as displayed by a pronounced ~ 2-7 year signal.

Our results are consistent with previous studies, in which the impact of ENSO on sea level at interannual scales was demonstrated [e.g., *Peng et al.*, 2013; *Rong et al.*, 2007; *Soumya et al.*, 2015]; this confirms the robustness of the analysis method.

However, the spatial variability of sea level-ENSO correlations observed in our results provides more detail than earlier studies, and there are several deviations from past studies. For instance, [*Soumya et al.*, 2015] argued for little correlation between sea level and ENSO in the Gulf of Tonkin and central Vietnam [*Soumya et al.*, 2015, their Fig. 5], whereas our analyses show low but still statistically significant correlation with ENSO at the Hon Dau, Da Nang and Vung Tau TGs (r = -0.32, -0.49 and -0.63 respectively). This dissimilarity may be attributed to the lack of the TGs used by *Soumya et al.* [2015] in the central and northern SCS.

Observations of the temporal variations in our analyses indicate a slightly stronger response from the Da Nang, Raffles Light House and northern TGs to the 1982/83 El Niño event, compared to the 1997/98 episode; these constitute the two strongest El Niño events on record. Sea levels drop dramatically (~ 7-10 cm or more) at those TGs in 1982/83 (Fig. 3.3). In contrast, the 1997/98 El Niño event appears to have had a much larger impact at Vung Tau with the same magnitude of sea-level drop, but smaller in the 1982/83 El Niño event. Due to inadequate data, we are not able to compare the two strong ENSO episodes at the southeast TGs. We are also unable to identify a clear trend at Geting and Kolak. We can only suggest that sea level at each TG responds differently to each El Niño events, which prompts the question of whether the SCS sea-level response varies considerably with the magnitude of ENSO episodes. *Wolter and Timlin* [1998] used the MEI and selected other conventional ENSO indices to rank the 1982/83 and 1997/98 El Niño events, and they found that, based on certain criteria, the former event is somewhat stronger than the latter event. If correct, one would expect that sea-level fall would be larger in the 1982/83 event than in 1997/98. We only observed such expectation at about half of the TGs in our study. However, as described above, data are insufficient at some sites, and therefore such a conclusion cannot be made in this study.

While the influence of ENSO on sea-level records is obvious, the correlation between ENSO Modoki and sea-level records around the SCS seems to be poor (Fig. 3.5). No significant correlations are found at Vung Tau and Kolak. Northern TGs only have weak correlation with ENSO Modoki (r ~ -0.1 to -0.2), whereas southern TGs are moderately correlated to ENSO Modoki with r ~ -0.4 (Fig. 3.5). As pointed out by *Ashok et al.* [2007] and *Chang et al.* [2008], a typical ENSO Modoki event usually occurs in the boreal summer, and hence, we calculated the summer mean of sea level (from June to August) and compared that to the summer average of the EMI. Yet, we found no significant correlations (Supp. Info Fig. S3.1a). Next, ENSO Modoki has been more pronounced since 1979 [*Ashok et al.*, 2007], we thus truncated our datasets and re-ran analyses for the 1979-2013 period. Despite that, we were still unable to obtain good results. The wavelet analysis also emphasizes the weak coherency between ENSO Modoki and sea level recorded by most of the TGs (Fig. 3.6). This lack of success suggests that in this case a direct comparison might not be sufficient. Given that, an alternative approach such as that by *Chang et al.* [2008], in which they acquired the second mode of SSH anomalies from the Empirical Orthogonal Function analysis, might be more suitable. That approach, however, is beyond the scope of our study. Even so, we noticed a high coherence of signal with ~2-4 year periods, especially in the southern TGs, starting from the mid-2000s (Fig. 3.6). This observation suggests promise for further studies, as ENSO Modoki activity has recently been more frequent [*Xie et al.*, 2014].

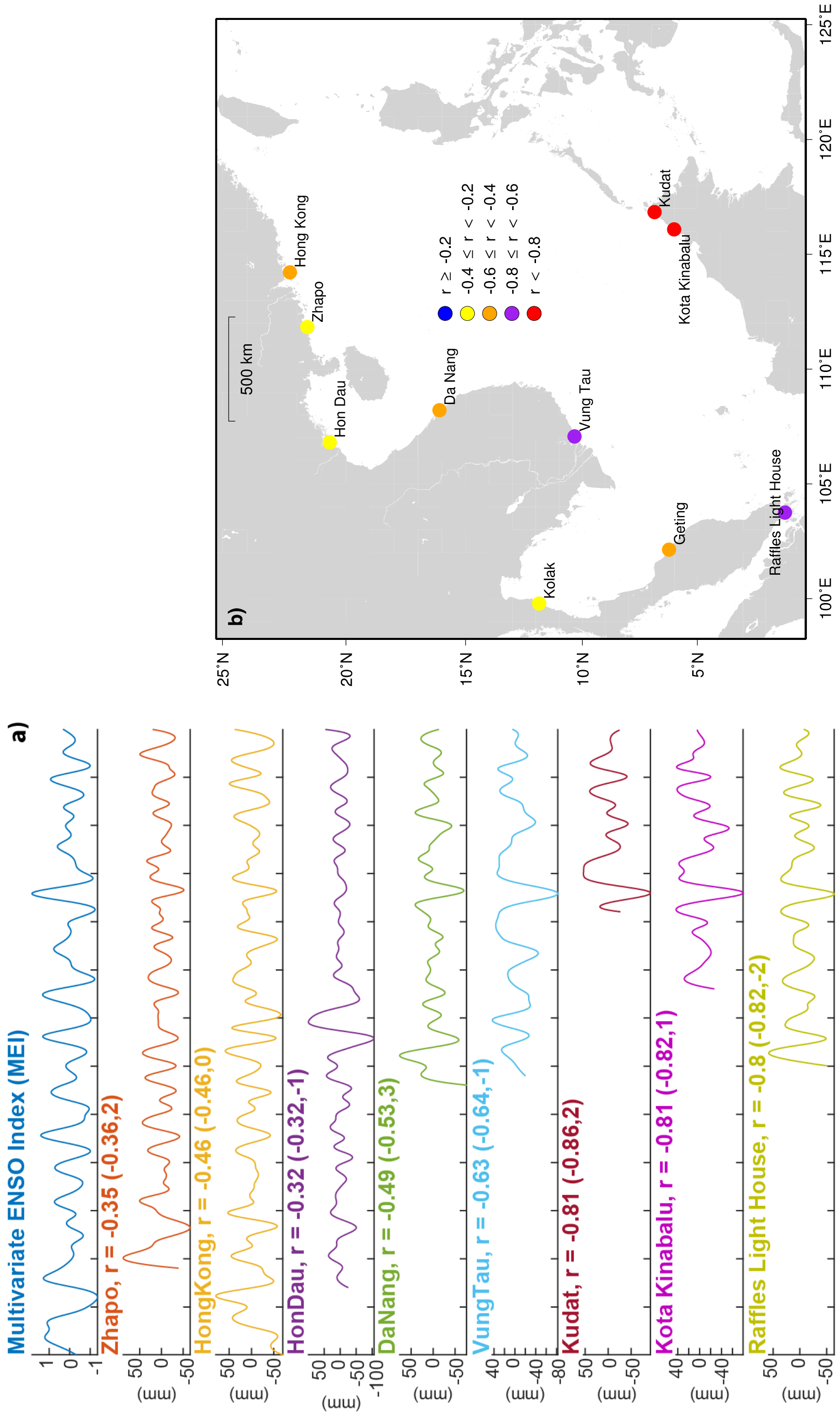

Figure 3. 3: (a) Relative sea level at each tide gauge responds well to ENSO such as the 1982-83 and 1997-98 strong events at interannual time scales. All multivariate ENSO Index (MEI)-sea level correlations are statistically significant based on the *t-test* at 95% confidence level. The numbers in parentheses represent the maximum correlations and time lag, respectively; (b) ENSO is more highly correlated to sea level at the southern tide gauges but less in the west and north of the SCS.

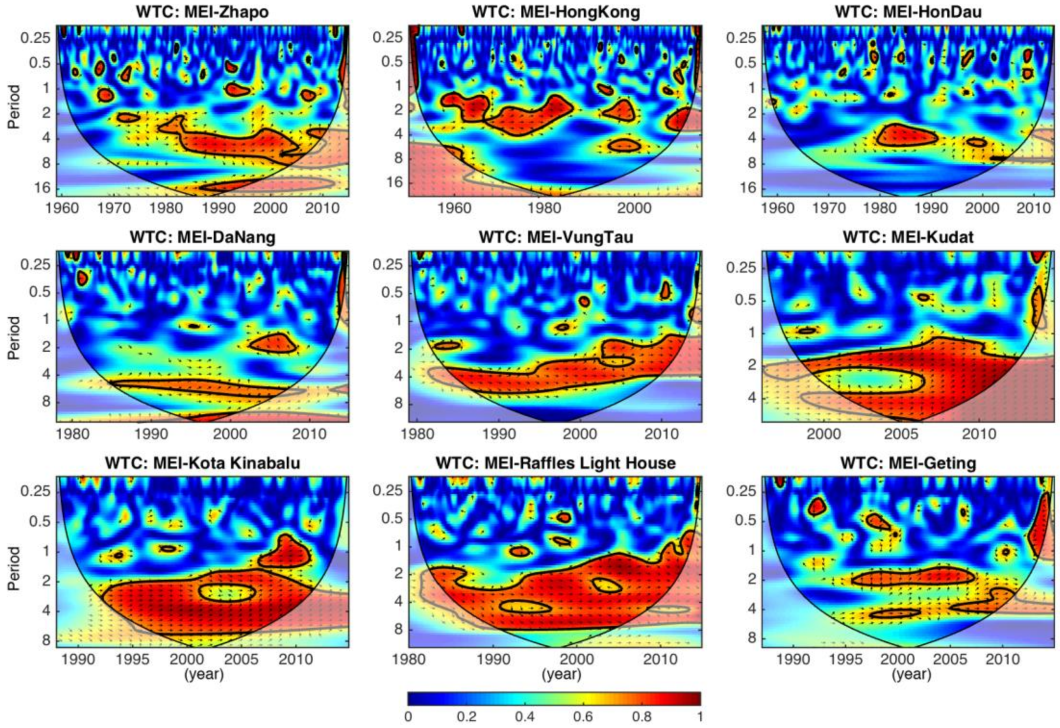

Figure 3. 4: Wavelet coherence analysis between interannual time series of multivariate ENSO Index (MEI) and relative sea level recorded at tide gauges. The clear and continuous 2-7 years' red band shows a better correspondence of the Southern tide gauges and ENSO strength. The black contours around the red band indicate the 95% significance level, and the vectors show phase relationships (in-phase pointing right out of-phase pointing left, and other angle shows lag/lead phase). For illustration purposes, we multiplied MEI values by (-1) prior to wavelet analysis. The white shaded area shows the cone of influence where the edge effect becomes more pronounced.

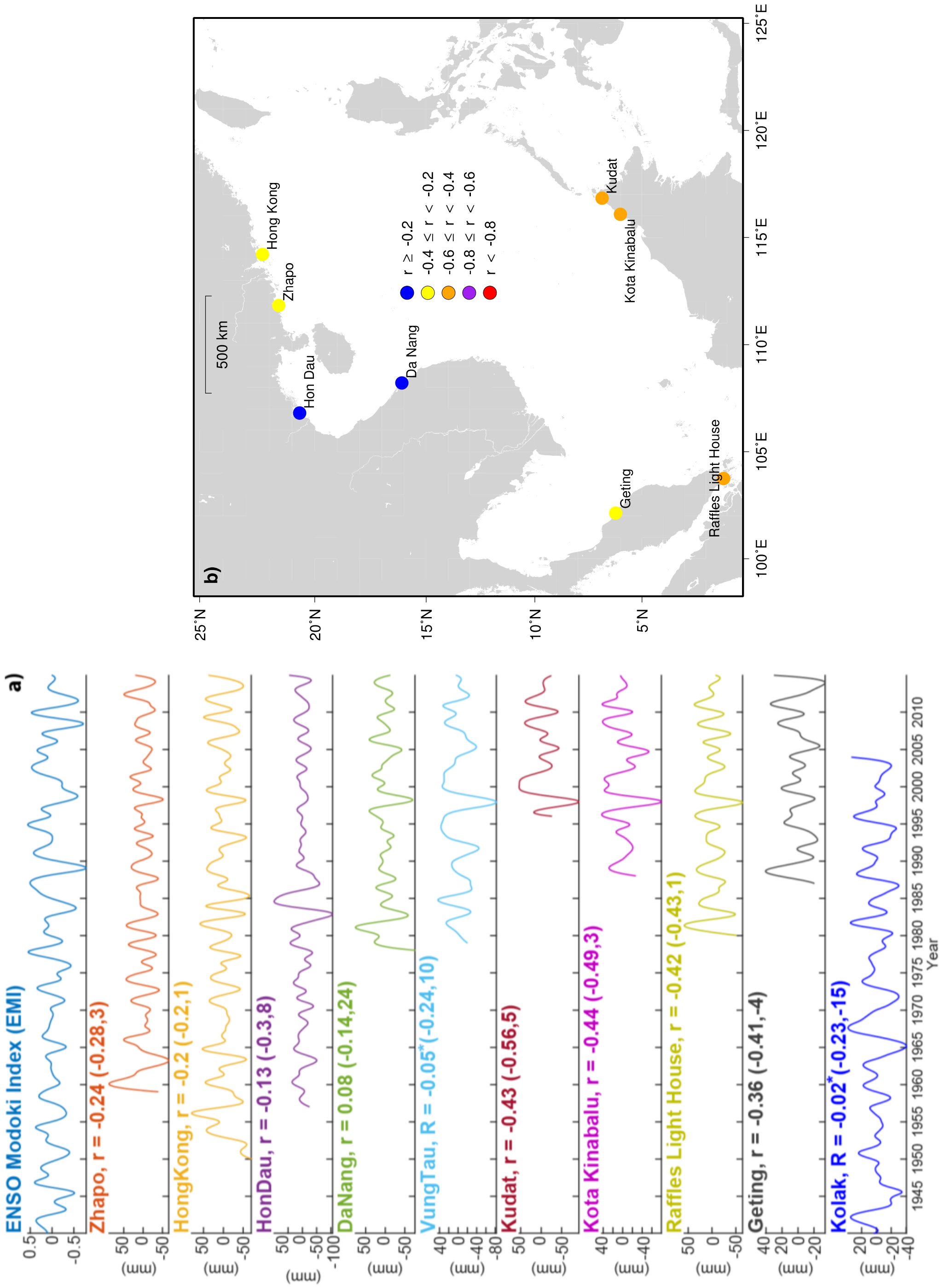

Figure 3. 5: (a) Correlations between interannual time series ENSO Modoki index (EMI) and relative sea levels are rather weak. Statistically insignificant correlations are marked with asterisks. Significance test is based on the *t-test* at 95% confidence level. The numbers in parentheses represent the maximum correlations and time lag, respectively. (b) Only relative sea levels at the southern tide gauges correlate moderately to EMI. Note that only tide gauges with statistically significant correlations are plotted.

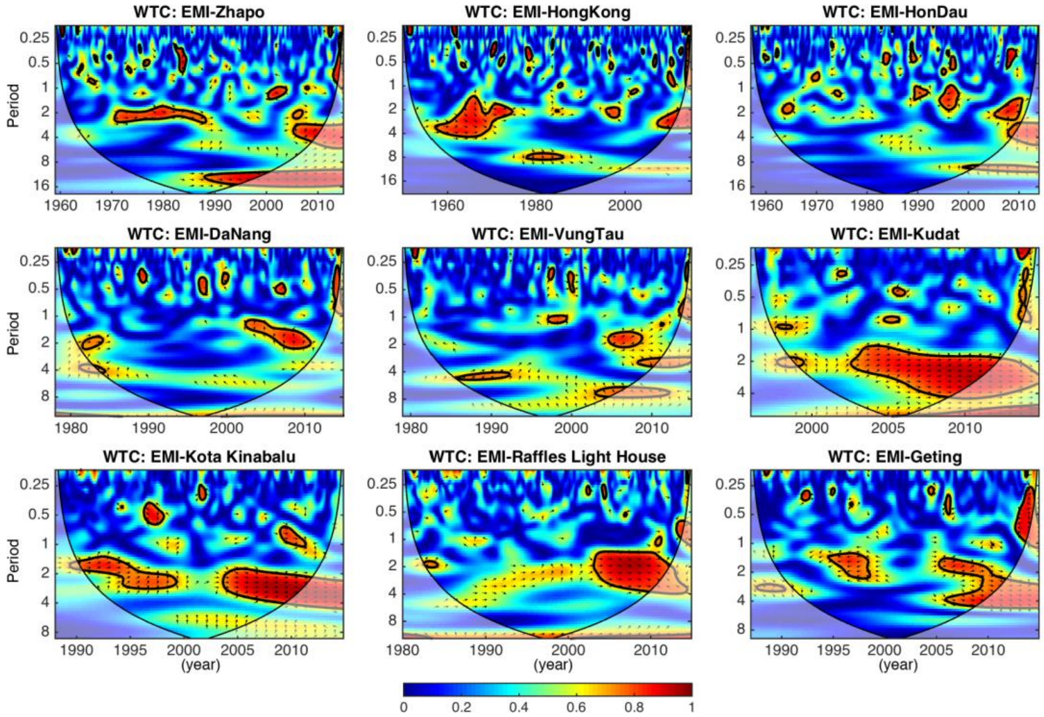

Figure 3. 6: Wavelet coherence analysis between interannual time series of multivariate ENSO Modoki Index (EMI) and relative sea level recorded at tide gauges. ENSO Modoki Index (EMI) and sea levels strongly co-vary only in recent years. The black contours around the red band indicate the 95% significance level, and the vectors show phase relationships (in-phase pointing right, out of-phase pointing left, and other angle shows lag/lead phase). For illustration purposes, we multiplied EMI values by (-1) prior to wavelet analysis. The white shaded area shows the cone of influence where the edge effect becomes more pronounced.

3.4.2. The role of monsoonal winds

On an interannual scale, we observe the influence of seasonal monsoons (via wind stress) on sea-level variations to be greater at the southern TGs when compared to the central and northern TGs (Fig. 3.7). The only exception is Kolak, where there is no correlation with wind stress, and this is likely due to the local geographical setting. The results show that sea level at most of the TGs is positively correlated with wind stress, with the highest correlation coefficients (at zero lag) observed at the southeast TGs, namely Kudat (r = 0.6) and Kota Kinabalu (r = 0.5) (Fig. 3.7). One outcome from the analysis is to show the significant correlation between sea level and wind stress during the strong 1997/98 El Niño event (Fig. 3.7). This is because El Niño also has an impact on wind stress, reducing wind stress magnitude and consequently causing a relative fall in sea level. As explained by *Clarke* [2008], in the warm phase of ENSO (i.e. an El Niño event), the Walker Circulation becomes weaker than normal and, as a result, the atmospheric convection in the far western Pacific weakens, causing less wind forcing.

To further examine the impact of winter and summer monsoons, we compared the mean of wind stress and sea level for each season. Our results demonstrate that across the SCS, in the winter, the northeasterly (NE) monsoon has a larger effect on sea level than the southwesterly (SW) monsoon in the summer (Fig. 3.8). In winter, most of the TGs are positively correlated to wind stress, excluding the Hon Dau tide gauge, and the southern TGs have higher correlation coefficients, ranging from $r \sim 0.3 - 0.8$ (Fig. 3.8a). In contrast to the NE monsoon, the SW monsoon shows much weaker correlations with sea level. Only five out of the 10 TGs are correlated with summer wind stress at a statistically significant level. Three TGs in the northern and central

SCS (Zhapo, Da Nang and Vung Tau) positively correlate to summer wind stress whereas two southern TGs (Raffles Light House and Geting) are negatively correlated (Fig. 3.8b).

Our results reveal that sea-level change in the SCS corresponds more strongly to the winter monsoon, from which we can infer that the winter monsoon is a clear forcing of local sea level. This inference supports earlier studies that showed that the winter monsoon is generally stronger than the summer monsoon in its fully developed period (i.e. Dec-Jan) [e.g., *Fang et al.*, 2006; *Liang et al.*, 2000]. We find that the effects of the NE monsoon are even greater in the southern SCS. This prompts the question of why the northern TGs do not respond well to the winter monsoon? One explanation may be that the influence of local geography and basin geometry prevent water from piling up near the tide gauges as a result of wind forcing. This could explain the lack of monsoon signal recorded by the Hon Dau tide gauge, located in the northwest of the Gulf of Tonkin (Vietnam); this is a semi-closed basin surrounded by Hainan Island and Leizhou Peninsula (Fig. 3.1) on the east that block wind fetch. Moreover, Hon Dau appears to be far off the strong basin-wide monsoon pathway that is the northeast-southwest axis stretching from Taiwan to offshore southwest Vietnam [e.g., *Fang et al.*, 2006, Fig. 2a and b]. As a result, this tide gauge shows no correlation with either the NE or the SW monsoon, indicating that the monsoon is not a major driver here.

Basin geometry and local geography are likely to have a greater contribution to sea level variations at the central and southwest TGs (Vung Tau, Geting and Raffles Light House). These TGs are positively correlated to the winter monsoon (Fig. 3.8a) but have negative or no correlation with the summer monsoon (Fig. 3.8b). This trend could be explained by the locations of those TGs (at the coastline) against the direction of monsoonal winds (i.e., the orientation of the coastline). When the wind blows southwesterly in summer, sea level is pulled away from the shore resulting in a relative lowering of sea level (i.e., negative correlation), whilst in the winter the northeasterly wind will pile water up against the shore causing relatively higher sea level (i.e., positive correlation). Our results and explanations show a good agreement with other studies such as *Saramul and Ezer* [2014] (for the Gulf of Thailand - GOT) and *Tkalich et al.* [2013] (for Singapore Strait) even though these studies focused on seasonal sea-level cycles. At Vung Tau, the effect of Ekman transport might be important – the coastline is oriented roughly parallel to the southwesterly wind direction. Here, the alongshore wind generates the coastal upwelling that forms a cold water region of the coast of Vietnam, maximum from 10^{o}N – 13^{o}N, in summer [*Xie et al.*, 2003]. Furthermore, the coastal cooling extends eastward to the open-ocean caused by a strong wind jet offshore, which is discussed by *Xie et al.* [2003]. The eastward extension of cold water from Vietnam coast was then defined as the "cold filament" [for more discussions on the mechanism of the cold filament, refer to *Xie et al.*, 2003]. We propose that the combination of Ekman upwelling and the wind jet offshore makes relative sea level at Vung Tau lower in summer and hence leads to negative correlation with the monsoon (r ~ -0.4, Fig. 3.8b).

As the winter monsoon's dominance over the SCS is clear, it is interesting to examine the winter monsoon - sea level relationship to a greater extent by using an index that measures the magnitude of the winter monsoon in East Asia. There are numerous winter monsoon indices that have been proposed in last two decades [*Wang and*

Chen, 2010]. Here, we used a new East Asian Winter Monsoon index (EAWM) proposed by *Wang and Chen* [2013b]. The EAWM index is defined as:

$$\mathrm{EAWM} = (2\mathrm{x}\mathrm{SLP}_1 - \mathrm{SLP}_2 - \mathrm{SLP}_3)/2, \qquad (3.3)$$

where SLP_1, SLP_2, and SLP_3 are the normalized area-averaged sea-level pressure (SLP) over Siberia (40^o-60^oN, 70^o-120^oE), the North Pacific (30^o-50^oN, 140^oE-170^oE) and the Maritime Continent (20^oS-10^oN, 110^o-160^oE, i.e., including the southern SCS). The primary advantage that EAWM has is that it considers not only the east-west but also the north-south sea-level pressure gradients over East Asia including the SCS [*Wang and Chen*, 2010, 2013b]. Hence, the index used here will be suitable for our purposes. Nevertheless, one should bear in mind that the index of *Wang and Chen* [2013a] is a Dec-Jan-Feb mean. Thus, to be consistent with our winter mean of sea level, we recalculated the EAWM for a Nov-Dec-Jan-Feb mean and compared that to sea level for the period 1979-2012. We used reanalysis monthly mean SLP from the Japanese 55-year Reanalysis "JRA-55" database (available at http://rda.ucar.edu/datasets/ds628.1/). The JRA-55 dataset has a spatial resolution of 1.25^o x 1.25^o and spans from 1958 - 2013.

The result from correlation analysis shows that most of the TGs are, to some extent, positively correlated with the EAWM, with the exception of Geting (Fig. 3.9). The correlation coefficients demonstrate little overall difference between the TGs ($r \sim 0.3$ - 0.5) but the coefficients for the northern TGs appear to be slightly higher than for the central and southern TGs, with the highest correlations in Hong Kong and Zhapo ($r = 0.5$ for both sites). When compared to the wind stress-sea level correlation presented in the preceding paragraphs, this result indicates that the northern TGs correspond better to the EAWM than to wind stress, especially for the case of the Hon Dau tide gauge.

This suggests that the impact of atmospheric pressure on sea level (i.e., the inverted barometer effect) is somewhat greater than wind stress in the northern SCS in the winter. A strong and positive EAWM index corresponds to the higher-than-normal SLP in the north side of the SCS and lower-than-normal SLP in the southern SCS (see equation (3.3)). In addition, strong EAWM is associated with stronger northeasterly wind that carries more water westward from the North Pacific to the SCS resulting the rise of winter mean sea level at northern TGs (Wang Lin, personal communication).

More interestingly, we find that, when using non-EEMD processed data for the winter season (i.e., raw winter mean sea level data prior to EEMD/HHT analysis), all northern TGs are closely related to the weak period of EAWM from the mid-1980s to the early 1990s [*Wang and Chen*, 2013a, 2013b]; furthermore, the winter mean sea level started rising in the mid-2000s, which coincides with the recent intensification of the EAWM winters [*Wang and Chen*, 2013a] (Supp Info Fig S3.1b). These correlations support the contention that the winter mean sea-level variations are attributed to the intensity of the winter monsoon. This may be an interesting topic for exploration in future studies.

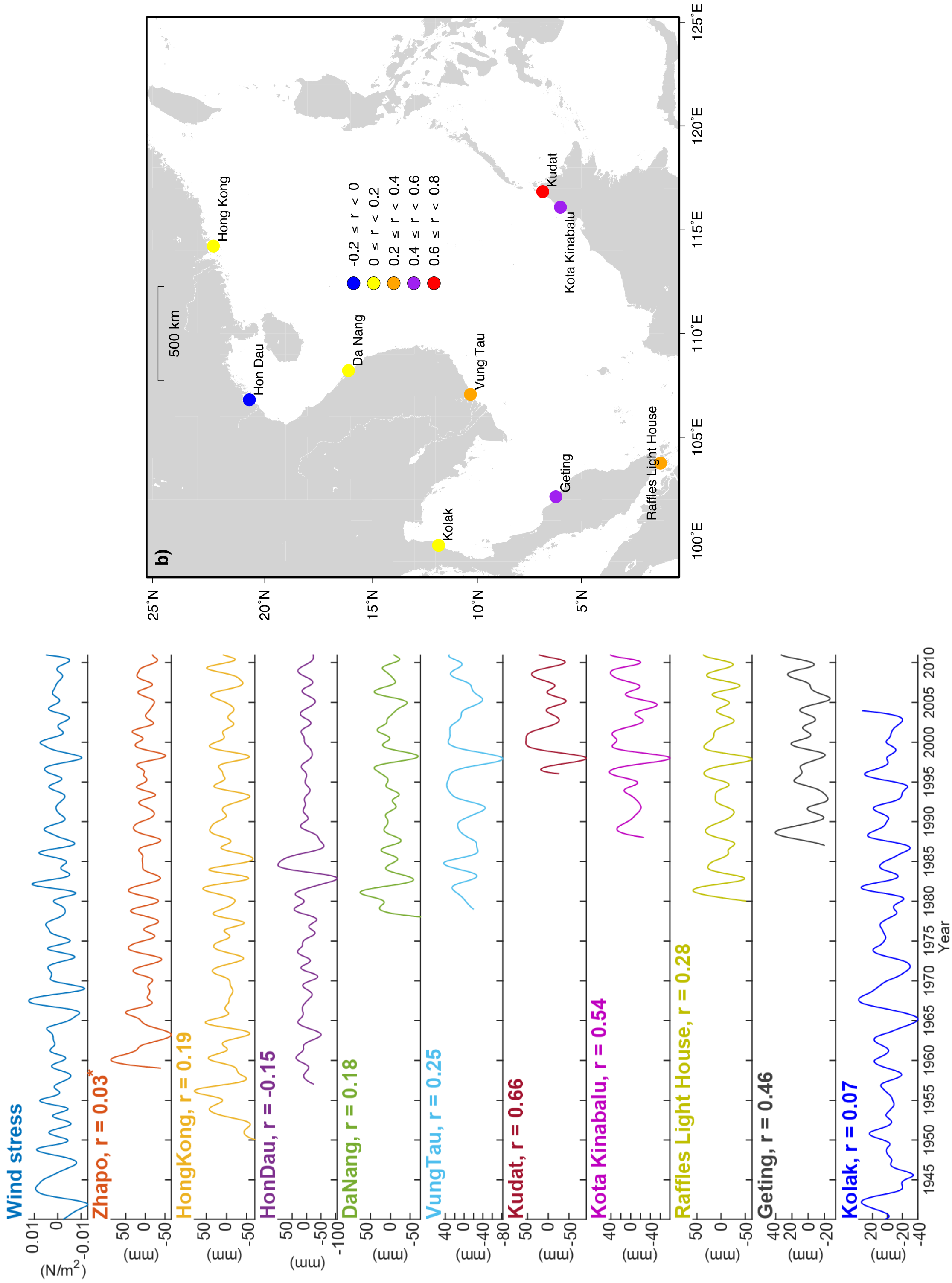

Figure 3. 7: (a) Relative sea levels at the southern tide gauges correlate highly to wind stress at interannual time scales. Statistically insignificant correlations are marked with asterisks. Significance test is based on the *t-test* at 95% confidence level. (b) Geographical distribution of wind stress - sea level correlations over the SCS. Note that only tide gauges with statistically significant correlations are plotted.

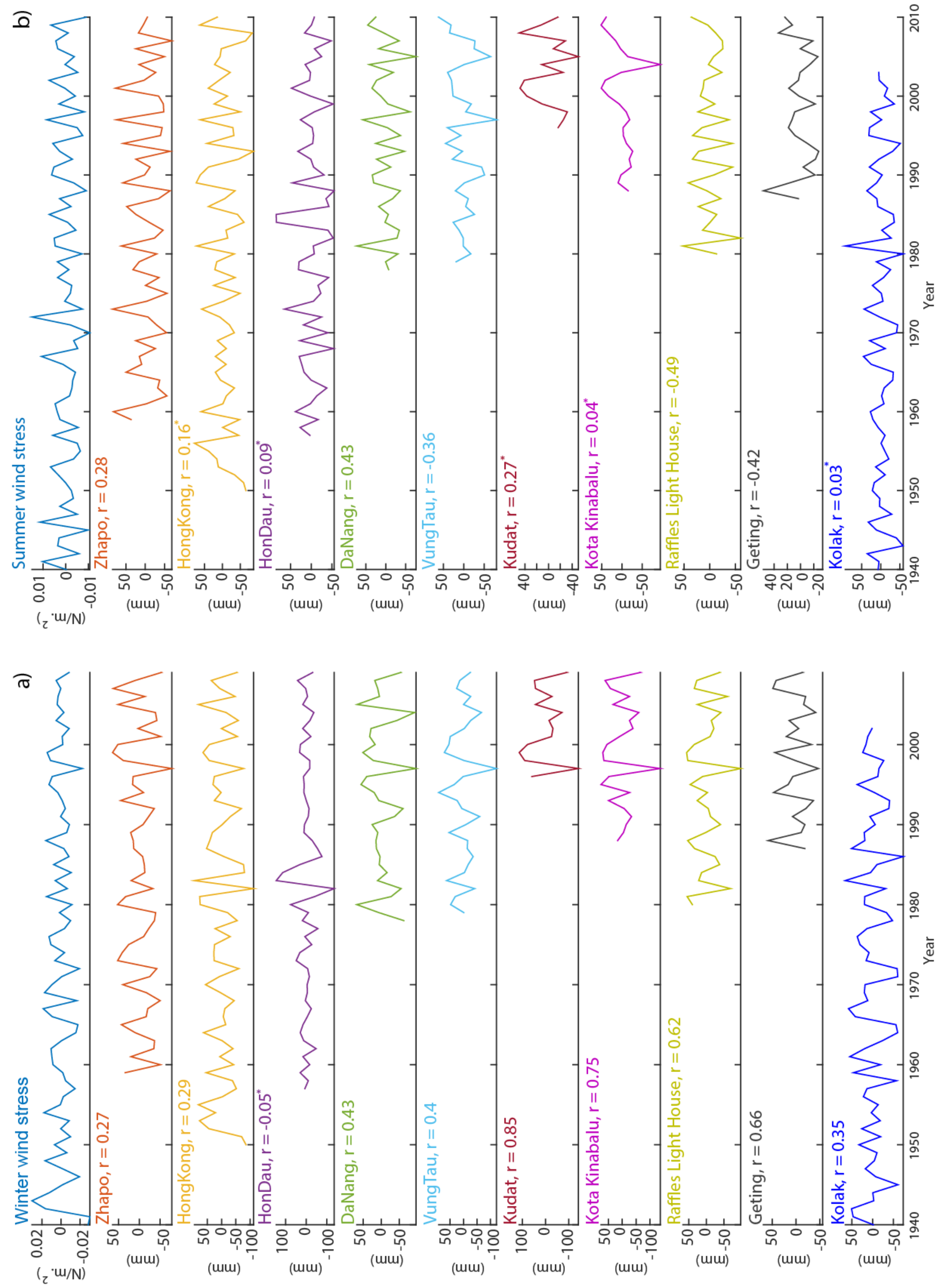

Figure 3. 8: Sea level variation at the southern tide gauges are more highly correlated to wind stress in the winter (a) as compared to the summer season (b). The seasonal mean time series were filtered by EEMD/HHT prior to cross-correlation analysis. Statistically insignificant correlations are marked with asterisks. Significance test is based on the *t-test* at 95% confidence level.

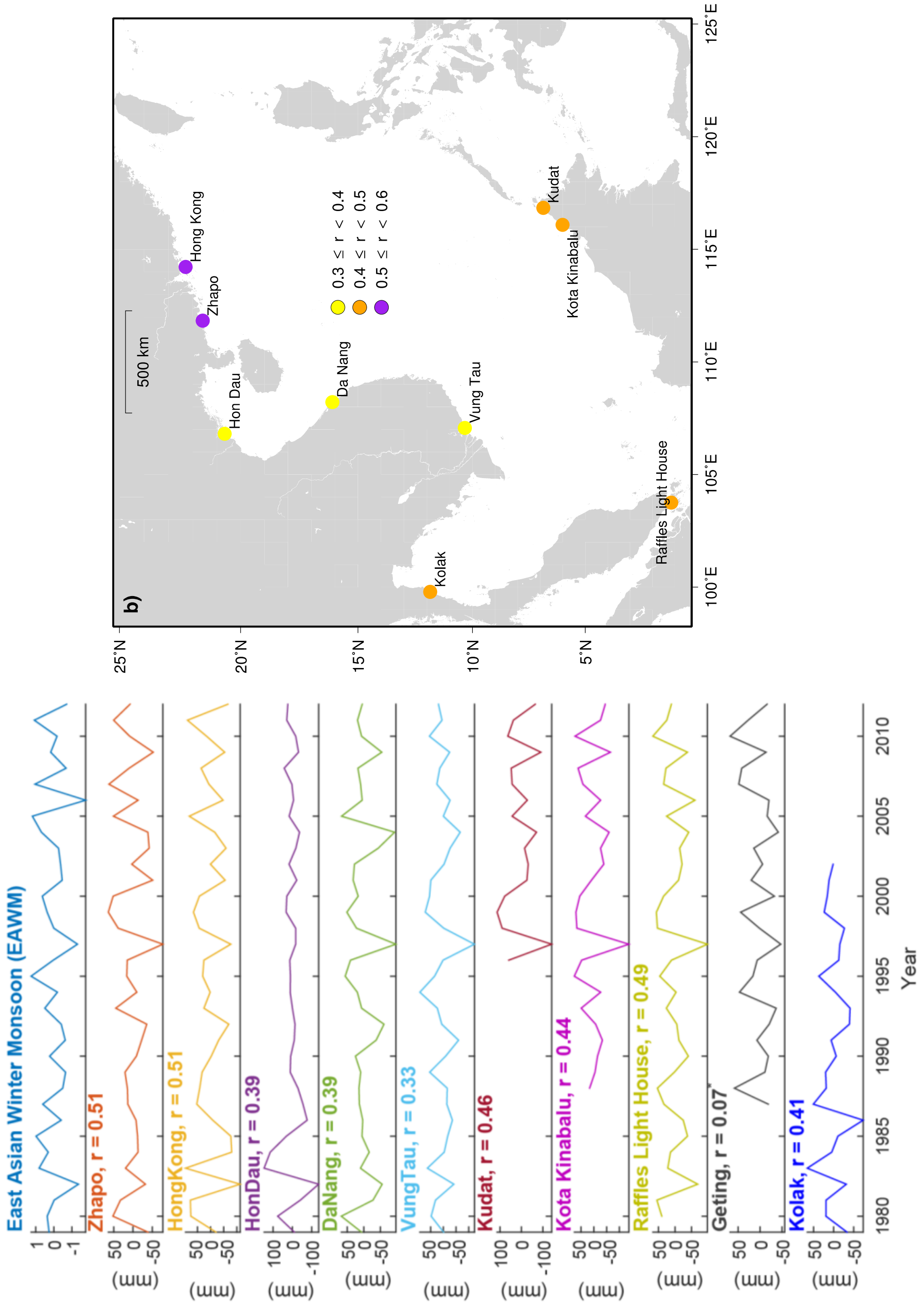

Figure 3. 9: (a) The East Asian Winter Monsoon index (EAWM) is highly correlated to relative sea levels recorded at the northern tide gauges. The seasonal mean of EAWM and relative sea levels were filtered by EEMD/HHT prior to cross-correlation analysis. Statistically insignificant correlations are marked with asterisks. Significance test is based on the *t-test* at 95% confidence level. (b) Geographical distribution of EAWM - sea level correlations over the SCS. Note that only tide gauges with statistically significant correlations are plotted.

3.4.3. The role of Luzon Strait Transport (LST)

Compared to ENSO and monsoonal winds, the role of LST in interannual sea-level variations at local TGs is minor with small positive correlation coefficients (at zero lag) (Fig. 3.10a). The highest correlation is seen at the Vung Tau tide gauge ($r = 0.37$) (Fig. 3.10a). Note that the negative values of volume transport are equivalent to westward transport (i.e., into the SCS interior) and positive values represent eastward transport (i.e., out of the SCS).

The lack of correlation of the LST with sea level around the SCS implies that LST does not directly affect sea level at coastal TGs on the SCS's shallow continental shelf (with depths <200 m). The LST, however, could play a role as a conveyor carrying more ENSO signals during its mature phase from the Pacific into the SCS [*Qu et al.*, 2009, Fig. 1]. During the El Niño phase, LST is more active, and transports more low-temperature sea water westward, producing strong cooling advection in the SCS, and that, in turn, results in the relative fall of sea level. This ENSO-associated correlation pattern can be seen in our results for two ENSO episodes in 1982/83 and 1997/98 (Fig. 3.10).

The highest correlation of the LST to the tide gauge at Vung Tau can be explained by the site’s geographical proximity to the SCSTF pathway. This condition may considerably contribute to significant sea level fall at this tide gauge (Fig. 3.10).

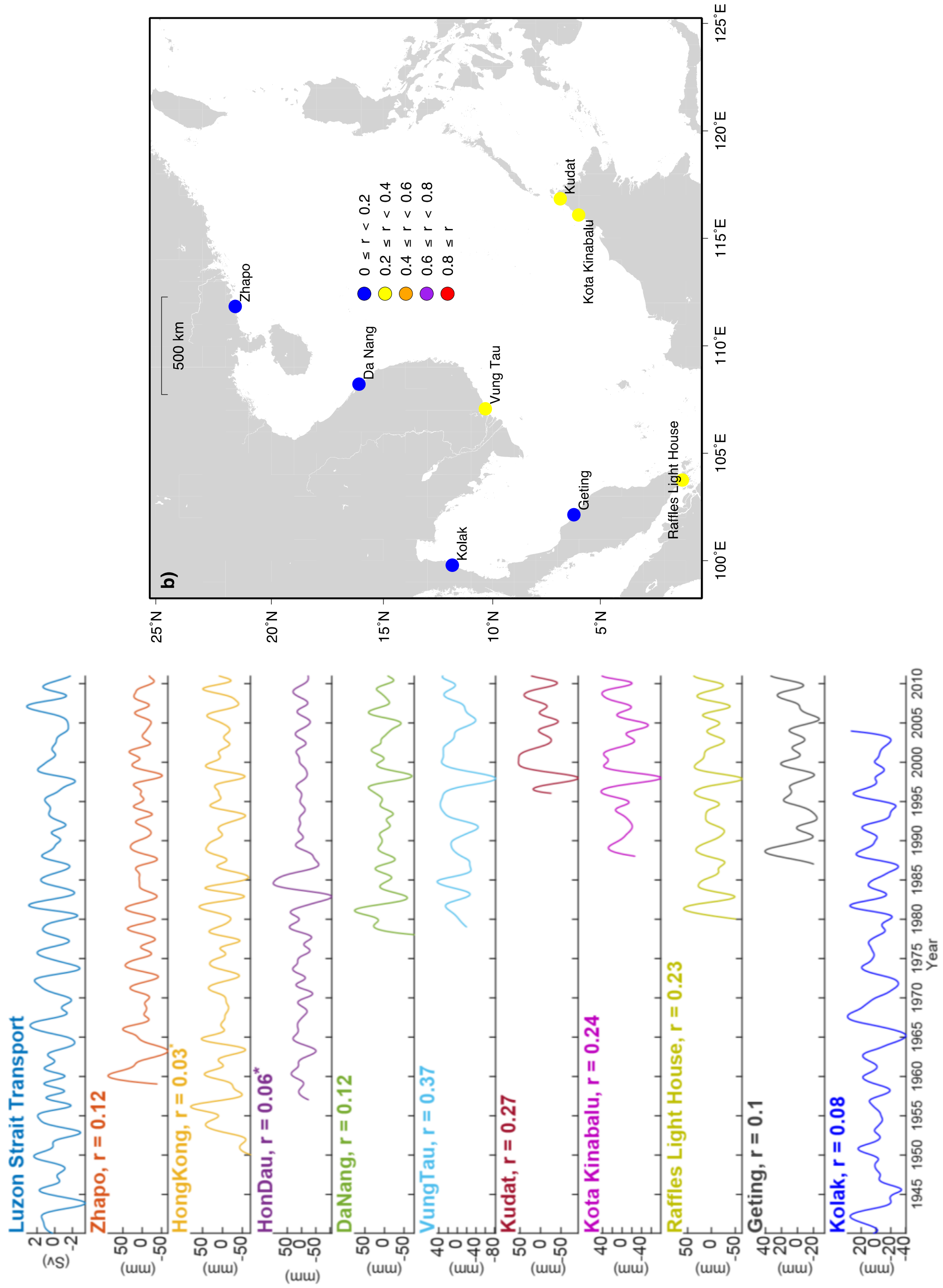

Figure 3. 10: (a) Sea levels correlate weakly to the Luzon Strait Transport (LST) at interannual time scales. Statistically insignificant correlations are marked with asterisks. Significance test is based on the *t-test* at 95% confidence level. The dashed line indicates the transport direction of LST (see the text). Statistically insignificant correlations are marked with asterisks. (b) Geographical distribution of LST-sea level correlations over the SCS. Note that, only tide gauges with statistically significant correlations are plotted.

3.4.4. The contribution of different forcings on sea-level variations

The result shows that the largest variance explained by the linear regression model is seen at Raffles Light House and the southeast TGs with adjusted-R^2 = 70%, whereas the average explained variance of other TGs is only about 30% (Fig. 3.11, Supp. Info. Table S3.1). The lowest value from the linear model is found at the Kolak tide gauge with adjusted-R^2 = 9% (Fig. 3.11, Supp. Info. Table 3.1). In most of the TGs, ENSO explains the majority of sea-level variance (~ 60-80% of adjusted-R^2), with the exception of Kolak (30%) and Geting (46%) (Fig. 3.11, Supp. Info. Table S3.1). This result is consistent with the correlation analyses above and implies that ENSO is the greatest contributor to sea-level variations in the region. An important point to note is that, we did not eliminate statistically insignificant predictor variables that come out from the linear regression model (as in previous studies). The reason is that insignificant variables might share explained variance with other significant variables, and if the significance rule is applied, we may leave out their important explanatory power (Ulrike Groemping, personal communication).

In the relation to the explained sea-level variance, without considering Raffles Light House and two southeast TGs, we found that the linear regression model is unable to describe 50% to 75% of sea-level variance at TGs around the SCS (Fig. 3.11, Supp. Info. Table S3.1). This tendency suggests that either the linear model is not good enough to explain all explanatory power of predictor variables or there are other forcings that control the interannual sea-level variations in different parts of the study area. The latter explanation is probable, considering the high proportion of explained variance at Raffles Light House and southeast TGs. Thus, further and more detail investigations should be carried out in the future to fully account for forcings of interannual sea-level variations around the SCS.

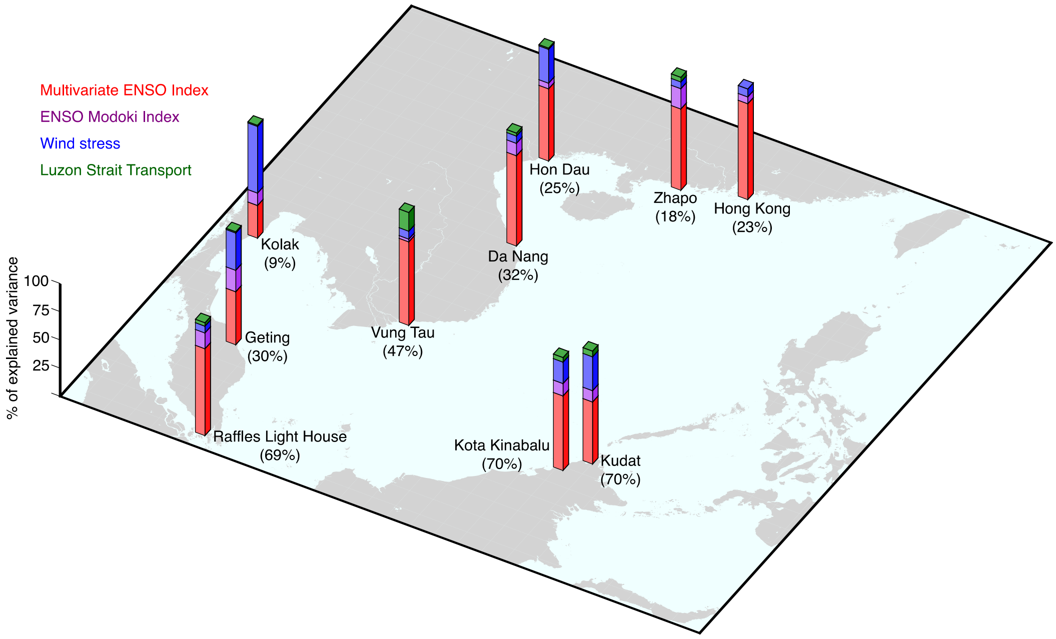

Figure 3. 11: At all tide gauges, ENSO accounts for the biggest portion of sea-level variance. At Raffles Light House, Kota Kinabalu and Kudat, the multiple linear regression model explains sea-level variance most clearly (~ 70%). The numbers in parentheses represent % of total sea-level variance explained by the model. All predictor variables are normalized to sum 100% for the ease of comparison.

3.5. Conclusion

In this study, we have investigated the interannual variability of sea levels at local TGs around the South China Sea using an Ensemble Empirical Mode Decomposition (EEMD) technique followed by other statistical analyses. The results indicate that EEMD is able to capture the interannual mode of sea-level data. Our analyses show that ENSO is a major forcing and a large contributor to sea-level variations in the study area at interannual scale. This climate mode's influence, however, varies significantly according to geographical location. In contrast, we were not able to see the significant linkage between sea level and ENSO Modoki, suggesting alternative approaches might be more appropriate to find out the correlation.

Our results also provide new insights into monsoon-driven sea-level variability. We found that the mean sea level in the north of the SCS is greatly influenced by the strength of the winter monsoon and the inverted barometer effect, and the winter mean of sea levels in this region seems to be amplified by recent intensification of the East Asian Winter Monsoon. In the southern part of the SCS, basin geometry and local geography may lead to sea-level rise in the winter monsoon season and sea-level fall during the summer monsoon season, resulting in sea-level fluctuations on an interannual scale.

The present study demonstrates the spatial distributions of large-scale oceanic-climatic variability on the interannual relative sea-level variations in the SCS. This confirms the need of regional sea-level studies in which the oceanic and climatic changes are extremely important. Such studies would be very valuable for the better understanding sea-level changes and preparation for coastal risks.

Acknowledgements

This research was supported by grants from National Research Foundation Singapore (National Research Fellow Award No. NRF-RF2010-04) and the Singapore Ministry of Education under the Research Centres of Excellence initiative and Academic Research Fund (AcRF) Complexity Tier 1 Project RGC4/14 “Preparing Asian mega cities for changing climate and the potential Increase in extreme sea levels and storm surges”. EH was supported by NRF Award No. NRF-NRFF2010-064. We acknowledge the Permanent Service for Mean Sea Level for tide gauge data; Zhaohua Wu and Norden E. Huang for the Matlab package EMD/EEMD (http://rcada.ncu.edu.tw/research1.htm) and Aslak Grinsted for the wavelet toolbox (http://www.glaciology.net/wavelet-coherence). We thank Hoang Trung Thanh (Vietnam Marine Hydrometeorological Centre) for providing data for Hon Dau, Da Nang and Vung Tau tide gauges. We appreciate Wang Lin for his guidance on the East Asian Winter Monsoon index. We are grateful to Wang Dongxiao and Liu Qinyan for their help and discussion on Luzon Strait Transport calculation. We would like to express our thanks to Pavel Adamek and Constance Chua for their linguistic advice that significantly improved this manuscript. This work comprises Earth Observatory of Singapore contribution No. 124.

Supporting Information

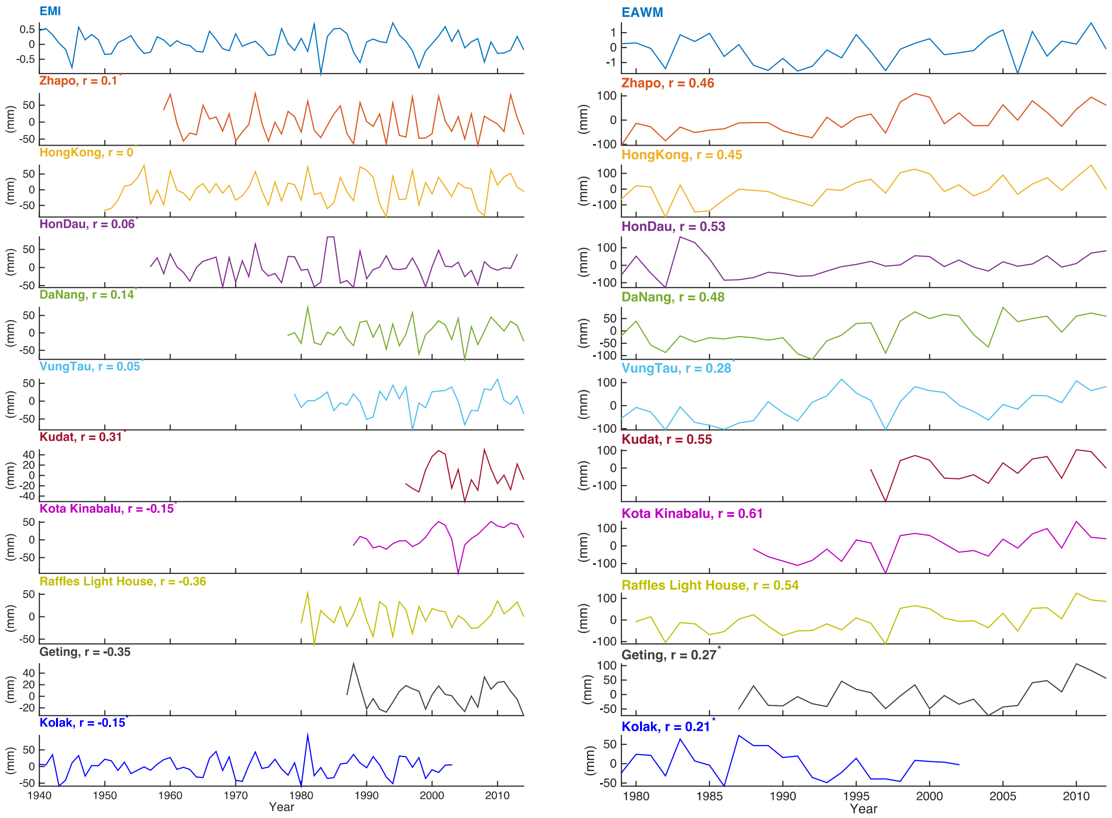

Figure S3. 1: a) Weak correlations between ENSO Modoki Index and sea levels were recorded at tide gauges in summer season. The seasonal mean time series were filtered by EEMD/HHT prior to cross-correlation analysis. Significance test is based on the *t-test* at 95% confidence level. Statistically insignificant correlations are marked with asterisks. b) Cross-correlation analysis between the yearly values of the EAWM and winter mean sea levels (no filtering with EEMD/HHT but the mean is removed). The seasonal mean time series were filtered by EEMD/HHT prior to cross-correlation analysis. Significance test is based on the *t-test* at 95% confidence level. Statistically insignificant correlations are marked with asterisks.

Table S3. 1: Normalized relative contribution of each forcing to total sea-level variance

Tide gauges	**% sea-level variance explained**				**Upper value at 95% confidence level**				**Lower value ast 95% confidence level**			
	MEI	EMI	WS	LST	MEI	EMI	WS	LST	MEI	EMI	WS	LST
Zhapo	72	17	6	4	57	9	4	1	82	29	12	12
Hong Kong	85	6	7	2	78	3	5	1	89	12	12	5
Hon Dau	64	5	30	1	52	3	21	1	72	12	40	4
Da Nang	80	11	6	2	69	6	4	1	84	17	14	7
Vung Tau	74	2	7	17	66	1	4	10	81	5	11	25
Kudat	55	10	30	5	48	4	21	2	61	21	37	9
Kota	66	11	19	4	60	5	12	1	70	20	27	9
Raffles	77	14	6	3	69	8	4	1	82	21	10	7
Geting	46	19	33	1	35	9	23	0	57	31	44	6
Kolak	29	11	59	1	15	2	34	1	46	28	74	11

MEI: Multivariate ENSO Index

EMI: El Nino Modoki Index

WS: Wind stress

LST: Luzon Strait Transport

Chapter 4:

Spatio-temporal variation of extreme sea level around the South China Sea using the Dynamic Linear Model for the Generalized Extreme Value distribution

---

(to be submitted to the *Journal of Geophysical Research: Oceans*)

Dat T. Pham[1,2], Adam D. Switzer[1,2], Gabriel Huerta[3], Aron J. Meltzner[2], Huan M. Nguyen[4] and Emma M. Hill[1,2]

[1]*Asian School of the Environment, Nanyang Technological University, Singapore 639798*

[2]*Earth Observatory of Singapore, Nanyang Technological University, Singapore 639798*

[3]*Department of Mathematics and Statistics, University of New Mexico, NM 87131-0001, USA.*

[4]*Department of Oceanography, Vietnam National University, Hanoi, Vietnam*

Abstract:

With sea level projected to rise as a result of climate change, it is imperative to understand not only long-term regional average trends, but also the spatial and temporal patterns of extreme sea level (ESL). In particular, the low-lying and densely populated margins of the South China Sea (SCS) are vulnerable and frequently exposed to flooding events, yet the few studies that have examined ESL are mostly confined to short periods or small areas. In this study, we use a comprehensive set of 30 tide gauges (TGs) spanning 1954–2014 to characterize the spatial and temporal variations of ESL around the SCS. We also explore the long-term evolution of ESL by applying a Dynamic Linear Model for the Generalized Extreme Value distribution (DLM-GEV). Our results show that the maxima distributions of sea level from the entire records range from ~ 900 to 4000 mm and occur seasonally in both the northern and southern SCS. In general, the sea level maxima at northern TGs are approximately 25-30% higher than those in the south and are highest in summer as tropical cyclone induced surges dominate the northern signal. In contrast, the smaller signal in the south is dominated by monsoonal winds in the winter. In the longer-term, the linear trends of ESL are broadly consistent with the changes in mean sea level (MSL). The DLM-GEV model clearly characterizes the interannual-decadal variability of ESL and hence, the 50-year return levels at most TGs in the region. When we compare our dataset with various climate and monsoon indices for the region we find significant (although small) correlations between ESL and both the Pacific Decadal Oscillation (PDO) and El Niño / Southern Oscillation (ENSO). Our study provides new insight into variability of ESL in relatively little studied area of the SCS, which profoundly contributes to preparing for coastal risks at multidecadal timescales.

Key words: extreme sea level, tide gauge, South China Sea, tropical cyclones, monsoons, DLM-GEV distribution.

4.1. Introduction

Extreme sea level (ESL) events arise from a variety of phenomena, including storm surges, seiches and meteorological and other tsunamis. At the scale of hours to days, most extreme sea level commonly results from tropical and extra-tropical cyclones [*Gönnert et al.*, 2001]. At higher-frequencies of minutes to hours, tsunamis, 'meteotsunamis', infragravity waves, and seiches can also raise sea level well above normal tidal levels [*Ozsoy et al.*, 2016]. Regardless of timeframe or driver, ESL events are a major contributor to coastal flooding in many locations globally [see *Ozsoy et al.*, 2016 and references therein]. Meteorologically-driven surges and seiches may behave differently under global climate change as storms, the key driver of meteorological surges, are likely to change in intensity, frequency, duration, and path (IPCC AR5, *Church et al.* [2013]). To prepare for such variability there is a clear need for improved assessments of surge events and accompanying ESL. For low-lying, highly-developed and densely-populated coastal areas, understanding the variability of ESL is at least as important as understanding trends in relative mean sea level (RMSL), as the amplitude of ESL can reach meters locally [*Lowe et al.*, 2010]. While there have been extensive studies of trends in RMSL both globally and regionally [e.g., *Church and White*, 2006; *Church and White*, 2011; *Jevrejeva et al.*, 2006; *Slangen et al.*, 2016; *White et al.*, 2014], patterns of ESL are less well studied.

A primary challenge comes from the lack of accessible high-frequency tide-gauge data (at hourly or even shorter intervals) [*Lowe et al.*, 2010]. The underlying importance of ESL is reflected in the rising number of ESL studies at a global scale [*Mawdsley and Haigh*, 2016; *Menéndez and Woodworth*, 2010; *Woodworth and Blackman*, 2004] or with a regional focus, in places such as U.S. coasts [*Wahl and Chambers*, 2015, 2016]; the Caribbean Sea [*Torres and Tsimplis*, 2014]; Southern Europe [*Marcos et al.*, 2009]; Bangladesh [*Lee*, 2013]; the eastern coast of China [*Feng and Tsimplis*, 2014]; and Australia [*Haigh et al.*, 2014a; *Haigh et al.*, 2014b].

Large variability in ESL (spatial maxima distributions and temporal changes) tends to arise in stormy regions, where large-scale atmospheric forcing exists, as highlighted in a number of the aforementioned studies. However, sea-level extremes are not always caused by storminess but can also result from ocean eddies [e.g., *Firing and Merrifield*, 2004], extreme tides [e.g., *Haigh et al.*, 2011], or other ocean phenomena. In other words, ESL variability in regions consisting of a complex air-sea coupled climate system commonly results in complicated ESL histories. In this study, we will present analysis of ESL in such an area: the South China Sea, the largest semi-enclosed marginal sea in the western Pacific [*Wyrtki*, 1961].

The South China Sea (SCS) region is densely populated and highly exposed to coastal hazards [*Neumann et al.*, 2015]. It is frequently affected by tropical cyclones, particularly north of 12^{o}N in boreal summer *Wang et al.* [2007]. In addition, the SCS experiences seasonal monsoonal winds that reverse direction from winter (the northeast monsoon) to summer (the southwest monsoon) [see a review in *Wang et al.*, 2009]. Given the dominance of climatically driven ESL globally it is important to investigate how these basin-wide atmospheric forcings affect ESL distributions around the SCS. Few studies in the region have paid attention to ESL variability in the study area but they are all locally focused. For example, *Chen et al.* [2012] and *Tkalich et al.* [2013] studied high surges (from sea level anomalies) in response to monsoonal winds, yet each of those studies focused on only a few TGs spanning a small area, over a short time period. More recently, *Feng and Tsimplis* [2014] mapped ESL distribution and calculated the changes of ESL focusing on the eastern coast of China although they included some TGs in the northern SCS and one tide gauge on the Vietnamese coastline. Yet, the lack of TGs in the south of the SCS prevents a full view of ESL variations in the study area. Furthermore, the researchers did not attempt to examine seasonal changes in ESL.

Coastal protection and adaptation require an assessment of return levels in given return periods. For example, the 100-year return level is defined as the level expected to be exceeded once in 100 years [*Coles*, 2001]. To do that, the Generalized Extreme Value (GEV) or Generalized Pareto Distribution (GPD) are extreme value probability distributions [*Coles*, 2001] that provide a statistical method to generate the return level curves according to a desired return period (e.g., the return level associated with a 100-year return period). Such extreme value distributions are commonly based on the assumption of stationarity which means that all parameters (e.g., the location, scale and shape parameters of GEV distribution) remain unchanged over time. However, climate change very likely lead to more frequent or intense storms that can alter the return levels of ESL. Such changes will invariably affect the predefined design levels for coastal infrastructure. As highlighted by *Wahl and Chambers* [2015], the widely-used method in which the future return levels are obtained by adding the expected mean sea level to current return levels has limitations as this approach does not account for non-stationary changes in ESL, biasing the estimations of return levels. Recent studies find strong evidence that ESL exhibits multi-decadal variability at local [e.g., *Talke et al.*, 2014], regional [e.g., *Wahl and Chambers*, 2015] and global [*Marcos et al.*, 2015] scales. These studies and others suggest a need to unravel the time-varying signals of ESL in order to forecast meaningful return levels.

In this study, we used a comprehensive tide-gauge data set of 30 tide gauges (TGs) from around the SCS (Fig. 1) to examine three main goals:

1) mapping the spatial distributions of ESL around the SCS over the entirety of the sea-level records, and in both the summer and winter seasons;

2) investigating the long-term trends of ESL; and

3) characterizing variability of ESL and its associated return levels over time at each site.

To the best of our knowledge, there has been no comprehensive ESL study in the SCS so far. In the present study, we are only concerned about high extremes (i.e., sea-level maxima).

To capture the time-varying evolution of ESL in sea-level records throughout the SCS, we use the Dynamic Linear Model (DLM) [*West and Harrison*, 1997]. The DLM model allows us to capture non-stationary behaviors in the data even with gaps. A detailed description of the DLM model will be presented in section 3. We describe the data sets used in this study in section 2 and discuss our major results in section 4. Finally, section 5 provides a summary and discussion of our key findings.

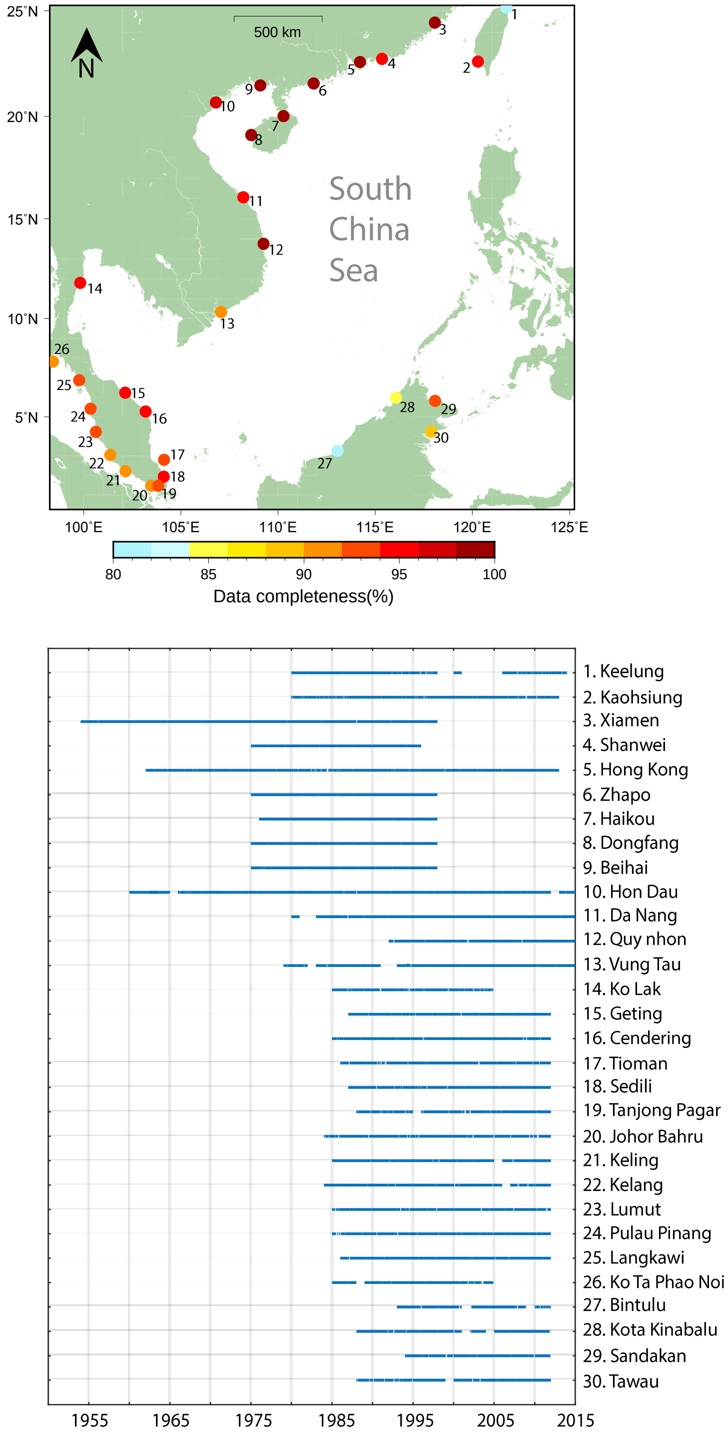

Figure 4. 1: (a) Location of tide gauges (coloured dots) in the South China Sea. The colour indicates the percentage of the completeness over time span of each site after processing. Available data lengths and data gaps (after processing) at each tide gauge from the UHSLC website.

4.2. Sea-level records

To study ESL, we complied a data set of hourly sea-level records from 30 TGs around the SCS (Fig. 1a). The periods of the various sea-level records differ and span between 1960 and 2014 (Fig. 1b). We chose records spanning at least 18-20 years to reduce the effect of the 18.6-year nodal cycle on long-term trend calculations [*Pugh and Woodworth*, 2014]. Twenty-six out of 30 quality-controlled sea-level records (research quality data) were obtained from the University of Hawaii Sea Level Center (UHSLC, available at http://uhslc.soest.hawaii.edu/data/?rq.). Sea-level data from four additional TGs along the Vietnamese coastline (Hon Dau, Da Nang, Quy Nhon and Vung Tau) were sourced from the Vietnam Marine Hydrometeorological Center, which had more complete data sets than the UHSLC for those sites.

Hourly sea-level data at Hong Kong was merged from two records: North Point (from 1962 – 1985) and Quarry Bay (from 1986 – 2012). These two TGs are not far away from each other (~ 500 m) and use the same datum reference with a small offset (~ 1.02 cm); hence, they can be used to form a continuous sea-level record [*Ding et al.*, 2001; *Feng and Tsimplis*, 2014].

ESL studies require careful data checking throughout the sea-level records to avoid having unreal extreme events [*Marcos et al.*, 2015; *Pugh and Woodworth*, 2014]. We inspected each tide gauge record in our data set in detail, as commonly done in ESL studies elsewhere [e.g., *Feng and Tsimplis*, 2014; *Marcos et al.*, 2015; *Torres and Tsimplis*, 2014; *Wahl and Chambers*, 2015]. Firstly, we ran the Tide Model Driver (v2.04) (TMD, a Matlab toolbox available from http://polaris.esr.org/ptm_index.html) to check the time shift at the beginning of each observed record (we found time-shift errors at Hon Dau tide gauge and corrected them accordingly). For each sea-level record, we only kept years having at least 75% data completeness because data gaps may affect the tidal analysis and hence extreme-event detection [e.g., *Wahl and Chambers*, 2015]. We then extracted tidal signals based on observed hourly sea levels by using the UTide program [*Codiga*, 2011]. This tide package is capable of dealing with uneven and gappy sea-level records. More importantly, the UTide program allows for analysis of a complete tidal record without a need to separately analyze individual years, as in other well-known tidal packages including T_TIDE [*Pawlowicz et al.*, 2002] and R_T_TIDE [*Leffler and Jay*, 2009]. The original observed sea levels and non-tidal residuals were plotted month-by-month for each calendar year in order to visually check and remove any suspect spikes, sudden jumps and datum shifts. At this step, we eliminated 16 years of data at Quy Nhon tide gauge (from 1976 – 1991), and one-year of data at each of Hon Dau (1965), Shanwei (1997) and Keelung (2004).

For TGs along the Malay-Thai Peninsula, the effect of the 2004 M_W 9.2 Sumatra-Andaman earthquake and resulting tsunami must also be considered. Although tsunami-induced values are ESL changes, they are not climate-related signals, and thus are not within the scope of our study. Taking this into account, we removed data recorded during 26/12/2004 from sea-level records at Langkawi, Lumut and Pinang. In addition, we discarded data from that date onwards at Ko Lak and Ko Taphao Noi TGs, because *Amiruddin et al.* [2015] found a large discrepancy in detrended monthly mean sea level data at these TGs before and after the 2004 earthquake.

4.3. Data acquisition

After checking and correcting the data sets, we used quality-controlled sea level records at each tide gauge to form various data subsets as described as follows:

Firstly, we removed the effect of RMSL by subtracting the 30-day running median from the original sea-level record. Here, the median was chosen instead of the mean due to its ability to reduce the impact of outliers [e.g., *Wahl and Chambers*, 2015]. Moreover, the use of 30-day running median eliminates not only the centennial trend but also removes the seasonal cycle from the sea-level records [*Mawdsley et al.*, 2015]. The seasonal cycle should be excluded from sea-level records because it may contain seasonal signals from a variety of processes such as: changes in sea water density, air pressure and winds or even run-off for TGs nearby large river mouth [*Pugh and Woodworth*, 2014]. Also, the seasonal cycle includes the two long-period tidal constituents: annual ($\boldsymbol{S_a}$) and semi-annual ($\boldsymbol{S_{sa}}$) of which have annual amplitudes varying from a few to tens of cm around the SCS [*Amiruddin et al.*, 2015; *Tsimplis and Woodworth*, 1994]. We then identified the highest value from the remaining sea-level record, which is free of RMSL and seasonal cycle, at each tide gauge. This set of highest sea-level values will be referred to SL_{max}. We also calculated the non-tidal residuals by subtracting the tidal prediction (from UTide program) from the de-trended sea-level records. We refer the non-tidal residual data sets to *NTRs*.

Secondly, we calculated annual and seasonal extreme percentiles of sea level following a procedure that has been extensively used in other ESL studies [e.g., *Torres and Tsimplis*, 2014; *Wahl and Chambers*, 2015; *Woodworth and Blackman*, 2004]. Here, we chose the 99.5th percentile to present in this study because it reliably represents for ESL compared to other percentile levels. For instance, the 99.9th percentile consists of only the eight or so highest hourly measurements in a calendar year and hence would provide limited data for regional comparison. In contrast, the 95th and 99th percentile levels may suppress some extreme events [*Woodworth and*

Blackman, 2004]. At this step, we computed 99.5th sea-level percentiles in three cases: from the raw hourly sea-level data (hereafter, this set will be referred to as SL_{995}), from hourly sea-level data without impact of RMSL (hereafter, this set will be referred to as $SL_{995freeMSL}$) and from hourly sea-level data without RMSL and tides (hereafter, this set will be referred to as $SL_{995freeMSL\_tide}$). To obtain the $SL_{995freeMSL}$, we used the same free-of-RMSL sea-level records as described in the SL_{max} calculation and then calculated the 99.5th percentile of sea level. For the $SL_{995freeMSL\_tide}$, we first used the UTide program to predict tidal oscillations at each TG and then computed the 99.5th percentile of tidal predictions. We next subtracted those percentiles from the $SL_{995freeMSL}$ to form sea-level percentile data sets which is free of RMSL and tidal components - $SL_{995freeMSL\_tide}$.

Thirdly, we identified skew surge (SK) values for each sea-level record. While the traditional *NTRs* have been widely used to assess ESL, the skew surges (SKs) have been used increasingly as an indicator for storminess [e.g., *Dangendorf et al.*, 2014; *Haigh et al.*, 2015; *Mawdsley and Haigh*, 2016]. A SK is defined as the difference between the highest observed sea level and the highest tidal prediction in a tidal cycle without considering timing between them [*Horsburgh and Wilson*, 2007]. Hence, for each tidal cycle, only one SK value exists. The use of SK likely avoids timing errors in sea-level records and serves as “an integrated and unambiguous measure of the storm surge” [*Haigh et al.*, 2015, p.4].

As described above, there is only one SK value in each tidal cycle. Consequently, the number of SK values in each record relies on the tidal regime at each site. For instance, in a calendar year, there are ~ 352 SK values for diurnal tides whereas the number at semi-diurnal TGs is ~ 705 [*Batstone et al.*, 2013; *Mawdsley and Haigh*, 2016]. We found the predicted high tide from a tidal cycle and then detected the largest local maxima of observed sea levels within a 3-hour time window before and after the predicted high tide. The chosen time window allows us to obtain the majority of the SK values [*Mawdsley and Haigh*, 2016]. However, detecting SK values becomes more complicated in sites exhibiting complex tidal characteristics [e.g., *Wahl and Chambers*, 2015]. In some cases, we found that tidal prediction produced more high tides within a tidal cycle leading to an inaccurate SK calculation. Thus, we set a "minimum distance" between two high tides to avoided including untrue high tide in a tidal cycle and hence, accurately captured SK values. The "minimum distance" depending on tidal regime: 6.5 hours for semi-diurnal and mixed with mainly semi-diurnal tides (i.e., half of a tidal cycle ~ 12 hours 25 minutes), and 13 hours for diurnal tides and mixed with mainly diurnal tides (i.e., half of a tidal cycle ~ 24 hours 50 minutes). The SK time series were then derived by subtracting the predicted high tide from the highest observed sea level within each cycle (hereafter, *SKs*). We note that the number of points in each SK data set is much smaller than that of the raw sea-level records; therefore, we only calculated the 95th percentile level for the SK time series for our long-term trend study (hereafter, the set of SK values above the 95th percentile will be referred to as SK_{95}). Higher percentile levels (e.g., the 99.5th percentile, which contains only few highest values), may produce large deviations [*Wahl and Chambers*, 2015].

To study seasonal ESL, we repeated the same calculations SL_{max}, SL_{995}, $SL_{995freeMSL}$, $SL_{995freeMSL\_tide}$ and SK_{95}, separately for the summer and winter seasons. We defined the summer season for the region to be April to September, and the winter season to be October to March. Our season definitions allowed to include extreme events that might otherwise not occur within boreal summer or boreal winter around the study area.

Fourthly, we generated time series of the five highest values per year (or block maxima), which are then considered as five extreme events, for hourly *NTR* values (calculated by subtracting tidal predictions from the free-of-RMSL observed sea levels) and the SK time series (as defined above). In order to ensure that each extreme event is independent of others in the same calendar year, a separation between them was required. A separation of 72 h has been widely used [e.g., *Marcos et al.*, 2015; *Marcos et al.*, 2009]. However, *Feng and Tsimplis* [2014] find that the effect of a tropical cyclone on sea-level records in the East China Sea and northern part of the SCS might last 80 h on average and hence, they suggested a separation of 120 h between extreme events. In the present study, we used the longer independent separation criterion of *Feng and Tsimplis* [2014] for the entire SCS. We then referred two extreme time series for NTR and SK to NTR_{max} and SK_{max}, respectively.

4.4. Method

4.4.1. Long-term trend calculations

We used the least squares regression (LS) method to calculate the long-term trends for the SL_{995}, $SL_{995freeMSL}$, $SL_{995freeMSL\_tide}$ and SK_{95} data sets for both the full data sets and the seasonal data sets. The sea-level observation equation is described as follows:

$$y(t) = a + bt + \varepsilon \qquad (4.1)$$

where a and b are regression coefficients, a is the intercept, b is the slope of the line or linear trend, ε is the error term and t represents in years.

One issue which may arise as a consequence of the use of the LS method is that the standard errors of the estimated coefficients might not be accurate due to the presence of autocorrelation (a.k.a. serial correlation) in the residuals, with the result being that the estimated *b* regression coefficients from the observation equations (4.1) could remain unchanged on the one hand, while the standard errors need to be corrected [*Baum*, 2006]. To avoid that, we conducted the Durbin-Watson test [*Durbin and Watson*, 1950, 1951, 1971] for each sea-level record, based on the residuals estimated by LS from equation (4.1), to detect the autocorrelation. The Durbin-Watson d-statistic test is described as below:

$$d = \frac{\sum_{t=2}^{N}(r_t - r_{t-1})^2}{\sum_{t=1}^{N} r_t^2} \tag{4.2}$$

where N is the number of observations and r_t is the residual at time *t*.

We then corrected the standard errors of estimated coefficient of sea-level records having autocorrelation in the residuals, by using the Newey-West Estimator [*Newey and West*, 1987]. This is a heteroscedasticity and autocorrelation consistent covariance matrix estimator that can deal with not only the presence of autocorrelation but also the heteroscedasticity in the data. The key step for this estimator is to compute a lag selection parameter or bandwidth *m*. In this study, we selected an automatic and nonparametric lag selection procedure developed by *Donald and Monahan* [1992] and enhanced by *Newey and West* [1994]:

$$m = 4 \times \left(\frac{N}{100}\right)^{\frac{2}{9}} \tag{4.3}$$

where N is the number of observations. The rate of each trend at each site was then calculated and tested at the 90% confidence level.

4.4.2. Time-varying model for extreme sea levels

Each of the two data sets *NTR*$_{max}$ and *SK*$_{max}$ can be represented as $Y_{max} = \{y_{m,1}, y_{m,2}, \dots, y_{m,n}\}$, where m is the number of extreme values in each year and n is the number of years for each sea-level record. In other words, $y_{m,i}$ is a vector of the m highest values in year i; in our study, $m = 5$, and Y_{max} is the combined vector of the five highest values recorded in each year. Assuming that $y_{m,i(i=1,2,\dots,n)}$ are independent and identically distributed random variables, Y_{max} then is considered following the Generalized Extreme Value (GEV) distribution [*Coles*, 2001, p.47-48] as presented below:

$$GEV(Y|\mu,\sigma,\xi) = exp\left\{-\left[1 + \xi\left(\frac{Y-\mu}{\sigma}\right)\right]^{\frac{-1}{\xi}}\right\} \qquad (4.4)$$

where μ, σ and ξ are the location, scale and shape parameters respectively. The GEV distribution might be one of three extreme value families depending on the value of the shape parameter ξ: Gumbel ($\xi = 0$), Fréchet ($\xi > 0$) or Weibull ($\xi < 0$). However, in this study, we are more concerned with the location parameter μ since it represents the intensity of extreme values whereas the scale and shape parameters do not show much difference over time [*Marcos et al.*, 2015]. Thus, we considered the location parameter as a time-dependent variable while the scale and shape parameters were treated as constants.

To model the location parameter as a function of time, we developed a Dynamic Linear Model (DLM) for block maxima extremes that was originally proposed by *Huerta and Sansó* [2007] and was later improved by *Huerta and Stark* [2013]. A brief description of the model follows, with additional details given in the references above.

The distribution in (4.4) now can be expressed as:

$$Y_t|\mu_t \sim GEV(\mu_t, \sigma, \xi) \quad (4.5)$$

$$\mu_t = \beta + \theta_t \quad (4.6)$$

Here Y is the observed sea-level record, and *t* is the time index in the sea-level record where the observations were measured; in equation (4.6), β is the intercept parameter (or model level) and θ_t is the unobserved state vector (or underlying process) of the location parameter that we need to define. The model described in (4.5) and (4.6) is considered as a first-order polynomial DLM-GEV model and provides a flexible way to detect both the deterministic trends and the changes with time (i.e., a stochastic process) throughout the records [*Huerta and Stark*, 2013]. Our main goal now is to determine the posterior density of the hidden non-stationary state based on measured sea level in the evolution equation (4.6). Note that our DLM model is a non-Gaussian model for the observations with unknown parameters, and therefore the solution should be based on Bayesian inference [*Durbin and Koopman*, 2012; *West and Harrison*, 1997].

Bayesian analysis allows us to estimate the posterior probability distribution of time-evolution of the latent state θ_t given Y_{max}, $p(\theta_t|Y_{max})$. To implement Bayesian inference for a non-Gaussian DLM, the Markov chain Monte Carlo (MCMC) method has been used extensively throughout the literature [*Durbin and Koopman*, 2012]. In this study, we solved the DLM-GEV model by using the open-source OpenBUGS software (Bayesian inference Using Gibbs Sampling) [*Lunn et al.*, 2009] via the

R2OpenBUGS *R* package [*Sturtz et al.*, 2005]. The OpenBUGS software can solve a state space model with an appropriate MCMC scheme using Gibbs sampling [*Lunn et al.*, 2009].

Prior to running the DLM-GEV model in OpenBUGS, we need to define the prior distributions for all parameters in the model. We chose the intrinsic Gaussian conditional autoregressive (CAR) prior distribution for the time-varying state θ_t. In this case, θ_t is a one-dimensional parameter, so the CAR distribution becomes a Gaussian first-order random walk [*Fahrmeir and Lang*, 2001]. We set the scale parameter σ following Gamma distribution $\sigma \sim Gamma(0.1, 0.1)$. For the shape parameter ξ, we followed the selection from *Rodríguez et al.* [2015] in which the authors limited ξ to a uniform prior distribution $\xi \sim U(-0.5,0.5)$. We also assigned β into a normal distribution $\beta \sim N(\mu, 0.01)$, and we calculated the mean of distribution (μ) by fitting the *GEV* function for each extreme sea-level record (i.e., NTR_{max} and SK_{max}) and then taking the value of the location parameter. This step allowed us to have a relatively accurate initial model level and, hence, the posterior mean of state vector. Thus, the amplitude of initial model level will depend on the amplitude of the highest values in NTR_{max} and SK_{max} data sets.

After defining the priors, we ran the DLM-GEV model in OpenBUGS with a burn-in period of 60,000 iterations, and added another 200,000 iterations for the MCMC simulations. We carefully monitored the convergence of MCMC, at each site, through the history and trace plots. Finally, we calculated the 50-year return level (RL50) for each site based on the location parameter resulting from the DLM-GEV model:

$$RL50_t = \mu_t - \frac{\sigma}{\xi}\left\{1 - \left[-log\left(1 - \frac{1}{5\times 50}\right)\right]^{-\xi}\right\} \tag{4.7}$$

Equation (4.7) implies that the temporal variability of RL50 will depend on the location parameter – the only parameter which is allowed to change with time in this study.

4.5. Results

4.5.1. Spatial distribution of maximum sea-level values

The maximum values of SL_{max}, *NTRs* and *SKs* (for the entire records and also for each season) are shown in Figs. 4.2a - 4.2i and Table 4.1. Overall, the results show clusters of maximum values in different parts of the SCS. In particular, the northern part of the SCS (from 15^{o}N northward) exhibits larger values than the south of the SCS, not only in maximum observed sea levels but also in the *NTRs* and *SKs* values. The sea-level maxima for the northern SCS range from 940 mm (at Kaohsiung) to 4070 mm (at Xiamen), whereas the maximum values in the southern SCS range from 990 mm (at Bintulu) to 2770 mm (at Kelang). This distribution is more evident when we look at the maxima in *NTRs* (Fig. 4.2d) and *SKs* (Fig. 4.2g) following the removal of tidal signals. In the north, *NTRs* range from 536 mm (at Kaohsiung) to 2064 mm (at Zhapo), and *SKs* are from 526 mm (at Dongfang) to 2014 mm (at Zhapo), while in the south *NTRs* are between 333 mm (at Lumut) and 1525 mm (at Vung Tau), and *SKs* are mostly below 500 mm (Table 4.1). Our results reveal that the highest sea-level maxima are observed at sites with large tidal range implying that tidal signals play an important role in the distribution of maximum values (for instance, the highest value is found at Xiamen where tidal range is ~ 6 m). Our study confirms the results of *Feng and Tsimplis* [2014], who find a statistically significant correlation between sea-level maxima and the sum of two major tidal constituents ($\mathbf{M_2} + \mathbf{K_1}$) in the northern SCS, and we find similar results in the southern part of the SCS as well.

Nevertheless, the results from *NTRs* and *SKs* maxima show that these two tide-surge interaction parameters are not always associated with the tidal range. For example, we detect the highest values of *NTRs* and *SKs* at Zhapo and Haikou (tidal ranges are ~ 3 m and 2 m, respectively) but not at Xiamen, where the highest sea level is seen. This evidence implies that in the study area there are significant non-linear tide-surge interactions [*Feng and Tsimplis*, 2014].

The seasonal distributions of SL_{max}, *NTRs* and *SKs* in the summer and the winter also present a spatial coherency in maxima; more interestingly, the results of summer and winter maxima in the northern and southern parts of the SCS show an opposite trend. In other words, in the north all maximum values are higher in the summer, indicating that the majority of events occur in the summer (Figs 4.2b, e, h), while in the southern SCS, higher maxima dominate in the winter (Figs 4.2c, f, i).

The dissimilarity in the timing of the sea-level maxima might imply that different forcing mechanisms dominate in the northern and southern parts of the SCS. *Feng and Tsimplis* [2014] argued that the extreme values in the northern SCS are strongly linked to tropical cyclones, which occur in the SCS – western Pacific area during the summer [*Wang et al.*, 2007]. For instance, the maximum values of *NTR* and *SK* at Zhapo (2064 mm and 2014 mm) and Haikou (2008 mm and 1875 mm) reflect typhoon Joe that passed over the Leizhou Peninsula and entered the Gulf of Tonkin on 22 July 1980 [*Hong Kong Royal Observatory*, 1980]. Typhoon Joe caused severe damage and 188 deaths, left about 50,000 homeless and "was the strongest over the region in 26 years" [*Hong Kong Royal Observatory*, 1980].

Our findings support the conclusion of *Feng and Tsimplis* [2014] that a link exists between SLEs and tropical cyclones in the northern SCS, but we disagree with their assertion that the area most affected by tropical cyclones is between 20°-30°N. Based on records from more TGs along the Vietnamese coastline, we suggest that the affected area extends southward to at least 15°N, as the Da Nang TG (in central Vietnam) has been severely affected by typhoons and super typhoons, e.g., super typhoon Xangxane in 2006 and super typhoon Ketsana in 2009. The TG at Da Nang recorded maximum *NTR* and *SK* of 1396 mm and 1169 mm, respectively, with both peaks occurring during typhoon Ketsana, which made landfall on 29 September 2009 and caused massive damage [*Switzer et al.*, 2011].

It is important to note that typhoon-induced surges might not always be recorded in the sea-level records due to a lack of available TG data. For instance, in our data sets, half of the northern TGs have not been updated since the year 2000, including those at Xiamen, Shanwei, Zhapo, Haikou, Dongfang and Beihai (Fig. 4.1b). Thus, some recent extreme events have not been recorded (e.g., typhoon Haiyan 2013), and hence the spatial distribution of extreme values may be biased [e.g., *Torres and Tsimplis*, 2014] or the return levels incorrectly estimated [e.g., *Marcos et al.*, 2009].

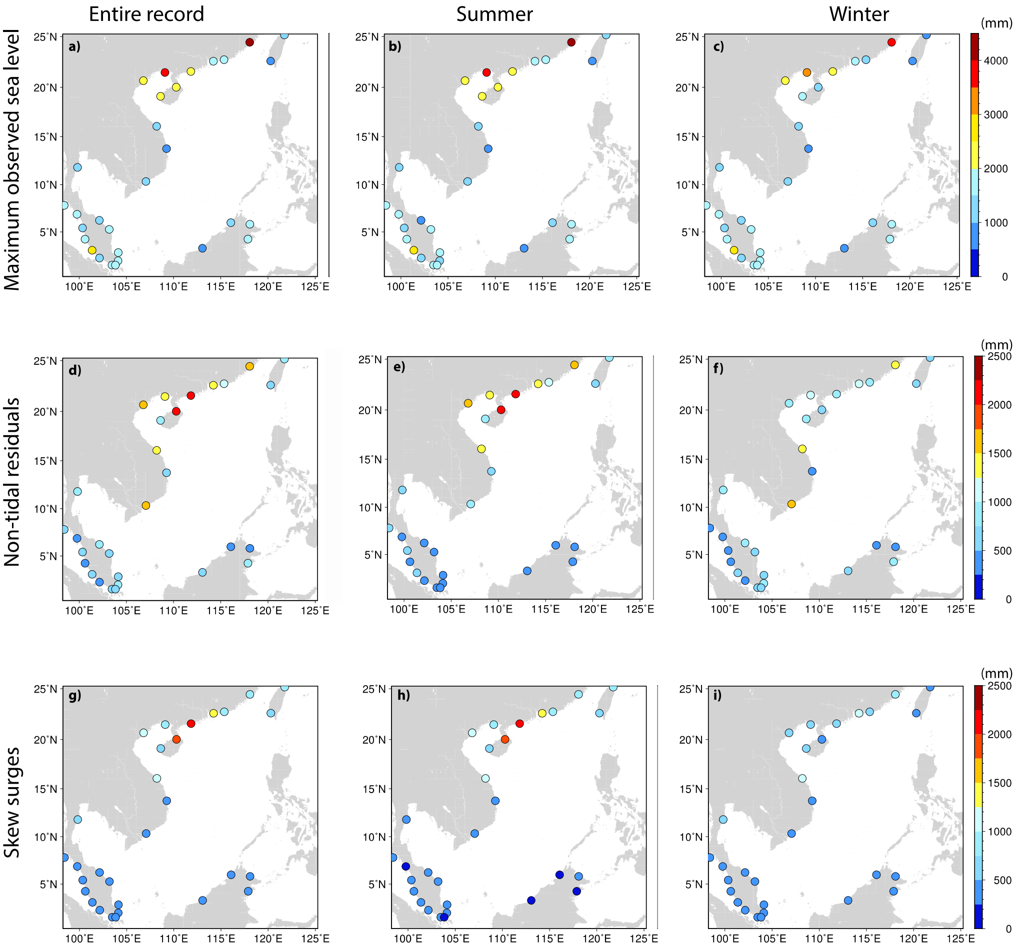

Figure 4. 2: The maxima distributions of three data sets show clear spatial and temporal patterns in the northern (north of 15^{o}N) and southern SCS. The maxima are higher in the north than in the south. In the north the values are higher in the summer, whereas in the south the values are higher in the winter. (a-c) the maximum observed sea level; (d-f) the maxima of non-tidal residuals; and (g-i) the maxima of the skew surges.

Table 4. 1: The maximum values of observed sea level, non-tidal residuals and skew surge

			Observed sea level		**Non-tidal residuals**		**Skew surge**	
Tide gauges	**Location**		Summer	Winter	Summer	Winter	Summer	Winter
Keelung	121.75°E	25.15°N	1030	800	863	688	790	464
Kaohsiung	120.283°E	22.617°N	940	900	534	536	533	405
Xiamen	118.067°E	24.45°N	4070	3540	1749	1490	1000	830
Shanwei	115.35°E	22.75°N	1595	1470	1136	851	821	704
Hong Kong	114.216°E	22.6°N	1990	1640	1489	1037	1393	1037
Zhapo	111.833°E	21.583°N	2425	2030	2064	1788	2014	599
Haikou	110.283°E	20.017°N	2170	1250	2008	749	1875	393
Dongfang	108.617°E	19.1°N	2030	1885	816	785	526	562
Beihai	109.083°E	21.483°N	3525	3190	1288	1014	992	560
Hon Dau	106.8°E	20.67°N	2285	2140	1641	788	1244	648
Da Nang	108.214°E	16.06°N	1390	1180	1396	1351	1170	1035
Qui Nhon	109.254°E	13.75°N	980	995	699	461	365	342
Vung Tau	107.07°E	10.33°N	1330	1395	926	1525	473	427
Ko Lak	99.82°E	11.8°N	1260	1290	593	943	406	628
Geting	102.136°E	6.23°N	990	1130	371	827	323	493
Cendering	103.183°E	5.267°N	1520	1550	349	641	260	406
Tioman	104.133°E	2.8°N	1700	1800	309	727	278	495
Sedili	104.117°E	1.933°N	1320	1540	335	835	305	470
Tanjong Pagar	103.833°E	1.467°N	1580	1675	368	632	243	388
Johor Bahru	103.47°E	1.47°N	1730	1785	412	744	291	471
Keling	102.15°E	2.217°N	1440	1495	399	372	371	298
Kelang	101.367°E	3.05°N	2745	2770	729	618	470	407
Lumut	100.62°E	4.23°N	1615	1640	324	333	256	283
Pulau Pinang	100.35°E	5.417°N	1450	1460	618	446	384	329
Langkawi	99.767°E	6.867°N	1790	1860	325	334	218	334
Ko Taphao Noi	98.417°E	7.817°N	1590	1640	630	437	290	319
Bintulu	113.06°E	3.26°N	900	990	296	654	222	407
Kota Kinabalu	116.067°E	5.983°N	1130	1265	386	278	220	254
Sandakan	118.08°E	5.817°N	1560	1650	324	335	323	267
Tawau	117.883°E	4.233°N	1790	1920	398	843	247	445

While tropical cyclones are the main factor affecting the maximum values in the northern SCS, the higher maxima in the southern TGs during winter suggest the impact of monsoons on extreme values, with different wind directions at different times of the year. The SCS experiences a seasonal, basin-wide, large-scale monsoon system blowing northeasterly in the winter (the NE monsoon) and southwesterly in the summer (the SW monsoon) [*Wang et al.*, 2009]. The NE monsoon has been shown to dominate over the entire SCS, reaching even the southern SCS [*Fang et al.*, 2006] where it can cause considerable sea-level surges [*Chen et al.*, 2012; *Tkalich et al.*, 2013]. For instance, *Tkalich et al.* [2013] highlight a strong correlation between sea level anomalies and the NE monsoon at the Tanjong Pagar TG (TG 19 in this study, Fig. 4.1a), and point out that the NE monsoonal wind drives sea level anomalies up to 300 mm. Furthermore, during the NE monsoon the shallow-water areas of the Sunda Shelf may considerably intensify surges [*Chen et al.*, 2012]. The above-mentioned studies support our hypothesis that the extreme sea-level values in the southern SCS are controlled by the winter monsoonal wind driving the maximum surges found in this study up more than 500 mm.

Besides the dominance of the NE monsoon, the maximum values are also impacted by the SW monsoon. In four TGs (Ko Ta Phao Noi, Pulau Pinang, Kelang and Keling), the SW monsoon drives sea level higher than the NE monsoon by ~ 70 - 200 mm (see non-tidal residual maxima in Table 4.1). This finding implies that during the SW monsoon, water piles up and surges at some TGs along the west coast of the Malay–Thai Peninsula. Overall, the impact of the NE monsoon seems to be greater over the study area.

4.5.2. Long-term trends

As outlined in Section 4.4.1, we calculated long-term trends for the SL_{995}, $SL_{995freeMSL}$, $SL_{995freeMSL\_tide}$ and SK_{95} data sets for both the full data sets and the seasonal data sets; the results are shown in Fig. 4.3 and Table 4.2.

The SL_{995} results show positive trends at all sites, though at seven of 30 TGs the trends were statistically insignificant (Fig. 4.3a). The estimated trends of SL_{995} vary in a wide range between ~ 0.5 and 10 mm/year. Regarding the spatial distribution, the difference between the northern and southern SCS is not as clear as for the SL_{max} values (see section *4.5.1* and Fig. 4.2); however, in general the sea levels recorded by the TGs along the Malay-Thai Peninsula are lower and less divergent than the trends in the northern and southeastern SCS (Fig. 4.3a). There are very high rates of SL_{995} at TGs in both the northern and southeastern SCS: Beihai and Haikou in the north (9.3 mm/year and 9.8 mm/year, respectively) and Sandakan and Bintulu in the southeast (11.7mm/year and 8.7 mm/year, respectively). However, we observed larger deviations in the trends between sea-level records in the northern SCS, even at two TGs that are close to each other. For example, the difference in sea level trends between the Hon Dau (3.4 mm/year) and Beihai (9.3 mm/year) TGs, which are ~ 250 km apart, is ~ 6 mm/year. This difference in ESL is considerable if we compare it to the difference in trends of the MSL (approximately the 50th percentile) at Hon Dau (2.0 mm/year) and Beihai (1.2 mm/year). Such differences between geographically close TGs with respect to ESL long-term trends are also seen in the Yellow Sea [*Feng and Tsimplis*, 2014] or along the Atlantic coast and in northern Gulf of Mexico [*Wahl and Chambers*, 2015]. Next, we look at the seasonal trends in the winter and the summer (Figs. 4.3b – 4.3c). One might expect that for the northern TGs, the trends in the summer (i.e., during the stormy season) to be greater than those in the winter. However, only Beihai and Xiamen TGs show larger trends in the summer, whereas other TGs show the opposite trend (Figs. 4.3b – 4.3c). In addition, in both seasons we observe a significant strongly negative trend at the Ko Lak tide gauge (~ -7 mm/year) as well as positive trends at four TGs in the southeastern SCS, where there is no obvious influence by tropical cyclones. The aforementioned examples highlight that local factors, such as basin shape, location relative to tropical cyclone paths or changes in tidal constituents, might greatly contribute to the trends of extreme sea levels in addition to meteorological forcings [e.g., *Feng and Tsimplis*, 2014; *Marcos et al.*, 2015; *Torres and Tsimplis*, 2014; *Wahl and Chambers*, 2015]. We conclude from this that, as suggested by *Wahl and Chambers* [2015], local effects should be taken into account for coastal infrastructure designs.

The long-term trends of *the* $SL_{995freeMSL}$ data set shows that the estimated trends are considerably lower, and more TG records show statistically insignificant trends (Figs. 4.3d – 4.3f). Among those TGs showing significant trends, we start to see clear differences. The northern and southeastern TGs still show positive trends, with an average range of 0.1 - 7 mm/year (note that we used the same color scale as for the trends of *PRC995*), except for the Da Nang TG, which shows a small negative value (-0.16 mm/year). Conversely, the southwestern TGs, with the exception of Geting, show a decreasing trend. In the summer, interestingly, we notice an increase in long-term trends (on the order of ~ 2 – 9 mm/year), and more TG records become statistically significant in the northern SCS (Fig. 4.3e). This tendency, however, decreases in the winter, with few TGs showing significant trends. The few significant winter trends in the southern SCS are positive (Fig. 4.3f).

The spatial distribution and magnitude of ESL trends changes again when we remove the predicted tides from the sea-level records (i.e., *the* $SL_{995freeMSL\_tide}$ *data set*). Few sites exhibit significant and lower trends compared to the trends of $SL_{995freeMSL}$ data set (Figs. 4.3g – 4.3i), which demonstrates the considerable impact of tidal components. The northern sites show statistically significant positive trends on the order of ~ 1 – 4 mm/year in both seasons, whereas the TGs in the southern SCS display complicated trends as they contain both significant negative and positive trends (for entire record and during the summer). Interestingly, in the winter, all sites in the SCS exhibit a statistically significant positive trend in the range of ~ 2-3 mm/year.

The SK_{95} data set shows even fewer significant trends (Fig. 4.3j – 4.3l). Note that both the $SL_{995freeMSL\_tide}$ and the SK_{95} data sets exclude the effects of tides and long-term trends in RMSL, but in both cases too many TGs have insignificant trends, which makes them difficult to directly compare to one another. In the summer, only four TGs with significant trends are common to both data sets: the Xiamen and Keelung TGs in the north, and the Johor Bahru and Kota Kinabalu TGs in the south. Among them, the Kota Kinabalu TG exhibits a positive trend in the $SL_{995freeMSL\_tide}$ data set, but a negative trend in the SK_{95} data set (Figs. 4.3h and 4.3k). Notably, though the trends are insignificant, we observe opposite trends at a few other TGs as well (not shown).

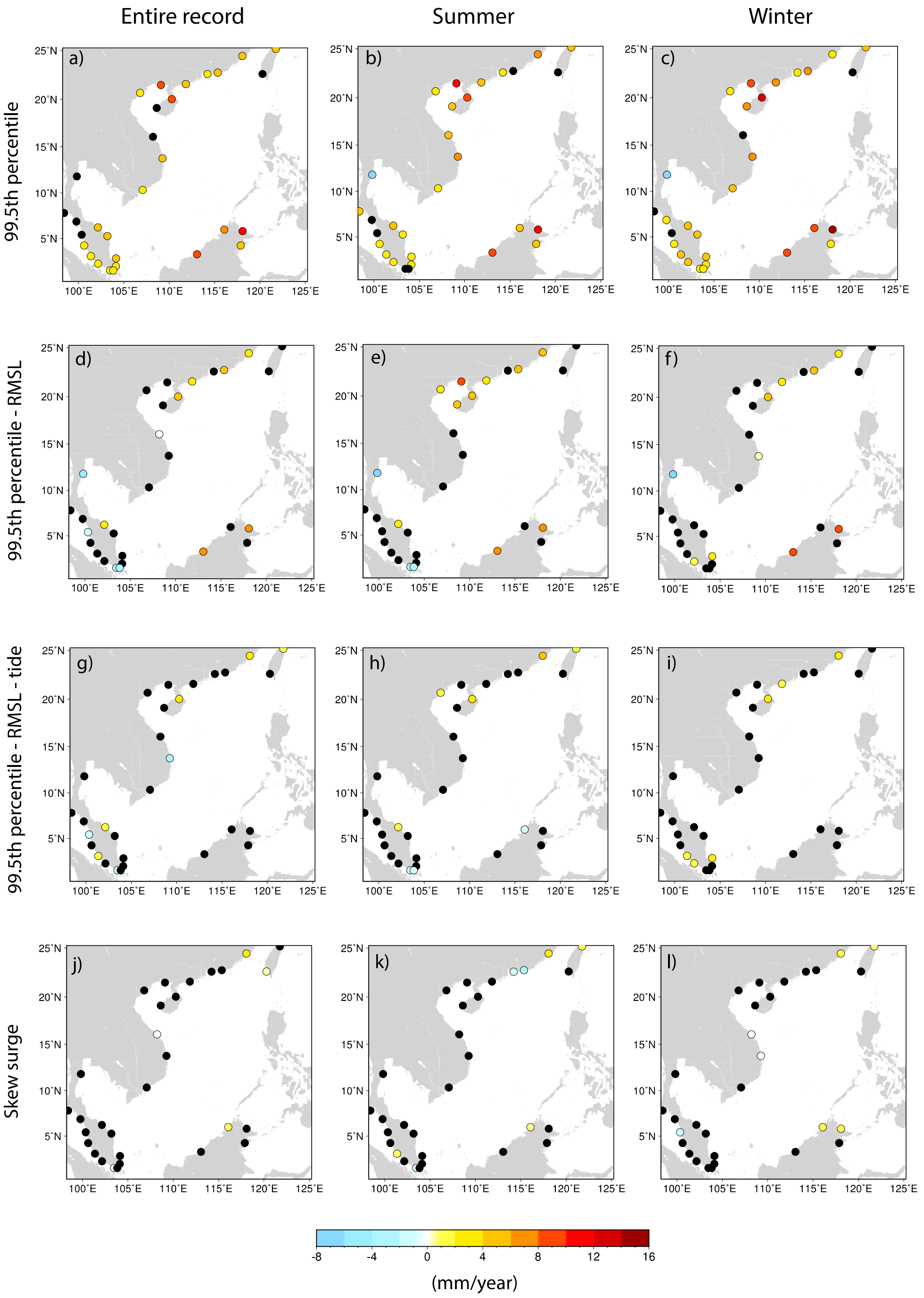

Figure 4. 3: Long-term trends for different data sets: (a-c) 99.5th percentile of observed sea level for the entire record, for summer and for winter; (d-f) 99.5th percentile of observed sea level with the long-term trend of relative mean sea level removed; (g-i) 99.5th percentile of observed sea level with tidal influences and the long-term trend of relative mean sea level removed; (j-l) 95th percentile for the skew surges. The majority of TGs show insignificant trends (black circles) when the RMSL and tides were removed.

Table 4. 2: Long-term trends of 99.5th percentiles, with RMSL removed, with RMSL and tide removed and skew surge. Only statistically significant trends are shown.

	Entire record				**Summer**				**Winter**			
Tide gauges	99.5th	99.5th - RMSL	99.5th - RMSL - tide	Skew surge	99.5th	99.5th - RMSL	99.5th - RMSL - tide	Skew surge	99.5th	99.5th - RMSL	99.5th - RMSL - tide	Skew surge
Keelung	4.4 ± 0.96	-	0.99 ± 0.39	-	4.61 ± 1.28	-	1.23 ± 0.54	1.2 ± 0.29	4.06 ± 0.81	-	-	0.79 ± 0.26
Kaohsiung	-	-	-	0.4 ± 0.23	-	-	-	-	-	-	-	-
Xiamen	4.69 ± 0.72	3.5 ± 0.65	3.67 ± 0.53	2.25 ± 0.27	6.83 ± 1.15	4.21 ± 1.14	4.18 ± 0.70	2.46 ± 0.40	3.71 ± 0.81	2.91 ± 0.65	3.38 ± 0.59	1.95 ± 0.33
Shanwei	4.18 ± 2.13	4.94 ± 2.22	-	-	-	4.22 ± 2.55	-	-2.29 ± 1.15	6.86 ± 2.35	5.48 ± 2.40	-	-
Hong Kong	2.79 ± 0.67	-	-	-	2.2 ± 0.73	-	-	-0.69 ± 0.40	3.01 ± 0.87	-	-	-
Zhapo	4.68 ± 1.14	3.01 ± 1.59	-	-	4.82 ± 1.91	3.33 ± 1.7	-	-	6.35 ± 1.28	3.61 ± 1.48	1.9 ± 0.73	-
Haikou	9.81 ± 2.93	4.96 ± 3.68	2.8 ± 1.50	-	9.0 ± 2.24	4.95 ± 3.56	2.56 ± 1.42	-	12.18 ± 3.65	5.88 ± 4.14	2.75 ± 1.67	-
Dongfang	-	-	-	-	4.78 ± 3.44	4.55 ± 3.5	-	-	6.19 ± 4.0	-	-	-
Beihai	9.31 ± 6.15	-	-	-	10.1 ± 5.85	9.20 ± 5.7	-	-	9.98 ± 6.45	-	-	-
Hon Dau	3.4 ± 2.02	-	-	-	3.9 ± 1.8	2.02 ± 1.81	1.12 ± 0.69	-	3.23 ± 1.89	-	-	-
Da Nang	-	-0.16 ± 0.09	-	-0.15 ± 0.03	4.38 ± 2.32	-	-	-	-	-	-	-0.17 ± 0.06
Qui Nhon	5.42 ± 1.90	-	-2.5 ± 2.0	-	7.1 ± 2.07	-	-	-	6.49 ± 2.33	0.4 ± 0.18	-	-0.14 ± 0.08
Vung Tau	3.82 ± 0.83	-	-	-	3.49 ± 1.08	-	-	-	4.53 ± 1.02	-	-	-
Ko Lak	-	-5.51 ± 4.53	-	-	-7.05 ± 4.61	-6.6 ± 5.11	-	-	-7.50 ± 5.32	-6.04 ± 4.24	-	-
Geting	4.46 ± 1.54	2.09 ± 0.98	1.28 ± 0.67	-	4.92 ± 1.42	2.1 ± 1.03	1.5 ± 0.80	-	4.80 ± 1.6	-	-	-
Cendering	4.95 ± 1.98	-	-	-	3.35 ± 1.67	-	-	-	4.89 ± 1.83	-	-	-
Tioman	4.39 ± 1.44	-	-	-	2.43 ± 1.48	-	-	-	4.73 ± 1.8	2.42 ± 1.40	2.52 ± 1.01	-
Sedili	3.31 ± 1.49	-	-	-	2.07 ± 1.06	-	-	-	3.1 ± 1.73	-	-	-
Tanjong Pagar	3.56 ± 1.90	-2.06 ± 0.82	-	-	-	-2.50 ± 1.04	-1.62± 0.84	-	3.81 ± 1.36	-	-	-
Johor Bahru	2.55 ± 0.88	-2.23 ± 1.08	-1.45 ± 0.97	-0.85 ± 0.47	-	-2.77 ± 1.12	-1.85 ± 0.98	-1.2 ± 0.54	2.51 ± 0.99	-	-	-
Keling	3.17 ± 1	-	-	-	2.39 ± 0.98	-	-	-	4.45 ± 1.4	1.58 ± 0.1	1.70 ± 0.81	-
Kelang	3.2 ± 1.25	-	1.58 ± 0.80	-	3.0 ± 1.63	-	-	0.82 ± 0.41	4.78 ± 1.68	-	1.71 ± 0.98	-
Lumut	2.68 ± 0.97	-	-	-	2.47 ± 0.97	-	-	-	3.32 ± 1.80	-	-	-
Penang	-	-0.94 ± 0.52	-0.96 ± 0.40	-	-	-	-	-	-	-	-	-1.13 ± 0.37
Langkawi	-	-	-	-	-	-	-	-	3.37 ± 1.62	-	-	-
Ko Taphao Noi	-	-	-	-	4.4 ± 2.3	-	-	-	-	-	-	-
Bintulu	8.7 ± 2.45	6.53 ± 1.53	-	-	9.0 ± 1.7	6.34 ± 2.41	-	-	9.6 ± 4.56	8.19 ± 2.14	-	-
Kota Kinabalu	6.93 ± 2.12	-	-	0.93 ± 0.25	4.19 ± 2.41	-	-1.04 ± 0.5	0.62 ± 0.35	8.40 ± 2.59	-	-	1.13 ± 0.28
Sandakan	11.74 ± 2.03	7.24 ± 3.08	-	-	11.2 ± 2.94	7.79 ± 3.19	-	-	14.31 ± 3.48	9.05 ± 2.37	-	0.9 ± 0.24
Tawau	5.02 ± 1.79	-	-	-	4.29 ± 2.01	-	-	-	3.79 ± 1.75	-	-	-

These opposite trends might be explained by the different methods with which the two data sets were extracted [*Mawdsley and Haigh*, 2016; *Wahl and Chambers*, 2015]. We also find that the magnitude of trends from the SK_{95} data set is generally smaller compared to those of the $SL_{995freeMSL\_tide}$. We observe statistically significant negative SK_{95} summer trends at the Hong Kong and Shanwei TGs, but positive trends at the Xiamen and Keelung TGs, even though they are geographically proximal to each other (Fig. 4.3k). This dissimilarity again likely imply the impact of local forcings mentioned above.

In summary, in this section we have examined the long-term trends for various data sets in order to determine whether change in ESL are influenced by tides or changes in RMSL. Overall, our results reveal that few TGs in the SCS show significant trends that are not related to either tides or changes in RMSL, regardless of the season. This outcome indicates that the ESL trends are mostly driven by trends in RMSL and by tidal influences. Our calculations are broadly consistent with the results (for the northern SCS) of a study by *Feng and Tsimplis* [2014], even though they calculated long-term trends for the 99.9th percentile level. Yet our results and those derived from *Feng and Tsimplis* [2014] show some dissimilarities in the significance of long-term trends at individual site (*Feng and Tsimplis* [2014] found no significant trends for sites in the northern SCS), which we believe come from different extreme percentiles computed, confidence levels accessed, and/or data processed.

Likewise, the present study shows a good agreement with other studies focusing on the U.S. coast [*Wahl and Chambers*, 2015] and the coast of southern Europe [*Marcos et al.*, 2009], where the researchers found evidence that the changes in ESL are dominated by mean sea level changes.

4.5.3. Extreme sea-level variability

4.5.3.1. Spatial variability of the RL50

RL50, which is resulted from equation (4.7), is generally higher at the northern TGs than in the south with higher magnitudes found in the NTR_{max} data set than in the $SK_{\max}$ data set, with the exception of the Kaohsiung TG (Figs 4.4 – 4.7, Supp. Info Figs S4.1-S4.6).

In the north, the RL50 values based on NTR results range from ~ 600 – 2500 mm (if we exclude two Taiwan TGs, Keelung and Kaohsiung, the RL50 is ~ 1800 - 2000 mm on average), but sharply drop to ~ 350 – 1200 mm in the south (Figs. 4.4 – 4.5, Supp. Info. Fig. S4.1-S4.3). An exceptional case is the Kaohsiung tide gauge, where the RL50 values are remarkably lower than at other TGs in the northern SCS (Supp. Info. Fig. S4.1). For the SK results, we observe a similar spatial pattern of RL50, but with a lower range of the RL50 values at most individual sites: ~ 600 – 2500 mm in the north (if we remove the Zhapo tide gauge, the upper bound is reduced to ~ 1700 mm), and ~ 250 – 700 mm in the south (Figs. 4.6 – 4.7, Supp. Info. Fig. S4.4-S4.6). Overall, the spatial distribution of the RL50 values agrees with the spatial distribution of the SL_{max} that have been already described in section *4.5.1*. This agreement is not surprising as data sets used to run the DLM-GEV model were built in a similar way as the data sets used to calculate the SL_{max}. However, we notice that the values of RL50 at the Zhapo, Keelung and Kaohsiung TGs are similar in both NTR_{max} and SK_{max} data sets.

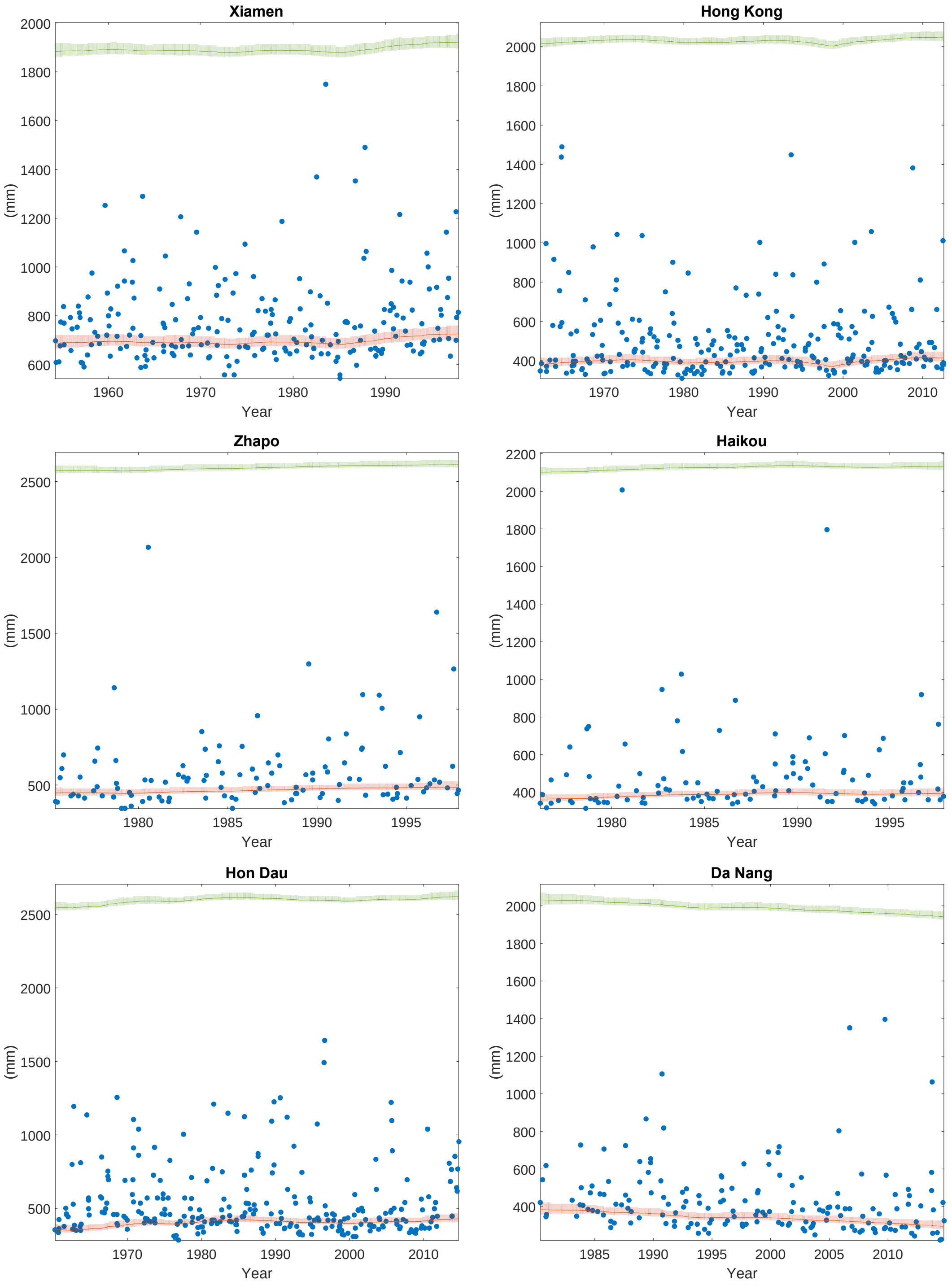

Figure 4. 4: Results from the DLM-GEV model for the five highest non-tidal residuals per year (blue dots) at selected TGs in the north show time-varying variability for the location parameter (orange solid line) and the 50-year return levels (green solid line). The shaded areas show the 95% credible intervals.

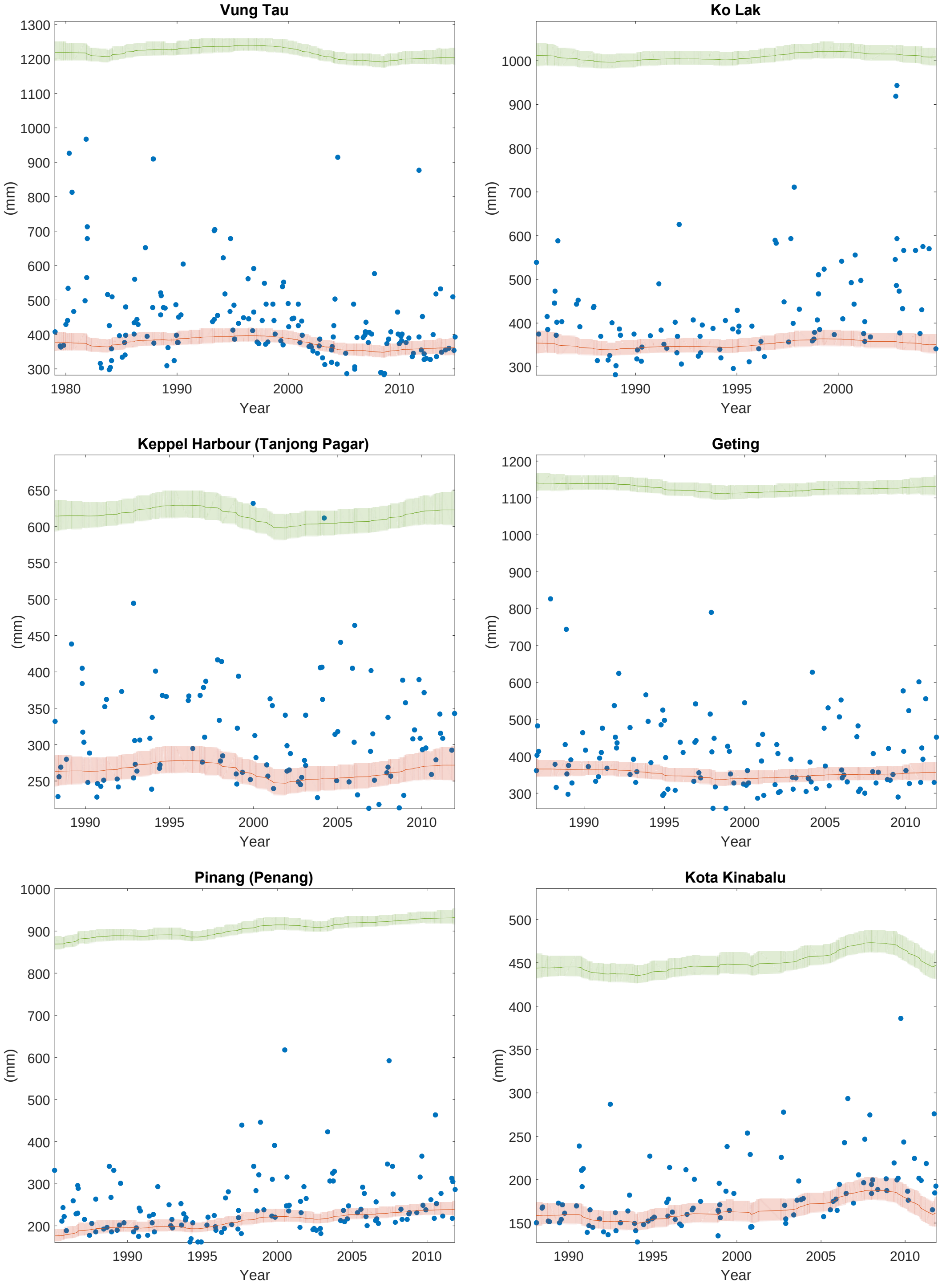

Figure 4. 5: Results from the DLM-GEV model for the five highest non-tidal residuals per year (blue dots) at selected TGs in the south show time-varying (mostly interannual) variability for the location parameter (orange solid line) and the 50-year return levels (green solid line). The shaded areas show the 95% credible intervals.

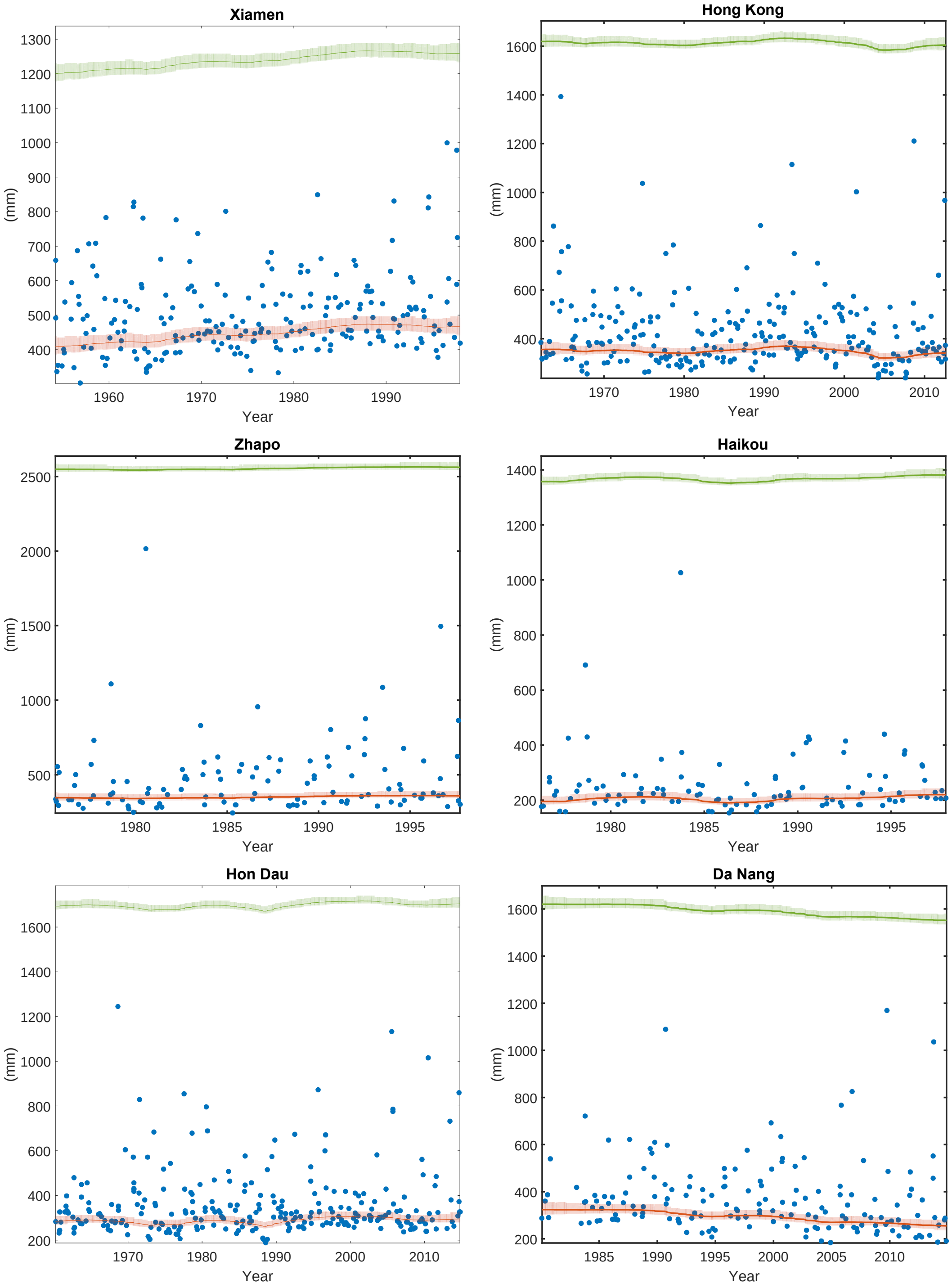

Figure 4. 6: Results from the DLM-GEV model for the five highest skew surges per year (blue dots) at selected TGs in the north show time-varying variability for the location parameter (orange solid line) and the 50-year return levels (green solid line). The shaded areas show the 95% credible intervals.

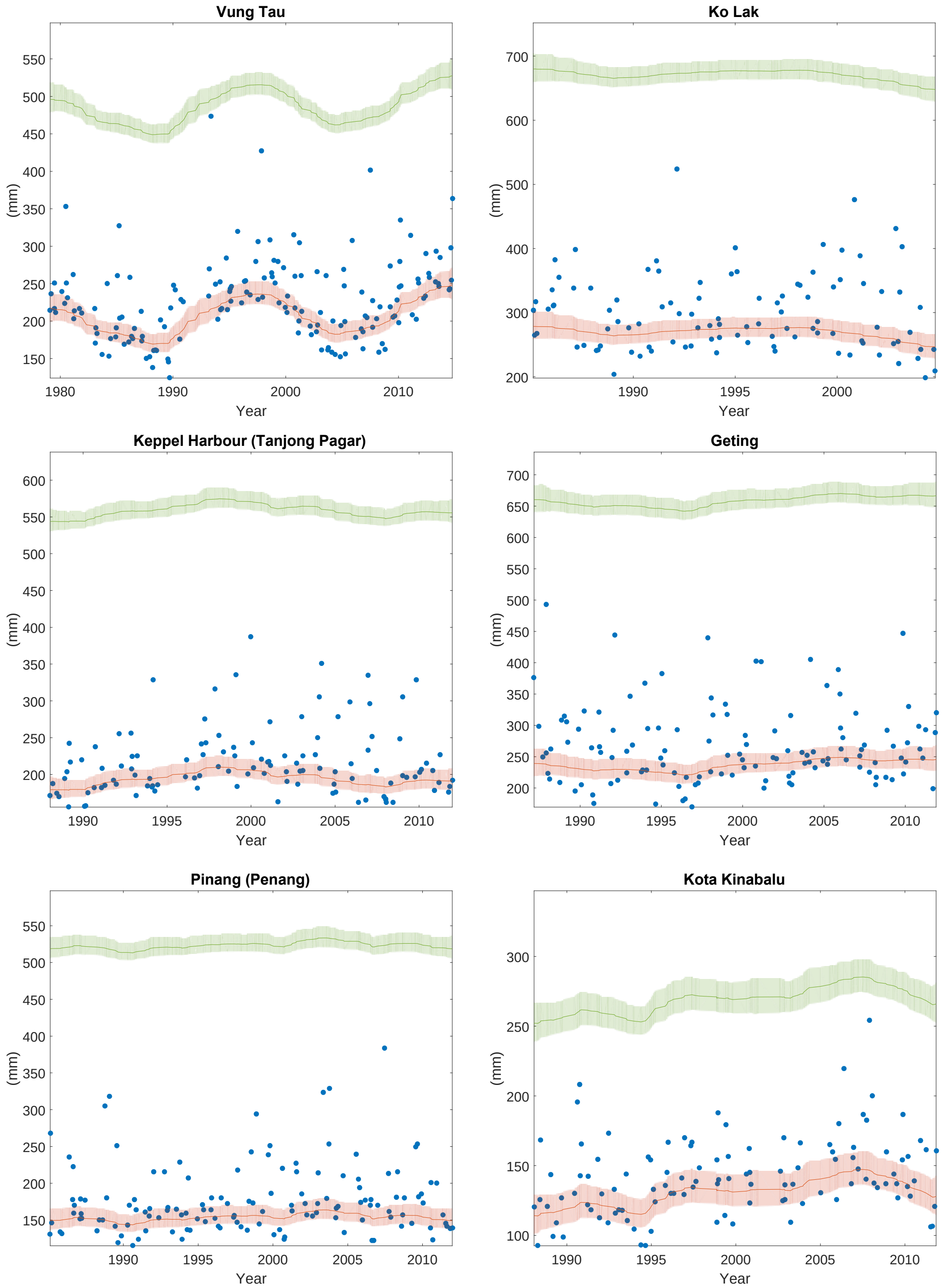

Figure 4. 7: Results from the DLM-GEV model for the five highest skew surges per year (blue dots) at selected TGs in the south show time-varying (mostly interannual) variability for the location parameter (orange solid line) and the 50-year return levels (green solid line). The shaded areas show the 95% credible intervals.

4.5.3.2. Temporal variability of the RL50

At all TGs and in both data sets, we observe clear non-stationary variations of the RL50. To clearly illustrate non-stationary signals, we calculated the deviations relative to the mean of each RL50 time series at each site and then plotted the results over time, ordered as in Fig. 4.1), in Fig. 4.8a (for NTR_{max}) and Fig. 4.8b (for SK_{max}). The results in Fig. 4.8 reveal that our time-varying DLM-GEV model successfully captures interannual to decadal variability in extreme sea levels (which are not related to the RMSL) at most TGs. In some long TG records we even detect signals of decadal (e.g., at Hong Kong) or multi-decadal variability (e.g., at Hon Dau – the longest tide gauge in this study). We note that non-stationary signals derived from the DLM-GEV model for both data sets are broadly consistent for the majority of sites, and that the changes of the RL50 values derived from the NTR_{max} data set are generally larger than those from the SK_{max} data set (Fig. 4.8). We recognize a few discrepancies with contrary temporal patterns, e.g., Kaohsiung, Hong Kong, Beihai, Vung Tau and Tioman TGs, where there are opposite signs in the RL50 changes between the NTR_{max} and SK_{max} data sets (Fig. 4.8).

The temporal variability of ESL unveiled by the DLM-GEV allows us to either discover the common time period over which TGs show regional coherence and to detect whether the intensity of ESL has been increasing in recent decades, which can be related to an enhancement of the storminess. In the northern SCS, due to different time periods covered by TGs in this study, we cannot draw conclusions about changes since the year of 2000 for all TGs but we still observe a rising of the RL50 at most TGs in the period 1990 – 2000. A close look at TGs that extend to 2014 (Keelung, Hon Dau and Da Nang) shows an increase of the RL50 values at Hon Dau and

Keelung whilst Da Nang reveals a clear decline since 2000. In the southern SCS, the regional coherency is more evident. RL50 increased at most southwestern TGs since 1995 whereas a rise of RL50 at four TGs in the southeast (Bintulu, Kota Kinabalu, Sandakan and Tawau) generally started around 2005. Together with the results at northern TGs, we suggest that the temporal variability of ESL is very likely affected by regional-scale climate-related forcings. We thus conducted a further analysis to better understand the physical mechanisms underlying the interannual-decadal variability of ESL shown in this study, which was presented in the next section.

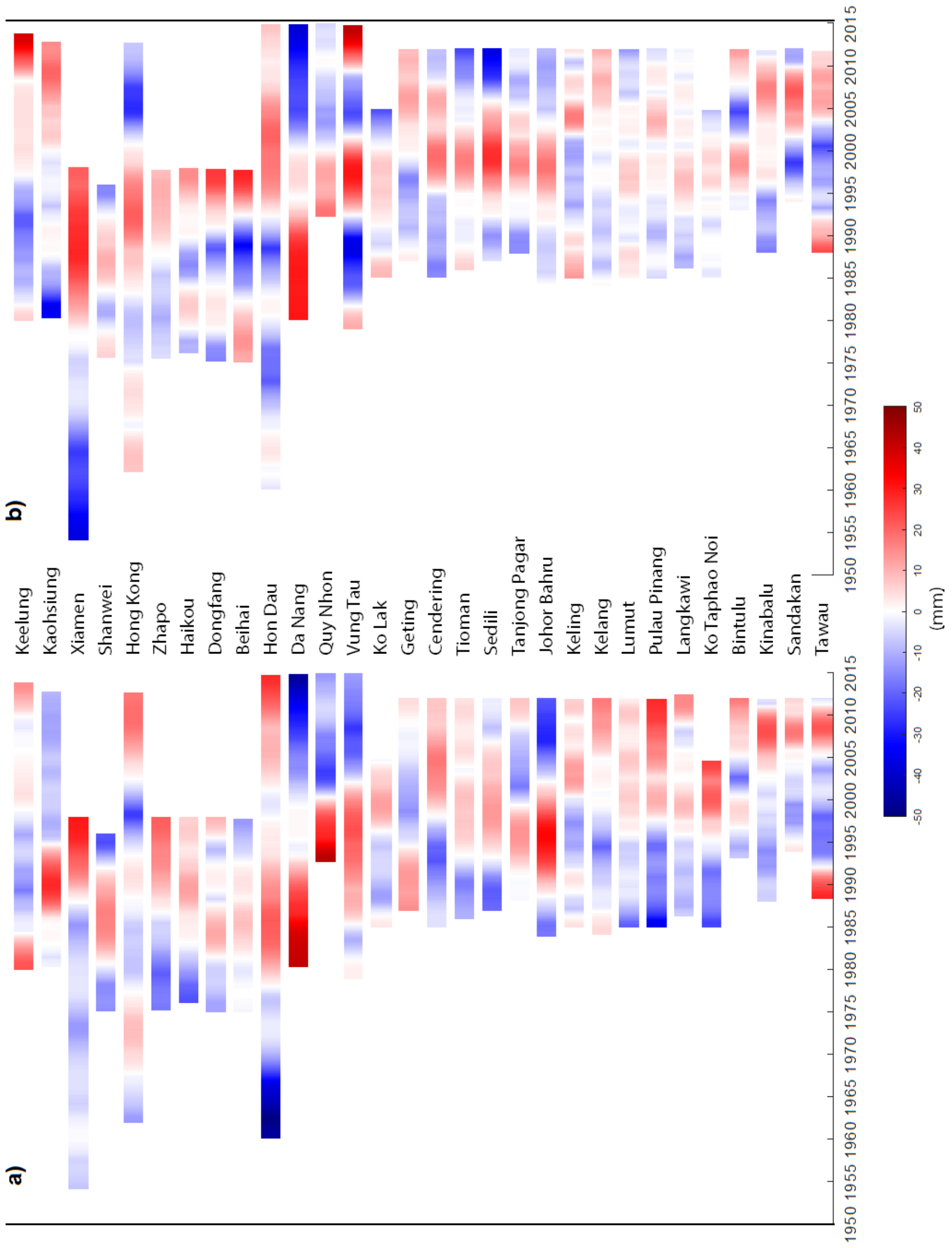

Figure 4. 8: The changes of the 50-year return levels for non-tidal residuals (**a**) and skew surges (**b**) relative to the mean value of each site. There are clear interannual variability, but are more evident in the south. The order of TGs follows that in Fig. 4.1.

4.5.4. Possible links to climate indices

We explored possible correlations between ESL (here we used the RL50 time series from the NTR_{max} results) and different climate and monsoon indices (hereafter indices) that we expect to be the most relevant forcings in the study area, namely: the Pacific Decadal Oscillation (PDO); the Multivariate ENSO Index (MEI); the Dipole Mode Index (DMI, which represents the Indian Ocean Dipole, or IOD); and two monsoon indices, the East Asian Winter Monsoon Index (EAWMI) and the South China Sea Summer Monsoon Index (SCSSMI). References and brief descriptions of all indices are presented in Table 4.3.

We first calculated the mean of all indices and the RL50 for each calendar year due to different temporal resolution of each time series. While climate indices (PDO, MEI, DMI) are determined on a monthly basis, monsoon indices (EAWMI and SCSSMI) contain one value per year, and the RL50 time series have only five values per year, as described above. We then low-pass filtered the annualized data sets by the Ensemble Empirical Mode Decomposition (EEMD) - a component of the Hilbert-Huang Transform method (HHT). This method is an adaptive data analysis technique that can provide meaningful non-linear and non-stationary signals hidden in the data sets [*Huang et al.*, 1998; *Wu and Huang*, 2009]. For the RL50 time series data, we also used the EEMD method to remove the trend (i.e., the last mode from the EEMD analysis), and we then normalized the detrended RL50 data, in order to make those data comparable with indices. The correlations were statistically tested at the 90% confidence level by a *t-test*. Only statistically significant correlations are plotted.

Table 4. 3: Brief description and references of climate and monsoon indices

Index	**Description**	**Data sources**
Pacific Decadal Oscillation (PDO)	The leading principle component of North Pacific monthly sea surface temperature (poleward of 20°N) [*Mantua et al.*, 1997]	http://ds.data.jma.go.jp/tcc/tcc/products/elnino/decadal/annpdo.txt
Multivariate ENSO Index (MEI)	The first unrotated principal component of six major variables over the tropical Pacific: sea-level pressure, zonal and meridional components of the surface wind, sea surface temperature, surface air temperature, and total cloudiness fraction of the sky [*Wolter and Timlin*, 1993, 1998]	http://www.esrl.noaa.gov/psd/enso/mei/table.html
Dipole Mode Index (DMI)	The sea surface temperature gradient between the western (50°E – 70°E, 10°S-10°N) and the south eastern (90°E – 110°E, 10°S – 0°N) equatorial Indian Ocean [*Saji et al.*, 1999]	http://stateoftheocean.osmc.noaa.gov/sur/ind/dmi.php
East Asian Winter Monsoon (EAWM)	The difference of normalized area-averaged sea-level pressure over Siberia (40°-60°N, 70°-120°E), the North Pacific (30°-50°N, 140°E-170°E) and the Maritime Continent (20°S–10°N, 110°–160°E) [*Wang and Chen*, 2013b]	Personal communication
South China Sea Summer Monsoon Index (SCSSMI)	The area-averaged seasonally (from June to September) at 925 hPa over the domain of the South China Sea (0°-25°N, 100°-125°E) [*Li and Zeng*, 2002]	http://ljp.gcess.cn/dct/page/65578

The results of correlation analysis show that only the PDO and MEI indices exhibit consistent correlations with the RL50 at TGs around the SCS (Table 4.4). Although the correlation coefficients are small (*r* ~ -0.2 to -0.6), the majority of TGs are negatively correlated to the mode of Pacific climate variability and the ENSO index (Table 4.4). These features highlight the same correlation patterns as the RMSL in the SCS and its vicinity. Previous studies have pointed out the out-of-phase correlations between the RMSL and the PDO [e.g., *Han and Huang*, 2008b; *Soumya et al.*, 2015] as well as the ENSO [e.g., *Rong et al.*, 2007]. The significant correlations between ESL and the large-scale atmospheric forcings have also been reported by *Marcos et al.* [2015] at multi-decadal time scales. Our results, however, slightly contrast those of *Feng and Tsimplis* [2014], who found that the PDO and ENSO only significantly correlate with moderate-to-high water levels (i.e., 50th – 80th percentiles) at the northern TGs. This difference might be attributed to the DLM-GEV model used in this study rather than a simple linear model. Nevertheless, *Feng and Tsimplis* [2014] point out that ENSO may influence the path of tropical cyclones hitting the Chinese coast more when La Niña occurs and less during El Niño phase. This interaction is likely to be an explanation for the negative correlations at northern TGs Zhapo, Hong Kong, Kaohsiung and Beihai (Table 4.4).

The IOD negatively correlates with the RL50 at most TGs in the northern SCS but it shows a complicated relationship at the southern TGs (Table 4.4). Three TGs around the Singapore Strait (Tioman, Tanjong Pagar and Johor Bahru) positively correlate with the IOD (*r* ~ 0.3-0.5) whereas the TGs along the southwestern and northeastern coasts of the Malay Peninsula negatively correlate with the IOD (Cendering, Keling and Pulau Pinang). In recent studies, *Soumya et al.* [2015] and *Luu et al.* [2015] find strong negative correlations between RMSL and IOD at interannual scales in the southern SCS. However, *Luu et al.* [2015] note that there is a considerable shift around the Singapore Strait when the negative coefficients sharply reduce to very low values at Johor Bahru and Tanjong Pagar (Fig. 4.8, in their study). This change are reflected in our results even though the coefficients in the present study are highly positive. Yet, the physical mechanism that might explain this remains unclear.

The two monsoon indices (EAWM and SCSSMI) show different relations with the RL50s. Only a few TGs significantly correlate with the EAWM, so a comparison between the two monsoon indices cannot be seen for the entire study area. Among TGs that show significant correlations in both indices, we observe some opposite responses. For example, the two TGs near the Singapore Strait (Tioman and Tanjong Pagar) are positively correlated with the EAWM but are negatively correlated with the SCSSMI (Table 4.4). Conversely, the two TGs in the southeast SCS (Kota Kinabalu and Tawau) show negative correlations with the EAWM but positive correlations with the SCSSMI (Table 4.4). This contradiction suggests that ESL responds differently to different monsoonal winds at various sub-regions. Our results also might be related to the contrasting mechanisms causing the maxima at the southern TGs in the winter and summer, which has been discussed above.

Our correlation analyses show that the time-varying changes in the RL50 around the SCS are significantly correlated to the major modes of climate variability or large-scale forcing. The results also suggest a spatial pattern of ESL variability with respect to climate variations. This leads to a need for a detailed study to unveil the physical mechanisms that contribute to ESL variability. Such efforts are not within the scope of this study but they are a likely goal in future studies.

Table 4.4: Correlation analyses show negative correlations between the 50-year return levels and the PDO and ENSO whereas the IOD (via the DMI) exhibits a complicated relationship. Only statistically significant correlations are shown. Significance test is based on the *t-test* at the 90% confidence level.

	PDO	**ENSO**	**DMI**	**EAWM**	**SCSMI**
Keelung	-	-	-	-	-
Kaohsiung	-0.33	-0.34	-0.32	-0.41	-
Xiamen	-	-	0.49	-	0.5
Shanwei	-	-	-0.62	-	-0.43
Hong Kong	-0.43	-0.4	-	-	-
Zhapo	-0.82	-0.79	-0.38	-	0.49
Haikou	-	-	-0.45	-	-
Dongfang	-	0.4	-	-	-
Beihai	-0.45	-0.51	-0.77	0.47	0.34
Hon Dau	-	-	-	-	-
Da Nang	-	-	-0.31	-	-
Qui Nhon	-	-	0.58	-	-0.66
Vung Tau	-	-	-	-	-
Ko Lak	-	-	-	-	-0.31
Geting	-	0.3	-	-	0.65
Cendering	-	-	-0.62	-	-
Tioman	-	-	0.39	0.54	-0.32
Sedili	0.4	0.32	-	-	-0.34
Tanjong Pagar	-	-	0.55	0.41	-0.58
Johor Bahru	-	-	0.52	-	-0.26
Keling	-	-	-0.74	-	0.33
Kelang	-0.41	-0.4	-	-	-
Lumut	-0.32	-	-	-	-
Pulau Pinang	-0.45	-0.49	-0.36	-0.71	-
Langkawi	-	-	-	-	-0.37
Ko Taphao Noi	-	-	-	-	-0.5
Bintulu	-0.47	-0.48	-	-	-0.61
Kota Kinabalu	-	-	-	-0.52	0.51
Sandakan	-	-	0.43	-	0.57
Tawau	-0.3	-0.3	-	-0.55	0.43

4.6. Summary and conclusions

In this study, we have used hourly sea-level records measured at 30 TGs to investigate ESL variability around the SCS. Overall, our results show evident temporal and spatial variations of ESL. The maxima distributions reveal a clear spatial and seasonal contrast between the northern (north of 15°N) and southern parts of the study area. This regional coherency indicates different physical mechanisms are responsible for generating extreme surges. Tropical cyclones are the major contributor to ESL at northern TGs whereas the winter monsoonal wind plays an important role at southern sites. The results for the northern TGs show general agreement with *Feng and Tsimplis* [2014], but more importantly, our results indicate that dividing the observations into the summer and winter seasons provides a more meaningful and detailed understanding than in previous studies. Hence, we recommend that future studies consider such seasonal variations in the SCS.

Our results also reveal that the mean sea level and tidal components have substantial impact on the long-term trends of ESLs. Only few TGs show statistically significant trends of rising ESLs with a magnitude of 2- 3 mm/year. Overall, we find that long-term trends at the majority of TGs (and in both seasons) are in line with the mean sea level.

By using the DLM-GEV model, we find evidence of interannual variability in ESL and the 50-year return levels. Our analyses also show that the regional major climate modes (PDO and ENSO) possibly govern ESL, although the detailed mechanism is not known. The finding of time-varying ESL is significant and provides insight for coastal planning and adaptation for some of the most important cities around the SCS coastline.

Acknowledgements

This research was supported by grants from National Research Foundation Singapore (National Research Fellow Award No. NRF-RF2010-04) and the Singapore Ministry of Education under the Research Centres of Excellence initiative Academic Research Fund (AcRF) Complexity Tier 1 Project RGC4/14 “Preparing Asian mega cities for changing climate and the potential increase in extreme sea levels and storm surges”. E. Hill was supported by NRF Award No. NRF-NRFF2010-064. H. Nguyen was supported by QGTD 13.09/2014 project (Vietnam National University). We acknowledge the University of Hawaii Sea Level Center (UHSLC) for hourly tide gauge data at most sites; Hoang Trung Thanh (Vietnam Marine Hydrometeorological Centre) for providing hourly data for Hon Dau, Da Nang, Quy Nhon and Vung Tau tide gauges. We appreciate Francisco M. Calafat for sharing the training data set so that we could test our model; Wang Lin for his East Asian Winter Monsoon index data; Xiangbo Feng, Marcos Marta and Robert Mawdsley for discussing on method and data processing. We would like to express our thanks to Pavel Adamek and Constance Chua for their linguistic advice that significantly improved this manuscript. This work comprises Earth Observatory of Singapore contribution No. XX.

Supporting Information

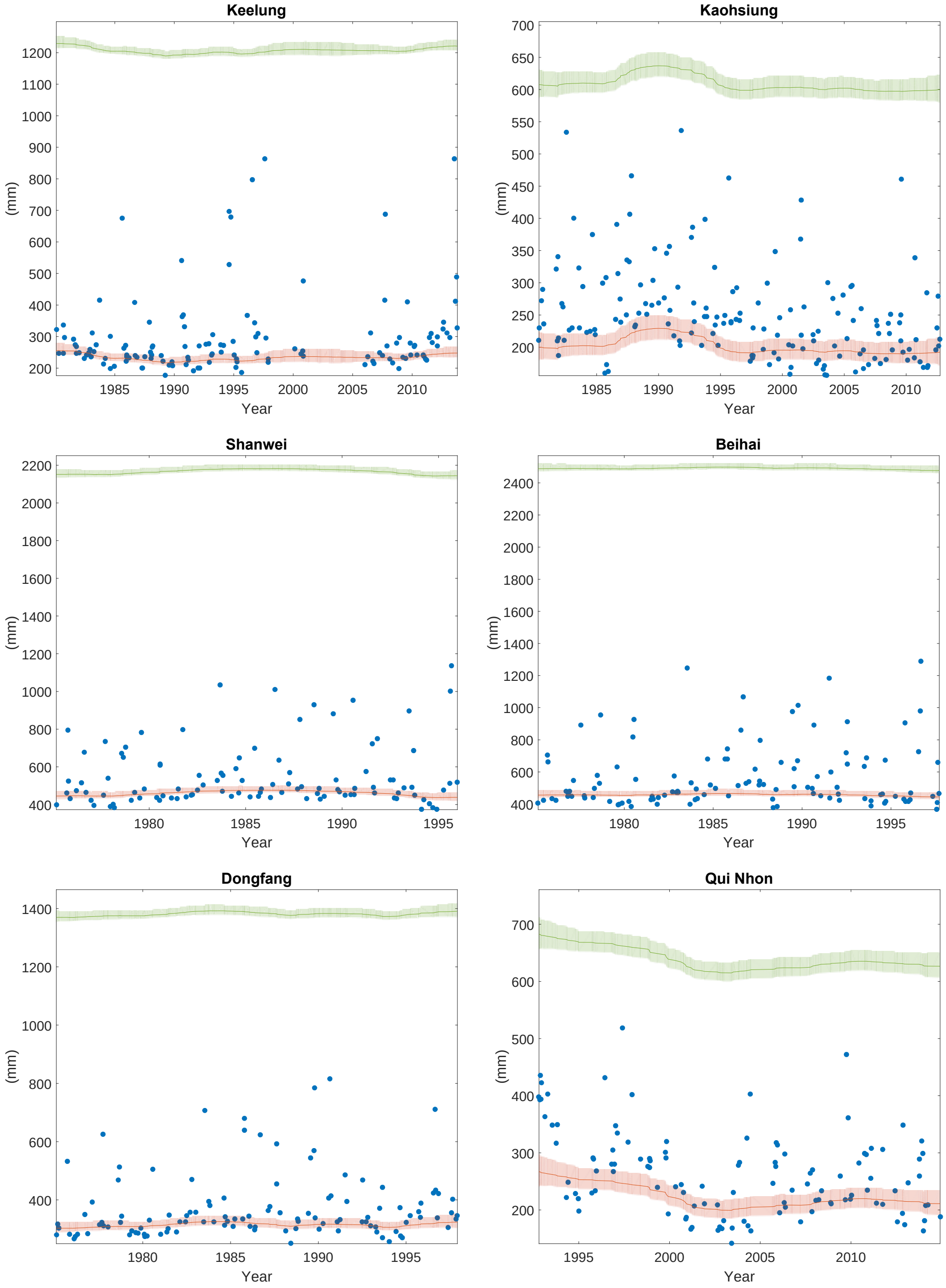

Figure S4. 1: Results from the DLM-GEV model for the five highest non-tidal residuals per year (blue dots) at TGs in the north and one TG in the south (Qui Nhon) show time-varying (mostly interannual) variability for the location parameter (orange solid line) and the 50-year return levels (green solid line). The shaded areas show the 95% credible intervals.

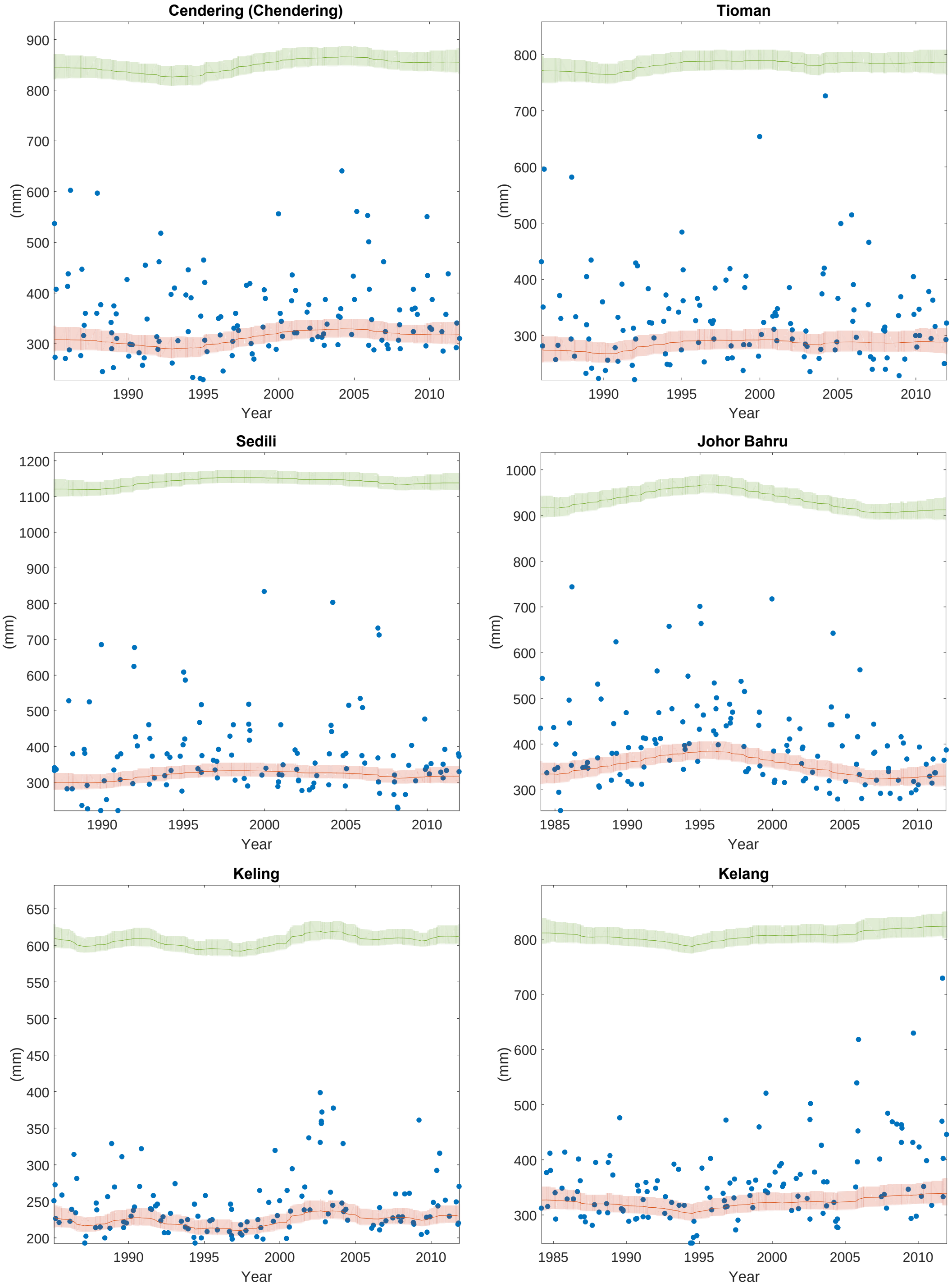

Figure S4. 2: Results from the DLM-GEV model for the five highest non-tidal residuals per year (blue dots) at selected TGs in the south show time-varying (mostly interannual) variability for the location parameter (orange solid line) and the 50-year return levels (green solid line). The shaded areas show the 95% credible intervals.

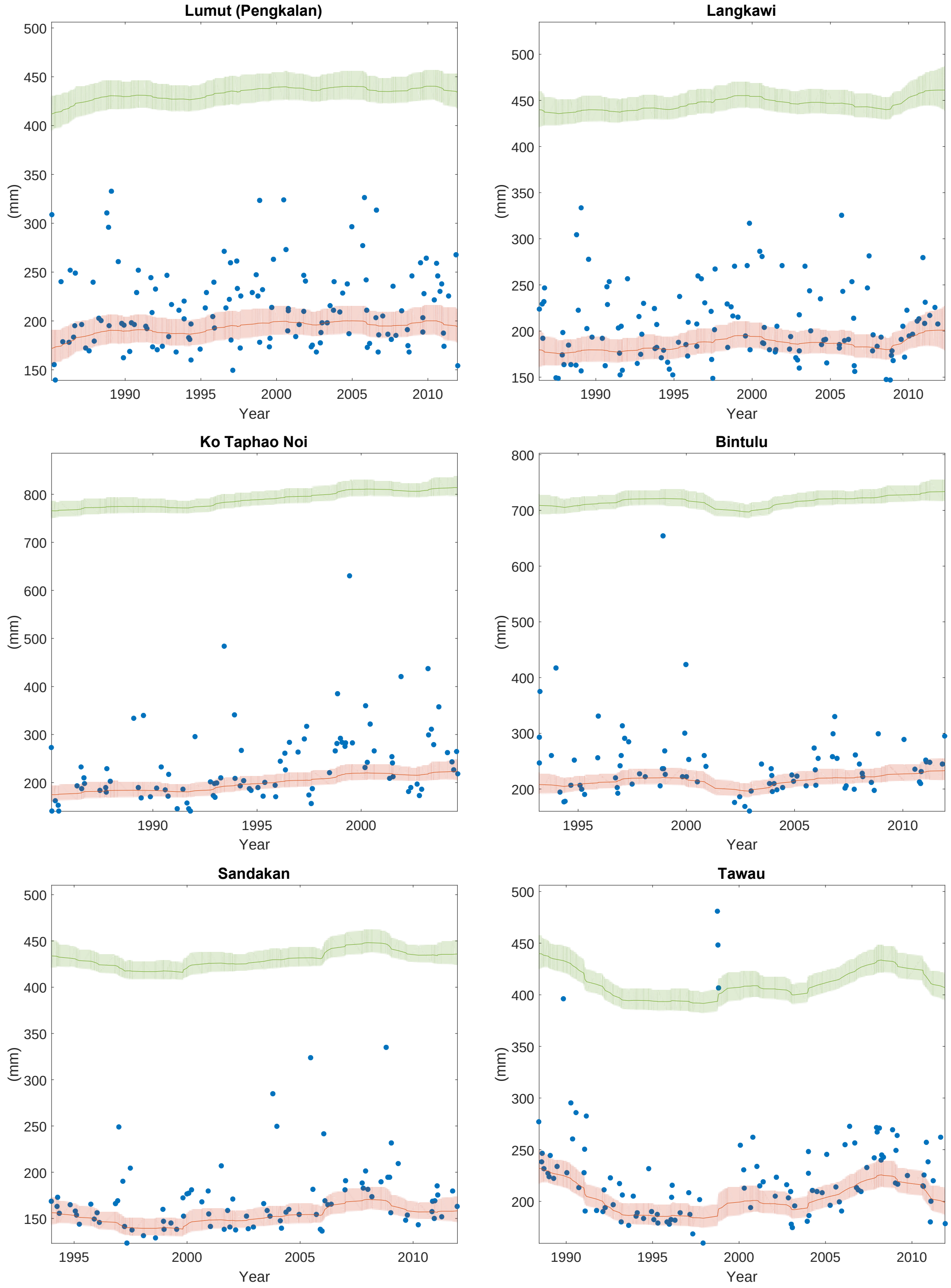

Figure S4. 3: Results from the DLM-GEV model for the five highest non-tidal residuals per year (blue dots) at selected TGs in the south show time-varying (mostly interannual) variability for the location parameter (orange solid line) and the 50-year return levels (green solid line). The shaded areas show the 95% credible intervals.

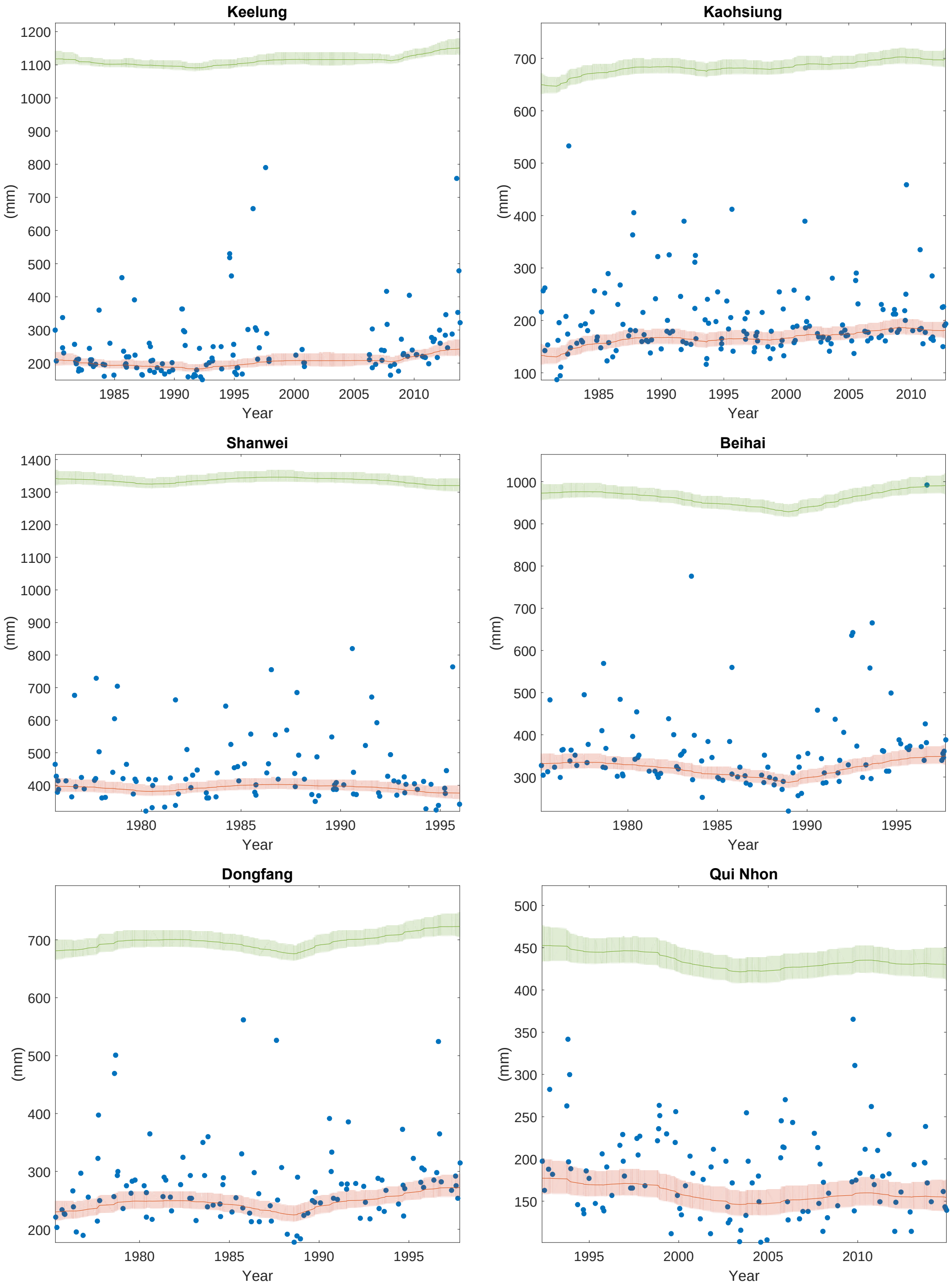

Figure S4. 4: Results from the DLM-GEV model for the five highest skew surges per year (blue dots) at TGs in the north and one TG in the south (Qui Nhon) show time-varying (mostly interannual) variability for the location parameter (orange solid line) and the 50-year return levels (green solid line). The shaded areas show the 95% credible intervals.

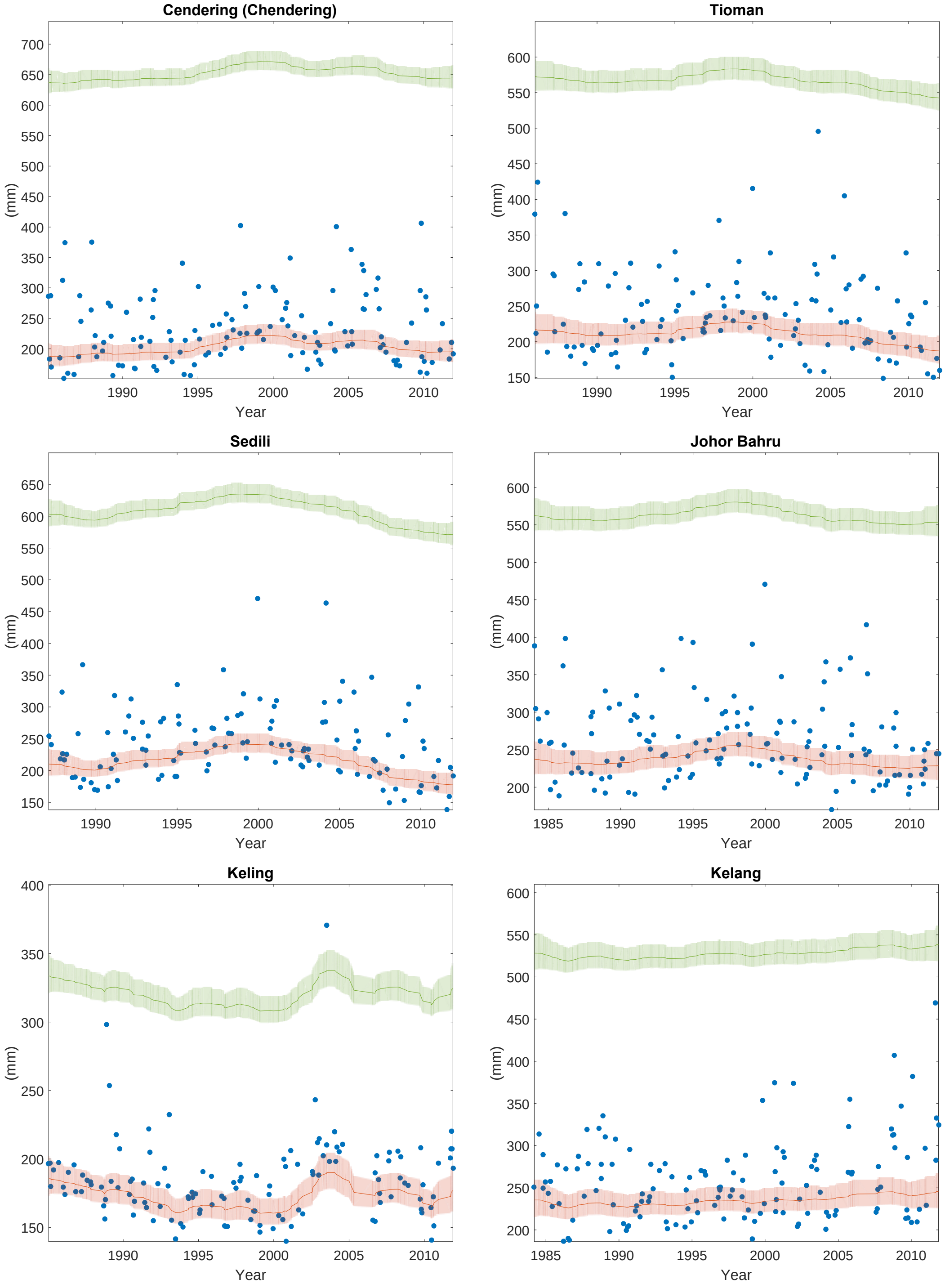

Figure S4. 5: Results from the DLM-GEV model for the five highest skew surges per year (blue dots) at selected TGs in the south show time-varying (mostly interannual) variability for the location parameter (orange solid line) and the 50-year return levels (green solid line). The shaded areas show the 95% credible intervals.

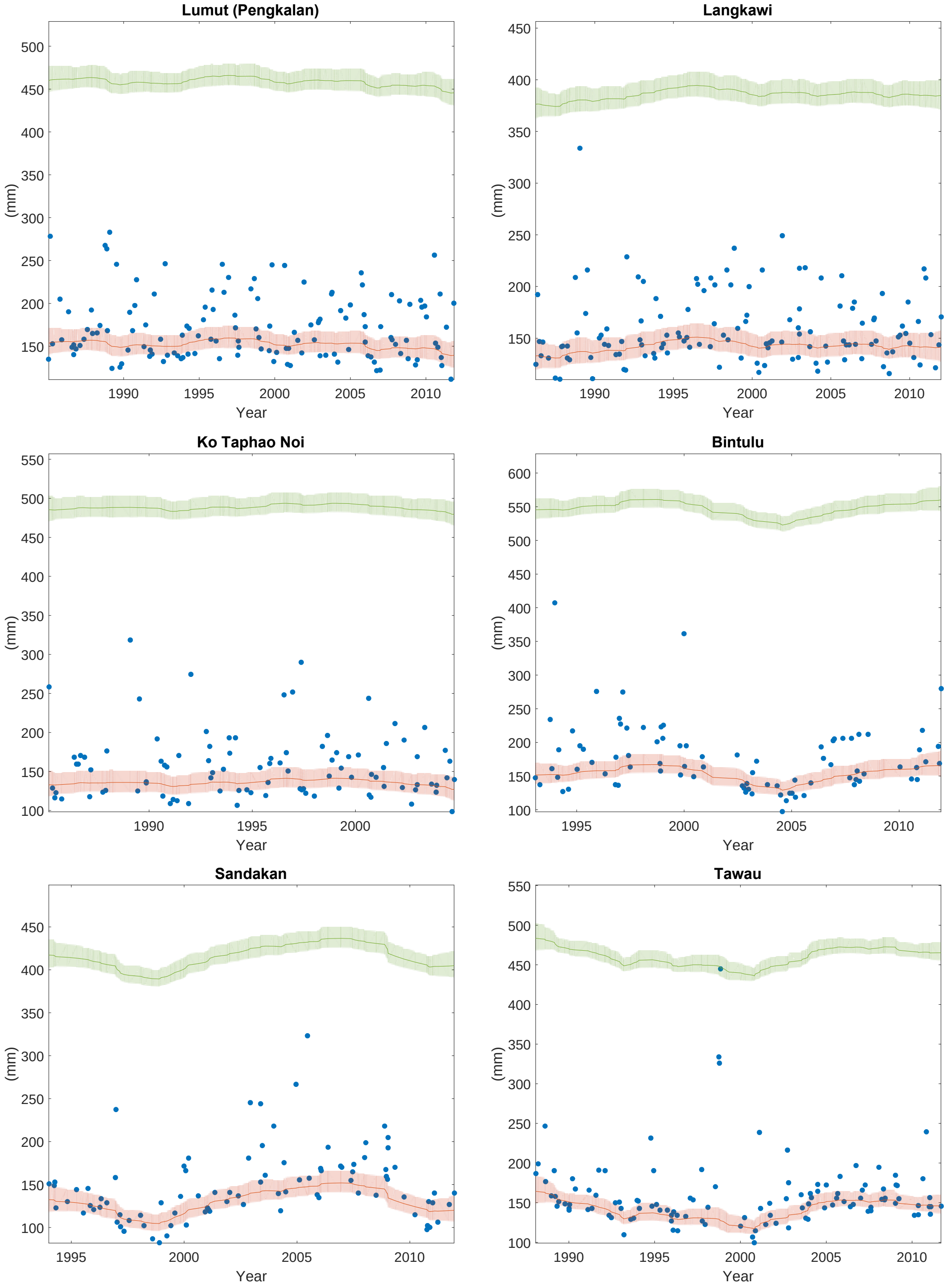

Figure S4. 6: Results from the DLM-GEV model for the five highest skew surges per year (blue dots) at selected TGs in the south show time-varying (mostly interannual) variability for the location parameter (orange solid line) and the 50-year return levels (green solid line). The shaded areas show the 95% credible intervals.

Chapter 5:

Summary and future work

In this thesis, I have used a variety of statistical techniques to address three major scientific aims/questions that can significantly contribute to regional coastal hazard assessments. In this chapter, I summarize my research and discuss limitations as well as future work that may improve on and extend the work presented here.

5.1. Thesis summary

Chapter 2 presents an improved multivariate statistical approach to study the provenance of coastal overwash deposits of different extreme events (the 2004 IOT, three paleo-tsunami and the 2007 storm) on Phra Thong Island, Thailand using grain size parameters, mineralogy and geochemistry data sets. I also examined whether the grain size and geochemistry can be used to discriminate the 2004 IOT and 2007 storm surge deposits.

The multivariate statistical analyses suggest that the mean grain size parameter appears to be a good discriminator of modern storm and tsunami deposits. In contrast, geochemical signatures cannot distinguish those overwash deposits.

I found that the provenance of each coastal overwash deposit in this study is diverse. The 2004 IOT deposits were mainly generated from the shallow nearshore environment whereas the first paleo-tsunami is very likely a mixture of onshore and nearshore sediments. The sediment sources of the second and third paleo-tsunami, however, are not clearly defined by the data sets used in this study. Meanwhile, the provenance of the Storm deposits is most likely the onshore sediments. Furthermore, trace elements exhibit complicated data sets between the 2004 tsunami deposits and three other paleo-tsunami deposits. I then suggest that geochemical signatures need to be carefully used in tsunami studies to avoid misleading interpretations.

Chapter 3 addresses what major forcings govern sea-level variability on an interannual time scale in the South China Sea (SCS) and how sea level around the SCS responds to them. To extract the interannual sea-level signals, I applied an adaptive and data-driven time series analysis method Ensemble Empirical Mode Decomposition (EEMD). I then explored the links between sea level (measured at tide gauges – TGs) and climatic/oceanic-related indices, namely, the El Niño-Southern Oscillation (ENSO), monsoons, and oceanic currents, with the last index represented by the Luzon Strait Transport (LST). The results reveal that on an interannual scale, sea levels across the study area respond differently to external forcings. The ENSO strongly contributes to sea-level variations in the whole study area on an interannual time scale, but it has a greater impact at the southern and central TGs of the SCS. Meanwhile, the winter monsoon clearly influences sea level at the northern TGs. The LST correlates with sea levels least. Apart from the three forcings studied, the multiple linear regression model I used suggests additional forcings not examined in this thesis likely play important roles on interannual sea-level variations. As such, more detailed future investigations are needed to fully account for the additional forcings.

Chapter 4 also investigates sea-level variability around the SCS, but on an hourly scale and focused on extreme sea level (ESL). I have answered how ESL around the

SCS vary spatially and temporally. By using a comprehensive set of 30 TGs around the SCS, I have found that ESL in the northern (north of 15°N) and southern SCS are generated by different physical mechanisms. In general, the sea level maxima at northern TGs are approximately 25-30% higher than those in the south, with the highest values in the summer when tropical cyclone-induced surges dominate the northern signal. In contrast, the lower values in the south reflect the dominance of monsoonal winds in the winter. With regard to temporal variations, the linear long-term trends of ESL are broadly consistent with changes in the mean sea level (MSL) rather than with storminess, a result which demonstrates consistency with studies conducted elsewhere.

I also used the Dynamic Linear Model for the Generalized Extreme Value distribution (DLM-GEV) and found that the temporal variability of ESL in the present study is significantly correlated with major climate modes of ENSO and Pacific Decadal Oscillation. This finding suggests that the return levels for given periods should not be considered as stationary values.

5.2. Suggestions for future work

The use of statistical techniques for different data sets in chapter 2 provides significant insights into quantifying and comparing the provenance of overwash deposits. My results suggest that PAM is less diagnostic for mineralogical and geochemical data sets as the number of variables increases and becomes more complicated. Conversely, PCA and DFA analyses are more powerful in high-dimensional multivariate analyses compared to simple cluster methods. Overall, my statistical approach can be applied not only to proxies presented in this study but also to other suitable criteria such as geo-microbiology and micropaleontology. Thus, the approach is relevant to a wide range of studies focusing on identifying the provenance of extreme event deposits at locations where such deposits are preserved.

In chapters 3 and 4, I have used sea-level records solely from TGs to study sea-level variability. Nevertheless, the TG data sets cover only relatively short periods ranging from 18 to 60 years. The majority of the monthly sea-level records are available only from the 1980s onwards, which limits the extent of climate variability we can capture. On an hourly timescale, data from half of the TGs in the northern SCS ended in 1997, and hence later data about storminess in this stormy area is not available. Given such difficulties, other freely-assessable sea-level data sources could be used alongside TG data. One excellent sea-level data bank is Archiving, Validation and Interpretation of Satellite Oceanographic data (AVISO), which comprises satellite altimetry data available since 1992 – present, thus allowing to fill the data gap.

In addition, the uneven temporal resolution of sea-level records prevents us from synthetically analyzing the entire SCS. While AVISO data provides opportunities to study high frequency sea-level variability on both regional and global scales, the data spans only ~ 25 years, making it inadequate to study events in the last several decades. Thus, past sea-level variability could be studied from reconstructed sea-level data based on the combination of TG data and satellite altimetry data. One such data set is provided by *Hamlington et al.* [2011] who used the cyclostationary empirical orthogonal functions (CSEOFS) to reconstruct global sea level back to the 1950s. However, such globally reconstructed sea level data should be used carefully in regional sea-level studies because global data may not accurately capture signals from complex forcings like those in the SCS.

REFERENCES

Amiruddin, A. M., I. D. Haigh, M. N. Tsimplis, F. M. Calafat, and S. Dangendorf (2015), The seasonal cycle and variability of sea level in the South China Sea, *Journal of Geophysical Research: Oceans*, *120*(8), 5490-5513, doi:10.1002/2015JC010923.

Ashok, K., S. K. Behera, S. A. Rao, H. Weng, and T. Yamagata (2007), El Niño Modoki and its possible teleconnection, *Journal of Geophysical Research: Oceans*, *112*(11), doi:10.1029/2006JC003798.

Ashok, K., and T. Yamagata (2009), Climate change: The El Nino with a difference, *Nature*, *461*(7263), 481-484.

Barnhart, B. L. (2011), "The Hilber-Huang Transform: theory, applications, development.", PhD (Doctor of Philosophy) thesis, University of Iowa, 2011.

Batstone, C., M. Lawless, J. Tawn, K. Horsburgh, D. Blackman, A. McMillan, D. Worth, S. Laeger, and T. Hunt (2013), A UK best-practice approach for extreme sea-level analysis along complex topographic coastlines, *Ocean Eng.*, *71*, 28-39, doi:10.1016/j.oceaneng.2013.02.003.

Baum, C. F. (2006), *An introduction to modern econometrics using Stata*, College Station, Tex. : Stata Press, c2006.

Blott, S. J., and K. Pye (2001), Gradistat: A grain size distribution and statistics package for the analysis of unconsolidated sediments, *Earth Surface Processes and Landforms*, *26*(11), 1237-1248.

Breaker, L. C., and A. Ruzmaikin (2010), The 154-year record of sea level at San Francisco: extracting the long-term trend, recent changes, and other tidbits, *Climate Dynamics*, *36*(3-4), 545-559, doi:10.1007/s00382-010-0865-4.

Breaker, L. C., and A. Ruzmaikin (2013), Estimating Rates of Acceleration Based on the 157-Year Record of Sea Level from San Francisco, California, U.S.A, *Journal of Coastal Research, 286*(1), 43-51, doi:10.2112/JCOASTRES-D-12-00048.1.

Brill, D., K. Jankaew, and H. Brückner (2015), Holocene evolution of Phra Thong's beach-ridge plain (Thailand) — Chronology, processes and driving factors, *Geomorphology*, *245*, 117-134, doi:http://dx.doi.org/10.1016/j.geomorph.2015.05.035.

Brill, D., N. Klasen, H. Brückner, K. Jankaew, A. Scheffers, D. Kelletat, and S. Scheffers (2012a), OSL dating of tsunami deposits from Phra Thong Island, Thailand, *Quaternary Geochronology*, *10*(0), 224-229, doi:http://dx.doi.org/10.1016/j.quageo.2012.02.016.

Brill, D., N. Klasen, K. Jankaew, H. Brückner, D. Kelletat, A. Scheffers, and S. Scheffers (2012b), Local inundation distances and regional tsunami recurrence in the Indian Ocean inferred from luminescence dating of sandy deposits in Thailand, *Nat. Hazards Earth Syst. Sci.*, *12*(7), 2177-2192, doi:10.5194/nhess-12-2177-2012.

Brill, D., A. Pint, K. Jankaew, P. Frenzel, K. Schwarzer, A. Vött, and H. Brückner (2014), Sediment Transport and Hydrodynamic Parameters of Tsunami Waves Recorded in Onshore Geoarchives, *Journal of Coastal Research*, *297*, 922-941, doi:10.2112/JCOASTRES-D-13-00206.1.

Bryant, E. (2008), *Tsunami : The Underrated Hazard (Second Edition) / by Edward Bryant*, Berlin, Heidelberg : Praxis Publishing Ltd, Chichester, UK, 2008.

Calafat, F. M., and D. P. Chambers (2013), Quantifying recent acceleration in sea level unrelated to internal climate variability, *Geophys. Res. Lett.*, *40*(14), 3661-3666, doi:10.1002/grl.50731.

Canty, A. (2002), Resampling Methods in R: The boot Package, *R News*, *2(3)*(3), 2-7.

Canty, A., and B. Ripley (2016), boot: Bootstrap R (S-Plus) Functions. R package version 1.3-18., edited.

Capotondi, A., A. T. Wittenberg, M. Newman, E. Di Lorenzo, J.-Y. Yu, P. Braconnot, J. Cole, B. Dewitte, B. Giese, E. Guilyardi, F.-F. Jin, K. Karnauskas, B. Kirtman, T. Lee, N. Schneider, Y. Xue, and S.-W. Yeh (2014), Understanding ENSO Diversity, *Bull. Am. Meteorol. Soc.*, *96*(6), 921-938, doi:10.1175/BAMS-D-13-00117.1.

Carton, J. A., and B. S. Giese (2008), A Reanalysis of Ocean Climate Using Simple Ocean Data Assimilation (SODA), *Monthly Weather Review*, *136*(8), 2999-3017, doi:10.1175/2007MWR1978.1.

Chagué-Goff, C. (2010), Chemical signatures of palaeotsunamis: a forgotten proxy?, *Marine Geology*, *271*(1-2), 67-71.

Chagué-Goff, C., A. Andrew, W. Szczuciński, J. Goff, and Y. Nishimura (2012a), Geochemical signatures up to the maximum inundation of the 2011 Tohoku-oki tsunami - implications for the 869AD Jogan and other palaeotsunamis, *Sedimentary Geology*, *282*, 65-77.

Chagué-Goff, C., J. Goff, H. K. Y. Wong, and M. Cisternas (2015), Insights from geochemistry and diatoms to characterise a tsunami's deposit and maximum inundation limit, *Marine Geology, 359,* 22-34, doi:10.1016/j.margeo.2014.11.009.

Chagué-Goff, C., P. Niedzielski, H. K. Y. Wong, W. Szczuciński, D. Sugawara, and J. Goff (2012b), Environmental impact assessment of the 2011 Tohoku-oki tsunami on the Sendai Plain, *Sedimentary Geology*, *282,* 175-187, doi:10.1016/j.sedgeo.2012.06.002.

Chagué-Goff, C., J. L. Schneider, J. R. Goff, D. Dominey-Howes, and L. Strotz (2011), Expanding the proxy toolkit to help identify past events - lessons from the 2004 Indian Ocean Tsunami and the 2009 South Pacific Tsunami, *Earth-Science Reviews*, *107*(1-2), 107-122.

Chang, C. W. J., H.-H. Hsu, C.-R. Wu, and W.-J. Sheu (2008), Interannual mode of sea level in the South China Sea and the roles of El Niño and El Niño Modoki, *Geophys. Res. Lett.*, *35*(3), L03601, doi:10.1029/2007GL032562.

Chen, H., P. Tkalich, P. Malanotte-Rizzoli, and J. Wei (2012), The forced and free response of the South China Sea to the large-scale monsoon system, *Ocean Dynamics*, *62*(3), 377-393, doi:10.1007/s10236-011-0511-7.

Cheng, X., S.-P. Xie, Y. Du, J. Wang, X. Chen, and J. Wang (2015), Interannual-to-decadal variability and trends of sea level in the South China Sea, *Climate Dynamics*, doi:10.1007/s00382-015-2756-1.

Choowong, M., N. Murakoshi, K. Hisada, T. Charoentitirat, P. Charusiri, S. Phantuwongraj, P. Wongkok, A. Choowong, R. Subsayjun, V. Chutakositkanon, K. Jankaew, and P. Kanjanapayont (2008), Flow conditions of the 2004 Indian Ocean tsunami in Thailand, inferred from capping bedforms and sedimentary structures, *Terra Nova, 20*(2), 141-149, doi:10.1111/j.1365-3121.2008.00799.x.

Church, J. A., P. U. Clark, A. Cazenave, J. M. Gregory, S. Jevrejeva, A. Levermann, M. A. Merrifield, G. A. Milne, R. S. Nerem, P. D. Nunn, A. J. Payne, W. T. Pfeffer, D. Stammer, and A. S. Unnikrishnan (2013), Sea Level Change., in *Climate Change 2013: The Physical Science Basis. Contribution of Working Group I to the Fifth Assessment Report of the Intergovernmental Panel on Climate Change*, edited by T. F. Stocker, D. Qin, G.-K. Plattner, M. Tignor, S.K. Allen, J. Boschung, A. Nauels, Y. Xia, V. Bex and P.M. Midgley, Cambridge University Press, Cambridge, United Kingdom and New York, NY, USA.

Church, J. A., and N. J. White (2006), A 20th century acceleration in global sea-level rise, *Geophys. Res. Lett., 33*(1), doi:10.1029/2005GL024826.

Church, J. A., and N. J. White (2011), Sea-Level Rise from the Late 19th to the Early 21st Century, *Surveys in Geophysics*, *32*(4), 585-602, doi:10.1007/s10712-011-9119-1.

Cisternas, M., B. F. Atwater, F. Torrejon, Y. Sawai, G. Machuca, M. Lagos, A. Eipert, C. Youlton, I. Salgado, T. Kamataki, M. Shishikura, C. P. Rajendran, J. K. Malik, Y. Rizal, and M. Husni (2005), Predecessors of the giant 1960 Chile earthquake, *Nature*, *437*(7057), 404-407, doi:http://www.nature.com/nature/journal/v437/n7057/suppinfo/nature03943_S1.html.

Clarke, A. J. (2008), *An Introduction to the Dynamics of El Nino & the Southern Oscillation.*, Burlington : Elsevier, 2008.

Codiga, D. L. (2011), Unified Tidal Analysis and Prediction Using the UTide Matlab Functions., *Technical Rep. 2011-01*, 59 pp, Graduate School of Oceanography, University of Rhode Island, Narragansett, RI. ftp://www.po.gso.uri.edu/ pub/downloads/codiga/pubs/2011Codiga-UTide-Report.pdf, ftp://www.po.gso.uri.edu/ pub/downloads/codiga/pubs/2011Codiga-UTide-Report.pdf.

Coles, S. (2001), *An Introduction to Statistical Modeling of Extreme Values*, London : Springer London : Imprint: Springer, 2001.

Cuven, S., R. Paris, S. Falvard, E. Miot-Noirault, M. Benbakkar, J. L. Schneider, and I. Billy (2013), High-resolution analysis of a tsunami deposit: case-study from the 1755 Lisbon tsunami in southwestern Spain, *Marine Geology*, *337*, 98-111, doi:10.1016/j.margeo.2013.02.002.

Dangendorf, S., S. Müller-Navarra, J. Jensen, F. Schenk, T. Wahl, and R. Weisse (2014), North Sea Storminess from a Novel Storm Surge Record since AD 1843, *Journal of Climate*, *27*(10), 3582-3595, doi:doi:10.1175/JCLI-D-13-00427.1.

Davis, J. C. (2002), *Statistics and Data Analysis in Geology* third ed., 646 pp., John Wiley & Sons, New York.

Ding, X., D. Zheng, Y. Chen, J. Chao, and Z. Li (2001), Sea level change in Hong Kong from tide gauge measurements of 1954-1999, *Journal of Geodesy*, *74*(10), 683-689, doi:10.1007/s001900000128.

Donald, W. K. A., and J. C. Monahan (1992), An Improved Heteroskedasticity and Autocorrelation Consistent Covariance Matrix Estimator, *Econometrica*, *60*(4), 953-966, doi:10.2307/2951574.

Durbin, J., and S. J. Koopman (2012), *Time series analysis by state space methods.* , Oxford : Oxford University Press, 2012.

2nd ed.

Durbin, J., and G. S. Watson (1950), Testing for Serial Correlation in Least Squares Regression: I, *Biometrika, 37*(3/4), 409-428, doi:10.2307/2332391.

Durbin, J., and G. S. Watson (1951), Testing for Serial Correlation in Least Squares Regression. II, *Biometrika, 38*(1/2), 159-177, doi:10.2307/2332325.

Durbin, J., and G. S. Watson (1971), Testing for serial correlation in least squares regression.III, *Biometrika*, *58*(1), 1-19, doi:10.1093/biomet/58.1.1.

Efron, B., and R. Tibshirani (1993), *An introduction to the bootstrap,* New York : Chapman & Hall, c1993.

Everitt, B., and T. Hothorn (2011)*, An Introduction to Applied Multivariate Analysis with R: Use R!*, Springer, New York, doi:10.1007/978-1-4419-9650-3.

Ezer, T. (2013), Sea level rise, spatially uneven and temporally unsteady: Why the U.S. East Coast, the global tide gauge record, and the global altimeter data show different trends, *Geophys. Res. Lett.*, *40*(20), 5439-5444, doi:10.1002/2013GL057952.

Ezer, T. (2015), Detecting changes in the transport of the Gulf Stream and the Atlantic overturning circulation from coastal sea level data: The extreme decline in 2009–2010 and estimated variations for 1935–2012, *Global and Planetary Change*, *129*, 23-36, doi:10.1016/j.gloplacha.2015.03.002.

Ezer, T., and W. B. Corlett (2012), Is sea level rise accelerating in the Chesapeake Bay? A demonstration of a novel new approach for analyzing sea level data, *Geophys. Res. Lett.*, *39*(19), doi:10.1029/2012GL053435.

Fahrmeir, L., and S. Lang (2001), Bayesian inference for generalized additive mixed models based on Markov random field priors, *Journal of the Royal Statistical Society: Series C (Applied Statistics)*, *50*(2), 201-220, doi:10.1111/1467-9876.00229.

Fang, G., H. Chen, Z. Wei, Y. Wang, X. Wang, and C. Li (2006), Trends and interannual variability of the South China Sea surface winds, surface height, and surface temperature in the recent decade, *Journal of Geophysical Research: Oceans*, *111*(11), doi:10.1029/2005JC003276.

Feldens, P., K. Schwarzer, D. Sakuna, W. Szczuciński, and P. Sompongchaiyakul (2012), Sediment distribution on the inner continental shelf off Khao Lak (Thailand) after the 2004 Indian Ocean tsunami, *Earth, Planets and Space*, *64*(10), 875-887, doi:10.5047/eps.2011.09.001.

Feng, X., and M. N. Tsimplis (2014), Sea level extremes at the coasts of China, *Journal of Geophysical Research: Oceans*, *119*(3), 1593-1608, doi:10.1002/2013JC009607.

Firing, Y. L., and M. A. Merrifield (2004), Extreme sea level events at Hawaii: Influence of mesoscale eddies, *Geophys. Res. Lett.*, *31*(24), n/a-n/a, doi:10.1029/2004GL021539.

Folk, R. L., and W. C. Ward (1957), Brazos River bar [Texas]; a study in the significance of grain size parameters, *Journal of Sedimentary Research*, *27*(1), 3-26.

Font, E., C. Veiga-Pires, M. Pozo, S. Nave, S. Costas, F. Ruiz Muñoz, M. Abad, N. Simões, S. Duarte, and J. Rodríguez-Vidal (2013), Benchmarks and sediment source(s) of the 1755 Lisbon tsunami deposit at Boca do Rio Estuary, *Marine Geology*, *343*, 1-14, doi:10.1016/j.margeo.2013.06.008.

Fujino, S., H. Naruse, D. Matsumoto, T. Jarupongsakul, A. Sphawajruksakul, and N. Sakakura (2009), Stratigraphic evidence for pre-2004 tsunamis in southwestern Thailand, *Marine Geology*, *262*(1-4), 25-28.

Fujino, S., H. Naruse, D. Matsumoto, N. Sakakura, A. Suphawajruksakul, and T. Jarupongsakul (2010), Detailed measurements of thickness and grain size of a widespread onshore tsunami deposit in Phang-nga Province, southwestern Thailand, *Island Arc*, *19*(3), 389-398.

Fujino, S., H. Naruse, A. Suphawajruksakul, T. Jarupongsakul, M. Murayama, and T. Ichihara (2008), Thickness and grain-size distribution of Indian Ocean Tsunami Deposits at Khao Lak and Phra Thong Island, south-western Thailand, in *Tsunamiites - Features and Implications*, edited by T. Shiki, Y. Tsuji, T. Yamazaki and K. Minoura, pp. 123-132, Elsevier Inc., Amsterdam, doi:10.1016/B978-0-444-51552-0.00008-4.

Goff, J., C. Chagué-Goff, S. Nichol, B. Jaffe, and D. Dominey-Howes (2012), Progress in palaeotsunami research, *Sedimentary Geology*, *243-244*, 70-88, doi:10.1016/j.sedgeo.2011.11.002.

Goff, J., and D. Dominey-Howes (2013), 13.13 Tsunami, in *Treatise on Geomorphology*, edited by J. F. Shroder, pp. 204-218, Academic Press, San Diego, doi:http://dx.doi.org/10.1016/B978-0-12-374739-6.00359-6.

Goff, J., B. G. McFadgen, and C. Chagué-Goff (2004), Sedimentary differences between the 2002 Easter storm and the 15th-century Okoropunga tsunami, southeastern North Island, New Zealand, *Marine Geology*, *204*(1-2), 235-250.

Gönnert, G., S. K. Dube, T. Murty, and W. Siefert (2001), *Global Storm Surges: Theory, Observations and Applications*, 623 pp., Die Küste.

Gouramanis, C., A. D. Switzer, D. T. Pham, C. Rubin, Y. S. Lee, C. Bristow, and K. Jankaew (2014a), Thin-bed Ground-penetrating radar analysis of preserved modern and palaeotsunami deposits from Phra Thong Island, Thailand, paper presented at 15th International Conference on Ground Penetrating Radar, GPR 2014, Institute of Electrical and Electronics Engineers Inc.

Gouramanis, C., A. D. Switzer, P. M. Polivka, C. S. Bristow, K. Jankaew, P. T. Dat, J. Pile, C. M. Rubin, L. Yingsin, S. R. Ildefonso, and H. M. Jol (2015), Ground penetrating radar examination of thin tsunami beds — A case study from Phra Thong Island, Thailand, *Sedimentary Geology*, *329*, 149-165, doi:http://dx.doi.org/10.1016/j.sedgeo.2015.09.011.

Gouramanis, C., A. D. Switzer, S. Seshachalam, A. Karthikeyan, D. T. Pham, S. Carson, J. Pilarczyk, S. M. Hussain, and W. Yap (2014b), Same Same, But Different: Sedimentological Comparison of Recent Storm and Tsunami Deposits from the South-Eastern Coastline of India, *Abstract NH21A-3811 presented at 2014 Fall Meeting, AGU, San Francisco, Calif., 15-19 Dec.*

Grinsted, A., J. C. Moore, and S. Jevrejeva (2004), Application of the cross wavelet transform and wavelet coherence to geophysical times series, *Nonlinear Processes Geophys.*, *11*(5-6), 561-566, doi:10.1029/2003JD003417.

Groemping, U. (2006), Relative Importance for Linear Regression in R: The Package relaimpo, *2006*, *17*(1), 27, doi:10.18637/jss.v017.i01.

Haigh, I. D., M. Eliot, and C. Pattiaratchi (2011), Global influences of the 18.61 year nodal cycle and 8.85 year cycle of lunar perigee on high tidal levels, *Journal of Geophysical Research*, *116*(C6), doi:10.1029/2010jc006645.

Haigh, I. D., L. R. MacPherson, M. S. Mason, E. M. S. Wijeratne, C. B. Pattiaratchi, R. P. Crompton, and S. George (2014a), Estimating present day extreme water level exceedance probabilities around the coastline of Australia: tropical cyclone-induced storm surges, *Climate Dynamics*, *42*(1), 139-157, doi:10.1007/s00382-012-1653-0.

Haigh, I. D., M. P. Wadey, S. L. Gallop, H. Loehr, R. J. Nicholls, K. Horsburgh, J. M. Brown, and E. Bradshaw (2015), A user-friendly database of coastal flooding in the United Kingdom from 1915–2014, *Scientific Data*, *2*, 150021, doi:10.1038/sdata.2015.21.

Haigh, I. D., E. M. S. Wijeratne, L. R. MacPherson, C. B. Pattiaratchi, M. S. Mason, R. P. Crompton, and S. George (2014b), Estimating present day extreme water level exceedance probabilities around the coastline of Australia: tides, extra-tropical storm surges and mean sea level, *Climate Dynamics*, *42*(1), 121-138, doi:10.1007/s00382-012-1652-1.

Hamlington, B. D., R. R. Leben, R. S. Nerem, W. Han, and K. Y. Kim (2011), Reconstructing sea level using cyclostationary empirical orthogonal functions, *Journal of Geophysical Research: Oceans*, *116*(12), doi:10.1029/2011JC007529.

Han, G., and W. Huang (2008a), Low-frequency sea-level variability in the South China Sea and its relationship to ENSO, *Theoretical and Applied Climatology*, *97*(1-2), 41-52, doi:10.1007/s00704-008-0070-0.

Han, G., and W. Huang (2008b), Pacific Decadal Oscillation and Sea Level Variability in the Bohai, Yellow, and East China Seas, *Journal of Physical Oceanography*, *38*(12), 2772-2783, doi:10.1175/2008JPO3885.1.

Hanson, S., R. Nicholls, N. Ranger, S. Hallegatte, J. Corfee-Morlot, C. Herweijer, and J. Chateau (2011), A global ranking of port cities with high exposure to climate extremes, *Climatic Change*, *104*(1), 89-111, doi:10.1007/s10584-010-9977-4.

Hill, E. M., R. M. Ponte, and J. L. Davis (2007), Dynamic and regression modeling of ocean variability in the tide-gauge record at seasonal and longer periods, *Journal of Geophysical Research: Oceans*, *112*(C05007), doi:10.1029/2006JC003745.

Holgate, S. J., A. Matthews, P. L. Woodworth, L. J. Rickards, M. E. Tamisiea, E. Bradshaw, P. R. Foden, K. M. Gordon, S. Jevrejeva, and J. Pugh (2013), New data systems and products at the permanent service for mean sea level, *Journal of Coastal Research*, *29*(3), 493-504, doi:10.2112/JCOASTRES-D-12-00175.1.

Hong Kong Royal Observatory (1980), Meteorological Results 1980. Part III-Tropical Cyclone Summaries*Rep.*, 86 pp, Royal Observatory, Hong Kong (http://www.hko.gov.hk/publica/tc/tc1980.pdf), http://www.hko.gov.hk/publica/tc/tc1980.pdf.

Horsburgh, K. J., and C. Wilson (2007), Tide-surge interaction and its role in the distribution of surge residuals in the North Sea, *Journal of Geophysical Research: Oceans*, *112*(C8), n/a-n/a, doi:10.1029/2006JC004033.

Huang, N. E., Z. Shen, S. R. Long, M. C. Wu, H. H. Shih, Q. Zheng, N.-C. Yen, C. C. Tung, and H. H. Liu (1998), The empirical mode decomposition and the Hilbert spectrum for nonlinear and non-stationary time series analysis, *Proceedings of the Royal Society of London A: Mathematical, Physical and Engineering Sciences*, *454*(1971), 903-995, doi:10.1098/rspa.1998.0193.

Huang, N. E., and Z. Wu (2008), A review on Hilbert-Huang transform: Method and its applications to geophysical studies, *Reviews of Geophysics*, *46*(2), n/a-n/a, doi:10.1029/2007RG000228.

Huerta, G., and B. Sansó (2007), Time-varying models for extreme values, *Environmental and Ecological Statistics*, *14*(3), 285-299, doi:10.1007/s10651-007-0014-3.

Huerta, G., and G. A. Stark (2013), Dynamic and spatial modelling of block maxima extremes., in *Bayesian Theory and Applications*, edited by P. Damien, P. Dellaportas, N. G. Polson and D. A. Stephens, pp. 183-199, Oxford University Press, Oxford, doi:10.1093/acprof:oso/9780199695607.001.0001.

Intergovernmental Oceanographic Commission (2016), Tsunami glossary *IOC Technical Series Rep. 85*, Paris, UNESCO, (English, French, Spanish, Arabic, Chineses), http://itic.ioc-unesco.org/images/stories/about_tsunamis/tsunami_glossary/tsunami_glossary_en_2016_sm.pdf.

Jackson, D. A. (1993), Stopping rules in principal components analysis: a comparison of heuristical and statistical approaches, *Ecology*, *74*(8), 2204-2214.

Jagodziński, R., B. Sternal, W. Szczuciński, C. Chagué-Goff, and D. Sugawara (2012), Heavy minerals in the 2011 Tohoku-oki tsunami deposits-insights into sediment sources and hydrodynamics, *Sedimentary Geology*, *282*, 57-64, doi:10.1016/j.sedgeo.2012.07.015.

Jagodziński, R., B. Sternal, W. Szczuciński, and S. Lorenc (2009), Heavy minerals in the 2004 tsunami deposits on Kho Khao Island, Thailand, *Polish Journal of Environmental Studies 18 (1)*(1), 103-110.

Jankaew, K., B. F. Atwater, Y. Sawai, M. Choowong, T. Charoentitirat, M. E. Martin, and A. Prendergast (2008), Medieval forewarning of the 2004 Indian Ocean tsunami in Thailand, *Nature*, *455*(7217), 1228-1231.

Jankaew, K., D. Brill, M. E. Martin, and Y. Sawai (2011), Distribution and sedimentary characteristics of tsunami depostits on Phra Thong Island, Thailand, in *2nd INQUA-IGCP-567 International Workshop on Active Tectonics, Earthquake Geology, Archaeology and Engineering*, edited, pp. 99-101, Corinth, Greece.

Jevrejeva, S., A. Grinsted, J. C. Moore, and S. Holgate (2006), Nonlinear trends and multiyear cycles in sea level records, *Journal of Geophysical Research*, *111*(C9), C09012, doi:10.1029/2005JC003229.

Kain, C. L., C. Gomez, D. E. Hart, P. Wassmer, J. Goff, and C. Starheim (2014), Assessing topographic controls on flow direction in washover deposits using measurements of Magnetic Fabric, *Marine Geology*, *350*, 16-26, doi:http://dx.doi.org/10.1016/j.margeo.2014.01.010.

Kaufman, L., and P. J. Rousseeuw (2005), *Finding groups in data : an introduction to cluster analysis*, Wiley, Hoboken, N.J.

Kortekaas, S., and A. G. Dawson (2007), Distinguishing tsunami and storm deposits: an example from Martinhal, SW Portugal, *Sedimentary Geology*, *200*(3–4), 208-221, doi:http://dx.doi.org/10.1016/j.sedgeo.2007.01.004.

Kuwatani, T., K. Nagata, M. Okada, T. Watanabe, Y. Ogawa, T. Komai, and N. Tsuchiya (2014), Machine-learning techniques for geochemical discrimination of 2011 Tohoku tsunami deposits, *Scientific Reports*, *4*, doi:10.1038/srep07077

http://www.nature.com/srep/2014/141117/srep07077/abs/srep07077.html#supplementary-information.

Lau, A. Y. A., A. D. Switzer, D. Dominey-Howes, J. C. Aitchison, and Y. Zong (2010), Written records of historical tsunamis in the northeastern South China Sea – challenges associated with developing a new integrated database, *Nat. Hazards Earth Syst. Sci.*, *10*(9), 1793-1806, doi:10.5194/nhess-10-1793-2010.

Lee, H. S. (2013), Estimation of extreme sea levels along the Bangladesh coast due to storm surge and sea level rise using EEMD and EVA, *Journal of Geophysical Research: Oceans*, *118*(9), 4273-4285, doi:10.1002/jgrc.20310.

Leffler, K. E., and D. A. Jay (2009), Enhancing tidal harmonic analysis: Robust (hybrid) solutions, *Continental Shelf Research*, *29*(1), 78-88, doi:http://dx.doi.org/10.1016/j.csr.2008.04.011.

Legendre, P., and L. Legendre (2012), *Numerical ecology*, Amsterdam : Elsevier, 2012.

Third English edition.

Li, J., and Q. Zeng (2002), A unified monsoon index, *Geophys. Res. Lett.*, *29*(8), 115-111-115-114, doi:10.1029/2001GL013874.

Li, L., A. D. Switzer, Y. Wang, R. Weiss, Q. Qiu, C.-H. Chan, and P. Tapponnier (2015), What caused the mysterious eighteenth century tsunami that struck the southwest Taiwan coast?, *Geophys. Res. Lett.*, *42*(20), 8498-8506, doi:10.1002/2015GL065567.

Liang, W.-D., J. C. Jan, and T. Y. Tang (2000), Climatological Wind and Upper Ocean Heat Content in the South China Sea *Acta Oceanographica Taiwanica 38*, 91-114.

Liu, K., and M. L. Fearn (2000), Reconstruction of prehistoric landfall frequencies of catastrophic hurricanes in northwestern Florida from lake sediment records, *Quaternary Research*, *54*(2), 238-245, doi:http://dx.doi.org/10.1006/qres.2000.2166.

Liu, Q., A. Kaneko, and S. Jilan (2008), Recent progress in studies of the South China Sea circulation, *Journal of Oceanography*, *64*(5), 753-762, doi:10.1007/s10872-008-0063-8.

Lowe, J. A., P. L. Woodworth, T. Knutson, R. E. McDonald, K. L. McInnes, K. Woth, H. von Storch, J. Wolf, V. Swail, N. B. Bernier, S. Gulev, K. J. Horsburgh, A. S. Unnikrishnan, J. R. Hunter, and R. Weisse (2010), Past and Future Changes in Extreme Sea Levels and Waves, in *Understanding Sea-Level Rise and Variability*, edited, pp. 326-375, Wiley-Blackwell, doi:10.1002/9781444323276.ch11.

Lunn, D., D. Spiegelhalter, A. Thomas, and N. Best (2009), The BUGS project: Evolution, critique and future directions, *Statistics in Medicine*, *28*(25), 3049-3067, doi:10.1002/sim.3680.

Luu, Q. H., P. Tkalich, and T. W. Tay (2015), Sea level trend and variability around Peninsular Malaysia, *Ocean Sci.*, *11*(4), 617-628, doi:10.5194/os-11-617-2015.

Maechler, M., P. Rousseeuw, A. Struyf, M. Hubert, and K. Hornik (2014), cluser: Cluster Analysis Basics and Extensions. R package version 1.15.3, edited.

Mantua, N. J., S. R. Hare, Y. Zhang, J. M. Wallace, and R. C. Francis (1997), A Pacific interdecadal climate oscillation with impacts on salmon production, *Bull. Am. Meteorol. Soc.*(6), 1069.

Marcos, M., F. M. Calafat, Á. Berihuete, and S. Dangendorf (2015), Long-term variations in global sea level extremes, *Journal of Geophysical Research: Oceans*, *120*(12), 8115-8134, doi:10.1002/2015JC011173.

Marcos, M., M. N. Tsimplis, and A. G. P. Shaw (2009), Sea level extremes in southern Europe, *Journal of Geophysical Research: Oceans*, *114*(C1), doi:10.1029/2008JC004912.

Mawdsley, R., and I. D. Haigh (2016), Spatial and temporal variability and long-term trends in skew surges globally, *Frontiers in Marine Science*, *3*, doi:10.3389/fmars.2016.00029.

Mawdsley, R. J., I. D. Haigh, and N. C. Wells (2015), Global secular changes in different tidal high water, low water and range levels, *Earth's Future*, *3*(2), 66-81, doi:10.1002/2014EF000282.

Menéndez, M., and P. L. Woodworth (2010), Changes in extreme high water levels based on a quasi-global tide-gauge data set, *Journal of Geophysical Research*, *115*(C10), C10011-C10011, doi:10.1029/2009JC005997.

Milne, G. A., W. R. Gehrels, C. W. Hughes, and M. E. Tamisiea (2009), Identifying the causes of sea-level change, *Nature Geosci*, *2*(7), 471-478.

Minoura, K., F. Imamura, D. Sugawara, Y. Kono, and T. Iwashita (2001), The 869 Jogan tsunami deposit and recurrence interval of large-scale tsunami on the Pacific coast of northeast Japan, *Journal of Natural Disaster Science 23*(2), 83-88.

Monecke, K., W. Finger, D. Klarer, W. Kongko, B. G. McAdoo, A. L. Moore, and S. U. Sudrajat (2008), A 1,000-year sediment record of tsunami recurrence in northern Sumatra, *Nature*, *455*(7217), 1232-1234.

Morton, R. A., G. Gelfenbaum, and B. E. Jaffe (2007), Physical criteria for distinguishing sandy tsunami and storm deposits using modern examples, *Sedimentary Geology*, *200*(3–4), 184-207, doi:http://dx.doi.org/10.1016/j.sedgeo.2007.01.003.

Muis, S., M. Verlaan, H. C. Winsemius, J. C. J. H. Aerts, and P. J. Ward (2016), A global reanalysis of storm surges and extreme sea levels, *Nat Commun*, *7*, doi:10.1038/ncomms11969.

Nanayama, F., K. Shigeno, K. Satake, K. Shimokawa, S. Koitabashi, S. Miyasaka, and M. Ishii (2000), Sedimentary differences between the 1993 Hokkaido-nansei-oki tsunami and the 1959 Miyakojima typhoon at Taisei, southwestern Hokkaido, northern Japan, *Sedimentary Geology*, *135*(1–4), 255-264, doi:http://dx.doi.org/10.1016/S0037-0738(00)00076-2.

Neumann, B., A. T. Vafeidis, J. Zimmermann, and R. J. Nicholls (2015), Future Coastal Population Growth and Exposure to Sea-Level Rise and Coastal Flooding - A Global Assessment, *PLoS ONE*, *10*(3), 1-34, doi:10.1371/journal.pone.0118571.

Newey, W. K., and K. D. West (1987), A Simple, Positive Semi-Definite, Heteroskedasticity and Autocorrelation Consistent Covariance Matrix, *Econometrica*, *55*(3), 703-708, doi:10.2307/1913610.

Newey, W. K., and K. D. West (1994), Automatic Lag Selection in Covariance Matrix Estimation, edited, p. 631, Review of Economic Studies Ltd.

Nicholls, R. J. (2010), Impacts of and Responses to Sea-Level Rise, in *Understanding Sea-Level Rise and Variability*, edited, pp. 17-51, Wiley-Blackwell, doi:10.1002/9781444323276.ch2.

Nott, J. (2011), A 6000 year tropical cyclone record from Western Australia, *Quat. Sci. Rev.*, *30*(5–6), 713-722, doi:http://dx.doi.org/10.1016/j.quascirev.2010.12.004.

Oksanen, J., F. G. Blanchet, R. Kindt, P. Legendre, P. R. Minchin, R. B. O'Hara, G. L. Simpson, P. Solymos, and M. H. H. S. H. Wagner (2016), vegan: Community Ecology Package, edited.

Ozsoy, O., I. D. Haigh, M. P. Wadey, R. J. Nicholls, and N. C. Wells (2016), High-frequency sea level variations and implications for coastal flooding: A case study of the Solent, UK, *Continental Shelf Research*, *122*, 1-13, doi:http://dx.doi.org/10.1016/j.csr.2016.03.021.

Paris, R., A. D. Switzer, M. Belousova, A. Belousov, B. Ontowirjo, P. L. Whelley, and M. Ulvrova (2014), Volcanic tsunami: a review of source mechanisms, past events and hazards in Southeast Asia (Indonesia, Philippines, Papua New Guinea), *Natural Hazards*, *70*(1), 447-470, doi:10.1007/s11069-013-0822-8.

Parker, B. B. (1992), Sea Level as an Indicator of Climate and Global Change, *Marine Technology Society Journal*, *Vol. 25*(No. 4).

Pawlowicz, R., B. Beardsley, and S. Lentz (2002), Classical tidal harmonic analysis including error estimates in MATLAB using T_TIDE, *Computers & Geosciences*, *28*(8), 929-937, doi:http://dx.doi.org/10.1016/S0098-3004(02)00013-4.

Peng, D., H. Palanisamy, A. Cazenave, and B. Meyssignac (2013), Interannual Sea Level Variations in the South China Sea Over 1950-2009, *Mar. Geod.*, *36*(2), 164-182, doi:10.1080/01490419.2013.771595.

Permanent Service for Mean Sea Level (PSMSL) (2016), "Tide Gauge Data", Retrieved 29 Feb 2016 from http://www.psmsl.org/data/obtaining/. edited.

Phantuwongraj, S., and M. Choowong (2012), Tsunamis versus storm deposits from Thailand, *Natural Hazards*, *63*(1), 31-50.

Prendergast, A., M. Cupper, K. Jankaew, and Y. Sawai (2012), Indian Ocean tsunami recurrence from optical dating of tsunami sand sheets in Thailand, *Marine Geology*, *295-298*, 20-27, doi:10.1016/j.margeo.2011.11.012.

Pugh, D., and P. L. Woodworth (2014), *Sea-Level Science: Understanding Tides, Surges, Tsunami and Mean Sea-Level Changes*, 407 pp., Cambridge University Press, New York.

Pugh, D. T. (1987), *Tide, Surges and Mean Sea Level*, 472 pp., John Wiley, Chichester, U.K.

Qu, T., Y. Y. Kim, M. Yaremchuk, T. Tozuka, A. Ishida, and T. Yamagata (2004), Can Luzon Strait Transport Play a Role in Conveying the Impact of ENSO to the South China Sea?, *Journal of Climate*, *17*(18), 3644-3657, doi:10.1175/1520-0442(2004)017<3644:CLSTPA>2.0.CO;2.

Qu, T., Y. T. Song, and T. Yamagata (2009), An introduction to the South China Sea throughflow: Its dynamics, variability, and application for climate, *Dynamics of Atmospheres and Oceans*, *47*(1-3), 3-14, doi:10.1016/j.dynatmoce.2008.05.001.

R Core Team (2014), R: A language and environment for statistical computing, edited, R Foundation for Statistical Computing, Vienna, Austria.

Rao, A., and E.-C. Hsu (2008), *Hilbert-Huang Transform Analysis Of Hydrological And Environmental Time Series.*, Dordrecht : Springer Science+Business Media B.V., 2008.

Rodolfo, K. S., and F. P. Siringan (2006), Global sea-level rise is recognised, but flooding from anthropogenic land subsidence is ignored around northern Manila Bay, Philippines, *Disasters*, *30*(1), 118-139, doi:10.1111/j.1467-9523.2006.00310.x.

Rodríguez, S., G. Huerta, and H. Reyes (2015), A study of trends for Mexico City ozone extremes, *Communications in Statistics: Case Studies, Data Analysis and Applications*, *1*(3), 151-160, doi:10.1080/23737484.2015.1121791.

Rong, Z., Y. Liu, H. Zong, and Y. Cheng (2007), Interannual sea level variability in the South China Sea and its response to ENSO, *Global and Planetary Change*, *55*(4), 257-272, doi:10.1016/j.gloplacha.2006.08.001.

Rousseeuw, P. J. (1987), Silhouettes: a graphical aid to the interpretation and validation of cluster analysis, *Journal of Computational and Applied Mathematics*, *20*(0), 53-65, doi:http://dx.doi.org/10.1016/0377-0427(87)90125-7.

Saji, N. H., B. N. Goswami, P. N. Vinayachandran, and T. Yamagata (1999), A dipole mode in the tropical Indian Ocean, *Nature*, *401*(6751), 360-363.

Saramul, S., and T. Ezer (2014), Spatial variations of sea level along the coast of Thailand: Impacts of extreme land subsidence, earthquakes and the seasonal monsoon, *Global and Planetary Change*, *122*, 70-81, doi:10.1016/j.gloplacha.2014.08.012.

Sawai, Y., K. Jankaew, M. E. Martin, A. Prendergast, M. Choowong, and T. Charoentitirat (2009), Diatom assemblages in tsunami deposits associated with the 2004 Indian Ocean tsunami at Phra Thong Island, Thailand, *Marine Micropaleontology*, *73*(1-2), 70-79.

Scheffers, A., D. Brill, D. Kelletat, H. Brückner, S. Scheffers, and K. Fox (2012), Holocene sea levels along the Andaman Sea coast of Thailand, *Holocene*, *22*(10), 1169-1180, doi:10.1177/0959683612441803.

Shanmugam, G. (2012), Process-sedimentological challenges in distinguishing paleo-tsunami deposits, *Natural Hazards*, *63*(1), 5-30.

Slangen, A. B. A., F. Adloff, S. Jevrejeva, P. W. Leclercq, B. Marzeion, Y. Wada, and R. Winkelmann (2016), A Review of Recent Updates of Sea-Level Projections at Global and Regional Scales, *Surveys in Geophysics*, 1-22, doi:10.1007/s10712-016-9374-2.

Soria, J. L. A., A. D. Switzer, C. L. Villanoy, H. M. Fritz, P. H. T. Bilgera, O. C. Cabrera, F. P. Siringan, Y. Y.-S. Maria, R. D. Ramos, and I. Q. Fernandez (2015), Repeat Storm Surge Disasters of Typhoon Haiyan and Its 1897 Predecessor in the Philippines, *Bull. Am. Meteorol. Soc.*, *97*(1), 31-48, doi:10.1175/BAMS-D-14-00245.1.

Soumya, M., P. Vethamony, and P. Tkalich (2015), Inter-annual sea level variability in the southern South China Sea, *Global and Planetary Change*, *133*, 17-26, doi:10.1016/j.gloplacha.2015.07.003.

Spiske, M., J. Piepenbreier, C. Benavente, and H. Bahlburg (2013), Preservation potential of tsunami deposits on arid siliciclastic coasts, *Earth-Science Reviews*, *126*, 58-73, doi:http://dx.doi.org/10.1016/j.earscirev.2013.07.009.

Sturtz, S., U. Ligges, and A. Gelman (2005), R2WinBUGS: A Package for Running WinBUGS from R, *Journal of Statistical Software*, *12*(3), 1-16.

Sugawara, D., K. Goto, and B. E. Jaffe (2014), Numerical models of tsunami sediment transport — current understanding and future directions, *Marine Geology*, *352*(0), 295-320, doi:http://dx.doi.org/10.1016/j.margeo.2014.02.007.

Sweeney-Reed, C. M., and S. J. Nasuto (2007), A novel approach to the detection of synchronisation in EEG based on empirical mode decomposition, *Journal of Computational Neuroscience*, *23*(1), 79-111, doi:10.1007/s10827-007-0020-3.

Switzer, A. D., C. Gouramanis, T. Dura, D. D. Lam, L. V. Hoang, C. R. Sloss, Q. D. Hoang, Y. S. Lee, M. M. Chan, and D. T. Pham (2011), Geological and Geomorphological Impacts of Two Large Typhoons from the Central Coast Of Vietnam paper presented at AGU Fall Meeting San Francisco, CA, USA, 5-9, 2011

Switzer, A. D., and B. G. Jones (2008), Large-scale washover sedimentation in a freshwater lagoon from the southeast Australian coast: sea-level change, tsunami or exceptionally large storm?, *Holocene*, *18*(5), 787-803.

Switzer, A. D., K. Pucillo, R. A. Haredy, B. G. Jones, and E. A. Bryant (2005), Sea level, storm, or tsunami: Enigmatic sand sheet deposits in a sheltered coastal embayment from Southeastern New South Wales, Australia, *Journal of Coastal Research*, *21*(4), 655-663.

Switzer, A. D., S. Srinivasalu, N. Thangadurai, and V. Ram Mohan (2012), Bedding structures in Indian tsunami deposits that provide clues to the dynamics of tsunami inundation, *Geological Society Special Publication*, *361*(1), 61-77.

Switzer, A. D., F. Yu, C. Gouramanis, J. Soria, and T. D. Pham (2014), An integrated approach to assessing coastal hazards at multi-century timescales, *Journal of Coastal Research*, *Special Issue No.70*, 723-728.

Syvitski, J. P. M., A. J. Kettner, I. Overeem, E. W. H. Hutton, M. T. Hannon, G. R. Brakenridge, J. Day, C. Vorosmarty, Y. Saito, L. Giosan, and R. J. Nicholls (2009), Sinking deltas due to human activities, *Nature Geoscience*, *2*(10), 681-686, doi:http://www.nature.com/ngeo/journal/v2/n10/suppinfo/ngeo629_S1.html.

Szczuciński, W., N. Chaimanee, P. Niedzielski, G. Rachlewicz, D. Saisuttichai, T. Tepsuwan, S. Lorenc, and J. Siepak (2006), Environmental and geological impacts of the 26 December 2004 tsunami in coastal zone of Thailand - overview of short and long-term effects, *Polish Journal of Environmental Studies*, *15*(5), 793-810.

Szczuciński, W., P. Niedzielski, L. Kozak, M. Frankowski, A. Zioła, and S. Lorenc (2007), Effects of rainy season on mobilization of contaminants from tsunami deposits left in a coastal zone of Thailand by the 26 December 2004 tsunami, *Environmental Geology*, *53*(2), 253-264.

Szczuciński, W., P. Niedzielski, G. Rachlewicz, T. Sobczyński, A. Zioła, A. Kowalski, S. Lorenc, and J. Siepak (2005), Contamination of tsunami sediments in a coastal zone inundated by the 26 December 2004 tsunami in Thailand, *Environmental Geology*, *49*(2), 321-331.

Tabachnick, B. G., and L. S. Fidell (2013), *Using multivariate statistics*, sixth ed., Pearson Education, Boston.

Talke, S. A., P. Orton, and D. A. Jay (2014), Increasing storm tides in New York Harbor, 1844–2013, *Geophys. Res. Lett.*, *41*(9), 3149-3155, doi:10.1002/2014GL059574.

Tanaka, G., H. Naruse, S. Yamashita, and K. Arai (2012), Ostracodes reveal the sea-bed origin of tsunami deposits, *Geophys. Res. Lett.*, *39*(5), doi:10.1029/2012GL051320.

Thai Meteorological Department (2007), Report for 40th Session of ESCAP/WMO Typhoon Committee*Rep.*, 40th Session of Typhoon Committee, 21-26 November, Macao http://severe.worldweather.org/tcc/creport.htm.

Thai Meteorological Department (2012), Climate of Thailand*Rep.*, Bangkok http://www.tmd.go.th/en/archive/thailand_climate.pdf, http://www.tmd.go.th/en/archive/thailand_climate.pdf.

Tkalich, P., P. Vethamony, M. T. Babu, and P. Malanotte-Rizzoli (2013), Storm surges in the Singapore Strait due to winds in the South China Sea, *Natural Hazards*, *66*(3), 1345-1362, doi:10.1007/s11069-012-0211-8.

Torrence, C., and G. P. Compo (1998), A Practical Guide to Wavelet Analysis, *Bull. Am. Meteorol. Soc.*, *79*(1), 61-78.

Torres, R. R., and M. N. Tsimplis (2014), Sea level extremes in the Caribbean Sea, *Journal of Geophysical Research: Oceans*, *119*(8), 4714-4731, doi:10.1002/2014JC009929.

Trauth, M. H. (2015), *MATLAB® Recipes for Earth Sciences*, 4 ed., 427 pp., Springer-Verlag Berlin Heidelberg, doi:10.1007/978-3-662-46244-7.

Trisirisatayawong, I., M. Naeije, W. Simons, and L. Fenoglio-Marc (2011), Sea level change in the Gulf of Thailand from GPS-corrected tide gauge data and multi-satellite altimetry, *Global and Planetary Change*, *76*(3-4), 137-151, doi:10.1016/j.gloplacha.2010.12.010.

Tsimplis, M. N., and P. L. Woodworth (1994), The global distribution of the seasonal sea level cycle calculated from coastal tide gauge data, *Journal of Geophysical Research*, *99*(C8), 16031-16031, doi:10.1029/94JC01115.

Tsuji, Y., Y. Namegaya, H. Matsumoto, S.-I. Iwasaki, W. Kanbua, M. Sriwichai, and V. Meesuk (2006), The 2004 Indian tsunami in Thailand: Surveyed runup heights and tide gauge records, *Earth, Planets and Space 58*(2), 223-232.

Tuttle, M. P., A. Ruffman, T. Anderson, and H. Jeter (2004), Distinguishing tsunami from storm deposits in eastern North America: the 1929 Grand Banks tsunami versus the 1991 Halloween storm, *Seismological Research Letters*, *75*(1), 117-131, doi:10.1785/gssrl.75.1.117.

Venables, W. N., and B. D. Ripley (2002), *Modern applied statistics with S*, fourth ed., Springer, New York.

Vinogradov, S. V., and R. M. Ponte (2011), Low-frequency variability in coastal sea level from tide gauges and altimetry, *Journal of Geophysical Research: Oceans*, *116*(C7), doi:10.1029/2011JC007034.

Wahl, T., and D. P. Chambers (2015), Evidence for multidecadal variability in US extreme sea level records, *Journal of Geophysical Research: Oceans*, *120*(3), 1527-1544, doi:10.1002/2014JC010443.

Wahl, T., and D. P. Chambers (2016), Climate controls multidecadal variability in U. S. extreme sea level records, *Journal of Geophysical Research: Oceans*, *121*(2), 1274-1290, doi:10.1002/2015JC011057.

Wang, B. (2006), *The Asian Monsoon*, Berlin, Heidelberg : Praxis Publishing Ltd, Chichester, UK, 2006.

Wang, B., F. Huang, Z. Wu, J. Yang, X. Fu, and K. Kikuchi (2009), Multi-scale climate variability of the South China Sea monsoon: A review, *Dynamics of Atmospheres and Oceans*, *47*(1–3), 15-37, doi:http://dx.doi.org/10.1016/j.dynatmoce.2008.09.004.

Wang, C., W. Wang, D. Wang, and Q. Wang (2006a), Interannual variability of the South China Sea associated with El Niño, *Journal of Geophysical Research*, *111*(C3), C03023, doi:10.1029/2005JC003333.

Wang, D., Q. Liu, R. X. Huang, Y. Du, and T. Qu (2006b), Interannual variability of the South China Sea throughflow inferred from wind data and an ocean data assimilation product, *Geophys. Res. Lett.*, *33*(14), L14605, doi:10.1029/2006GL026316.

Wang, G., J. Su, Y. Ding, and D. Chen (2007), Tropical cyclone genesis over the south China sea, *Journal of Marine Systems*, *68*(3–4), 318-326, doi:http://dx.doi.org/10.1016/j.jmarsys.2006.12.002.

Wang, L., and W. Chen (2010), How well do existing indices measure the strength of the East Asian winter monsoon?, *Advances in Atmospheric Sciences*, *27*(4), 855-870, doi:10.1007/s00376-009-9094-3.

Wang, L., and W. Chen (2013a), The East Asian winter monsoon: re-amplification in the mid-2000s, *Chinese Science Bulletin*, *59*(4), 430-436, doi:10.1007/s11434-013-0029-0.

Wang, L., and W. Chen (2013b), An Intensity Index for the East Asian Winter Monsoon, *Journal of Climate*, *27*(6), 2361-2374, doi:10.1175/JCLI-D-13-00086.1.

Wang, Y., G. Fang, Z. Wei, F. Qiao, and H. Chen (2006c), Interannual variation of the South China Sea circulation and its relation to El Niño, as seen from a variable grid global ocean model, *Journal of Geophysical Research*, *111*(C11), C11S14, doi:10.1029/2005JC003269.

West, M., and J. Harrison (1997), *Bayesian Forecasting and Dynamic Models.* , 2nd ed., New York, NY : Springer New York : Imprint: Springer, 1989., doi:10.1007/b98971.

White, N. J., I. D. Haigh, J. A. Church, T. Koen, C. S. Watson, T. R. Pritchard, P. J. Watson, R. J. Burgette, K. L. McInnes, Z. J. You, X. Zhang, and P. Tregoning (2014), Australian sea levels-Trends, regional variability and influencing factors, *Earth-Science Reviews*, *136*, 155-174, doi:10.1016/j.earscirev.2014.05.011.

Wien, K., D. Wissmann, M. Kölling, and H. D. Schulz (2005), Fast application of X-ray fluorescence spectrometry aboard ship: how good is the new portable Spectro Xepos analyser?, *Geo-Marine Letters*, *25*(4), 248-264, doi:10.1007/s00367-004-0206-x.

Williams, M. L., B. G. Jones, and P. F. Carr (2012), Geochemical consequences of the Permian–Triassic mass extinction in a non-marine succession, Sydney Basin, Australia, *Chemical Geology*, *326–327*, 174-188, doi:http://dx.doi.org/10.1016/j.chemgeo.2012.07.021.

Williamson, F., R. Allan, A. D. Switzer, J. C. L. Chan, R. J. Wasson, R. D’Arrigo, and R. Gartner (2015), New directions in hydro-climatic histories: observational data recovery, proxy records and the atmospheric circulation reconstructions over the earth (ACRE) initiative in Southeast Asia, *Geoscience Letters*, *2*(1), 1-12, doi:10.1186/s40562-015-0018-z.

Wolter, K., and M. S. Timlin (1993), Monitoring ENSO in COADS with a seasonally adjusted principal component index in *17th Climate Diagnostics Workshop*, edited, pp. 52-57, NOAA/NMC/CAC, NSSL, Oklahoma Clim. Survey, CIMMS and the School of Meteor., Univ. of Oklahoma, Norman, OK.

Wolter, K., and M. S. Timlin (1998), Measuring the strength of ENSO events: How does 1997/98 rank?, *Weather*, *53*(9), 315-324, doi:10.1002/j.1477-8696.1998.tb06408.x.

Woodworth, P. L., and D. L. Blackman (2004), Evidence for systematic changes in extreme high waters since the mid-1970s, *Journal of Climate*, *17*(6), 1190-1197.

Wu, C.-R., and C. W. J. Chang (2005), Interannual variability of the South China Sea in a data assimilation model, *Geophys. Res. Lett.*, *32*(17), L17611, doi:10.1029/2005GL023798.

Wu, Z., and N. E. Huang (2009), Ensemble Empirical Mode Decomposition: A noise-assisted data analysis method, *Advances in Adaptive Data Analysis*, *01*(01), 1-41, doi:10.1142/S1793536909000047.

Wu, Z., N. E. Huang, S. R. Long, and C.-K. Peng (2007), On the trend, detrending, and variability of nonlinear and nonstationary time series, *Proceedings of the National Academy of Sciences*, *104*(38), 14889-14894.

Wyrtki, K. (1961), Physical Oceanography of the Southeast Asian Waters*Rep.*, 27-27 pp.

Xie, F., J. Li, W. Tian, J. Zhang, and C. Sun (2014), The relative impacts of El Niño Modoki, canonical El Niño, and QBO on tropical ozone changes since the 1980s, *Environmental Research Letters*, *9*(6), doi:10.1088/1748-9326/9/6/064020.

Xie, S.-P., Q. Xie, D. Wang, and W. T. Liu (2003), Summer upwelling in the South China Sea and its role in regional climate variations, *Journal of Geophysical Research: Oceans*, *108*(C8), doi:10.1029/2003JC001867.

Zhang, Z., W. Zhao, J. Tian, Q. Yang, and T. Qu (2015), Spatial structure and temporal variability of the zonal flow in the Luzon Strait, *Journal of Geophysical Research C: Oceans*, *120*(2), 759-776, doi:10.1002/2014JC010308.